



National Library
of Canada

Acquisitions and
Bibliographic Services Branch

395 Wellington Street
Ottawa, Ontario
K1A 0N4

Bibliothèque nationale
du Canada

Direction des acquisitions et
des services bibliographiques

395, rue Wellington
Ottawa (Ontario)
K1A 0N4

Your file *Votre référence*

Our file *Notre référence*

NOTICE

The quality of this microform is heavily dependent upon the quality of the original thesis submitted for microfilming. Every effort has been made to ensure the highest quality of reproduction possible.

If pages are missing, contact the university which granted the degree.

Some pages may have indistinct print especially if the original pages were typed with a poor typewriter ribbon or if the university sent us an inferior photocopy.

Reproduction in full or in part of this microform is governed by the Canadian Copyright Act, R.S.C. 1970, c. C-30, and subsequent amendments.

AVIS

La qualité de cette microforme dépend grandement de la qualité de la thèse soumise au microfilmage. Nous avons tout fait pour assurer une qualité supérieure de reproduction.

S'il manque des pages, veuillez communiquer avec l'université qui a conféré le grade.

La qualité d'impression de certaines pages peut laisser à désirer, surtout si les pages originales ont été dactylographiées à l'aide d'un ruban usé ou si l'université nous a fait parvenir une photocopie de qualité inférieure.

La reproduction, même partielle, de cette microforme est soumise à la Loi canadienne sur le droit d'auteur, SRC 1970, c. C-30, et ses amendements subséquents.

UNIVERSITY OF ALBERTA

Relativistic Treatment of Pion Photoproduction on Nuclei

BY

Jon Ingvar Johansson



**A thesis submitted to the Faculty of Graduate Studies and Research in partial fulfillment
of the requirements for the degree of DOCTOR OF PHILOSOPHY**

IN

Nuclear Physics

DEPARTMENT OF PHYSICS

EDMONTON, ALBERTA

SPRING 1993



National Library
of Canada

Acquisitions and
Bibliographic Services Branch

395 Wellington Street
Ottawa, Ontario
K1A 0N4

Bibliothèque nationale
du Canada

Direction des acquisitions et
des services bibliographiques

395, rue Wellington
Ottawa (Ontario)
K1A 0N4

Your file *Votre référence*

Our file *Notre référence*

The author has granted an irrevocable non-exclusive licence allowing the National Library of Canada to reproduce, loan, distribute or sell copies of his/her thesis by any means and in any form or format, making this thesis available to interested persons.

L'auteur a accordé une licence irrévocable et non exclusive permettant à la Bibliothèque nationale du Canada de reproduire, prêter, distribuer ou vendre des copies de sa thèse de quelque manière et sous quelque forme que ce soit pour mettre des exemplaires de cette thèse à la disposition des personnes intéressées.

The author retains ownership of the copyright in his/her thesis. Neither the thesis nor substantial extracts from it may be printed or otherwise reproduced without his/her permission.

L'auteur conserve la propriété du droit d'auteur qui protège sa thèse. Ni la thèse ni des extraits substantiels de celle-ci ne doivent être imprimés ou autrement reproduits sans son autorisation.

ISBN 0-315-82160-4

Canada

UNIVERSITY OF ALBERTA

RELEASE FORM

NAME OF AUTHOR: Jon Ingvar Johansson

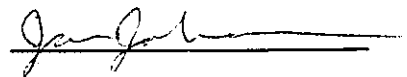
TITLE OF THESIS: Relativistic Treatment of Pion
Photoproduction on Nuclei

DEGREE: Doctor of Philosophy

YEAR THIS DEGREE GRANTED: 1993

Permission is hereby granted to the University of Alberta Library to reproduce single copies of this thesis and to lend or sell such copies for private, scholarly or scientific research purposes only.

The author reserves all other publication and other rights in association with the copyright in the thesis, and except as hereinbefore provided neither the thesis nor any substantial portion thereof may be printed or otherwise reproduced in any material form whatever without the author's prior written permission.



Department of Physics
University of Alberta
Edmonton, Alberta
Canada, T6G 2J1

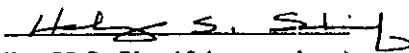
DATE: April 23, 1993

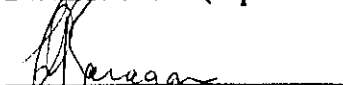


UNIVERSITY OF ALBERTA

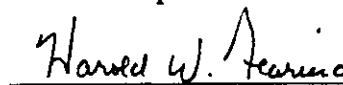
FACULTY OF GRADUATE STUDIES AND RESEARCH

The undersigned certify that they have read, and recommend to the Faculty of Graduate Studies and Research for acceptance, a thesis entitled RELATIVISTIC TREATMENT OF PION PHOTOPRODUCTION ON NUCLEI submitted by JON INGVAR JOHANSSON in partial fulfillment of the requirements for the degree of Doctor of Philosophy in Nuclear Physics.

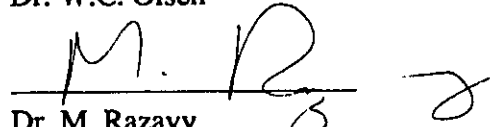

Dr. H.S. Sherif (supervisor)


Dr. F.A. Baragar


Dr. A.Z. Capri


Dr. H. Fearing (external examiner)


Dr. W.C. Olsen


Dr. M. Razavy

DATE: April 19, 1993

Abstract

A relativistic one-nucleon model for the charged pion photoproduction reaction on a nucleus is discussed. The specific reactions considered are $(\gamma, \pi^- p)$ and the related process $(\pi^+, \gamma p)$. The incident particle reacts with a single nucleon, while the rest of the nucleus acts as a spectator. The interaction of the projectile with the target nucleon is comprised of the gauge invariant set of Born terms, arising from the pseudovector form of the pion-nucleon interaction lagrangian, as well as s- and u-channel diagrams involving delta propagation. The latter are each separately gauge invariant. The calculations are done in coordinate space and require the solution of eight-dimensional space-time integrals, which are simplified by making the following approximations for diagrams that involve intermediate state propagation: i) the intermediate particle propagates without interaction with the nuclear medium, and ii) the outer legs of one vertex are plane waves. The propagator for each diagram is then the free momentum-space propagator for the particle times a coordinate-space delta-function (a local operator), and the integration at one vertex is done trivially. The remaining calculations of the amplitude are then carried out in the distorted wave framework. Both the bound and continuum state nucleons are described by solutions of the Dirac equation with appropriate vector and scalar potentials. The pion wave function is a solution of the Klein-Gordon equation; the interaction of the pion with the residual nucleus is taken into account by including an optical potential. The contribution of each of the diagrams to the differential cross section and the final proton's polarization, under different kinematic conditions, are explored. In particular we study the role of the Δ resonance in the reaction. We find the contribution of the delta to be important in the resonance region, but for the $(\gamma, \pi^- p)$ reaction there was no case found in which that contribution is the dominant one. For the $(\pi^+, \gamma p)$ reaction we found one kinematic arrangement for which the delta provides the largest contribution to the cross section. The effects of changes in the binding and interaction potentials are also studied. Finally the results of the model are compared to the existing data. Qualitative agreement with the few data sets available is achieved. This study points out the need for more precise measurements of these reactions.

Acknowledgements

I would like to express my gratitude to my supervisor, Dr. H.S. Sherif, for allowing me the freedom to choose my own way through the jungle of relativistic nuclear physics, and for his kindness and insight when I needed guidance to find the path when I strayed.

I am indebted to Dr. E.D. Cooper for invaluable discussions concerning nuclear physics and field theory, and also for sharing with me some of the art of computer programming.

Evans Hayward of the National Institute of Standards and Technology very generously shared with me an unpublished manuscript [Hay92] which reviewed and clarified the physics of total photonuclear absorption above the pion production threshold. She also very thoughtfully provided me with some of the absorption data on nuclei which she had compiled. John H. Hubbell also of the National Institute of Standards and Technology kindly provided me with a great deal of invaluable information about photon absorption.

Finally I would like to extend my thanks and warmest wishes to all the people who make up the Department of Physics at the University of Alberta. They are a unique group who have made my experience as a graduate student much more than an education in physics; they made graduate work a lot of fun.

Table of Contents

Relativistic Treatment of Pion Photoproduction on Nuclei

Chapter 1 - Introduction	1
1.1 The Quasifree Region and the Distorted Wave Impulse Approximation	3
1.2 Experiments and Their Interpretation	7
1.3 A Dirac Equation Based Model of Pion Photoproduction on a Nucleus	12
Chapter 2 - A One Nucleon Model for the Reaction $A(\gamma, \pi^- p)A-1$	15
2.1 Model Lagrangian	15
2.2 Scattering Matrix	20
2.2.1 Seagull Diagram	21
2.2.2 The Pion Pole	25
2.2.3 The Nucleon Poles	27
2.2.4 $\Delta(1232)$ Poles	30
2.3 Plane Waves	34
2.4 Distorted Waves	36
2.5 Gauge Invariance	40
2.6 Observables for $A(\gamma, \pi^- p)A-1$	41
2.7 Programming Tests	42
Chapter 3 - Relativistic Potential Models for the Pion and the Nucleon	44
3.1 A Simple Model	44
3.2 Nonrelativistic Optical Model for Nucleon-Nucleus Scattering	47
3.3 Relativistic Description of Nucleon-Nucleus Elastic Scattering	48
3.4 Bound State Wave Function	55
3.5 Pion Phenomenology	56
3.5.1 Pion-Nucleon Scattering	56
3.5.2 Pion-Nucleus Scattering	61
3.5.3 Radial Equation for the Pion	65
Chapter 4 - Results for the Reaction $A(\gamma, \pi^- p)A-1$	68
4.1 Sensitivity to Changes in the Wave Functions	68
4.2 Nearly Free Kinematics	91

4.3 Behaviour Under Kinematic Changes	113
4.4 Comparison With Experimental Data	131
4.4.1 The Tomsk 1979 Experiment	131
4.4.2 The Tomsk 1990 Experiment	135
4.4.3 The MIT Experiment	147
Chapter 5 - A One Nucleon Model for the Reaction $A(\pi^+, \gamma p)A-1$	170
5.1 The Reaction Amplitude	172
5.2 Plane Waves	174
5.3 Distorted Waves	174
5.4 Gauge Invariance	177
5.5 Observables for $A(\pi^+, \gamma p)A-1$	178
5.6 Results for the Reaction $A(\pi^+, \gamma p)A-1$	179
Chapter 6 - Conclusion	196
References	202
Appendix A - Isospin Considerations	207
A.1 Field Operators	207
A.2 The $T=1/2$ to $T=3/2$ Isospin Transition Operator	212
Appendix B - Approximating Propagators	215
Appendix C - Angular Integrals	219
Appendix D - Observables	225
D.1 Cross Section	225
D.2 Polarization	227
D.3 Asymmetry (or Analyzing Power)	229
Appendix E - Time Ordering With Derivative Coupling	230
Appendix F - Free Process $\gamma + n \rightarrow \pi^- + p$	232
F.1 Elementary Pion Photoproduction $\gamma + N \rightarrow \pi + N$	232
F.2 The Pion Photoproduction Operator of Blomqvist and Laget	242

List of Figures

Figure	Description	Page
1-1.	Total photonuclear absorption as a function of photon lab energy.	2
1-2.	Generic inelastic scattering spectrum.	4
2-1.	The one nucleon model for $A(\gamma, \pi^- p)A-1$.	15
2-2.	Diagrams contributing to pion photoproduction on a nucleus.	16
2-3.	Coordinate system for pion photoproduction on a nucleus.	38
3-1.	Projectiles incident from the left on a semi-infinite slab of nuclear matter.	45
3-2.	Potentials for proton elastic scattering from ^{12}C at $T_p = 160$ MeV.	53
3-3.	Elastic scattering observables for $p + ^{12}\text{C}$ at $T_p = 160$ MeV.	54
3-4.	Momentum space bound state wave functions for the $1p_{3/2}$ level in ^{12}C .	57
3-5.	Pion-nucleon scattering in the center of momentum system.	58
3-6.	Diagram contributing to second order corrections in the pion-nucleus optical potential.	61
3-7.	Nucleon- and Δ -hole intermediate states contributing to the pion self energy.	64
3-8.	π^- elastic scattering from ^{12}C at $T_\pi = 50$ MeV.	66
4-1.	Variation of kinematic quantities for the reaction $^{12}\text{C}(\gamma, \pi^- p)^{11}\text{C}_{\text{g.s.}}$, with $E_\gamma = 380$ MeV, $(\theta_\pi = 120^\circ, \phi_\pi = 0^\circ)$ and $(\theta_p = 20^\circ, \phi_p = 180^\circ)$.	69
4-2.	Dependence of the cross section on distortions of the final proton and pion.	71
4-3.	Dependence of the spin observables on distortions of the final proton and pion.	73
4-4.	Dependence of the cross section on changes in pion distortion.	74
4-5.	Dependence of the spin observables on changes in pion distortion.	76
4-6.	Dependence of the cross section on changes in proton distortion.	77
4-7.	Dependence of the spin observables on changes in proton distortion.	79
4-8.	Sensitivity of the cross section to changes in the bound state wave function.	80
4-9.	Sensitivity of the spin observables to changes in the bound state wave function.	81
4-10.	Momentum transfer when the proton angle is increased so we have $E_\gamma = 380$ MeV, $(\theta_\pi = 120^\circ, \phi_\pi = 0^\circ)$ and $(\theta_p = 70^\circ, \phi_p = 180^\circ)$.	83
4-11.	Sensitivity of the cross section to changes in the bound state wave function for large momentum transfer, with pion and proton plane waves.	84
4-12.	Sensitivity of the cross section to changes in the bound state wave function for large momentum transfer, with pion and proton distorted waves.	85

4-13. Sensitivity of the spin observables to changes in the bound state wave function for large momentum transfer, with pion and proton plane waves.	86
4-14. Sensitivity of the spin observables to changes in the bound state wave function for large momentum transfer, with pion and proton distorted waves.	87
4-15. Sensitivity of the cross section to changes in the separation energy of the $1p_{3/2}$ neutron wave function.	88
4-16. Sensitivity of the spin observables to changes in the separation energy of the $1p_{3/2}$ neutron wave function.	90
4-17. Variation of kinematic quantities for the reaction $^{12}\text{C}(\gamma, \pi^- p)^{11}\text{C}_{\text{g.s.}}$, with nearly free kinematics and the c.m. pion angle fixed at $\theta_\pi = 45^\circ$.	93
4-18. The cross section near free kinematics with the c.m. pion angle $\theta_\pi = 45^\circ$, PW and DW calculations.	94
4-19. The cross section near free kinematics with the c.m. pion angle $\theta_\pi = 45^\circ$, DW calculations, compare Born and delta contributions.	95
4-20. Contribution of the individual diagrams to the DW calculation of the cross section.	97
4-21. The spin observables near free kinematics with the c.m. pion angle $\theta_\pi = 45^\circ$.	98
4-22. Variation of kinematic quantities for the reaction $^{12}\text{C}(\gamma, \pi^- p)^{11}\text{C}_{\text{g.s.}}$, with nearly free kinematics and the c.m. pion angle fixed at $\theta_\pi = 90^\circ$.	100
4-23. The cross section near free kinematics with the c.m. pion angle $\theta_\pi = 90^\circ$, PW and DW calculations.	101
4-24. The cross section near free kinematics with the c.m. pion angle $\theta_\pi = 90^\circ$, DW calculations, compare Born and delta contributions.	103
4-25. Contribution of the individual diagrams to the DW calculation of the cross section.	104
4-26. The spin observables near free kinematics with the c.m. pion angle $\theta_\pi = 90^\circ$.	105
4-27. Variation of kinematic quantities for the reaction $^{12}\text{C}(\gamma, \pi^- p)^{11}\text{C}_{\text{g.s.}}$, with nearly free kinematics and the c.m. pion angle fixed at $\theta_\pi = 135^\circ$.	107
4-28. The cross section near free kinematics with the c.m. pion angle $\theta_\pi = 135^\circ$, PW and DW calculations.	108
4-29. The cross section near free kinematics with the c.m. pion angle $\theta_\pi = 135^\circ$, DW calculations, compare Born and delta contributions.	109
4-30. Contribution of the individual diagrams to the DW calculation of the cross section.	110
4-31. The spin observables near free kinematics with the c.m. pion angle $\theta_\pi = 135^\circ$.	111

4-32. Cross section calculated from Born, delta and all diagrams with: ($\theta_\pi = 120^\circ$, $\phi_\pi = 0^\circ$) and ($\theta_p = 20^\circ$, $\phi_p = 180^\circ$) for incident photon energies a) $E_\gamma = 220$ MeV and b) $E_\gamma = 260$ MeV.	114
4-33. Cross section calculated from Born, delta and all diagrams with for incident photon energies a) $E_\gamma = 300$ MeV and b) $E_\gamma = 340$ MeV.	115
4-34. Cross section calculated from Born, delta and all diagrams with for incident photon energies a) $E_\gamma = 380$ MeV and b) $E_\gamma = 420$ MeV.	116
4-35. Spin observables calculated from Born, delta and all diagrams with $E_\gamma = 220$ MeV.	118
4-36. Spin observables calculated from Born, delta and all diagrams with $E_\gamma = 260$ MeV.	119
4-37. Spin observables calculated from Born, delta and all diagrams with $E_\gamma = 300$ MeV.	120
4-38. Spin observables calculated from Born, delta and all diagrams with $E_\gamma = 340$ MeV.	121
4-39. Spin observables calculated from Born, delta and all diagrams with $E_\gamma = 380$ MeV.	122
4-40. Spin observables calculated from Born, delta and all diagrams with $E_\gamma = 420$ MeV.	123
4-41. Cross section and momentum transfer for various pion angles with $E_\gamma = 380$ MeV and ($\theta_p = 20^\circ$, $\phi_p = 180^\circ$).	125
4-42. Spin observables for various pion angles with $E_\gamma = 380$ MeV and ($\theta_p = 20^\circ$, $\phi_p = 180^\circ$).	126
4-43. Cross section and momentum transfer for various pion angles with $E_\gamma = 380$ MeV and ($\theta_p = 40^\circ$, $\phi_p = 180^\circ$).	127
4-44. Spin observables for various pion angles with $E_\gamma = 380$ MeV and ($\theta_p = 40^\circ$, $\phi_p = 180^\circ$).	128
4-45. Cross section and momentum transfer for various pion angles with $E_\gamma = 380$ MeV and ($\theta_p = 60^\circ$, $\phi_p = 180^\circ$).	129
4-46. Spin observables for various pion angles with $E_\gamma = 380$ MeV and ($\theta_p = 60^\circ$, $\phi_p = 180^\circ$).	130
4-47. Comparison between the DW calculation and data from [G189].	133
4-48. Comparison between the DW calculation and data from [G189].	134
4-49. Dependence of the cross section on the separation energy of the $1s_{1/2}$ neutron.	136
4-50. Variation of kinematic quantities for the reaction $^{12}\text{C}(\gamma, \pi^- p)^{11}\text{C}_{g.s.}$.	

with $E_\gamma = 340$ MeV, ($\theta_\pi = 120^\circ$, $\varphi_\pi = 0^\circ$) and ($\theta_p = 40^\circ$, $\varphi_p = 180^\circ$).	137
4-51. Comparison between the PW and DW calculations and data from [AG89].	138
4-52. Momentum transfer as a function of proton kinetic energy for different pion kinetic energies.	140
4-53. Incident photon energy as a function of proton kinetic energy for different pion kinetic energies.	141
4-54. DW cross section vs. proton kinetic energy with a) $T_\pi = 33.2$ MeV and b) $T_\pi = 44.3$ MeV with data from [AG90].	142
4-55. DW cross section vs. proton kinetic energy with a) $T_\pi = 54.9$ MeV and b) $T_\pi = 65.5$ MeV with data from [AG90].	143
4-56. DW cross section vs. proton kinetic energy with a) $T_\pi = 76.3$ MeV and b) $T_\pi = 87.2$ MeV with data from [AG90].	144
4-57. DW cross section vs. proton kinetic energy with a) $T_\pi = 97.7$ MeV and b) $T_\pi = 107.9$ MeV with data from [AG90].	145
4-58. DW cross section vs. proton kinetic energy with a) $T_\pi = 118.4$ MeV and b) $T_\pi = 129.5$ MeV with data from [AG90].	146
4-59. Kinematics for the MIT experiment.	148
4-60. Cross section vs. proton kinetic energy for four out-of-plane angles with: $E_\gamma = 350$ MeV, ($\theta_\pi = 120^\circ$, $\varphi_\pi = 0^\circ$) and ($\alpha_p = 20^\circ$, β_p varies).	151
4-61. Momentum transfer vs. proton kinetic energy for four out-of-plane angles.	152
4-62. Spin observables as a function of proton k.e. for four out-of-plane angles.	153
4-63. Cross section vs. proton kinetic energy for four out-of-plane angles with: $E_\gamma = 350$ MeV, ($\theta_\pi = 64^\circ$, $\varphi_\pi = 0^\circ$) and ($\alpha_p = 40^\circ$, β_p varies).	154
4-64. Momentum transfer vs. proton kinetic energy for four out-of-plane angles.	156
4-65. Spin observables as a function of proton k.e. for four out-of-plane angles.	157
4-66. DW cross section vs. proton out-of-plane angle with data from [Ph92].	158
4-67. DW cross section vs. proton out-of-plane angle with data from [Ph92].	159
4-68. DW calculations with different integration limits.	161
4-69. DW calculations with different integration limits.	162
4-70. DW cross section calculated from Born, delta and all diagrams.	164
4-71. Contribution of the individual diagrams to the DW cross section.	165
4-72. DW cross section calculated from Born, delta and all diagrams.	166
4-73. Contribution of the individual diagrams to the DW cross section.	167
5-1. The one nucleon model for $A(\pi^+, \gamma p)A-1$.	170
5-2. Diagrams contributing to $A(\pi^+, \gamma p)A-1$.	171
5-3. Coordinate system for $A(\pi^+, \gamma p)A-1$.	176

5-4.	DW cross section as a function of proton k.e. for four proton angles with: $T_{\pi} = 163.7$ MeV and $\theta_{\gamma} = 77.4^{\circ}$.	181
5-5.	Momentum transfer as a function of proton k.e. for four proton angles.	182
5-6.	PW cross section as a function of proton k.e. for four proton angles.	183
5-7.	DW spin observables as a function of proton k.e. for four proton angles.	184
5-8.	DW cross section from Born, delta and all diagrams.	185
5-9.	PW and DW cross section as a function of proton k.e.	186
5-10.	PW and DW calculations of proton polarization as a function of proton k.e.	187
5-11.	DW cross section as a function of proton k.e. for four proton angles with: $T_{\pi} = 218.6$ MeV and $\theta_{\gamma} = 75.2^{\circ}$.	188
5-12.	Momentum transfer as a function of proton k.e. for four proton angles.	189
5-13.	PW cross section as a function of proton k.e. for four proton angles.	190
5-14.	DW spin observables as a function of proton k.e. for four proton angles.	192
5-15.	DW cross section from Born, delta and all diagrams.	193
5-16.	PW and DW cross section as a function of proton k.e.	194
5-17.	PW and DW calculations of proton polarization as a function of proton k.e.	195
B-1.	Two scalar particles interact through the exchange of a different scalar particle.	215
B-2.	Two scalar particles interact through an s-channel Dirac particle.	217
F-1.	Diagrams contributing to the elementary pion photoproduction process $\gamma + n \rightarrow \pi^{-} + p$.	233
F-2.	Cross section and analyzing power as a function of pion c.m. angle for negative pion photoproduction on a free neutron with $E_{\gamma} = 250$ MeV.	237
F-3.	Cross section and analyzing power as a function of pion c.m. angle for negative pion photoproduction on a free neutron with $E_{\gamma} = 300$ MeV.	238
F-4.	Cross section and analyzing power as a function of pion c.m. angle for negative pion photoproduction on a free neutron with $E_{\gamma} = 350$ MeV.	239
F-5.	Cross section and analyzing power as a function of pion c.m. angle for negative pion photoproduction on a free neutron with $E_{\gamma} = 400$ MeV.	240
F-6.	Total cross section as a function of total c.m. energy.	241

List of Tables

Table	Description	Page
2-1.	Coupling constants of the lagrangian model.	19
3-1.	Woods-Saxon binding parameters for ^{12}C .	55
4-1.	Woods-Saxon potential parameters for ^{16}O .	149

Chapter 1 - Introduction

Consider a reaction in which a particle interacts with a single nucleon in the target nucleus. If the interaction results in the struck nucleon being knocked out of the nucleus the reaction can possibly be used to study the single nucleon properties of nuclei. The picture is that of the projectile and the struck nucleon interacting almost as if the nucleon were free and the rest of the target nucleus is simply a spectator. Typical reactions resulting in the removal of a single proton, and hence offering a probe of the proton distribution in the nucleus, are $(p, 2p)$, $(e, e'p)$ and $(\pi, \pi p)$. The neutron distribution can be examined by reactions such as (p, np) . These reactions provide a probe of individual nucleon motion within target nuclei as the quantities obtained must refer to the struck nucleon; for example, polarized $(\vec{p}, 2p)$ can detect the polarization of the proton in the nuclear environment [Ki85].

Because of its relatively small absorption cross section (relative to a hadron), a real photon provides a very clean probe of the entire nucleus. The total cross section for photon absorption by a free proton is shown as the solid curve in figure 1-1. The curve is a smooth fit to data by Arhens [Ah85]. The data points show the total photonuclear absorption cross section per nucleon on the nuclei ${}^9\text{Be}$ [Ah75, Ar81] and ${}^{208}\text{Pb}$ [Le81, Ch83]. Data from other nuclei follow the same curve [Ah85] in the region of the delta resonance. The resonance structure is smeared out by the Fermi motion of the nucleons in the nucleus and Pauli blocking effects reduce the magnitude of the cross section, but the evidence of enhancement in the delta is clear. The nucleon bound in a nucleus seems to have a universal response to the photon for photon energies in the delta region, but the important feature for us is that the nucleon and the delta exist in the nucleus without major modifications even in the presence of strong interactions with nearby nucleons.

The mean free path for a projectile traveling through a medium of constant density ρ_0 scatterers per unit volume can be written as

$$L = \frac{1}{\rho_0 \sigma_A} \quad (1-1)$$

where σ_A is the total cross section for the absorption of the incident particle through any channel. Consider a photon travelling through nuclear matter with a density of $\rho_0 = 0.17$ nucleons/fm³. From figure 1-1 we take an estimate of the peak absorption cross section

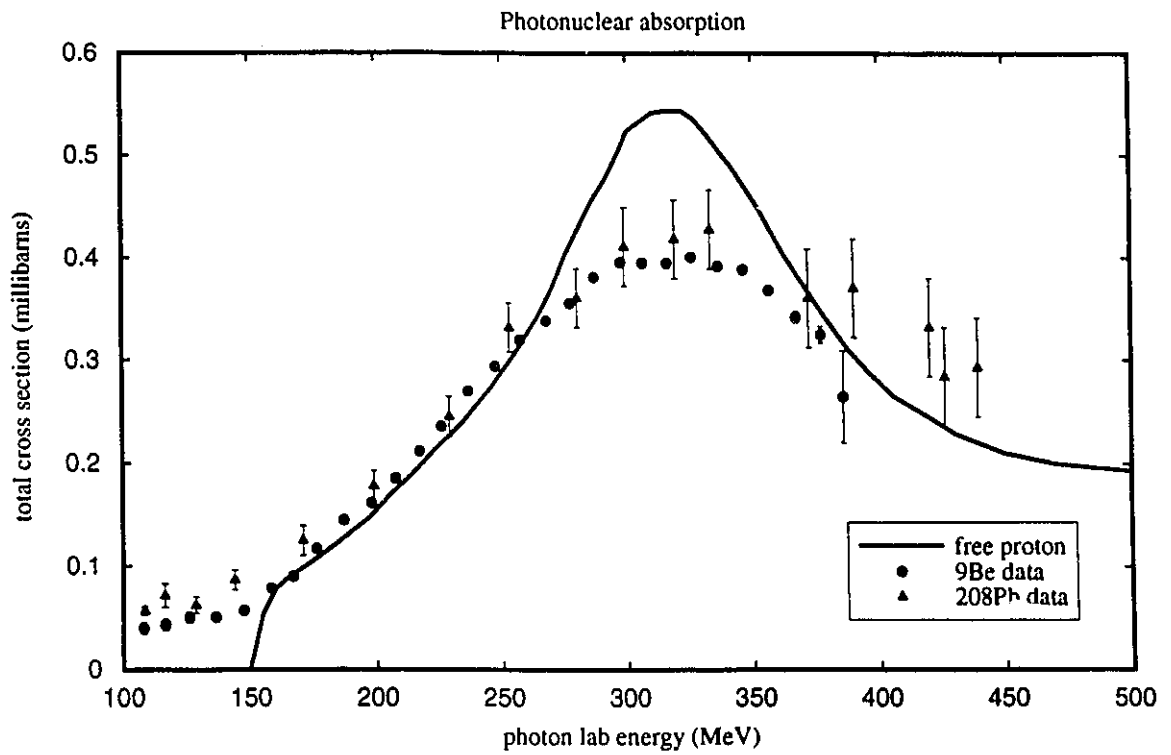


Figure 1-1. Total photonuclear absorption as a function of photon lab energy. Solid line; absorption by a free proton, data points; absorption in nuclei: ${}^9\text{Be}$ [Ah75, Ar81] and ${}^{208}\text{Pb}$ [Le81, Ch83].

for a photon incident on a nucleon, whether free or bound in a nucleus, to be about $\sigma_A \approx 0.5$ mb. This yields a minimum mean free path of $L = 120$ fm for a photon travelling through nuclear matter. Note that this is a very energy dependent quantity and can change by an order of magnitude over the range of energies shown in figure 1-1. Because of this large mean free path the flux of photons through any part of the nucleus is almost constant and the photon beam is probing the entire nuclear volume uniformly. This is very different from a pion beam which has a mean free path at $T_\pi = 195$ MeV of $L_\pi \approx 0.5$ fm, which localizes the pion interactions at the nuclear surface.

There is of course a price to be paid for using a probe with a small interaction cross section; that is the low count rate for the final state particles. Fortunately there is a new generation of machines providing high intensity electron and photon beams which will be able to perform a variety of interesting experiments in the next few years [Ko89] in the energy range 0.5 - 4.0 GeV.

1.1 The Quasifree Region and the Distorted Wave Impulse Approximation (DWIA)

Reactions in the quasifree region are used to study the shell structure of the nucleus (its single particle properties), as well as to test the effect that a nuclear environment has on the bound nucleons. The electromagnetic probes are particularly interesting as the wave function of the probe is not distorted by the strong interaction, making interpretation of the experimental results more straightforward than with a strongly interacting projectile. In order to clarify the meaning of the term 'quasifree' we have drawn a schematic inelastic spectrum in figure 1-2, for a reaction



in which we have a beam of incident photons impinging on a nucleus with A nucleons. The photons are observed in the final state at a fixed angle and their energy measured. The abscissa of figure 1-2 is the energy of the incident projectile minus the measured energy of the final projectile $E_\gamma - E'_\gamma$, the energy lost by the incident particle and gained by the final state X . The number of particles observed in the energy range E'_γ to $E'_\gamma + dE'_\gamma$ within the finite solid angle of the detector $d\Omega'_\gamma$ is proportional to the double differential

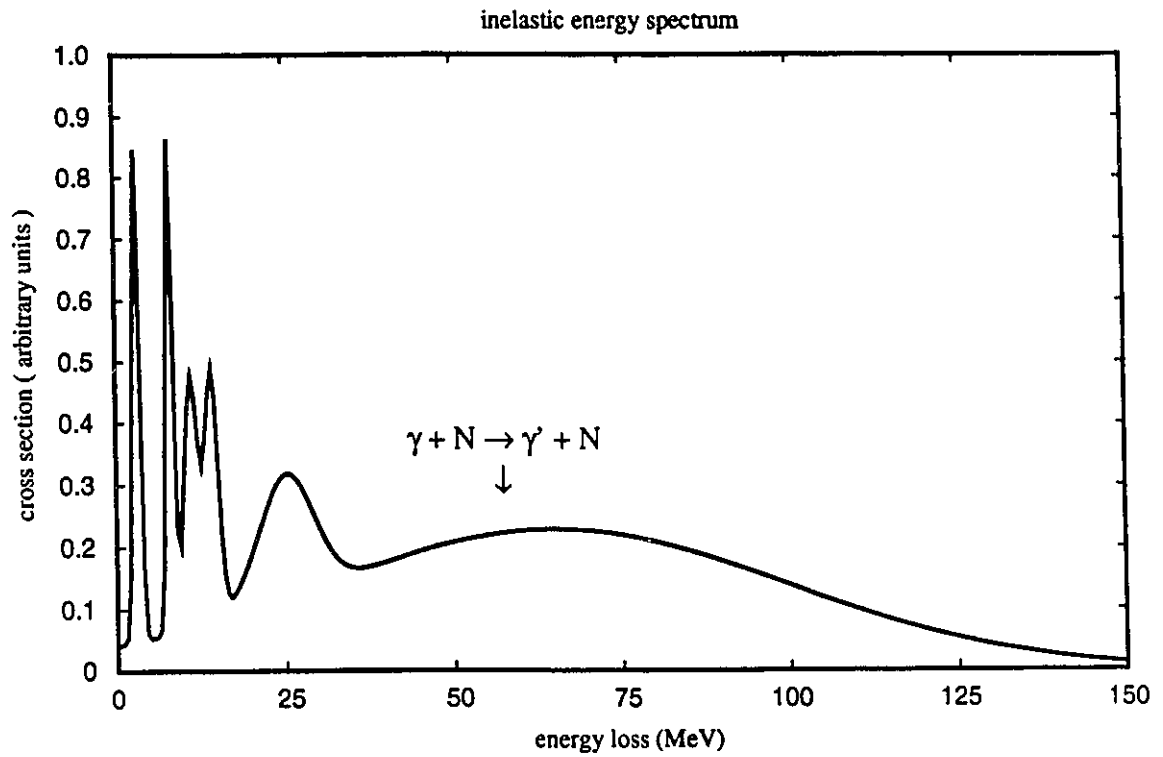


Figure 1-2. Generic inelastic scattering spectrum. The abscissa is the difference between the energies of the incident photon and the final photon $\Delta E = E_{\gamma_i} - E_{\gamma_f}$. The peaks are discussed in the text.

cross section $\frac{d^2\sigma}{d\Omega_\gamma dE_\gamma}$. The peaks in the cross section correspond to the observation of a favoured final state X, beginning with the excitation of states of the residual nucleus A, requiring a few MeV, which provide fairly sharp peaks. The broader peak at an energy loss of 25 MeV is a giant resonance which results from a collective excitation of the whole nucleus.

The broad peak at 60 MeV is the quasielastic peak which corresponds to the incident projectile actually knocking a nucleon out of its orbit so the final state X is now a free nucleon and a nucleus with A-1 nucleons. The energy of the final state projectile at the peak is close to the energy that the projectile would have if it had interacted with a free nucleon. The energy that a photon would have if it were scattered elastically from a free nucleon is close to the peak at 60 MeV, but is shifted a bit due to kinematic differences and the effect of nuclear binding. This is the origin of the term 'quasifree' or equivalently 'quasielastic'. The peak is very broad because the nucleon in the initial nucleus has a range of possible momenta. In a Fermi gas model, with Fermi momentum k_F and nucleons of mass m, the width of the quasifree peak is qk_F/m , where q is the momentum transferred to the nucleon which is knocked out of the nucleus. Note that this is a qualitative description only and the details of an actual spectrum can look quite different from our simple picture.

The spectrum is not divided into sharp regions, each corresponding to a specific process, rather the peaks blend gradually from one to the next. Neither does the spectrum simply die away as we have drawn it. At higher energies there will be peaks from other processes such as the excitation of a nucleon resonance (a $\Delta(1232)$ for example).

Frullani and Mougey [FM84] provide a very thorough discussion of the use of the quasifree (e, e' p) reaction to obtain nuclear structure information, and de Witt Huberts [Hu90] discusses results of recent high precision (e, e' p) data from NIKHEF. The application of quasifree (p, 2p) is discussed by Kitching et al. [Ki85] who also briefly discuss other quasifree reactions and provide references to other reviews. Much of the nonrelativistic DWIA approximation is discussed by Goldberger and Watson [GW64].

Of particular interest to us is the portion of the inelastic spectrum in which the photon provides sufficient energy to create a pion. We can then observe a final state in

which there is no photon, but instead we observe the pion and a nucleon which has been knocked out of the nucleus. The pion is created through the elementary photoproduction process



This channel opens and creates a peak in the inelastic spectrum at an energy higher than the peak due to the nucleon knockout, but the photoproduction peak is close to the kinematics of the free pion photoproduction reaction, so this peak is also quasifree.

In the factorized DWIA model the cross section for the reaction $A(\gamma, \pi^- p)A-1$ is related to the cross section for pion photoproduction on a free neutron $\gamma + n \rightarrow \pi^- + p$. Use of the DWIA reduces the large number of degrees of freedom of the nuclear many body problem by assuming that for sufficiently high momenta and energies the reaction occurs as if the target nucleon is moving without interacting with the rest of the nucleus. Specifically the impulse approximation assumes that the energy of the projectile is much larger than both the average kinetic energy of the bound nucleon and the average potential binding the nucleon [GW64]. Then the amplitude for the reaction in the nuclear medium can be written in terms of the amplitude for the free reaction. This results in an expression where the two-body scattering matrix element (for the free reaction) is the operator which takes the initial state (photon + bound neutron) to the final state (pion and proton distorted by interactions with the nucleus). The factorization is obtained by assuming that the two-body reaction occurs with the finally observed spins, isospins and momenta so the two-body operator can be removed from the integral. This results in the factored form

$$\frac{d^3\sigma}{d\Omega_\pi d\Omega_p dE_p} = K \frac{d\sigma}{d\Omega} \Big|_{\gamma n \rightarrow \pi p}^{c.m.} \rho(p_B) \quad (1-2)$$

where K is a factor involving kinematic quantities, the two body reaction cross section is evaluated in the center of mass of either the final pion and proton (final state prescription) or the initial photon and bound neutron (initial state prescription). The mass of the bound neutron is not the free neutron mass in the initial state prescription, but is taken to be the difference between the masses of the initial and final nuclei, so the results from the two prescriptions can differ a bit [Ki85]. We discuss the elementary process and the operator presented by Blomqvist and Laget, in Appendix F.

The distorted momentum distribution $\rho(p_B)$ is related to the nuclear overlap function

$$\psi_B(\vec{r}) = \langle \psi_f(\vec{r}_2, \dots, \vec{r}_A) | \psi_i(\vec{r}, \vec{r}_2, \dots, \vec{r}_A) \rangle \quad (1-3)$$

which in the shell model is just the bound state wave function with the required quantum numbers to specify the state. Note that we have given the target nucleon the coordinate \vec{r} , and the other nucleons are labeled from 2 to A. The distorted momentum distribution is then written as

$$\rho(p_B) = \left| \int d^3r \psi_p^{(-)*}(\vec{r}) \psi_\pi^{(-)*}(\vec{r}) \psi_B(\vec{r}) e^{i\vec{k}_\gamma \cdot \vec{r}} \right|^2 \quad (1-4)$$

where the wave functions of the final proton and pion are distorted through interaction with the final state nucleus. In the limit that the final proton and pion do not interact with the residual nucleus, the distorted momentum distribution is just the Fourier transform of the bound state wave function.

The factorized form of the cross section has a very simple interpretation. The cross section for pion photoproduction on a nucleus is given by the product of the cross section for the reaction to take place in free space with the probability of finding the struck nucleon in the initial nucleus in a state with the momentum demanded by energy conservation, while the rest of the nucleus is in the required final state.

1.2 Experiments and Their Interpretation

Coincidence measurements of pion photoproduction have been performed on deuterium in order to extract observables for the elementary charged pion photoproduction process on neutrons $\gamma + n \rightarrow \pi^- + p$. References to these experiments can be found in the compilation of photoproduction data by Menze, Pfeil and Wilcke [Me77].

The basic idea for these experiments is that the proton in deuterium is a spectator to the pion photoproduction reaction taking place on the neutron. This should be a good approximation when the momentum transfer to the spectator is small. Also the deuteron is the least bound nuclear system with a binding energy of only 2.22 MeV so kinematic shifts due to binding energy will be small. The energy of the incident photon from a Bremsstrahlung beam is not known exactly, so the momentum and direction of both the pion and ejected proton are measured and the energy of the incident photon calculated.

The first coincidence measurement on a slightly heavier nucleus was performed at Saclay by Argan and coworkers [Ar72]. They studied the reaction ${}^4\text{He}(\gamma, \pi^- p)\text{ppn}$ in the Δ region in an attempt to understand how the pion photoproduction mechanism on a free nucleon is modified by the presence of other nucleons.

The experiment was done in a coplanar geometry and the three-momenta of the pion and proton measured in coincidence. The differential cross section was measured as a function of the center of mass energy of the final proton-pion system for two values of momentum for the recoil nucleus: $p_R = 50 \text{ MeV}/c$ and $p_R = 200 \text{ MeV}/c$. The data were compared to the factorized calculations of Laget [La72] and at the lower recoil momentum the results of the calculation were multiplied by a factor of 1.25 to bring the calculations closer to the data. At the larger recoil momentum the calculation had a different shape from the data and the authors multiplied the results of the calculations by 2.1 to bring the calculation closer to the data, but this still did not provide agreement. Some of the data points were roughly a factor of four larger than the peak of the theoretical (not renormalized) calculations. The discrepancy between data and theory was attributed to possible resonant processes involving two or more nucleons. They concluded that for small recoil momenta ($\approx 50 \text{ MeV}/c$) a one nucleon description of the reaction is adequate, while for large recoil momenta ($\approx 200 \text{ MeV}/c$) other processes are important.

After this experiment coincidence measurements were largely restricted to deuterium [eg. Ar77] and the examination of the role of mechanisms other than that involving a single nucleon. The review by Laget [La81] discusses the results of these measurements and the many additions to the theoretical model required to describe the data at high recoil momenta. The important additions involve the rescattering of the pion from the recoil proton and the interaction of the two final state nucleons. These additions result in agreement between data and theory to a recoil momentum of $500 \text{ MeV}/c$.

I.V. Glavanakov and his coworkers at the Tomsk cyclotron have made two measurements of triple differential cross sections $\frac{d^3\sigma}{d\Omega_\pi d\Omega_p dE_p}$ on ${}^{12}\text{C}$ [GS79a, AG90] for the reaction ${}^{12}\text{C}(\gamma, \pi^- p){}^{11}\text{C}$ in which the pion and proton are detected in coincidence in a coplanar geometry with the proton detector on one side of the photon beam and the pion detector on the other.

In the first experiment [GS79a] pions were detected with kinetic energy in the range 40 MeV to 180 MeV, while the range of energy for the detected protons was 50 MeV to 190 MeV. The pion and proton angles were $\Theta_\pi = 120^\circ$ and $\Theta_p = 20^\circ$ respectively. Data were obtained for three values of incident photon energy $E_\gamma = 340, 360$ and 380 MeV. They obtained triple differential cross sections as a function of final proton kinetic energy for two ranges of excitation energy of the final ^{11}C nucleus. One set for $E_x < 10$ MeV, for which the primary contribution is the quasifree process removing a $p_{3/2}$ neutron and leaving a ground state ^{11}C . The other data include events with the final excitation energy of the residual nucleus in the range $10 \text{ MeV} < E_x < 40 \text{ MeV}$. The primary contribution to this data is the quasifree knockout of an $s_{1/2}$ neutron leaving a hole of excitation energy $E_x \approx 16$ MeV.

The data were compared to the factorized model mentioned above. Pion and proton distortions were included through the eikonal approximation [GW64] The momentum distribution was calculated using harmonic oscillator wave functions to describe the neutrons. The calculations were found to provide a qualitative description of the data. The shapes of the distributions for excitation energy in the range $10 \text{ MeV} < E_x < 40 \text{ MeV}$ were reproduced but the magnitudes of the data are slightly larger than the calculation, perhaps due to the inclusion of final states other than the $1s_{1/2}$ hole in ^{11}C .

The general features of the $1p_{3/2}$ distribution are reproduced in that the minimum where the momentum transfer is almost zero occurs in almost the same place in both data and calculations, and there is an asymmetry around this minimum. They state that the differences may be due to the limited energy resolution of the apparatus (which might be responsible for filling in the minimum where the momentum transfer is almost zero), the existence of a significant width for the hole states and/or the overlap of the shells.

The excitation spectrum of the data from reference [GS79a] was integrated over all energies to obtain inclusive data [GS79b] which were then compared with the factorized calculation in an attempt to disentangle the relative contributions from s- and p-shell knockout. the calculations couldn't reproduce the shape of the distributions, but one set of proton optical potentials yielded a magnitude of the cross section peak in agreement with data.

Comparison of the data for the reaction $^{12}\text{C}(\gamma, \pi^- p)$ with data for $^{12}\text{C}(\gamma, \pi^-)$ using the factorized approximation and a shell model description of the nucleus led to the

conclusion [G180] that the eikonal approximation provides a satisfactory description of the proton's final state interaction with the residual carbon nucleus. He also finds a significant quasifree component to the pion photoproduction reaction $^{12}\text{C}(\gamma, \pi^-)$.

In a further analysis of this data [G182] Glavanakov extracts cross sections for the elementary process $\gamma + n \rightarrow \pi^- + p$ using a model comprised of the factorized approximation for the quasifree component and the assumption that at large excitation energies of the residual nucleus an additional contribution to the cross section comes from the reaction $^{12}\text{C}(\gamma, \pi^- p) ^3\text{He} ^8\text{Be}$. He finds that the assumption of a considerable modification of the parameters of the $\Delta(1232)$ in photoproduction on carbon is not verified.

Glavanakov has made an attempt to allow for exchange effects [G189] related to the antisymmetry of the system of nucleons comprised of the free nucleon and the residual nucleus, which could be important for low momenta of the free proton. The impulse approximation was used to write the amplitude for the reaction $A(\gamma, \pi^- p)B$ as a sum of elementary pion photoproduction reactions taking place on all the nucleons in the nucleus. The multiparticle wave function of the initial nucleus is written as a linear combination of the products of wave functions for a system of $A-1$ nucleons and the target nucleon. In the plane wave approximation the amplitude can be written as the sum of two terms; a direct amplitude corresponding to the quasifree production of pions on the valence nucleon, and an exchange amplitude corresponding to the photoproduction of a pion on the residual nucleus without involvement from the detected proton. The direct term is unfactorized and this term alone is referred to as the 'quasifree approximation'.

Final state interactions are introduced through the eikonal approximation [GW64]. Harmonic oscillator wave functions are used to describe the nuclear single particle states, with levels separated by about 16 MeV. Deeply excited states of the residual nucleus are not considered in the model. The form for the one nucleon pion photoproduction is that introduced by Chew, Goldberger, Low and Nambu [Ch57] and the amplitudes are those of Berends, Donnachie and Weaver [Be57]. In the exchange term the elementary amplitude is averaged over the states of the nucleons bound in the nucleus. The model was compared with data for the neutral pion photoproduction reaction $^{12}\text{C}(\gamma, \pi^0 p)$ and the exchange amplitude was found to be the dominant contributor to the cross

section when the momentum transfer to the recoil nucleus is large, however the full calculation was a factor of 2 to 4 below the data.

In comparing with the charged pion photoproduction data [GS79a] the shapes of the curves were reproduced by both factorized and unfactorized forms of the direct portion of the model. The factorization didn't seem to have much effect for the kinematical region covered by the data. The factorization was shown to have a large effect for a plane wave calculation of neutral pion photoproduction when the residual nucleus is left in a $1s_{1/2}$ hole state. He concluded that when the momentum of the ejected nucleon is small there must be some sort of resonance contribution to the reaction in which the pion is produced and the nucleus excited which then decays by emitting a nucleon.

The results of the second coincidence experiment on ^{12}C were published in 1990 by Anan'in and Glavanakov [AG90]. The detected pions had kinetic energies in the range 30 MeV to 180 MeV while the protons were detected with kinetic energies in the range 30 MeV to 200 MeV. The pion and proton angles were $\Theta_{\pi} = 120^{\circ}$ and $\Theta_p = 40^{\circ}$. The experiment was carried out in the quasifree region where contribution to the reaction cross section from knockout of an s -shell nucleon was assumed to be less than ten percent of the total. The analysis was therefore carried out under the assumption that the residual ^{11}C nucleus was left in its ground state. The authors presented triple differential cross section data as a function of final proton kinetic energy. The final pion kinetic energy is held fixed in roughly 10 MeV steps from 33.2 MeV to 129.5 MeV in each of ten graphs, so the incident photon energy varies as the proton energy varies. The data are compared to the nonfactorized direct photoproduction calculation discussed previously (the quasifree approximation) [G189]. Both plane wave and distorted wave calculations have shapes close to that of the data but the plane wave curves are systematically larger than the data while the distorted wave calculations are generally below the data. The distorted calculations do pass through some of the data for high proton energy.

They conclude that the quasifree approximation provides a satisfactory description of the data for small values of momentum transfer to the recoil nucleus and large momentum of the free proton, exactly where the impulse approximation should work. When the pion or proton momenta are small the calculations are below the data due to other mechanisms not included in the model.

Pham and his coworkers [Ph89, Ph92] have performed a measurement of the reaction $^{16}\text{O}(\gamma, \pi^- p)^{15}\text{O}$ for an incident photon beam endpoint energy of $E_\gamma = 350$ MeV. Measurements were made at two pion-proton laboratory angle pairs:

- i) $\Theta_\pi = 64^\circ$ $\alpha_p = 40^\circ$
- ii) $\Theta_\pi = 120^\circ$ $\alpha_p = 20^\circ$

At each pion angle protons were detected in an array of seven plastic scintillator detectors arranged perpendicular to the plane defined by the photon and pion momenta. The data were compared with the factorized DWIA calculation of Laget [La72] using the pion photoproduction operator of Blomqvist and Laget. The calculations are about a factor of 3 larger than the data at the forward pion angle while the calculations are nearly a factor of 1.5 larger than the data at the backward pion angle.

The results from TRIUMF experiment 550 of a measurement of triple differential cross sections for the reaction $^{16}\text{O}(\pi^+, \gamma p)^{15}\text{O}$ will be available soon [Fa91], and there exists the possibility of data on carbon for the reaction $^{12}\text{C}(\gamma, \pi^- p)^{11}\text{C}$ at an incident photon energy of $E_\gamma = 230$ MeV from experiment #36 at the Saskatchewan Accelerator Laboratory [Hac92].

1.3 A Dirac Equation Based Model of Pion Photoproduction on a Nucleus

We consider a model of nuclear pion photoproduction using the photon, pion, nucleon and delta as the elementary particles in the problem. We ignore the fact that the hadrons are composite particles (in other words we ignore the quark and gluon degrees of freedom). In the region of the delta resonance ($E_\gamma \approx 300$ MeV) the spatial resolution of the photon is of the order of the nucleon size (1 - 2 fm), and so we will not be able to resolve the constituents of the nucleons.

Our model of pion photoproduction on a nucleus begins with the pion-nucleon interaction lagrangian with pseudovector coupling. The minimal gauge-invariant substitution yields photon-pion and photon-nucleon interaction terms, in addition to a lagrangian interaction allowing the interaction of the photon, the pion and two nucleons at one vertex, leading to the so-called seagull diagram. The lagrangians for the interaction between the photon, nucleon and delta as well as the pion, nucleon and delta, are also included. This model lagrangian was developed by Olsson and Osypowski [Ol75] and

later by Blomqvist and Laget [BL76]. We extend this to the case of production on a nucleon bound in a nucleus and treat the nuclear dynamics according to the model recently proposed by Walecka and his coworkers [SW86]. The pion and nucleon wave functions are solutions of relativistic equations; the pion being described by the Klein-Gordon equation, while the nucleons are described using the Dirac equation. The equations contain potential terms representing the interactions of these with the nucleus.

A relativistic description of the dynamics of nucleon interaction has been successful in reproducing the observed properties of nuclear matter and finite nuclei [SW86]. The use of the Dirac equation with scalar and zeroth-component vector potentials to describe the nucleon has provided a better explanation of proton elastic scattering observables at intermediate energies than the nonrelativistic Schrödinger equation based approach, particularly for the spin observables [Ko85]. In addition a relativistic model of inelastic proton scattering leading to the excitation of collective states [Jo88] is in good agreement with experimental data, and provides a better description of analyzing power data than the nonrelativistic theory. Dirac phenomenology has also resulted in improved descriptions of the cross sections and spin observables for the reactions (p, π) and (γ, p) [Co82, Lo92]. Because of these successes of Dirac phenomenology we propose to extend this to negative pion photoproduction on a nucleus.

Our model remains fully relativistic, and does not include a factorization approximation, in which case the cross section would have the form of equation (1-2). The diagrams containing two vertices involve evaluating six-dimensional space integrals. In addition, the propagating particle should be allowed to interact with the nucleus as it travels so the propagator is no longer free but must be modified to allow for the interaction. The calculations in this form have proven to be numerically intractable and we have had to make approximations in order to carry out the calculation. First, the propagators are taken to be the momentum space propagators times a coordinate space δ -function, removing the integration at one vertex, i.e. we have made the propagators local. This affects all the diagrams except the seagull, which is evaluated exactly. Second, the Born terms with the photon coupling to electric charge are not gauge invariant in the distorted wave calculations, although they are gauge invariant when the pion and proton are described by plane waves. The terms in which the photon couples to the anomalous

magnetic moment of the nucleon and the delta diagrams are each separately gauge invariant for both the plane and distorted wave calculations.

In chapter 2 we derive the s-matrix for the pion photoproduction reaction on a nucleus $A(\gamma, \pi^- p)A-1$. Chapter 3 includes a discussion of the Dirac equation based model of proton elastic scattering from a nucleus, and the optical potential model of pion-nucleus elastic scattering. In chapter 4 we discuss the sensitivity of our model to changes in the wave functions of the bound neutron, the pion and the proton. We then examine the behaviour of the results under changing kinematic conditions, and finally we compare with the available experimental data. In chapter 5 we derive the s-matrix for the reaction $A(\pi^+, \gamma p)A-1$ and present calculations for some of the angles and energies for which data were taken (TRIUMF experiment 550). Chapter 6 contains our conclusions.

Chapter 2 - A One Nucleon Model for the Reaction $A(\gamma, \pi^- p)A-1$

This model for the $(\gamma, \pi^- p)$ reaction has the incident photon interacting with a bound neutron through some process denoted by the blob in figure 2-1. A proton and a negatively charged pion are produced and are detected experimentally. The residual nucleus is left with a hole corresponding to the removal of the active nucleon. The wave functions for the initial neutron and final proton are solutions of the Dirac equation with appropriate scalar and vector potentials; these describe the interactions of the particles with the initial and final nuclei. The pion wave function is a solution of the Klein-Gordon equation with an appropriate optical potential for the pion-nucleus system. We will explore the importance of various contributions to the interaction blob by the diagrams shown in figure 2-2. The four diagrams, 2-2a) to 2-2d), are the Born terms, and the diagrams 2-2e) and 2-2f) are the s-channel and u-channel Δ diagrams. Note that in figure 2-2c) the photon can couple to the proton through both the electric charge and the anomalous magnetic moment of the proton, while in figure 2-2d) the photon can only couple to the neutron through the anomalous magnetic moment.

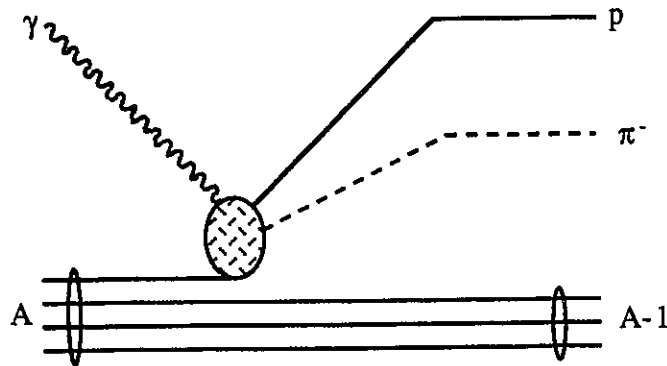


Figure 2-1. The one nucleon model for $A(\gamma, \pi^- p)A-1$

2.1 Model Lagrangian

The total lagrangian density for a system of pions and nucleons is the sum of the free lagrangians for the nucleon and pion and the lagrangian which provides for

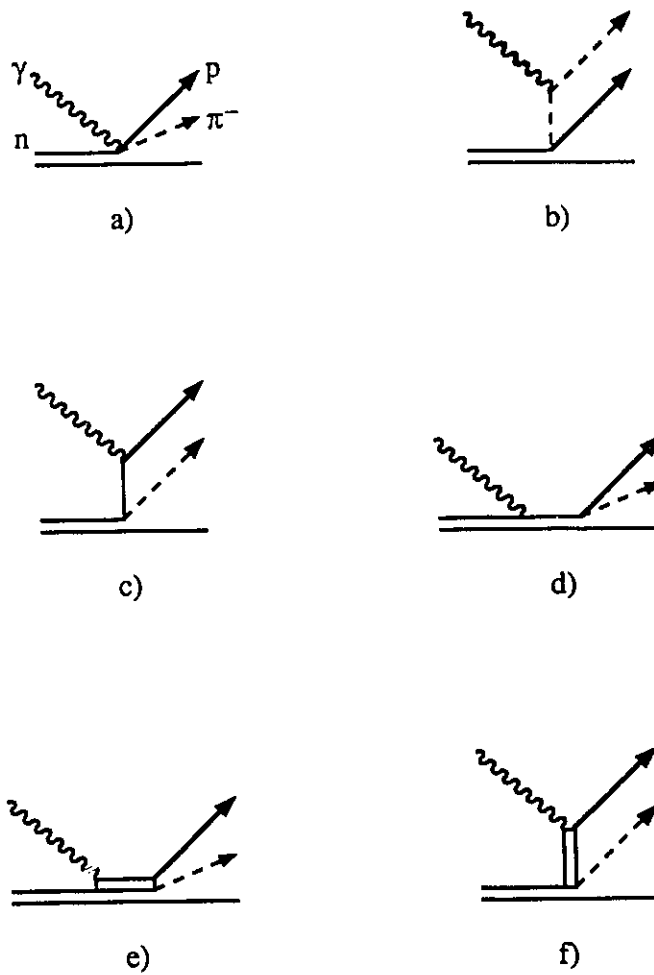


Figure 2-2. Diagrams contributing to pion photoproduction on a nucleus. a-d) the Born terms, e) the s-channel Δ diagram, and f) the u-channel Δ diagram. The line designations shown in a) will be used consistently throughout this work: photon (wavy line), pion (dashed line), nucleon (solid line) and $\Delta(1232)$ (double line).

interaction between the particles (we use natural units throughout this work $\hbar = c = 1$)

$$\mathcal{L} = \bar{\psi} (i \not{\partial} - m) \psi + \frac{1}{2} (\partial_\mu \vec{\phi} \cdot \partial^\mu \vec{\phi} - m_\pi^2 \vec{\phi} \cdot \vec{\phi}) + \mathcal{L}_{\pi NN} \quad (2-1)$$

where the interaction lagrangian can have two forms (fields: pion ϕ and nucleon ψ)

$$\text{pseudoscalar :} \quad -i g_\pi \bar{\psi} \gamma_5 \vec{\tau} \cdot \vec{\phi} \psi \quad (2-2a)$$

$$\text{pseudovector :} \quad -\frac{f_\pi}{m_\pi} \bar{\psi} \gamma_5 \vec{\tau} \cdot \not{\partial} \vec{\phi} \psi \quad (2-2b)$$

The Feynman slash notation for a vector A [BD64] means take the dot product of the vector with the Dirac gamma matrices $\not{A} = A^\mu \gamma_\mu = A^0 \gamma_0 - \vec{A} \cdot \vec{\gamma}$. We use the pseudovector pion-nucleon coupling because it satisfies the hypothesis of partial conservation of the axial vector current (is consistent with chiral invariance). In addition the Born terms calculated with pseudovector coupling are consistent with low energy theorems and current algebra predictions [BL77]. Blomqvist and Laget find that the pseudovector coupling is to be preferred over the pseudoscalar in a nonrelativistic calculation of the elementary pion photoproduction process.

We introduce interactions with photons by using the minimal substitution $\partial^\mu \rightarrow \partial^\mu + iq A^\mu$, where q is the charge of the field to which the photon couples, in the lagrangian (2-1) with the pseudovector interaction term (2-2b). We also include interaction terms which allow $\gamma N \Delta$ and $\pi N \Delta$ vertices. The resulting lagrangian is

$$\mathcal{L} = \mathcal{L}_{\text{FREE}} + \mathcal{L}_{\pi NN} + \mathcal{L}_{\gamma NN} + \mathcal{L}_{\gamma \pi \pi} + \mathcal{L}_{\gamma \pi \pi} + \mathcal{L}_{\gamma \pi NN} + \mathcal{L}_{\pi N \Delta} + \mathcal{L}_{\gamma N \Delta} \quad (2-3)$$

with the non-delta interaction terms

$$\begin{aligned} \mathcal{L}_{\pi NN} &= -\frac{f_\pi}{m_\pi} \bar{\psi} \gamma_5 [\tau_- \not{\partial} \pi^- + \tau_+ \not{\partial} \pi^+ + \tau_3 \not{\partial} \pi^0] \psi \\ \mathcal{L}_{\gamma NN} &= -e \bar{\psi} \not{A} \frac{1+\tau_3}{2} \psi - \frac{\kappa_p \mu_N}{2} \bar{\psi} \sigma^{\mu\nu} F_{\mu\nu} \frac{1+\tau_3}{2} \psi - \frac{\kappa_n \mu_N}{2} \bar{\psi} \sigma^{\mu\nu} F_{\mu\nu} \frac{1-\tau_3}{2} \psi \\ \mathcal{L}_{\gamma \pi \pi} &= \frac{ie}{2} A^\mu [\pi^+ \partial_\mu \pi^- + \partial_\mu \pi^- \pi^+ - \pi^- \partial_\mu \pi^+ - \partial_\mu \pi^+ \pi^-] \\ \mathcal{L}_{\gamma \pi \pi} &= \frac{e^2}{2} A_\mu A^\mu \{ \pi^+ \pi^- + \pi^- \pi^+ \} \\ \mathcal{L}_{\gamma \pi NN} &= -ie \frac{f_\pi}{m_\pi} \bar{\psi} \gamma_5 \not{A} [\tau_+ \pi^+ - \tau_- \pi^-] \psi \end{aligned} \quad (2-4)$$

where the unit of charge is positive ($e > 0$) throughout this work. The nucleon is described by a two component spinor in isospin space with the upper component describing the proton and the lower component describing the neutron

$$\psi = \begin{bmatrix} \psi_p \\ \psi_n \end{bmatrix} \quad (2-5)$$

The nucleon charge operator in $\mathcal{L}_{\gamma NN}$ is $q_N = \frac{e}{2} (1 + \tau_3)$ and takes the value e for the

proton and 0 for the neutron.

The magnetic dipole term has been added to $\mathcal{L}_{\gamma NN}$ to account for the anomalous magnetic moment of the nucleons [BD64]. The magnetic moment of the proton is $2.79\mu_N$ and the neutron magnetic moment is $-1.91\mu_N$ where the nuclear magneton is $\mu_N = \frac{e}{2m_p}$. The Dirac values of the magnetic moment are μ_N for the proton and 0 for the neutron. The anomalous magnetic moment is the difference between the actual value of the magnetic moment and the Dirac value and the magnitudes of the anomalous magnetic moments for the proton and neutron are $\kappa_p = 1.79$ and $\kappa_n = -1.91$.

The charged pion fields are written in terms of three components of a real pseudoscalar field as (appendix A)

$$\begin{aligned}\pi^\pm &= \frac{1}{\sqrt{2}} (\varphi_1 \mp i\varphi_2) \\ \pi^0 &= \varphi_3\end{aligned}\quad (2-6)$$

Note that + and - on the pion fields indicate the charge that the field destroys, so that the charged pion field with a + sign has the same effect on the charge as the positively charged nucleon field. Similarly the isospin raising and lowering operators for the nucleon are written in terms of the Pauli isospin matrices as

$$\tau_\pm = \frac{1}{\sqrt{2}} (\tau_1 \pm i\tau_2) \quad (2-7)$$

where the Pauli matrices are

$$\tau_1 = \begin{bmatrix} 0 & 1 \\ 1 & 0 \end{bmatrix} \quad \tau_2 = \begin{bmatrix} 0 & -i \\ i & 0 \end{bmatrix} \quad \tau_3 = \begin{bmatrix} 1 & 0 \\ 0 & -1 \end{bmatrix} \quad (2-8)$$

and the + and - on the τ matrices indicate that they raise or lower the isospin projection of the nucleon by one unit.

We will need to use an explicit representation of the gamma matrices and we use the representation that Bjorken and Drell have made standard [BD64]

$$\gamma_0 = \begin{bmatrix} \mathbf{1} & 0 \\ 0 & -\mathbf{1} \end{bmatrix} \quad \gamma_i = \begin{bmatrix} 0 & \sigma_i \\ -\sigma_i & 0 \end{bmatrix} \quad \gamma_5 = \begin{bmatrix} 0 & \mathbf{1} \\ \mathbf{1} & 0 \end{bmatrix} \quad (2-9)$$

where $\mathbf{1}$ is a 2x2 unit matrix and the σ_i are the usual Pauli spin matrices of equation (2-8), which makes the gamma matrices 4x4 matrices.

The interaction terms involving the propagation of a Δ isobar are [Ka88, Ol75]

$$\begin{aligned}\mathcal{L}_{\pi N\Delta} &= \frac{f_{\pi N\Delta}}{m_\pi} \{ \bar{\Psi}_\Delta^\mu \vec{T} \cdot \partial_\mu \vec{\phi} \Psi + \bar{\Psi} (\vec{T} \cdot \partial_\mu \vec{\phi})^\dagger \Psi_\Delta^\mu \} \\ \mathcal{L}_{\gamma N\Delta} &= ie \frac{f_{\gamma N\Delta}}{m_\pi} \{ \bar{\Psi}_\Delta^\mu T_3 \gamma^\nu \gamma_5 F_{\mu\nu} \Psi + \bar{\Psi} T_3^\dagger \gamma^\mu \gamma_5 F_{\mu\nu} \Psi_\Delta^\nu \}\end{aligned}\quad (2-10)$$

where the 4x2 isospin matrices \vec{T} which connect the isospin T=1/2 nucleon with the isospin T=3/2 isobar are of the form (appendix A)

$$T_1 = \frac{1}{\sqrt{2}} \begin{bmatrix} -1 & 0 \\ 0 & -1/\sqrt{3} \\ 1/\sqrt{3} & 0 \\ 0 & 1 \end{bmatrix} \quad T_2 = \frac{i}{\sqrt{2}} \begin{bmatrix} 1 & 0 \\ 0 & 1/\sqrt{3} \\ 1/\sqrt{3} & 0 \\ 0 & 1 \end{bmatrix} \quad T_3 = \sqrt{\frac{2}{3}} \begin{bmatrix} 0 & 0 \\ 1 & 0 \\ 0 & 1 \\ 0 & 0 \end{bmatrix} \quad (2-11)$$

The values which we use for the coupling constants are listed in table 2-1). The fine structure constant is taken from the Review of Particle Properties [Pa92] and is actually known more accurately than shown in the table. The pseudovector πNN coupling constant is typically taken to be [Ma89] $f_\pi = 1.0$ but some recent analyses [K191, Ar90] have been arguing for a smaller value for the coupling constant. From these analyses of increased data sets Klomp et al. recommend a value of $f_\pi = 0.97$ which is the value we adopt. The measured value for the width of the Δ resonance implies a $\pi N\Delta$ coupling constant of $f_{\pi N\Delta} = 2.1$, while the quark model [BW75] predicts a significantly smaller value of $f_{\pi N\Delta} = 1.7$. Another value of $f_{\pi N\Delta} = 1.9$, was obtained by Olsson and Osypowski [OI75] from an analysis of resonant multipoles and of the resonant elastic phase shifts. We choose the value obtained from the width of the Δ . Olsson and Osypowski also obtain a value for the $\gamma N\Delta$ coupling constant such that $f_{\gamma N\Delta} = 0.32$ which is close to the quark model value of $f_{\gamma N\Delta} = 0.30$.

coupling constant	value	$\frac{f^2}{4\pi}$
e	0.3028	$\frac{1}{137.036}$
f_π	0.97	0.075
$f_{\pi N\Delta}$	2.1	0.35
$f_{\gamma N\Delta}$	0.32	0.0081

Table 2-1. Coupling constants we choose in our lagrangian model (2-4) and (2-10).

2.2 Scattering Matrix

An interaction hamiltonian density, which has no derivatives acting on the fields, is simply the negative of the interaction lagrangian density

$$\mathcal{H}_{\text{int}} = - \mathcal{L}_{\text{int}} \quad (2-12)$$

We have a more complicated situation however since our interaction lagrangian density contains terms with derivatives of the photon and pion fields. The straightforward calculation of the hamiltonian density through the transformation

$$\mathcal{H} = \sum_i \pi_i \dot{\phi}_i - \mathcal{L} \quad (2-13)$$

where the sum extends over all the fields in the lagrangian density, has difficulties analogous to the problems encountered with a velocity dependent potential in classical mechanics [Go80].

The s-matrix can be expanded in terms of the interaction lagrangian as [Ni69]

$$S = 1 + \sum_{n=1}^{\infty} \frac{i^n}{n!} \int d^4x_1 \cdots d^4x_n T_W[\mathcal{L}_{\text{int}}(x_1) \cdots \mathcal{L}_{\text{int}}(x_n)] \quad (2-14)$$

where T_W refers to Wick time ordering [Bo80], which defines the time-ordering of fields which have derivatives acting on them as the derivative of the time ordered product of the fields

$$T_W[\partial_x^\mu \phi(x) \partial_y^\nu \phi(y)] \equiv \partial_x^\mu \partial_y^\nu T[\phi(x) \phi(y)] \quad (2-15)$$

This procedure avoids the noncovariant terms which arise in the hamiltonian formulation (appendix E).

In the following sections we consider the importance of contributions to the s-matrix for the reaction $A(\gamma, \pi N)A-1$, of the diagrams shown in figure 2-2. We will look at the diagrams roughly in increasing order of complexity in matrix structure. We start with a fairly detailed look at the seagull diagram and get an expression for the s-matrix which involves a three dimensional integral over the appropriate wave functions. We then consider the pion pole diagram which involves two vertices and show the approximations made to reduce the calculation to one three dimensional integral. The other diagrams follow similarly.

2.2.1 Seagull Diagram

The s-matrix to first order in the interaction lagrangian is

$$\langle f | S | i \rangle = i \int \langle f | \mathcal{L}_{\text{interaction}}(x) | i \rangle d^4x \quad (2-16)$$

For the reaction $A(\gamma, \pi^-)A-1$ the initial state $|i\rangle$ contains a photon and a nucleus with A nucleons while the final state $|f\rangle$ contains a pion, a nucleon ejected from the initial nucleus and a final nucleus with $A-1$ nucleons. In this one nucleon model for $(\gamma, \pi^- p)$ we can write the initial and final states using creation and annihilation operators. We write the initial state as [Ja71]:

$$|i\rangle = a_p^\dagger(\vec{k}_\gamma) \sum_{J_B M_B J} (J, J_B; M, M_B | J_i, M_i) \mathcal{J}_{J, J}(J_B) b_{J_B M_B}^\dagger | \phi_J^M \rangle \quad (2-17)$$

where $a_p^\dagger(\vec{k}_\gamma)$ creates a photon with momentum \vec{k}_γ and polarization p , while $b_{J_B M_B}^\dagger$ creates a bound nucleon with angular momentum J_B and projection M_B bound to the core $|\phi_J^M\rangle$. $\mathcal{J}_{J, J}(J_B)$ is a coefficient of fractional parentage such that $[\mathcal{J}_{J, J}(J_B)]^2$ is the probability that the target is in a configuration that consists of the vector product of a single particle bound state with angular momentum J_B and an eigenstate of $A-1$ nucleons with angular momentum J .

The final state is

$$|f\rangle = a_\pi^\dagger(\vec{k}_\pi) b_\mu^\dagger(\vec{k}_p) | \phi_{J_f}^{M_f} \rangle \quad (2-18)$$

where $a_\pi^\dagger(\vec{k}_\pi)$ creates a negative pion with momentum \vec{k}_π , $b_\mu^\dagger(\vec{k}_p)$ creates a nucleon with momentum \vec{k}_p and angular momentum projection μ while the state $|\phi_{J_f}^{M_f}\rangle$ describes the residual nucleus with angular momentum J_f and projection M_f .

The interaction lagrangian density which gives rise to the seagull diagram is, from our model lagrangian (2-4):

$$\mathcal{L}_{\gamma\pi NN} = -i e \frac{f_\pi}{m_\pi} \bar{\psi} \gamma_5 A [\tau_+ \pi^+ - \tau_- \pi^-] \psi \quad (2-19)$$

The charged pseudoscalar field (pion) is written in second quantized form (appendix A) as

$$\pi^+(x) = \frac{1}{(2\pi)^{3/2}} \int \frac{d^3k}{\sqrt{2\omega_k}} \{ a_\pi^\dagger(\vec{k}) v_\pi^*(k, x) + b_\pi(\vec{k}) u_\pi(k, x) \} \quad (2-20)$$

where $a_\pi^\dagger(\vec{k})$ creates pion with momentum \vec{k} and charge $-e$, while $b_\pi(\vec{k})$ destroys a pion

with momentum \vec{k} and charge e . The pion continuum states are written as $u_\pi(k, x)$ and $v_\pi^*(k, x)$ so the change to distorted waves will be transparent. The other pion fields are written similarly.

The Dirac spinor (nucleon) is expanded as

$$\Psi(x) = \frac{1}{(2\pi)^{3/2}} \sum_s \int d^3k \left(\frac{m}{E} \right)^{1/2} \{ b_s(\vec{k}) u_s(k, x) + d_s^\dagger(\vec{k}) v_s(k, x) \} + \sum_n \{ b_n u_n(x) + d_n^\dagger v_n(x) \} \quad (2-21)$$

where $b_s(\vec{k})$ destroys a nucleon with momentum \vec{k} , $d_s^\dagger(\vec{k})$ creates an antinucleon with momentum \vec{k} and $u_s(k, x)$ and $v_s(k, x)$ are continuum wave functions. Also b_n destroys a bound nucleon with angular momentum $n = \{ L_B, J_B, M_B \}$, d_n^\dagger creates a bound antinucleon and $u_n(x)$ and $v_n(x)$ are nucleon bound states.

The photon is expanded in a similar fashion as

$$A^\mu(x) = \frac{1}{(2\pi)^{3/2}} \sum_r \epsilon_r^\mu \int \frac{d^3k}{\sqrt{2\omega_k}} \{ a_r(\vec{k}) e^{-ik \cdot x} + a_r^\dagger(\vec{k}) e^{ik \cdot x} \} \quad (2-22)$$

where $a_r(\vec{k})$ destroys a photon with momentum \vec{k} and polarization r while $a_r^\dagger(\vec{k})$ creates a photon with momentum \vec{k} and polarization r . The photon polarization vector ϵ_r^μ is normal to the photon momentum with $\epsilon_{\mu r} k_\gamma^\mu = 0$ and also must be such that $\epsilon_{\mu r} \epsilon_r^\mu = -1$. We use the Coulomb gauge $\vec{\epsilon}_r \cdot \vec{k} = 0$, and we have a real photon so $\epsilon_{0r} = 0$.

Now we begin combining the bits and pieces to calculate the first order s-matrix element

$$\langle f | S | i \rangle \equiv S_{fi} = -i \int \langle f | i e^{\frac{f_\pi}{m_\pi} \bar{\Psi} \gamma_5 A [\tau_+ \pi^+ - \tau_- \pi^-] \Psi | i \rangle d^4x \quad (2-23)$$

The isospin raising and lowering operators have the following action on the nucleon spinor written in two component form as in equation (2-5):

$$\begin{aligned} \bar{\Psi} \tau_+ \Psi &= \sqrt{2} \bar{\Psi}_p \Psi_n \\ \bar{\Psi} \tau_- \Psi &= \sqrt{2} \bar{\Psi}_n \Psi_p \end{aligned} \quad (2-24)$$

so the s-matrix becomes

$$S_{fi} = \sqrt{2} e^{\frac{f_\pi}{m_\pi}} \int \langle f | [\bar{\Psi}_p \gamma_5 A \pi^+ \Psi_n - \bar{\Psi}_n \gamma_5 A \pi^- \Psi_p] | i \rangle d^4x \quad (2-25)$$

We begin the evaluation of the scattering matrix element by evaluating the various Fock space matrix elements using the properties of the creation and annihilation operators. The particles are all distinguishable so their matrix elements can be considered

individually.

Consider first the two pion matrix elements. Recall that we have a negatively charged pion in the final state and no pions in the initial state. Using equation (2-20) we write

$$\begin{aligned} \langle 0 | a_{\pi}(\vec{k}_{\pi}) \pi^+(x) | 0 \rangle \\ = \langle 0 | a_{\pi}(\vec{k}_{\pi}) \frac{1}{(2\pi)^{3/2}} \int \frac{d^3k}{\sqrt{2\omega_k}} \{ a_{\pi}^{\dagger}(\vec{k}) v_{\pi}^*(k, x) + b_{\pi}(\vec{k}) u_{\pi}(k, x) \} | 0 \rangle \end{aligned} \quad (2-26)$$

To calculate this we use the following properties of the pion creation and annihilation operators:

$$\begin{aligned} \langle 0 | a_{\pi}(\vec{k}_{\pi}) b_{\pi}(\vec{k}) | 0 \rangle &= 0 \\ \langle 0 | a_{\pi}(\vec{k}_{\pi}) a_{\pi}^{\dagger}(\vec{k}) | 0 \rangle &= \delta^3(\vec{k} - \vec{k}_{\pi}) \end{aligned} \quad (2-27)$$

and the result is

$$\langle 0 | a_{\pi}(\vec{k}_{\pi}) \pi^+(x) | 0 \rangle = \frac{1}{(2\pi)^{3/2}} \frac{1}{\sqrt{2\omega_{\pi}}} v_{\pi}^*(k_{\pi}, x) \quad (2-28)$$

where for an incoming plane wave pion we would have

$$v_{\pi}(k_{\pi}, x) = e^{-ik_{\pi} \cdot x} \quad (2-29)$$

The other pion matrix element that we need is $\langle 0 | a_{\pi}(\vec{k}_{\pi}) \pi^-(x) | 0 \rangle$, but the vacuum matrix elements are zero

$$\begin{aligned} \langle 0 | a_{\pi}(\vec{k}_{\pi}) b_{\pi}^{\dagger}(\vec{k}) | 0 \rangle &= 0 \\ \langle 0 | a_{\pi}(\vec{k}_{\pi}) a_{\pi}(\vec{k}) | 0 \rangle &= 0 \end{aligned} \quad (2-30)$$

thus the matrix element with the negative pion field is

$$\langle 0 | a_{\pi}(\vec{k}_{\pi}) \pi^-(x) | 0 \rangle = 0 \quad (2-31)$$

which is what we expect since $\pi^-(x)$ can create a positive pion or destroy a negative pion. The second term of the s-matrix therefore doesn't contribute and the contribution to the first term from the pion field is given by (2-28).

Now we consider the photon matrix element. There is a photon in the initial state and none in the final state and carrying out the calculation as we did for the pions we get

$$\langle 0 | A^{\mu}(x) a_{\gamma}^{\dagger}(\vec{k}_{\gamma}) | 0 \rangle = \frac{1}{(2\pi)^{3/2}} \frac{1}{\sqrt{2\omega_{\gamma}}} \epsilon^{\mu} e^{-ik_{\gamma} \cdot x} \quad (2-32)$$

Similarly the matrix element for the final state continuum proton is

$$\langle 0 | b_{s_f}(\vec{k}_p) \bar{\Psi}_p(x) | 0 \rangle = \frac{1}{(2\pi)^{3/2}} \left(\frac{m}{E_p} \right)^{1/2} \bar{u}_{s_f}(k_p, x) \quad (2-33)$$

where the adjoint proton field is $\bar{\Psi}_p(x) = \Psi_p^{\dagger}(x) \gamma_0$ and the hermitian conjugate is of the fermion field (2-21).

The initial neutron is coupled to the core vectorially making the result look a bit more complicated but the result is nevertheless obtained in the same manner as the above matrix element. We get

$$\begin{aligned} \langle \phi_{J_f}^{M_f} | \psi_n(x) \sum_{J_B M_B J} (J, J_B; M, M_B | J_i, M_i) \mathcal{J}_{JJ}(J_B) b_{J_B M_B}^\dagger | \phi_J^M \rangle \\ = \sum_{J_B M_B} (J_f, J_B; M_f, M_B | J_i, M_i) \mathcal{J}_{J_f J}(J_B) u_{J_B M_B}(x) \end{aligned} \quad (2-34)$$

In the reactions we consider, the initial target is a closed shell even-even nucleus with $J_i = 0$. Another case that can be quite simple to consider is a closed shell even-even final state with $J_f = 0$, but we will carry the general result along for now.

Combining these results (while paying attention to the order of gamma matrices) gives for the s-matrix

$$\begin{aligned} S_{fi} = \sqrt{2} e^{\frac{f_\pi}{m_\pi}} (2\pi)^{-9/2} \left(\frac{m}{E_p} \frac{1}{2E_\pi} \frac{1}{2E_\gamma} \right)^{1/2} \\ \times \sum_{J_B M_B} (J_f, J_B; M_f, M_B | J_i, M_i) \mathcal{J}_{J_f J_f}(J_B) \\ \times \int d^4x \bar{u}_{s_f}(k_p, x) \gamma_5 \not{e}_p u_{J_B M_B}(x) v_\pi^*(k_\pi, x) e^{-ik_\gamma \cdot x} \end{aligned} \quad (2-35)$$

We can separate the time dependence of the wave functions by writing

$$\begin{aligned} \bar{u}_{s_f}(k_p, x) &= e^{iE_p t} \bar{\psi}_{s_f}(k_p, \vec{x}) \\ u_{J_B M_B}(x) &= e^{-iE_B t} \psi_{J_B M_B}(\vec{x}) \\ v_\pi^*(k_\pi, x) &= e^{iE_\pi t} \phi_\pi^*(k_\pi, \vec{x}) \\ e^{-ik_\gamma \cdot x} &= e^{-iE_\gamma t} e^{i\vec{k}_\gamma \cdot \vec{x}} \end{aligned} \quad (2-36)$$

so the integration over time can be done to get a delta function which provides for conservation of energy in the reaction

$$\int e^{i(E_p + E_\pi - E_B - E_\gamma)t} dt = 2\pi \delta(E_p + E_\pi - E_B - E_\gamma) \quad (2-37)$$

The s-matrix is then

$$\begin{aligned} S_{fi} = \sqrt{2} e^{\frac{f_\pi}{m_\pi}} (2\pi)^{-7/2} \delta(E_p + E_\pi - E_B - E_\gamma) \left(\frac{m}{E_p} \frac{1}{2E_\pi} \frac{1}{2E_\gamma} \right)^{1/2} \\ \times \sum_{J_B M_B} (J_f, J_B; M_f, M_B | J_i, M_i) \mathcal{J}_{J_f J_f}(J_B) \\ \times \int d^3x \psi_{s_f}^\dagger(k_p, \vec{x}) \Gamma_{\text{seagull}} \psi_{J_B M_B}(\vec{x}) \phi_\pi^*(k_\pi, \vec{x}) e^{i\vec{k}_\gamma \cdot \vec{x}} \end{aligned} \quad (2-38)$$

where we have used the definition of the adjoint spinor $\bar{\psi}_{s_f} = \psi_{s_f}^\dagger \gamma_0$ and the vertex function Γ , which operates on the nucleon spinors is given by:

$$\Gamma_{\text{seagull}} = \gamma_0 \gamma_5 \not{p} \quad (2-39)$$

All the other diagrams that we will consider have two vertices, so they involve 8-dimensional integrals. We look at the pion pole diagram in detail to clarify the procedure and the approximations that are made to the propagators. The rest of the diagrams will vary in details but the major steps in the procedure will be the same.

2.2.2 The Pion Pole

The s-matrix for the pion pole contribution to the reaction $(\gamma, \pi^- p)$ shown in diagram 2-2b) in second order is:

$$\langle f | S | i \rangle = -\frac{1}{2} \int \langle f | T \{ \mathcal{L}_{\text{interaction}}(x) \mathcal{L}_{\text{interaction}}(y) \} | i \rangle d^4x d^4y \quad (2-40)$$

where T is the time ordering operator, which places events that happen first to the right of events that happen later

$$T \{ \mathcal{L}(x) \mathcal{L}(y) \} = \theta(x_0 - y_0) \mathcal{L}(x) \mathcal{L}(y) + \theta(y_0 - x_0) \mathcal{L}(y) \mathcal{L}(x) \quad (2-41)$$

and the θ function is given by

$$\theta(t) = \begin{cases} 0 & t < 0 \\ 1 & t > 0 \end{cases} \quad (2-42)$$

There are two terms which can contribute to the s-matrix for the pion pole diagram which we can combine into a single term since we have an even number of anticommuting fermion fields in the interaction lagrangians

$$\begin{aligned} \langle f | S | i \rangle &= -\frac{1}{2} \int \langle f | T \{ \mathcal{L}_{\pi NN}(x) \mathcal{L}_{\gamma\pi\pi}(y) + \mathcal{L}_{\gamma\pi\pi}(x) \mathcal{L}_{\pi NN}(y) \} | i \rangle d^4x d^4y \\ &= - \int \langle f | T \{ \mathcal{L}_{\pi NN}(x) \mathcal{L}_{\gamma\pi\pi}(y) \} | i \rangle d^4x d^4y \end{aligned} \quad (2-43)$$

Now expand the time-ordered product in terms of normal ordered products and contractions using Wick's theorem. The contraction of two fields is the vacuum expectation value of the time ordered product of the fields

$$\begin{aligned} \underline{\pi^+(x) \pi^-(y)} &= \langle 0 | T \{ \pi^+(x) \pi^-(y) \} | 0 \rangle \\ &= \theta(t_x - t_y) \langle 0 | \pi^+(x) \pi^-(y) | 0 \rangle + \theta(t_y - t_x) \langle 0 | \pi^-(y) \pi^+(x) | 0 \rangle \end{aligned} \quad (2-44)$$

and is interesting to us because it is actually i times the Feynman propagator. The only non-zero contractions for the charged pion field are

$$\underline{\pi^+(x) \pi^-(y)}, \underline{\pi^-(x) \pi^+(y)}, \underline{\pi^0(x) \pi^0(y)} \neq 0 \quad (2-45)$$

The isospin matrix elements (2-24) are used to give:

$$\begin{aligned}
& T \{ \mathcal{L}_{\pi NN}(x) \mathcal{L}_{\gamma\pi\pi}(y) \} \\
&= -\frac{i e}{2} \frac{f_\pi}{m_\pi} T \{ [\bar{\Psi} \gamma_5 (\tau_- \partial \pi^- + \tau_+ \partial \pi^+ + \tau_3 \partial \pi^0) \Psi]_x \\
&\quad \times [A^\mu (\pi^+ \partial_\mu \pi^- + \partial_\mu \pi^- \pi^+ - \pi^- \partial_\mu \pi^+ - \partial_\mu \pi^+ \pi^-)]_y \} \\
&= \sqrt{2} i e \frac{f_\pi}{m_\pi} \left\{ [\bar{\Psi}_p \gamma_5 \gamma_\mu \Psi_n]_x \partial_x^\mu \pi^+(x) \pi^-(y) [A_\nu \partial^\nu \pi^+]_y : \right. \\
&\quad - : [\bar{\Psi}_p \gamma_5 \gamma_\mu \Psi_n]_x \partial_x^\mu \pi^+(x) \partial_y^\nu \pi^-(y) [A_\nu \pi^+]_y : \\
&\quad \left. + \text{terms involving } : \bar{\Psi}_n \gamma_5 \partial \pi^- \Psi_p : \right\}
\end{aligned} \tag{2-46}$$

Take the Fock space matrix elements as we did for the seagull diagram. All the particles are distinguishable so normal ordering acts on single creation and annihilation operators. The s-matrix is then

$$\begin{aligned}
S_{fi} &= -\sqrt{2} i e \frac{f_\pi}{m_\pi} (2\pi)^{-9/2} \left[\frac{m}{E_p} \frac{1}{2E_\pi} \frac{1}{2E_\gamma} \right]^{1/2} \sum_{J_B M_B} (J_f, J_B; M_f, M_B | J_i, M_i) \mathcal{J}_{J_i, J_f}(J_B) \\
&\int d^4x d^4y \left\{ \bar{u}_{s_f}(k_p, x) \gamma_5 \gamma_\mu u_{J_B M_B}(x) \partial_x^\mu \pi^+(x) \pi^-(y) \epsilon_\nu^\rho e^{-ik_\gamma y} \partial_y^\nu v_\pi^*(k_\pi, y) \right. \\
&\quad \left. - \bar{u}_{s_f}(k_p, x) \gamma_5 \gamma_\mu u_{J_B M_B}(x) \partial_x^\mu \pi^+(x) \partial_y^\nu \pi^-(y) \epsilon_\nu^\rho e^{-ik_\gamma y} v_\pi^*(k_\pi, y) \right\}
\end{aligned} \tag{2-47}$$

Integrate the first term by parts once over y to remove the derivative from the pion wave function. This makes ∂_y^ν act on the contraction and on the photon wave function. The term with the gradient on the photon has $\epsilon_\mu^\rho \partial^\mu e^{-ik_\gamma y} = -i \epsilon_\mu^\rho k_\gamma^\mu e^{-ik_\gamma y} = 0$ since $\epsilon_\mu^\rho k_\gamma^\mu = 0$ for a real photon. The s-matrix for the pion pole contribution becomes

$$\begin{aligned}
S_{fi} &= 2\sqrt{2} i e \frac{f_\pi}{m_\pi} (2\pi)^{-9/2} \left[\frac{m}{E_p} \frac{1}{2E_\pi} \frac{1}{2E_\gamma} \right]^{1/2} \sum_{J_B M_B} (J_f, J_B; M_f, M_B | J_i, M_i) \mathcal{J}_{J_i, J_f}(J_B) \\
&\int d^4x d^4y \bar{u}_{s_f}(k_p, x) \gamma_5 \gamma_\mu u_{J_B M_B}(x) \partial_x^\mu \pi^+(x) \partial_y^\nu \pi^-(y) \epsilon_\nu^\rho e^{-ik_\gamma y} v_\pi^*(k_\pi, y)
\end{aligned} \tag{2-48}$$

The contraction of the pion fields is just i times the pion propagator, with the momentum of the propagating pion equal to the incident photon 4-momentum minus the final pion 4-momentum. The contraction of the derivatives of the pion fields yields the contraction of the pion fields times two factors of the propagating pion momentum and is (appendix B)

$$\partial_x^\mu \pi^+(x) \partial_y^\nu \pi^-(y) = i \frac{ (k_\gamma - k_\pi)^\mu (k_\gamma - k_\pi)^\nu }{ (k_\gamma - k_\pi)^2 - m_\pi^2 } \delta^4(x-y) \tag{2-49}$$

The delta function allows us to do the integration over y trivially. We separate the time dependence as we did for the seagull contribution (2-36) to do the time integration. The s-matrix can then be written in the same form as the seagull (2-38)

$$S_{fi} = \sqrt{2} e^{-\frac{f_\pi}{m_\pi}} (2\pi)^{-7/2} \delta(E_p + E_\pi - E_B - E_\gamma) \left(\frac{m}{E_p} \frac{1}{2E_\pi} \frac{1}{2E_\gamma} \right)^{1/2} \times \sum_{J_B M_B} (J_f, J_B; M_f, M_B | J_i, M_i) \mathcal{J}_{J_i J_f}(J_B) \times \int d^3x \psi_{s_f}^\dagger(k_p, \vec{x}) \Gamma_{\text{pion}} \psi_{J_B M_B}(\vec{x}) \phi_\pi^*(k_\pi, \vec{x}) e^{i\vec{k}_\gamma \cdot \vec{x}} \quad (2-50)$$

and the 4x4 matrix that operates on the nucleon spinors is

$$\Gamma_{\text{pion}} = -2 \frac{\epsilon_p \cdot k}{k^2 - m_\pi^2} \gamma_0 \gamma_5 \not{k} \quad (2-51)$$

The momentum of the propagating pion is the photon momentum minus the final pion momentum $k = k_\gamma - k_\pi$. All the other diagrams will be written in this form but with slightly more complicated Γ 's.

2.2.3 The Nucleon Poles

Terms contributing to the s-matrix involving nucleon propagators can arise from

$$\langle f | S | i \rangle = - \int d^4x d^4y \langle f | T \{ \mathcal{L}_{\gamma NN}(x) \mathcal{L}_{\pi NN}(y) \} | i \rangle \quad (2-52)$$

Take the interaction lagrangians from (2-4) and use the Wick expansion of the time ordered product to get three terms which can contribute to the reaction with a π^- in the final state.

$$S_{fi} = -\sqrt{2} \int d^4x d^4y \langle f | \left\{ e^{-\frac{f_\pi}{m_\pi}} : [\bar{\psi}_p \not{A} \psi_p]_x [\bar{\psi}_p \gamma_5 \not{\partial} \pi^+ \psi_n]_y : \right. \\ \left. + \frac{\kappa_p \mu_N}{2} \frac{f_\pi}{m_\pi} : [\bar{\psi}_p \sigma^{\mu\nu} F_{\mu\nu} \psi_p]_x [\bar{\psi}_p \gamma_5 \not{\partial} \pi^+ \psi_n]_y : \right. \\ \left. + \frac{\kappa_n \mu_N}{2} \frac{f_\pi}{m_\pi} : [\bar{\psi}_p \gamma_5 \not{\partial} \pi^+ \psi_n]_x [\bar{\psi}_n \sigma^{\mu\nu} F_{\mu\nu} \psi_n]_y : \right\} | i \rangle \quad (2-53)$$

where the third term has been rearranged using the fact that there are an even number of anticommuting fermion fields, to write

$$\underbrace{[\bar{\Psi}_n \sigma^{\mu\nu} F_{\mu\nu} \Psi_n]_x [\bar{\Psi}_p \gamma_5 \not{\partial} \pi^+ \Psi_n]_y} = [\bar{\Psi}_p \gamma_5 \not{\partial} \pi^+ \Psi_n]_y \underbrace{[\bar{\Psi}_n \sigma^{\mu\nu} F_{\mu\nu} \Psi_n]_x} \quad (2-54)$$

and the integration variables, x and y , have been interchanged.

The first two terms of (2-53) correspond to the proton pole term of figure 2-2c), where the first term is due to the photon coupling to the proton through the electric charge and the second term has the photon coupling to the proton through the anomalous magnetic moment. The third term is the neutron pole term of figure 2-2d) which allows the photon to couple to the uncharged neutron only through its anomalous magnetic moment.

The matrix elements between initial and final states are reduced as before. Thus for the proton pole term with the photon coupling through the electric charge we have

$$S_{fi}^{\text{proton}} = -\sqrt{2} e \frac{f_\pi}{m_\pi} (2\pi)^{-9/2} \left[\frac{m}{E_p} \frac{1}{2E_\pi} \frac{1}{2E_\gamma} \right]^{1/2} \sum_{J_B M_B} (J_f, J_B; M_f, M_B | J_i, M_i) \mathcal{J}_{J_i, J_f}(J_B) \quad (2-55)$$

$$\int d^4x d^4y \bar{u}_{s_f}(k_p, x) \not{\epsilon}_p e^{-ik_\gamma \cdot x} \underline{\Psi}_p(x) \bar{\Psi}_p(y) \gamma_5 \not{\partial} v_\pi^*(k_\pi, y) u_{J_B M_B}(y)$$

The contraction of the proton fields is i times the Dirac propagator with the momentum of the propagating particle given by the proton momentum minus the photon momentum. The contraction is then (appendix B)

$$\underline{\Psi}_p(x) \bar{\Psi}_p(y) = i \frac{k_p - k_\gamma + m}{(k_p - k_\gamma)^2 - m^2} \delta^4(x-y) \quad (2-56)$$

The y integration is again done using the delta function. Notice that we have a derivative acting on the pion wave function. We make the same approximation that we have made for the propagators, ie. the major contribution to the integral comes from the momentum components close to the plane wave value and we write

$$\not{\partial} v_\pi^*(k_\pi, y) \equiv i k_\pi v_\pi^*(k_\pi, y) \quad (2-57)$$

Performing the integration in time yields the s-matrix in the form (2-38) with the 4×4 matrix between the nucleon spinors

$$\Gamma_{\text{proton}}^e = \gamma_0 \not{\epsilon}_p \frac{k + m}{k^2 - m^2} \gamma_5 k_\pi \quad (2-58)$$

where the momentum of the propagating proton is the incident photon momentum minus the momentum of the final proton $k = k_p - k_\gamma$.

The anomalous magnetic moment portion of the proton pole term contains the Maxwell field tensor which is written in terms of the photon field as

$$\begin{aligned}
F_{\mu\nu} &= \partial_\mu A_\nu - \partial_\nu A_\mu \\
&= \frac{i}{(2\pi)^{3/2}} \sum_r \int \frac{d^3k}{\sqrt{2\omega_k}} (k_\nu \epsilon_{\mu r} - k_\mu \epsilon_{\nu r}) \{ a_r(\vec{k}) e^{-ik \cdot x} + a_r^\dagger(\vec{k}) e^{ik \cdot x} \}
\end{aligned} \tag{2-59}$$

The matrix element of $F_{\mu\nu}$ between initial and final states is

$$\langle 0 | F_{\mu\nu}(x) a_p^\dagger(\vec{k}_\gamma) | 0 \rangle = \frac{i}{(2\pi)^{3/2}} \frac{1}{(2\omega_k)^{1/2}} (k_\nu^\gamma \epsilon_{\mu p} - k_\mu^\gamma \epsilon_{\nu p}) e^{-ik_\gamma \cdot x} \tag{2-60}$$

and we use $\sigma^{\mu\nu} = \frac{i}{2} [\gamma^\mu, \gamma^\nu]$ to write

$$\langle 0 | \sigma^{\mu\nu} F_{\mu\nu}(x) a_p^\dagger(\vec{k}_\gamma) | 0 \rangle = \frac{1}{(2\pi)^{3/2}} \frac{1}{(2\omega_k)^{1/2}} [k_\gamma, \not{\epsilon}_p] e^{-ik_\gamma \cdot x} \tag{2-61}$$

The s-matrix for the anomalous proton pole contribution is then

$$\begin{aligned}
S_{fi}^{\text{proton}} &= -i\sqrt{2} (2\pi)^{-9/2} \frac{\kappa_p \mu_N}{2} \frac{f_\pi}{m_\pi} \left[\frac{m}{E_p} \frac{1}{2E_\pi} \frac{1}{2E_\gamma} \right]^{1/2} \\
&\sum_{J_B M_B} (J_f, J_B; M_f, M_B | J_i, M_i) \mathcal{J}_{J_i J_f}(J_B) \\
&\int d^4x d^4y \bar{u}_{s_f}(k_p, x) [k_\gamma, \not{\epsilon}_p] e^{-ik_\gamma \cdot x} \underline{\psi_p(x)} \bar{\psi_p}(y) \gamma_5 \not{k}_\pi v_\pi^*(k_\pi, y) u_{J_B M_B}(y)
\end{aligned} \tag{2-62}$$

and we use the contraction of the proton field (2-56) to get the Γ matrix for the anomalous proton pole contribution to be (using $\mu_N = e/2m$ with m the nucleon mass)

$$\Gamma_{\text{proton}}^\mu = \frac{\kappa_p}{4m} \gamma_0 [k_\gamma, \not{\epsilon}_p] \frac{\not{k} + m}{k^2 - m^2} \gamma_5 \not{k}_\pi \tag{2-63}$$

The contribution due to the neutron pole term is evaluated in the same manner and when we use the contraction of the neutron fields

$$\begin{aligned}
\underline{\psi_n(x)} \bar{\psi_n}(y) &= i \frac{\not{k}_3 + \not{k}_4 + m}{(k_3 + k_4)^2 - m^2} \delta^4(x-y) \\
&\text{with } k_3 \rightarrow k_\pi \text{ and } k_4 \rightarrow k_p
\end{aligned} \tag{2-64}$$

we get the Γ matrix to be

$$\Gamma_{\text{neutron}} = \frac{\kappa_n}{4m} \gamma_0 \gamma_5 \not{k}_\pi \frac{\not{k} + m}{k^2 - m^2} [k_\gamma, \not{\epsilon}_p] \tag{2-65}$$

and the four-momentum of the intermediate neutron is the sum of the momenta of the final proton and pion $k = k_\pi + k_1$.

2.2.4 $\Delta(1232)$ Poles

The $\Delta(1232)$ is the first excited state of the nucleon, and has total spin $J = 3/2$ and isospin $T = 3/2$. The latest nominal mass of the four charge states of the Δ is $M_\Delta = 1232$ MeV [Pa92] with a width $\Gamma = 120 \pm 5$ MeV (or a lifetime of 5.5×10^{-24} seconds).

The spin 3/2 field (Rarita-Schwinger field) [Um56, Be89] has four Lorentz components, each of which is a solution of a Dirac equation. For the free field with mass M we have

$$[i \gamma^\mu \partial_\mu - M] \psi_\nu = 0 \quad (2-66)$$

where each ψ_ν is a four component spinor, ie the wave function has sixteen components. The Lorentz components are related through the subsidiary condition

$$\gamma^\mu \psi_\mu = 0 \quad (2-67)$$

Equation (2-66) and the condition (2-67) are known as the Rarita-Schwinger equations [RS41]. Multiplying equation (2-66) from the left by γ^ν gives the additional condition

$$\partial^\mu \psi_\mu = 0 \quad (2-68)$$

Equation (2-66) allows us to eliminate either the upper or lower components from each component of the Lorentz four-vector, and the subsidiary condition (2-67) provides four constraints leaving four independent components for the spin 3/2 field (ie $2J+1$ independent components).

The Rarita-Schwinger equations can be obtained from the lagrangian density

$$\mathcal{L}_\Delta = \bar{\psi}_\mu \Lambda^{\mu\nu} \psi_\nu \quad (2-69)$$

where

$$\begin{aligned} \Lambda^{\mu\nu} = & [i \gamma^\alpha \partial_\alpha - M] g^{\mu\nu} + i A [\gamma^\mu \partial^\nu + \gamma^\nu \partial^\mu] \\ & + \frac{i}{2} [3A^2 + 2A + 1] \gamma^\mu \partial^\alpha \gamma_\alpha \gamma^\nu \\ & + M [3A^2 + 3A + 1] \gamma^\mu \gamma^\nu \end{aligned} \quad (2-70)$$

and A is an arbitrary parameter with the restriction $A \neq -1/2$. The physical properties of the free field do not depend on the parameter A and we choose $A = -1$ to get the form of the propagator which we will use later. This gives

$$\begin{aligned} \Lambda^{\mu\nu} = & [i \gamma^\alpha \partial_\alpha - M] g^{\mu\nu} - i [\gamma^\mu \partial^\nu + \gamma^\nu \partial^\mu] \\ & + i \gamma^\mu \partial^\alpha \gamma_\alpha \gamma^\nu + M \gamma^\mu \gamma^\nu \end{aligned} \quad (2-71)$$

Note that Umezawa's [Um56] expressions for the free field are reproduced if we set $A = -1/3$.

Application of the Euler-Lagrange equation to this lagrangian gives the equations of motion for the free field

$$\Lambda^{\mu\nu} \psi_\nu = 0 \quad (2-72)$$

This equation contains the form of the Rarita-Schwinger equations which we have already seen. First multiply from the left by γ_μ to get

$$-2i \partial^\mu \psi_\mu + 2i \partial \cdot \gamma \gamma^\mu \psi_\mu + 3M \gamma^\mu \psi_\mu = 0 \quad (2-73)$$

while multiplication by ∂_μ yields

$$\partial^\mu \psi_\mu = \partial \cdot \gamma \gamma^\mu \psi_\mu \quad (2-74)$$

From these two equations we find the conditions (2-67) and (2-68) which we use in the equation of motion to get the Dirac equation (2-66) for each of the components.

The propagator for the Rarita-Schwinger field satisfies the equation

$$\Lambda^{\mu\delta} P_\delta^\nu(x) = g^{\mu\nu} \delta^4(x) \quad (2-75)$$

We Fourier transform this equation using the standard transformation, and the expansion of the Dirac delta function

$$\begin{aligned} P_\delta^\nu(x) &= (2\pi)^{-4} \int d^4p P_\delta^\nu(p) e^{-i p \cdot x} \\ \delta^4(x) &= (2\pi)^{-4} \int d^4p e^{-i p \cdot x} \end{aligned} \quad (2-76)$$

to get the momentum space equation for the propagator

$$\Lambda^{\mu\delta}(p) P_\delta^\nu(p) = g^{\mu\nu} \quad (2-77)$$

where

$$\begin{aligned} \Lambda^{\mu\delta}(p) &= [p \cdot \gamma - M] g^{\mu\delta} - [\gamma^\mu p^\delta + \gamma^\delta p^\mu] \\ &\quad + \gamma^\mu p \cdot \gamma \gamma^\delta + M \gamma^\mu \gamma^\delta \end{aligned} \quad (2-78)$$

This momentum space equation can be inverted to find the propagator for the free spin-3/2 field to be

$$P_\delta^\nu(p) = \frac{p \cdot \gamma + M}{p^2 - M^2} \left\{ g_\delta^\nu - \frac{1}{3} \gamma_\delta \gamma^\nu - \frac{2}{3M^2} p_\delta p^\nu + \frac{1}{3M} [p_\delta \gamma^\nu - \gamma_\delta p^\nu] \right\} \quad (2-79)$$

That this is indeed a solution of equation (2-77) can be checked by direct, although tedious, multiplication. This is the form of the propagator we will use for the $\Delta(1232)$

with the modification of the denominator to include the width of the Δ

$$p^2 - M^2 \rightarrow p^2 - M^2 + i M \Gamma \quad (2-80)$$

The Δ -pole contributions come from the interaction lagrangians (2-10) which lead to the diagrams 2-2e) and 2-2f) from the s-matrix

$$\langle f | S | i \rangle = - \int d^4x d^4y \langle f | T \{ \mathcal{L}_{\pi N \Delta}(x) \mathcal{L}_{\gamma N \Delta}(y) \} | i \rangle \quad (2-81)$$

The Δ has isospin 3/2 which means it has four charge states. We write the Δ wave function in terms of its charge states as a four component isospinor

$$\Delta^\mu = \begin{bmatrix} \Delta_{++}^\mu \\ \Delta_+^\mu \\ \Delta_0^\mu \\ \Delta_-^\mu \end{bmatrix} \quad (2-82)$$

where the subscript indicates the charge of the field. We form 4x2 isospin raising and lowering operators $T_\pm = \frac{1}{\sqrt{2}}(T_1 \pm T_2)$ allowing us to expand the isospin scalar product with the pion as $\vec{T} \cdot \vec{\phi} = (T_+ \pi^+ + T_- \pi^- + T_3 \pi^0)$. Note that the T_i are not hermitian matrices (see appendix A) so $(\vec{T} \cdot \vec{\phi})^\dagger = (T_+^\dagger \pi^- + T_-^\dagger \pi^+ + T_3^\dagger \pi^0)$.

Take the interaction lagrangians from (2-10) and use the Wick expansion of the time ordered product to get two terms which contribute to the reaction with a π^- in the final state

$$S_{fi} = i \frac{\sqrt{2}}{3} e \frac{f_{\gamma N \Delta} f_{\pi N \Delta}}{m_\pi^2} \int d^4x d^4y \langle f | \{ : [\bar{\psi}_p \gamma^\rho \gamma_5 F_{\mu\rho} \Delta_+^\mu]_y [\bar{\Delta}_+^\nu \partial_\nu \pi^+ \psi_n]_x : \quad (2-83) \\ - : [\bar{\psi}_p \partial_\mu \pi^+ \Delta_0^\mu]_x [\bar{\Delta}_0^\nu \gamma^\rho \gamma_5 F_{\nu\rho} \psi_n]_y : \} | i \rangle$$

The first term of (2-83) corresponds to the u-channel Δ contribution of figure 2-2f) and the second term is the s-channel Δ of figure 2-2e). Evaluating the matrix elements between initial and final states yields

$$S_{fi}^{\Delta-u} = - \frac{\sqrt{2}}{3} (2\pi)^{-9/2} e \frac{f_{\gamma N \Delta} f_{\pi N \Delta}}{m_\pi^2} \left[\frac{m}{E_p} \frac{1}{2E_\pi} \frac{1}{2E_\gamma} \right]^{1/2} \sum_{J_B M_B} (J_f, J_B; M_f, M_B | J_i, M_i) \mathcal{J}_{J_i J_f}(J_B) \\ \int d^4x d^4y \bar{u}_s(k_p, x) \gamma_5 [\not{k}^\gamma \epsilon_{\mu\rho} - k_\mu^\gamma \not{\epsilon}_\rho] e^{-ik_\gamma x} \Delta_+^\mu(x) \bar{\Delta}_+^\nu(y) \partial_\nu v_\pi^*(k_\pi, y) u_{J_B M_B}(y) \quad (2-84)$$

$$S_{fi}^{\Delta-s} = \frac{\sqrt{2}}{3} (2\pi)^{-9/2} e^{\frac{f_{\gamma N\Delta} f_{\pi N\Delta}}{m_\pi^2} \left[\frac{m}{E_p} \frac{1}{2E_\pi} \frac{1}{2E_\gamma} \right]^{1/2}} \sum_{J_B M_B} (J_f, J_B; M_f, M_B | J_i, M_i) \mathcal{J}_{J_i J_f}(J_B) \int d^4x d^4y \bar{u}_{s_f}(k_p, x) \partial_\mu v_\pi^*(k_\pi, x) \underline{\Delta_0^\mu(x)} \overline{\Delta_0^\nu(y)} [k_\gamma^\nu \epsilon_{\nu p} - k_\nu^\gamma \epsilon_p] \gamma_5 e^{-ik_\gamma \cdot y} u_{J_B M_B}(y) \quad (2-85)$$

The contractions we need for the delta are (appendix B)

$$\underline{\Delta_c^\mu(x)} \overline{\Delta_c^\nu(y)} = i \frac{\not{p}_\Delta + m_\Delta}{p_\Delta^2 - m_\Delta^2 + im_\Delta \Gamma_\Delta} \left[g^{\mu\nu} - \frac{1}{3} \gamma^\mu \gamma^\nu - \frac{1}{3m_\Delta} (\gamma^\mu p_\Delta^\nu - \gamma^\nu p_\Delta^\mu) - \frac{2}{3m_\Delta^2} p_\Delta^\mu p_\Delta^\nu \right] \delta^4(x-y) \quad (2-86)$$

where in the s-channel the Δ is uncharged ($c=0$) and the momentum of the Δ is the sum of the pion and proton momenta $p_\Delta = k_\pi + k_p$. In the u-channel the Δ has a positive charge ($c=+$) and the momentum of the Δ is the difference between the proton and photon momenta $p_\Delta = k_p - k_\gamma$.

We do the four dimensional integration over y and the time integration for x to get the s-matrix in the form of (2-38) with the 4x4 operator for the s-channel Δ as

$$\Gamma_{\Delta-s} = -\frac{f_{\gamma N\Delta} f_{\pi N\Delta}}{3 f_\pi m_\pi} \gamma_0 \frac{\not{p}_\Delta + m_\Delta}{p_\Delta^2 - m_\Delta^2 + im_\Delta \Gamma_\Delta} k_\mu^\pi \left[g^{\mu\nu} - \frac{1}{3} \gamma^\mu \gamma^\nu - \frac{1}{3m_\Delta} (\gamma^\mu p_\Delta^\nu - \gamma^\nu p_\Delta^\mu) - \frac{2}{3m_\Delta^2} p_\Delta^\mu p_\Delta^\nu \right] [k_\gamma^\nu \epsilon_{\nu p} - k_\nu^\gamma \epsilon_p] \gamma_5 \quad (2-87)$$

with the momentum of the intermediate Δ as the sum of the momenta of the final proton and pion $p_\Delta = k_\pi + k_p$.

For the u-channel Δ the Γ matrix takes the form

$$\Gamma_{\Delta-u} = \frac{f_{\gamma N\Delta} f_{\pi N\Delta}}{3 f_\pi m_\pi} \gamma_0 \gamma_5 [k_\gamma^\nu \epsilon_{\nu p} - k_\mu^\gamma \epsilon_p] \frac{\not{p}_\Delta + m_\Delta}{p_\Delta^2 - m_\Delta^2 + im_\Delta \Gamma_\Delta} \left[g^{\mu\nu} - \frac{1}{3} \gamma^\mu \gamma^\nu - \frac{1}{3m_\Delta} (\gamma^\mu p_\Delta^\nu - \gamma^\nu p_\Delta^\mu) - \frac{2}{3m_\Delta^2} p_\Delta^\mu p_\Delta^\nu \right] k_\nu^\pi \quad (2-88)$$

with the momentum of the propagating Δ as the difference between the momenta of the incoming photon and the final state proton $p_\Delta = k_p - k_\gamma$.

The total s-matrix for the reaction $A(\gamma, \pi^- p)A-1$ can then be written as

$$S_{fi} = \sqrt{2} e^{-\frac{i\pi}{m\pi}} (2\pi)^{-7/2} \delta(E_p + E_\pi - E_B - E_\gamma) \left(\frac{m}{E_p} \frac{1}{2E_\pi} \frac{1}{2E_\gamma} \right)^{1/2} \times \sum_{J_B M_B} (J_f, J_B; M_f, M_B | J_i, M_i) \mathcal{J}_{J_i J_f}(J_B) \times \int d^3x \psi_{s_f}^\dagger(\mathbf{k}_p, \vec{x}) \Gamma_{\text{total}} \psi_{J_B M_B}(\vec{x}) \phi_\pi^*(\mathbf{k}_\pi, \vec{x}) e^{i\vec{k}_\gamma \cdot \vec{x}} \quad (2-89)$$

where the total 4x4 operator acting on the nucleon wave functions is the sum of the operators from all of the diagrams we consider $\Gamma_{\text{total}} = \sum_i \Gamma_i$, where the Γ_i are given in equations (2-39, 2-51, 2-58, 2-63, 2-65, 2-87 and 2-88).

To evaluate this further we must specify the wave functions describing the continuum and bound nucleons as well as the final state pion. We first do the calculation using plane waves for both the pion and the proton and obtain an expression for the s-matrix which is straightforward to evaluate. We then consider distorted waves for the pion and proton, which results in a more complicated form for the s-matrix but in the absence of distorting potentials must yield the same results as the PW calculations.

2.3 Plane Waves

The lowest order approximation is to neglect the final state interactions of the pion and proton with the residual nucleus. The pion wave function is a solution of the free Klein-Gordon equation with outgoing boundary conditions and is simply

$$\phi_\pi^*(\vec{k}_\pi, \vec{x}) = e^{-i\vec{k}_\pi \cdot \vec{x}} \quad (2-90)$$

The positive energy solution of the free Dirac equation with spin projection s_f and momentum \vec{k}_p is [BD64]

$$\psi_{s_f}(\vec{k}_p, \vec{x}) = \left[\frac{E_p + m}{2m} \right]^{1/2} \begin{bmatrix} \mathbb{1} \\ \frac{\vec{\sigma} \cdot \vec{k}_p}{E_p + m} \end{bmatrix} e^{i\vec{k}_p \cdot \vec{x}} |1/2, s_f\rangle \quad (2-91)$$

where $\mathbb{1}$ is the 2x2 unit matrix and the σ_i are the Pauli spin matrices.

The simple description used above for the continuum nucleon wave function cannot be used for the bound state neutron. The interaction between the neutron and the rest of

nucleus is what binds the neutron therefore we can't ignore that interaction. We describe the neutron as a solution of the Dirac equation with real scalar and vector potentials

$$\{ \vec{\alpha} \cdot \vec{p} + \beta [m + S(r)] + V(r) \} \psi(\vec{r}) = E \psi(\vec{r}) \quad (2-92)$$

where $\beta = \gamma_0$ and $\alpha_i = \gamma_0 \gamma_i$. There is no Coulomb potential included since the neutron has zero charge. The potential is spherically symmetric so it depends only on the magnitude of the radius vector $r = |\vec{r}|$, and the neutron is described in the rest frame of the nucleus with the origin at the center of the nucleus.

The bound nucleon has definite angular momentum quantum numbers (L_B, J_B, M_B) and we can write the wave function as

$$\psi_B(\vec{x}) = \begin{bmatrix} f_B(r) \\ -i g_B(r) \vec{\sigma} \cdot \hat{r} \end{bmatrix} \mathcal{Y}_{L_B 1/2 J_B}^{M_B} \quad (2-93)$$

The i appears in the lower component of the bound state wave function so that f_B and g_B are real relative to each other. The total energy of the bound neutron is less than the rest mass of the neutron by the binding energy $E_n = m - E_t$.

The generalized spherical harmonic $\mathcal{Y}_{L 1/2 J}^M$ is formed by combining a spherical harmonic of order L with an eigenfunction of spin as

$$\mathcal{Y}_{L 1/2 J}^M = \sum_{m_L m_s} (L, 1/2; m_L, m_s | JM) Y_L^{m_L}(\Omega) |1/2, m_s\rangle \quad (2-94)$$

This function is an eigenfunction of L^2 , S^2 , J^2 and J_z and has the useful property that

$$\vec{\sigma} \cdot \hat{r} \mathcal{Y}_{L 1/2 J}^M = - \mathcal{Y}_{L' 1/2 J}^M \quad (2-95)$$

with $L' = 2J - L$.

The bound state wave function is normalized such that the total probability of finding the particle somewhere in space is one, which gives the condition

$$\int \psi_B^\dagger(\mathbf{x}) \psi_B(\mathbf{x}) d^3x = \int_0^\infty [f_B^2(r) + g_B^2(r)] r^2 dr = 1 \quad (2-96)$$

We write the complex 4x4 operator Γ in terms of complex 2x2 matrix operators as

$$\Gamma = \begin{bmatrix} \Gamma_{11} & \Gamma_{12} \\ \Gamma_{21} & \Gamma_{22} \end{bmatrix} \quad (2-97)$$

and some straightforward algebra yields for the s-matrix (2-89)

$$\begin{aligned}
S_{fi} = & \sqrt{2} e^{\frac{f_{\pi}}{m_{\pi}}} (2\pi)^{-7/2} \delta(E_p + E_{\pi} - E_B - E_{\gamma}) \left[\frac{E_p + m}{2E_p} \frac{1}{2\omega_{\pi}} \frac{1}{2\omega_{\gamma}} \right]^{1/2} \\
& \times \sum_{J_B M_B} (J_f, J_B; M_f, M_B | J_i, M_i) \mathcal{J}_{J_i J_f}(J_B) \\
& \times \int d^3x e^{i\vec{q} \cdot \vec{x}} \{ f_B(r) < 1/2, s_f | \Gamma_f | \mathcal{Y}_{L_B 1/2 J_B}^{M_B} > \\
& \quad + i g_B(r) < 1/2, s_f | \Gamma_g | \mathcal{Y}_{L_B 1/2 J_B}^{M_B} > \}
\end{aligned} \tag{2-98}$$

where the momentum transfer to the nucleus is $\vec{q} = \vec{k}_{\gamma} - \vec{k}_{\pi} - \vec{k}_p$ and we have defined the 2x2 matrices

$$\Gamma_f = \Gamma_{11} + \frac{\vec{\sigma} \cdot \vec{k}_p}{E_p + m} \Gamma_{21} \quad \Gamma_g = \Gamma_{12} + \frac{\vec{\sigma} \cdot \vec{k}_p}{E_p + m} \Gamma_{22} \tag{2-99}$$

Apart from some spin dependent factors the s-matrix looks like the Fourier transform of the bound state wave function. The cross section is then nearly proportional to the square of the Fourier transform of the bound state wave function. The momentum transfer in the reaction we are considering is in the range 0-2 fm⁻¹ (0-400 MeV/c), so if the plane wave approximation is good we have the opportunity to examine the nuclear wave function over a wide range of momentum transfers.

2.4 Distorted Waves

We now allow the proton and pion to interact with the final state nucleus by introducing appropriate potentials into the wave equation describing the motion of the particle.

The proton is described by a solution of the Dirac equation with scalar and vector potentials. The elastic scattering solution is asymptotically an incident plane wave with spherical outgoing scattered waves and is denoted by $\psi_{s_f}^{(+)}(\vec{x})$, where the superscript (+) signifies outgoing boundary conditions. The final state proton wave function is the time reversed state of $\psi_{s_f}^{(+)}(\vec{x})$ so it is asymptotically a plane wave with incoming spherical waves and is denoted by $\psi_{s_f}^{(-)}(\vec{x})$ [Jo86], where the superscript (-) indicates its incoming boundary conditions. This is exactly analogous to the nonrelativistic description of scattering states [Ja70]. The final state proton wave function is then written as

$$\psi_{sr}^{(-)\dagger}(\vec{x}) = 4\pi \left[\frac{E+m}{2m} \right]^{1/2} \sum_{LJM} i^{-L} Y_L^{M-s_f}(\hat{\mathbf{k}}_p) (L, 1/2; M-s_f, s_f | JM) \times \mathcal{Y}_{L1/2J}^{M\dagger} \left[f_{LJ}(r), i g_{LJ}(r) \vec{\sigma} \cdot \hat{\mathbf{r}} \right] \quad (2-100)$$

The pion wave function is expanded similarly as

$$\varphi_{\pi}^*(\mathbf{k}_{\pi}, \vec{x}) = 4\pi \sum_{L_{\pi} M_{\pi}} i^{-L_{\pi}} v_{L_{\pi}}(\mathbf{k}_{\pi} r) Y_{L_{\pi}}^{M_{\pi}}(\hat{\mathbf{k}}_{\pi}) Y_{L_{\pi}}^{M_{\pi}*}(\Omega) \quad (2-101)$$

In the limit that the pion potentials are zero the radial functions reduce to spherical Bessel functions and the pion wave function is exactly the plane wave function (2-90) [Ja75]. Also if the Dirac potentials are set to zero the upper component radial function reduces to a spherical Bessel function while the lower component is related to the derivative of the spherical Bessel function and the proton wave function is exactly the plane wave solution of the Dirac equation (2-91). The potentials describing proton and pion elastic scattering from a nucleus are discussed in chapter 3.

We haven't talked about a choice of coordinate system up to this point but now we are going to choose one in order to simplify the expansion of the photon wave function. We choose the photon momentum to lie along the z-axis such that the photon momentum vector is $\vec{\mathbf{k}}_{\gamma} = (0, 0, k_{\gamma})$. The details of the coordinate system are shown in figure 2-3. For the case of coplanar geometry the pion momentum is in the first quadrant of the x-z plane so the azimuthal angle is $\phi_{\pi} = 0$ while for the proton we have $\phi_p = \pi$. For non-coplanar geometry we hold the pion momentum in the x-z plane and let the proton momentum come out of the plane. The photon polarization vector has components perpendicular to the z-axis and we write $\epsilon_p^{\mu} = (0, \cos\xi, \sin\xi, 0)$ where we choose linearly polarized light by selecting our two basis vectors with $\xi=0$ and $\xi = \pi/2$. This gives two linear polarization vectors (where the label p is now the polarization angle ξ) as $\epsilon_{\xi=0}^1 = \epsilon_{p=1}^1 = (0, 1, 0, 0)$ and $\epsilon_{\xi=\pi/2}^2 = \epsilon_{p=2}^2 = (0, 0, 1, 0)$. We also have $\epsilon^0 = \epsilon^3 = (0, 0, 0, 0)$.

The photon is described by

$$e^{i\vec{\mathbf{k}}_{\gamma} \cdot \vec{x}} = e^{ik_{\gamma} z} = \sqrt{4\pi} \sum_{L_{\gamma}} i^{L_{\gamma}} (2L_{\gamma} + 1)^{1/2} j_{L_{\gamma}}(k_{\gamma} r) Y_{L_{\gamma}}^0(\Omega) \quad (2-102)$$

where $j_{L_{\gamma}}(k_{\gamma} r)$ is the spherical Bessel function of order L_{γ} .

Using these expansions for the wave functions describing the continuum particles,

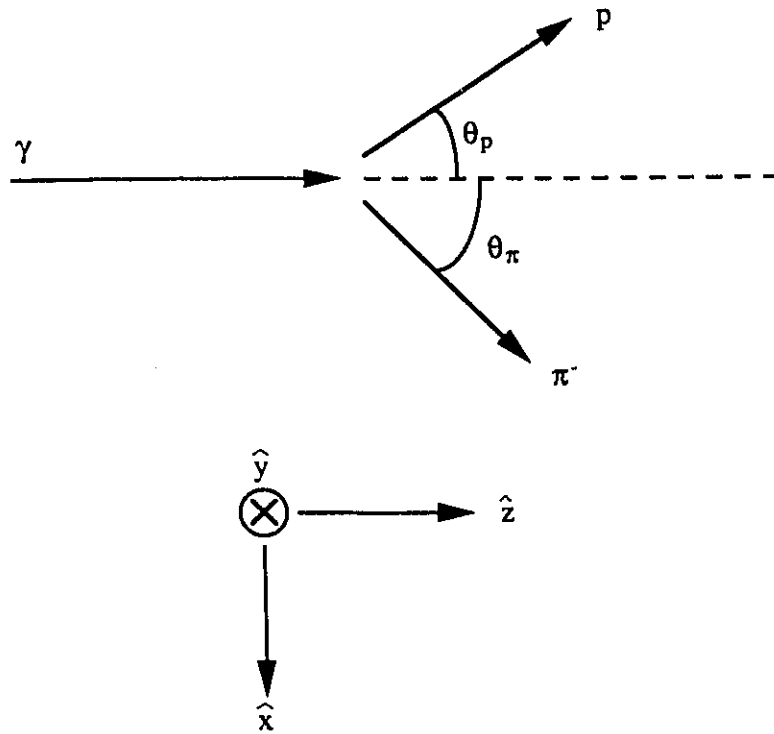


Figure 2-3. Coordinate system for pion photoproduction on a nucleus. The z-axis is chosen along the photon momentum and the pion momentum lies in the first quadrant of the x-z plane.

the form (2-93) for the bound state wave function and writing the Γ operator in terms of 2x2 complex matrices as in (2-97) the s-matrix can be written as

$$\begin{aligned}
S_{fi} = & \frac{\sqrt{2}}{\pi} e^{-\frac{f_{\pi}}{m_{\pi}}} \left(\frac{E_p + m}{E_p \omega_{\pi} \omega_{\gamma}} \right)^{1/2} \delta(E_p + E_{\pi} - E_B - E_{\gamma}) \\
& \times \sum_{J_B M_B} (J_f, J_B; M_f, M_B | J_i, M_i) \mathcal{J}_{J_i J_f}(J_B) \\
& \times \sum_{L J L_{\pi} L_{\gamma}} i^{L_{\gamma} - L - L_{\pi}} (2L_{\gamma} + 1)^{1/2} \\
& \times \sum_{M M_{\pi}} Y_L^{M - s_f}(\hat{\mathbf{k}}_p) Y_{L_{\pi}}^{M_{\pi} *}(\hat{\mathbf{k}}_{\pi}) (L, \frac{1}{2}; M - s_f, s_f | J, M) \\
& \times \left\{ R_{ff}[\kappa \kappa_B L_{\pi} L_{\gamma}] A_{11} \begin{bmatrix} \kappa & \kappa_B & L_{\pi} & L_{\gamma} & \xi \\ M & M_B & M_{\pi} & & \end{bmatrix} \right. \\
& + R_{gg}[\kappa \kappa_B L_{\pi} L_{\gamma}] A_{22} \begin{bmatrix} \kappa' & \kappa_B & L_{\pi} & L_{\gamma} & \xi \\ M & M_B & M_{\pi} & & \end{bmatrix} \\
& + i R_{fg}[\kappa \kappa_B L_{\pi} L_{\gamma}] A_{12} \begin{bmatrix} \kappa & \kappa_B & L_{\pi} & L_{\gamma} & \xi \\ M & M_B & M_{\pi} & & \end{bmatrix} \\
& \left. - i R_{gf}[\kappa \kappa_B L_{\pi} L_{\gamma}] A_{21} \begin{bmatrix} \kappa' & \kappa_B & L_{\pi} & L_{\gamma} & \xi \\ M & M_B & M_{\pi} & & \end{bmatrix} \right\} \quad (2-103)
\end{aligned}$$

where the radial integrals are defined as [with $\kappa = (L - J)(2J + 1)$ and $L' = 2J - L$]

$$R_{SB}[\kappa \kappa_B L_{\pi} L_{\gamma}] = \int S_{LJ}(r) B_{L_B M_B}(r) v_{L_{\pi}}(k_{\pi} r) j_{L_{\gamma}}(k_{\gamma} r) r^2 dr \quad (2-104)$$

and $S(r)$ is either the upper or lower component radial function for the scattered proton while $B(r)$ is either the upper or lower component radial function of the bound neutron. Also define the angular integrals as

$$A_{ij} \begin{bmatrix} \kappa & \kappa_B & L_{\pi} & L_{\gamma} & \xi \\ M & M_B & M_{\pi} & & \end{bmatrix} = \int \mathcal{Y}_{L 1/2 J}^M \dagger \Gamma_{ij} \mathcal{Y}_{L_B 1/2 J_B}^{M_B} Y_{L_{\pi}}^{M_{\pi}}(\Omega) Y_{L_{\gamma}}^0(\Omega) d\Omega \quad (2-105)$$

These angular integrals require a good deal more work before we can actually calculate them and the way we do this is addressed in appendix C. Note that the angular integral is a scalar (a complex number) since the 2x2 matrix is sandwiched between spin functions as well as spherical harmonics.

We calculate the energies and momenta of the final particles using the constraints provided by conservation of energy and momentum. These are not enough to fix the kinematics of the outgoing particles since the final state has three particles, so we fix the directions of two particles and the energy of one of the particles and the kinematics for

the reaction are fixed. The integrals over radial functions are strongly convergent because the bound state wave function decreases exponentially for large r . These integrals are done numerically using Bode's rule [AS72]. The sums over angular momenta converge and in our calculations the sums over proton and pion angular momenta are cut off at some maximum L which limits the maximum value of the photon angular momentum to roughly $2L$ through angular momentum coupling rules (appendix C).

2.5 Gauge invariance

The four-vector potential (2-22) which we use to describe the photon field is not a unique choice. The vector potential can undergo a gauge transformation of the form

$$A_\mu \rightarrow A'_\mu = A_\mu + \partial_\mu G \quad (2-106)$$

and the electric and magnetic fields will be unaltered. The observables which we calculate should be independent of the choice of the gauge function G , or by an appropriate choice of G we could get any answer we desire.

The gauge transformation amounts to changing the polarization vector of the photon by a constant times the photon momentum

$$\epsilon_{\mu p} \rightarrow \epsilon'_{\mu p} = \epsilon_{\mu p} + a k_\mu \quad (2-107)$$

which still obeys $\epsilon'_p \cdot k_\gamma = 0$ since $k_\gamma \cdot k_\gamma = 0$ for real photons. To test whether our calculation is gauge invariant we make the substitution [BD64]

$$\epsilon_{\mu p} \rightarrow k_\mu \quad (2-108)$$

and if the calculation is gauge invariant the result will be zero.

First we consider the case of couplings involving the Maxwell tensor $F_{\mu\nu}$. We have four diagrams which contain couplings to the Maxwell tensor, two due to anomalous magnetic moments and two due to the delta. The Fock space matrix element of the Maxwell tensor of equation (2-60) is

$$\langle F_{\mu\nu} \rangle \propto k_\nu^\gamma \epsilon_{\mu p} - k_\mu^\gamma \epsilon_{\nu p} \quad (2-109)$$

and when we make the replacement (2-108) we see that any diagram with the photon described by the Maxwell tensor is gauge invariant. This is true for both plane wave and distorted wave calculations.

The remaining diagrams have the photon coupling to a particle through the electric

charge. The sum of the Γ matrices for the three diagrams given in equations (2-39), (2-51) and (2-58) is

$$\Gamma = \gamma_0 \gamma_5 \left[\not{\epsilon}_p - 2 \frac{\epsilon_p \cdot k}{k^2 - m_\pi^2} \not{k} + \not{\epsilon}_p \frac{\not{p} - m}{p^2 - m^2} \not{k}_\pi \right] \quad (2-110)$$

where the momentum of the intermediate pion is $k = k_\gamma - k_\pi$ and the momentum of the propagating proton is $p = k_p - k_\gamma$. To test for gauge invariance we make the replacement (2-108) to get the transformed Γ matrix to be

$$\Gamma' = - \frac{1}{2k_\gamma \cdot k_p} \gamma_0 [\not{k}_p - m] \gamma_5 \not{k}_\gamma \not{k}_\pi \quad (2-111)$$

If we now use this Γ matrix in the s-matrix (2-38) we have the final state proton on the right of Γ' and we have the combination $\bar{\psi}_{s_f} [\not{k}_p - m]$ in our s-matrix element. From the Dirac equation for a free fermion field ψ with 4-momentum p , $[\not{p} - m] \psi = 0$ we can show that $\bar{\psi} [\not{p} - m] = 0$, so that in the plane wave approximation the combination of the three Born terms is gauge invariant. It is also clear that when the proton wave function is a solution of an equation with potentials the s-matrix is no longer gauge invariant, but we have no clear remedy for this and we continue on with a calculation that is gauge invariant in the limit of vanishing potentials.

2.6 Observables for $A(\gamma, \pi^- p)A-1$

The s-matrix is labelled by the projection of the target nucleus M_i and the polarization of the photon, as well as the projections of the proton s_f and the final nucleus M_f . We define a matrix element $Z_{\xi M_B}^{s_f}$ which is labelled by the projection of the bound target nucleon such that the coupling between the initial nucleus, the final nucleus and the bound nucleon is taken care of through a Clebsch-Gordan coefficient. We can then write the s-matrix in a more concise form as follows

$$S_{fi} = \frac{\sqrt{2}}{\pi} e \frac{f_\pi}{m_\pi} \left(\frac{E_p + m}{E_p E_\pi E_\gamma} \right)^{1/2} \delta(E_p + E_\pi - E_B - E_\gamma) \quad (2-112)$$

$$\times \sum_{J_B M_B} (J_f, J_B; M_f, M_B | J_i, M_i) \mathcal{J}_{J_i J_f}(J_B) Z_{\xi M_B}^{s_f}$$

where $Z_{\xi M_B}^{s_f}$ is a function of the polarization of the initial photon, the spin projection of the final proton and the projection of the nuclear bound state. $Z_{\xi M_B}^{s_f}$ contains the radial and angular integrals and the sums over all the angular momenta. The exact form for

$Z_{\xi M_B}^{sr}$ can be obtained by comparing with (2-98) for the plane wave calculation or (2-103) for the distorted wave calculation.

The cross section is then calculated through the usual procedure [BD64] of squaring the s-matrix to get a transition probability, multiplying by the number of available final states and dividing by the incident flux. We finally average over initial spin projections and sum over final spin projections to get (appendix D)

$$\frac{d\sigma}{d\Omega_\pi d\Omega_p dE_p} = 4 (4\pi)^2 \frac{1}{\hbar c} \frac{\alpha \beta}{m_\pi^2 c^4} \left(\frac{E_p + mc^2}{E_\gamma} \right) p_{\pi c} p_{p c} \sum_{J_B M_B} \sum_{s_r \xi} \frac{J_{J_i}^2 J_r(J_B)}{2J_B+1} |Z_{\xi M_B}^{sr}|^2 \quad (2-113)$$

The polarization of the final proton is found by

$$P = -2 \frac{\text{Im} \sum_{\xi M_B} Z_{\xi M_B}^{1/2} [Z_{\xi M_B}^{-1/2}]^*}{\sum_{s_r \xi M_B} Z_{\xi M_B}^{s_r} [Z_{\xi M_B}^{s_r}]^*} \quad (2-114)$$

The analyzing power due to linearly polarized incident photons is

$$A = \frac{d\sigma_\perp - d\sigma_\parallel}{d\sigma_\perp + d\sigma_\parallel} \quad (2-115)$$

where $d\sigma_\perp$ is the cross section due to a photon with polarization vector perpendicular to the scattering (x - z) plane, ie. the polarization vector points along the y-axis. Similarly $d\sigma_\parallel$ is the cross section measured with photon polarization vector in the scattering plane (along the x-axis here).

2.7 Programming Tests

We have written programs to calculate observables for the ($\gamma, \pi^- p$) reaction using both the plane wave expression for the s-matrix (2-98) (PW) and the distorted wave form (2-103) (DW).

The Γ matrices are common to both programs and are functions of the four-momenta of the particles, and the Dirac gamma matrices. The calculation of the Γ matrices involves multiplication of complex 4x4 matrices and we tested our subroutines by selecting a set of momentum four-vectors and doing the matrix multiplication for each Γ by hand and comparing the results to the results of our subroutines. We obtain agreement to the accuracy of the machine for these calculations. The s-matrix for the

elementary process $\gamma + n \rightarrow \pi^- + p$ can also be written in terms of these same matrices, and we have calculated observables for this process and obtained agreement with experimental data.

The z-matrix defined in equation (2-112) is related to the t-matrix through a kinematic factor. In the limit that the potentials (nuclear and Coulomb) are turned off, the separate PW and DW codes should give the same results for the z-matrix. We get the z-matrix elements for the two calculations agreeing to at least four significant figures depending on the values of several parameters governing the sums of the partial wave series and the number integration steps we use.

The convergence of the sums in equation (2-103) as functions of the maximum angular momenta of the pion and the proton have been tested. Holding the maximum pion angular momentum constant at $L_{\pi}^{\max} = 15$ while the maximum proton angular momentum is increased from 10 to 25, shows the calculated cross section converge to the plane wave calculation with no discernible difference for calculations which have $L_p^{\max} \geq 16$.

Similarly when the maximum proton orbital angular momentum is held constant at $L_p^{\max} = 20$ and the maximum pion angular momentum is increased from 7 to 15 we again see the DWBA results converge to the PW results.

The inclusion of distortions modifies the radial wave functions describing the pion and proton from a spherical Bessel function but doesn't affect the machinery of the radial integration. The distorting potentials have been tested by calculating elastic scattering observables and comparing with experimental data.

Chapter 3 - Relativistic Potential Models for the Pion and Nucleon

In chapter 2 we derived an expression for the s-matrix for charged pion photoproduction on a nucleus, equation (2-103), in which the proton and pion wave functions are solutions of equations containing complex potentials. In this chapter we discuss the optical models for proton and pion elastic scattering. We begin with a simple model in order to clarify the origin and meaning of the imaginary part of the optical potential. We then describe the nonrelativistic optical model of nucleon-nucleus elastic scattering, which is discussed at length by Hodgson [Ho63]. We then make the transition to the relativistic description of the nucleon-nucleus dynamics, Dirac phenomenology, which we actually use in the current calculation to describe both bound and continuum states of the nucleons [Co92]. Finally we discuss the phenomenology of pion-nucleus elastic scattering with emphasis on the potential model of Stricker, McManus and Carr [SMC79, SMC80].

3.1 A Simple Model

A particle can interact with a nucleus through a variety of processes. The particle may simply change direction with no change in energy in the center of momentum system, while the nucleus is left in its ground state; this process is called elastic scattering. Alternatively the nucleus may be left in an excited state (inelastic scattering), the projectile may knock one or more nucleons out of the nucleus, or the nucleus may even be shattered by the collision. The projectile can be absorbed into the nucleus with the production of a photon or a meson and a variety of other processes can occur. The probability that a process occurs depends on the choice of projectile and nucleus as well as the relative momentum of the projectile and target.

The incident projectile can interact with any one of the nucleons in the nucleus or a combination of nucleons on the way to a final state which is actually detected. The description of a projectile-nucleus interaction through summing the relevant projectile-nucleon possibilities can be very complicated. As an alternative we use an optical model description of the projectile-nucleus interaction. This model is called the optical model

because the replacement of the many body nuclear interactions by a two body projectile-target complex potential is analogous to the description of the propagation of light in a refracting and absorbing medium by a complex index of refraction.

We begin by examining a model simple enough to allow us to see the effects of the imaginary part of the potential analytically.

Consider a particle travelling from left to right along the z-axis, incident on a semi-infinite slab of nuclear matter as shown in figure 3-1. Describe the interaction of the projectile with the nuclear medium through a potential $U = - (V_r + i V_i)$ where V_r and V_i are positive real numbers, so the potential is cut off sharply at the edge of the medium and is of uniform strength throughout the medium.

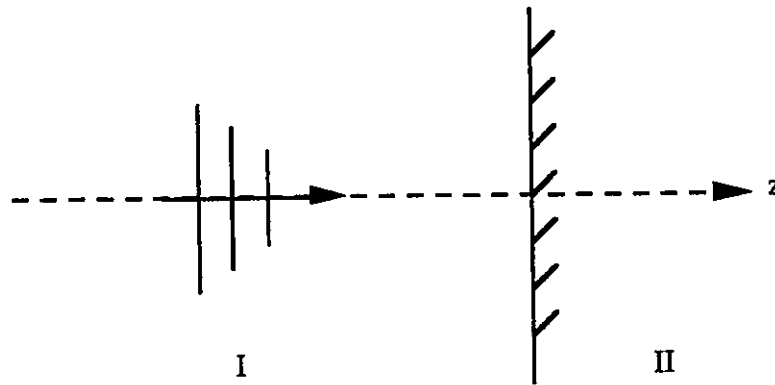


Figure 3-1. Projectiles incident from the left on a semi-infinite slab of nuclear matter.

This model is translationally invariant in the x-y plane so the projectiles are described by solutions of the one dimensional Schrödinger equation (with $\hbar = c = 1$)

$$\left[-\frac{1}{2m} \partial_z^2 + U \right] \psi(z) = E \psi(z) \quad (3-1)$$

which we can rewrite by defining the wave vector of the particles as

$$k = [2m (E - U)]^{1/2} \quad (3-2)$$

so the wave vector of the particle changes as it enters the nuclear medium. The wave function is then a solution of

$$[\partial_z^2 + k^2] \psi(z) = 0 \quad (3-3)$$

The solution is the plane wave

$$\psi(z) = e^{ikz} \quad (3-4)$$

where the wave vector is

$$k = \begin{cases} [2m E]^{1/2} & \text{region I} \\ [2m (E - U)]^{1/2} & \text{region II} \end{cases} \quad (3-5)$$

Note that in region II the wave vector is now complex since the potential is complex

$$k_{II} = [2m (E + V_r + iV_i)]^{1/2} \\ = k_r + ik_i \quad (3-6)$$

and in region II the wave function is then

$$\psi(z) = e^{-k_i z} e^{ik_r z} \quad (3-7)$$

i.e. the incident wave function is exponentially damped when it enters the nuclear medium. The probability density of the incident particles is

$$\rho(z) = |\psi(z)|^2 = e^{-2k_i z} \quad (3-8)$$

which decreases as the particles move into the medium.

If we assume that the sum of the energy of the projectiles and the real part of the potential $E + V_r$ is large compared to the imaginary part of the potential V_i we can write the wavevector in region II as

$$k_{II} \cong [2m (E + V_r)]^{1/2} \left[1 + i \frac{1}{2} \frac{V_i}{E + V_r} \right] \quad (3-9)$$

The measure of the penetration of the particles into the medium is the distance at which the probability density falls to $1/e$ of its initial value, the mean free path (or penetration depth) L . Here we have the mean free path

$$L = \frac{1}{2k_i} \\ \propto \frac{[E + V_r]^{1/2}}{V_i} \quad (3-10)$$

Thus as we make the imaginary part of the optical potential stronger the mean free path decreases (the absorption becomes stronger), while increasing the energy of the projectiles allows them to penetrate deeper into the medium.

Note that we must have the imaginary part of the optical potential negative to provide absorption. If the imaginary part is positive the probability density of the projectiles will increase exponentially with depth into the medium and the nuclear matter will be producing particles.

The current density of the projectiles is given by

$$J_z = \frac{1}{2im} [\psi^* \partial_z \psi - (\partial_z \psi^*) \psi] \quad (3-11)$$

and the probability density is given by equation (3-8). From the wave equation (3-1) with

$E \rightarrow i\partial_t$ we try to construct a continuity equation and find

$$\partial_z J_z + \partial_t \rho(z) = -2 V_i \rho(z) \quad (3-12)$$

where V_i is greater than zero so again we see that the current of incident particles is not conserved. The negative imaginary part of the optical potential leads to the absorption of these particles in the nuclear medium.

In conclusion we note that nuclear reactions are included by adding an imaginary part to the potential, which says nothing about which reactions occur, but is simply a way of recording the loss of particles from the elastic channel. It must be stressed that while the real part of the potential describes mostly the elastic scattering and the imaginary part describes mostly the nonelastic channels, the separation is not exact and there is some crossover in the description.

We have looked at a simple but instructive model, however a real nucleus is clearly not well approximated by a semi-infinite slab. Realistic models have been developed in the past few decades which provide an excellent description of the elastic scattering of protons and pions from nuclei. In the next section we will discuss the nonrelativistic optical model description of proton-nucleus elastic scattering. We then consider the relativistic description of proton elastic scattering, in which the proton wave function is a solution of the Dirac equation with complex scalar and vector potentials, yielding the continuum wave functions which we use in our model. The description of the bound nucleon as a solution of the Dirac equation with real scalar and vector potentials is then considered. Finally we will discuss the description of pion-nucleus elastic scattering.

3.2 Nonrelativistic Optical Model for Nucleon-Nucleus Elastic Scattering

The potential which describes the nucleon-nucleus interaction nonrelativistically normally contains two terms; a term which is a function of the radial distance between the projectile and the origin of potential, called the central potential, and a term which can act on the spin of the incident particle to change its polarization state. The latter is the spin-orbit term. The potential thus has the form

$$U(\mathbf{r}) = U_C(\mathbf{r}) + U_{s.o.}(\mathbf{r}) \vec{\sigma} \cdot \vec{L} \quad (3-13)$$

The central potential is parametrized with a function having a shape similar to the nuclear density. We write the central part of the potential as

$$U_C(r) = V f(r, R_1, a_1) + i W f(r, R_2, a_2) \quad (3-14)$$

where the shape functions are commonly chosen to be the Woods-Saxon function

$$f(r, R, a) = [1 + \exp(\frac{r-R}{a})]^{-1} \quad (3-15)$$

In the simple impulse approximation the potential is found to be proportional to the nuclear density, and here we see that at $r=R$ the potential has fallen to about one half of its value at the origin, a value which gives us an indication of the position of the nuclear surface. The radius parameter is usually given by the relation

$$R = cA^{1/3} \quad (3-16)$$

where c is a parameter and A is the mass number of the nucleus. The parameter a is called the diffuseness parameter and measures the thickness of the surface of the nucleus.

The spin-orbit potential is usually surface peaked and is parametrized using the derivative of a Woods-Saxon function

$$U_{so}(r) = \frac{1}{m_\pi^2} V_{so} \frac{1}{r} \frac{\partial}{\partial r} f(r, R_1^{so}, a_1^{so}) + i \frac{1}{m_\pi^2} W_{so} \frac{1}{r} \frac{\partial}{\partial r} f(r, R_2^{so}, a_2^{so}) \quad (3-17)$$

where the pion mass (in fm^{-1}) is introduced as a matter of convention to give the potential the correct units.

We next consider a description of the nucleon motion using the Dirac equation instead of the Schrödinger equation. This approach is found to provide an improved description of nucleon elastic scattering.

3.3 Relativistic Description of Nucleon-Nucleus Elastic Scattering

The nucleon distorted wave needed in the evaluation the s -matrix (2-103) is a solution of the Dirac equation with an optical potential consisting of a Lorentz scalar, $S(r)$, and the zeroth component of a Lorentz 3-vector, $V(r)$. The Dirac equation is then

$$\{ \vec{\alpha} \cdot \vec{p} + \beta [m + S(r)] + V(r) + C(r) \} \psi(\vec{r}) = E \psi(\vec{r}) \quad (3-18)$$

where \vec{p} , m and E are the nucleon momentum, rest mass and total energy respectively. The nucleon is described by a four component spinor and the 4×4 Dirac matrices have the standard representation [BD64]

$$\vec{\alpha} = \begin{bmatrix} 0 & \vec{\sigma} \\ \vec{\sigma} & 0 \end{bmatrix} \quad \beta = \begin{bmatrix} \mathbf{1} & 0 \\ 0 & -\mathbf{1} \end{bmatrix} \quad (3-19)$$

where $\mathbb{1}$ is a 2x2 unit matrix and the σ_i are the usual Pauli spin matrices.

$C(r)$ is the Coulomb potential due to the target nucleus. The Coulomb potential that we use is due to a charge distribution of the form

$$\rho(r) = N \left[1 - \text{ERF}\left(\frac{r-R}{2a}\right) \right] \quad (3-20)$$

where $\text{ERF}(x)$ is the error function. The normalization constant is determined by integrating the charge density over all space to get the total charge of the nucleus. This form for the charge distribution is very close to the Woods-Saxon shape inside the nucleus if we set $R_{WS} = R_{\text{ERF}}$ and $a_{WS} = \sqrt{\pi}/2 a_{\text{ERF}}$. Outside the nucleus the Coulomb potential falls off as $1/r$ as it must. This choice of R_{WS} and a_{WS} also matches the gradient of the Woods-Saxon function at $r=R$ to that of $\rho(r)$.

The vector and scalar potentials are parametrized as

$$V(r) = V_v f(r, R_{v1}, a_{v1}) + i W_v f(r, R_{v2}, a_{v2}) \quad (3-21)$$

$$S(r) = V_s f(r, R_{s1}, a_{s1}) + i W_s f(r, R_{s2}, a_{s2}) \quad (3-22)$$

where the shape functions, $f(r, R_i, a_i)$ are symmetrized Woods-Saxon functions

$$f(r, R, a) = \left[1 + \exp\left(\frac{r-R}{a}\right) \right]^{-1} \left[1 + \exp\left(\frac{-(r+R)}{a}\right) \right]^{-1} \quad (3-23)$$

where the radius and diffuseness parameters are as for the nonrelativistic potentials. These symmetrized functions are chosen instead of the standard Woods-Saxon functions because they give a zero first derivative at the center of the nucleus which must be the case if our potential is to follow the nuclear density.

The Dirac wave function of equation (3-18) is written in a simple two component form as

$$\psi = \begin{bmatrix} u \\ \chi \end{bmatrix} \quad (3-24)$$

where the upper and lower components u and χ are both two component spinors and are solutions of the coupled equations arising from (3-18). We can reduce equation (3-18) to a Schrödinger-like equation containing effective central and spin-orbit potentials which can be compared with the nonrelativistic optical potential [Jo86]. A bit of algebra yields the equation

$$\left[\frac{-\nabla^2}{2m} + V_C(r) + V_{so}(r) \vec{\sigma} \cdot \vec{L} \right] \psi_S = T \psi_S \quad (3-25)$$

where T is the kinetic energy of the incoming proton. The Schrödinger equivalent wave function ψ_S is related to the upper component of the Dirac wave function by

$$\psi_S = s^{-1/2} u \quad (3-26)$$

and the effective central and spin-orbit potentials are

$$V_C(r) = -\frac{1}{2m} [(E - V - C)^2 - (m + S)^2 - (E^2 - m^2) + \frac{1}{r} \frac{s'}{s} - \frac{3}{4} \left(\frac{s'}{s}\right)^2 + \frac{1}{2} \frac{s''}{s}] \quad (3-27)$$

$$V_{so}(r) = -\frac{1}{2mr} \frac{s'}{s}$$

where primes denote differentiation with respect to r and we have defined the function $s(r)$ as

$$s(r) = \frac{1}{E + m} [E - V(r) - C(r) + m + S(r)] \quad (3-28)$$

The reduction of the Dirac equation results in a central potential which is quite different from the Woods-Saxon form. The Woods-Saxon central potential simply scales the same functional shape as the energy of the projectile changes while the effective central potential has a more dramatic energy dependence. At low energies the potential is close to the Woods-Saxon shape and attractive, and as the projectile energy increases the strength of the potential decreases in magnitude and eventually becomes repulsive at about 200 MeV. The center of the potential becomes more repulsive as the incident energy is increased but there remains an attractive pocket at the nuclear surface.

The parameters of the optical potential are determined by fitting to proton-nucleus elastic scattering data. The potentials obtained in this way [Ko85] are much deeper than those obtained through a similar procedure based on the Schrödinger equation. The real depths are typically $V_v \sim 300$ MeV and $V_s \sim -400$ MeV, with the scalar potential being attractive and the vector repulsive. The real depths can vary quite a bit with proton energy. The imaginary depths are generally around 100 MeV, with the scalar repulsive and the vector attractive, and are weakly dependent on the incident proton energy.

Impulse approximation (IA) calculations give potential depths in qualitative agreement with phenomenological results both relativistically and nonrelativistically. IA calculations begin with the nucleon-nucleon t -matrix and sum over all possible nucleon-nucleon pairs in the nucleon-nucleus interaction. The required nucleon-nucleon amplitudes can be obtained from the phase shift analysis of Arndt et al. [Ar87 and references therein].

The nonrelativistic IA calculations are discussed by Kerman, McManus and Thaler [KMT55]. They use the nonrelativistic nucleon-nucleon scattering amplitude comprised

of functions of energy and angle, multiplying combinations of Pauli matrices for the two nucleons, and a nucleon-nucleus optical potential is calculated which is in general agreement with the nonrelativistic phenomenology.

The relativistic impulse approximation begins with a form for the nucleon-nucleon t-matrix [Mc83] involving functions of energy and angle, multiplying combinations of Dirac matrices for the two nucleons. This t-matrix is constrained by the necessity that matrix elements of the relativistic and nonrelativistic amplitudes give the same result. The amplitudes for the relativistic t-matrix are found by fitting to the observables and/or phase shifts of nucleon-nucleon scattering. The potential for nucleon-nucleus scattering is then calculated using the free nucleon-nucleon t-matrix and summing over all the nucleons in the target nucleus. The potential depths are found to be a bit larger at low energies than Dirac phenomenology would require, and the inclusion of meson effects [Wa85] brings the depths into agreement with the phenomenological analyses.

The phenomenology described above provides a set of potential parameters for protons of kinetic energy T_p incident on a nucleus with atomic number A . These parametrizations are useful for calculations involving a proton at that energy and interacting with the nucleus for which elastic scattering data exists, however elastic scattering data is not available for all spherical nuclei for which calculations could be done. This limitation has been addressed by S. Hama and his coworkers [Ha90] who have simultaneously fit elastic scattering data for six different nuclei from ^{40}Ca to ^{208}Pb covering the energy range $65 < T_p < 1040$ MeV. They allow the potential depths to become energy dependent while the radius and diffuseness parameters are functions of both energy and atomic number. The best description of elastic scattering observables using the global fit potentials occurs when the potential is calculated for projectile energies and target masses close to those for which data were included in the search.

These parametrizations have recently been extended by the Ohio State group [Co92] to include nuclei as light as ^{12}C . We use the Ohio state global potential which has been parametrized with dependence on both proton energy E and atomic mass A , as well as a potential specific to ^{12}C which has been parametrized with energy dependence only [Ha92, Co92]. Our calculations require proton-nucleus potentials for the residual nuclei ^{11}C and ^{15}O which are calculated from the potentials parametrized with both ^{12}C and ^{16}O data included in the global fitting.

Figure 3-2a shows the Dirac potentials given by the fit parametrized with both E and A dependence for the elastic scattering of protons from ^{12}C at a proton laboratory energy of $T_p = 160$ MeV. Figure 3-2b shows the Schrödinger equivalent potentials (SEPs) calculated from the Dirac potentials of figure 3-2a. Note that the SEPs can vary quite a bit from the Woods-Saxon shape of equation 3-15 because of the fairly complex functional dependence of the SEPs on the Dirac potentials.

The potential parameters were determined by fitting to elastic scattering data such as the data shown in figure 3-3. The differential cross section is shown in figure 3-3a while the polarization is shown in figure 3-3b. The search included data up to 90° or a momentum transfer of 3 fm^{-1} , whichever was smallest, so the description of the data past 90° can be fairly poor.

Dirac based calculations have also been successful in reaction calculations. In inelastic scattering to collective states, (p, p') [Jo88], a Dirac based DWBA model provides a good description for small deformations of the final nucleus while for larger deformations coupled channel effects become important and a Dirac based coupled channels description [Ra89] does a good job. Similarly for (p, γ) [Lo88, Mc88, Lo92] and (p, π) [Co82] a Dirac based calculation describes the data at forward angles while other mechanisms become important at larger angles. In these cases treatment of the nucleon as a Dirac particle gives improvement over treatments where the proton is described by the Schrödinger equation, particularly for spin observables. Similarly Dirac based DWIA calculations of proton inelastic scattering [Sh84, Do91] show a slight preference for the relativistic calculation over the nonrelativistic. There are also Dirac models of reactions to three particle final states such as $(\vec{p}, n \pi)$ [Co87] and $(p, 2p)$ [Co89].

The wave functions which we use to describe the continuum proton are solutions of the Dirac equation, with the energy and mass number dependent scalar and vector potentials of Cooper et al. [Co92] included.

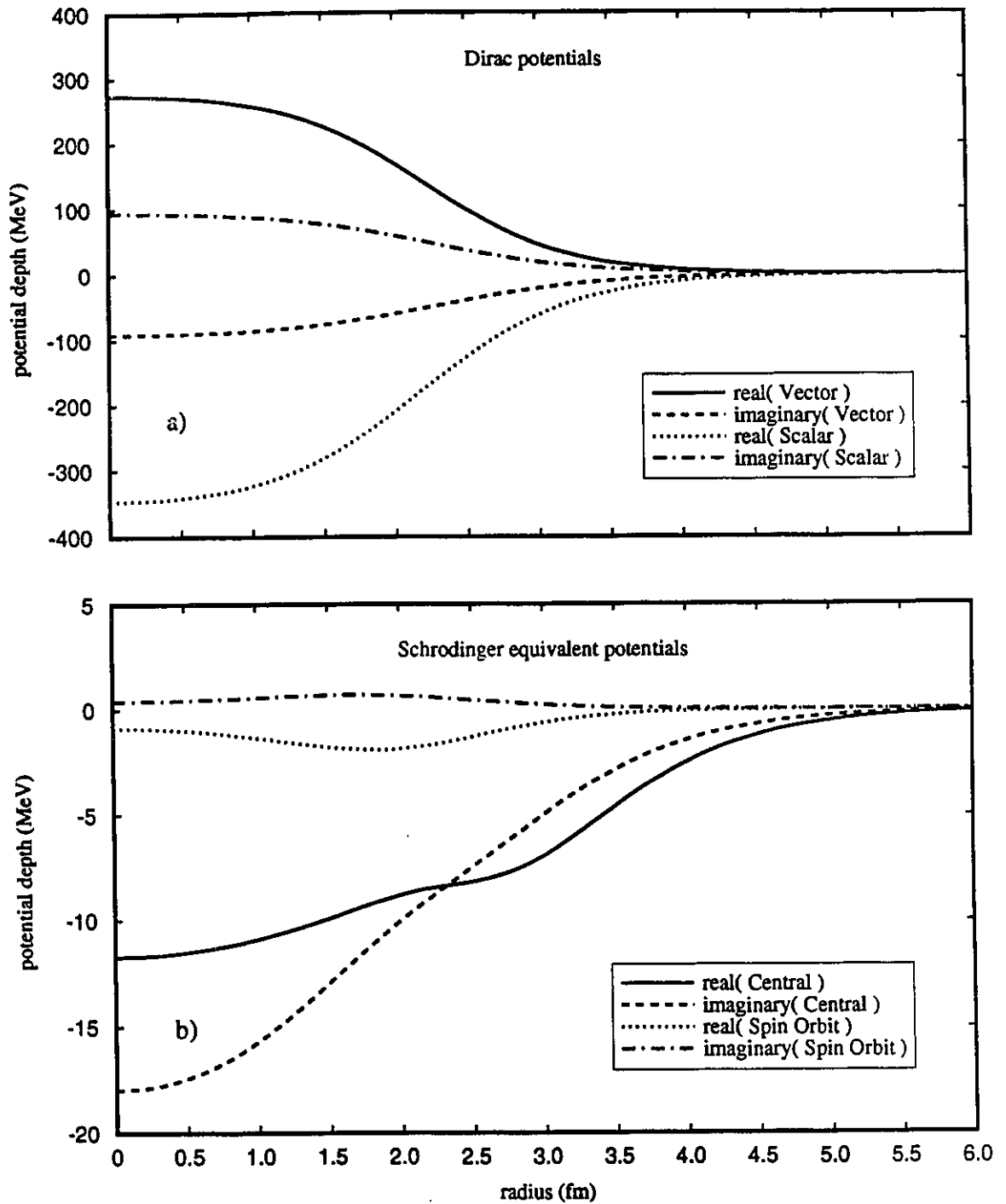


Figure 3-2. Potentials for proton elastic scattering from ^{12}C at $T_p = 160$ MeV.
 a) Dirac potentials from the E and A dependent fit of Hama et al.[Ha90],
 b) the Schrodinger equivalent potentials.

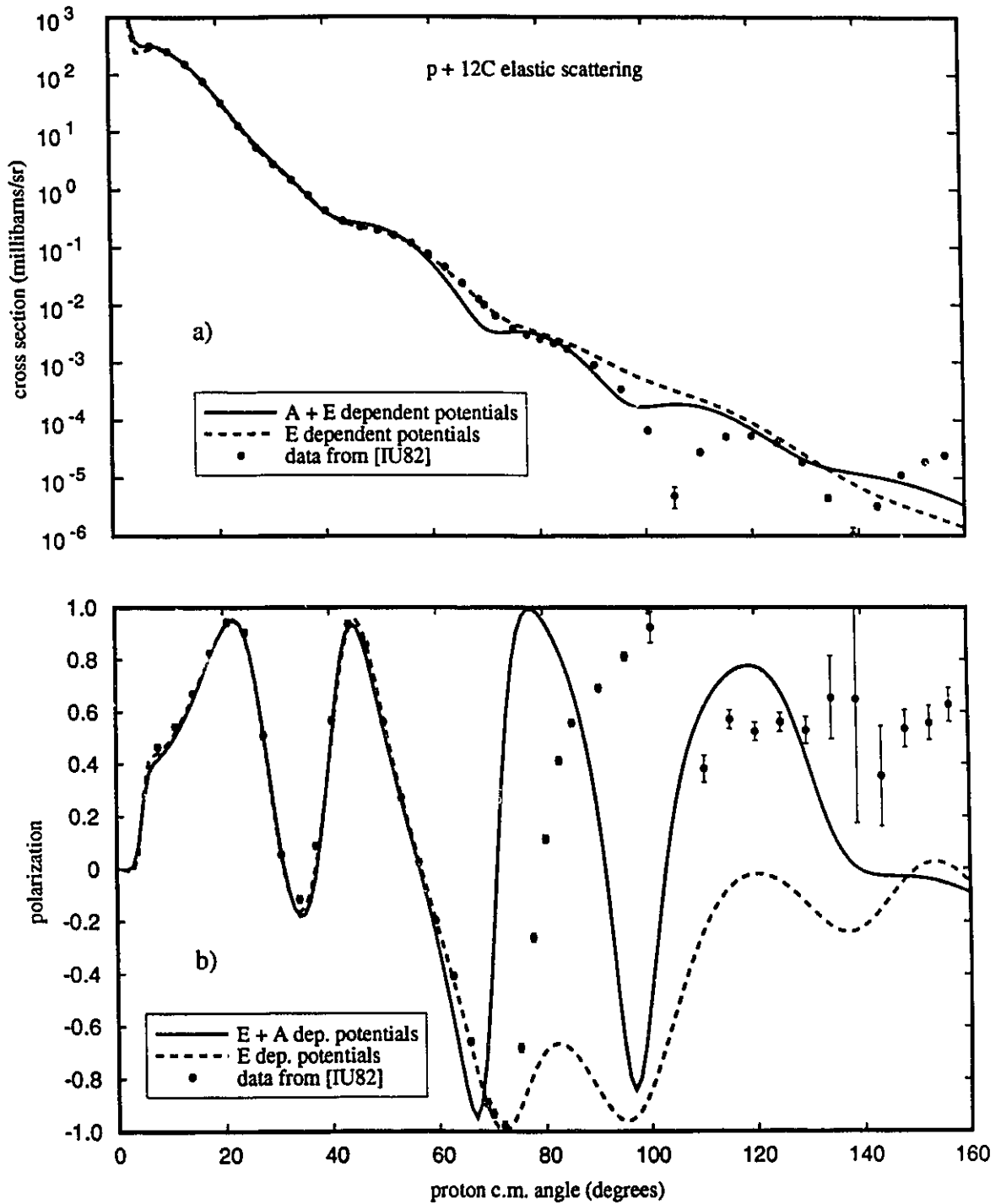


Figure 3-3. Elastic scattering observables for $p + {}^{12}\text{C}$ at $T_p = 160$ MeV calculated using the global potentials of Hama et al. a) differential cross section and b) polarization.

3.4 Bound State Wave Function

The wave function describing the bound neutron is also a solution of the Dirac equation (3-18), but the potentials have no complex parts. The bound state spinor is written as in equation (2-93). The radial Dirac equation is solved for a given set of potential parameters, and the depth of either the scalar or the vector potential is varied until the experimentally measured separation energy is reproduced.

A set of Woods-Saxon parameters for the binding potential for ^{12}C is given in table 3-1. Note that these potentials are purely real since we are dealing with the bound state wave function.

	vector	scalar
V (MeV)	300.00	-378.63
c (fm)	1.0176	1.0379
a (fm)	0.5410	0.5609

Table 3-1. Woods-Saxon binding parameters for ^{12}C from [Lo89].

The potential parameters give good results in a Dirac description of the reaction data [Lo89] for $^{11}\text{B}(\vec{p}, \gamma)^{12}\text{C}$, and so refer to the $p_{3/2}$ level in the ground state of ^{12}C . The parameters of the binding potential can vary considerably when the only constraint is that the energy eigenvalue of the hamiltonian containing the Woods-Saxon binding potential correspond to the measured binding energy. The results of calculations for the (p, γ) reaction are sensitive to the choice of the bound state parameters [Lo92] and if the relativistic one nucleon model provides a good description of the reaction mechanism it can be used to constrain the bound state wave function.

We can also obtain a relativistic bound state wave function from a Hartree calculation [SW86]. This self-consistent calculation provides a unique bound state for a choice of meson masses and coupling constants determined from the bulk properties of nuclei.

Figure 3-4 shows the momentum space bound state wave function obtained from a

Hartree calculation for the $1p_{3/2}$ level of ^{12}C , as well as two bound states calculated from Woods-Saxon parameters. The upper graph shows the Hartree bound state and the wave function calculated with the parameters of table 3-1, while the lower graph shows the same Hartree bound state with a wave function which has the same geometry as that of table 3-1 but the depth of the vector potential has been set to $V_v = 400$ MeV, and the scalar depth searched on in order to reproduce the experimental binding energy.

Notice that the wave functions of the first graph differ very little up to a momentum transfer of 1.5 fm^{-1} and even when the potential depth is changed significantly the requirement that the binding energy be reproduced is sufficient to keep the wave functions close on a logarithmic scale for small momentum transfers. This is a very nice feature since our model can explore a large range of momentum transfers via changes in the kinematics. We can explore how well our model works at low momentum transfers where the bound state is fairly well known, and then consider the high momentum transfer region of the bound state wave function using a reaction model which we are confident describes the process well at low momentum transfers.

3.5 Pion Phenomenology

The pion-nucleus interaction, unlike the nucleon-nucleus interaction, is dominated by one inelastic channel, the formation of a delta isobar of mass $m_\Delta = 1232$ MeV, with spin $J=3/2$ and isospin $T=3/2$. The formation of the delta takes place when the pion interacts with one of the nucleons in the nucleus, so a reasonable sequence would seem to be to try to describe the pion-nucleon interaction and then use that description to model the pion-nucleus interaction. We will outline the development of the pion-nucleus potential due to Stricker, McManus and Carr which arises from these considerations.

3.5.1 Pion-Nucleon Scattering

The pion has three charge states so it has isospin $t = 1$ while the nucleon, with two charge states, has isospin $\tau = 1/2$. A pion-nucleon interaction can therefore proceed through two possible channels of total isospin $T = 1/2$ and $T = 3/2$, where we have defined the total isospin of the pion-nucleon system in terms of the isospin operator of the

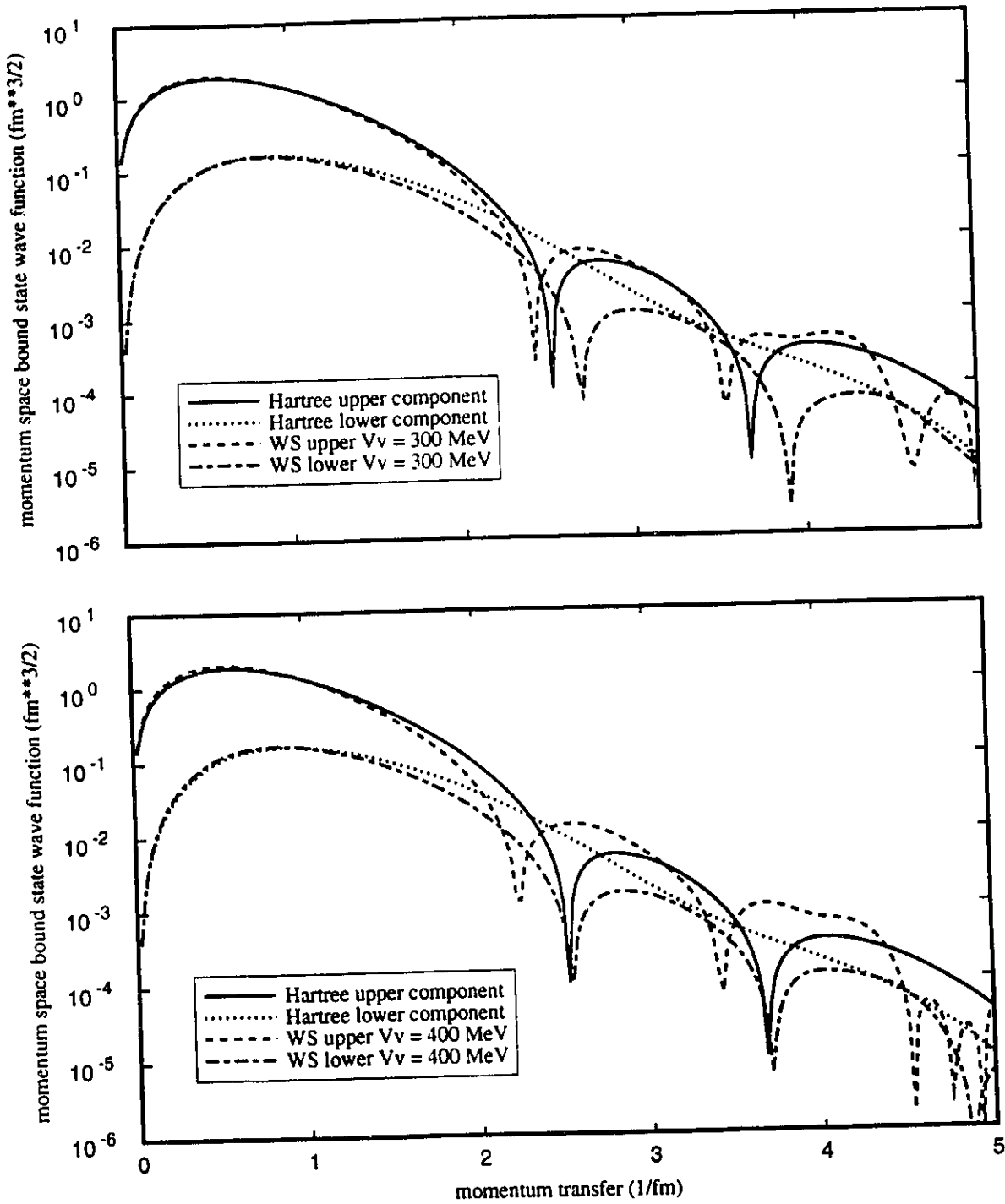


Figure 3-4. Momentum space bound state wave functions for the $1p_{3/2}$ level in ^{12}C .

pion \vec{t} and the isospin operator of the nucleon $\vec{\tau}$ as $\vec{T} = \vec{t} + \vec{\tau}$. Figure 3-5 shows the kinematics for pion-nucleon scattering in the center of momentum system.

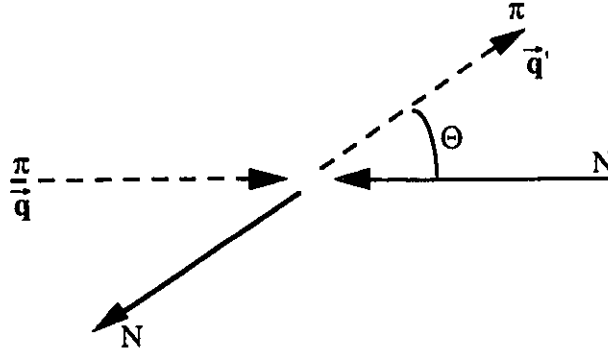


Figure 3-5. Pion-nucleon scattering in the center of momentum system.

The scattering amplitude for a spin zero, isospin $t = 1$ particle with a spin $s = 1/2$, isospin $\tau = 1/2$ particle can be written in the form

$$f(E_{cm}, \Theta) = g(E_{cm}, \Theta) - i h(E_{cm}, \Theta) \vec{\sigma} \cdot \hat{n} \quad (3-29)$$

where we have defined the unit vector normal to the scattering plane by

$$\hat{n} = \frac{\vec{q} \times \vec{q}'}{|\vec{q} \times \vec{q}'|} = \frac{1}{\sin\Theta} \hat{q} \times \hat{q}' \quad (3-30)$$

and unit vectors are denoted by the circumflex. The differential elastic scattering cross section for pion-nucleon scattering can then be written in terms of the amplitudes g and h as

$$\frac{d\sigma}{d\Omega} = |g(E_{cm}, \Theta)|^2 + |h(E_{cm}, \Theta)|^2 \quad (3-31)$$

The amplitudes g and h are expanded in terms of Legendre polynomials as

$$g(E_{cm}, \Theta) = \sum_{T=\frac{1}{2}, \frac{3}{2}} \sum_{\ell=0}^{\infty} \hat{P}_T [(\ell+1) A_{\ell+}^T + \ell A_{\ell-}^T] P_{\ell}(\cos\Theta) \quad (3-32)$$

$$h(E_{cm}, \Theta) = \sum_{T=\frac{1}{2}, \frac{3}{2}} \sum_{\ell=1}^{\infty} \hat{P}_T [A_{\ell+}^T - \ell A_{\ell-}^T] P_{\ell}^1(\cos\Theta)$$

where we have defined the partial wave scattering amplitude for the channel with isospin T , orbital angular momentum ℓ and total angular momentum $j = \ell \pm 1/2$ as

$$A_{\ell \pm}^T = \frac{1}{2iq} [s_{\ell \pm}^T - 1] \quad (3-33)$$

and the s-matrix element for the channel is related to the phase shift by

$$\begin{aligned} s_{\ell \pm}^T &= \exp(2i\delta_{\ell \pm}^T) \\ &= \exp(2i\text{Re}[\delta_{\ell \pm}^T]) \eta_{\ell \pm}^T \end{aligned} \quad (3-34)$$

The inelasticity parameter is related to the imaginary part of the phase shift by

$$\eta_{\ell \pm}^T = \exp(-2\text{Im}[\delta_{\ell \pm}^T]) \quad (3-35)$$

If there are no inelastic channels open the imaginary part of the phase shift is zero and $\eta_{\ell \pm}^T = 1$. When there are inelastic channels the absorption parameter lies in the range zero to one.

The operator \hat{P}_T projects the two possible total isospin channels from the scattering amplitude. We can write the projection operators for the two states as

$$\hat{P}_{\frac{1}{2}} = \frac{1}{3} (1 - \vec{\tau} \cdot \vec{t}) \quad \hat{P}_{\frac{3}{2}} = \frac{1}{3} (2 + \vec{\tau} \cdot \vec{t}) \quad (3-36)$$

Inelasticities only begin to appear in pion-nucleon scattering above the threshold for the reaction $\pi N \rightarrow \pi \pi N$, so for pion kinetic energies below approximately 170 MeV in the laboratory frame the phase shifts are purely real.

We can define another useful matrix through its relation to the s-matrix by

$$s_{\ell \pm}^T = \frac{1 + iq K_{\ell \pm}^T}{1 - iq K_{\ell \pm}^T} \quad (3-37)$$

which we can invert to give the K-matrix as

$$\begin{aligned} K_{\ell \pm}^T &= \frac{1}{iq} \frac{s_{\ell \pm}^T - 1}{s_{\ell \pm}^T + 1} \\ &= \frac{1}{q} \tan \delta_{\ell \pm}^T \end{aligned} \quad (3-38)$$

If the phase shift is real the K-matrix is also real and the s-matrix is unitary.

When the particle kinetic energies are small the scattering amplitude is proportional to $q^{2\ell}$ [EW88] in a channel with angular momentum ℓ . We define scattering parameters for the channel with quantum numbers (T, ℓ, j) through

$$a_{\ell \pm}^T = \lim_{q \rightarrow 0} [q^{-2\ell} K_{\ell \pm}^T] \quad (3-39)$$

where for s-waves ($\ell = 0$) the parameters are scattering lengths while for p-waves ($\ell = 1$) the parameters are called scattering volumes. There are two s-wave scattering lengths denoted by a_1 and a_3 which correspond to the $T = 1/2$ and $T = 3/2$ isospin channels

respectively. For p-waves we have four scattering volumes denoted as $a_{2T, 2J}$.

The pion-nucleon scattering lengths have the following empirical values [EW88]

$$\begin{aligned}
 a_1 &= (0.173 \pm 0.003) m_\pi^{-1} = 0.245 \pm 0.004 \text{ fm} \\
 a_3 &= (-0.101 \pm 0.004) m_\pi^{-1} = -0.143 \pm 0.006 \text{ fm} \\
 a_{11} &= (-0.081 \pm 0.002) m_\pi^{-3} = -0.229 \pm 0.006 \text{ fm}^3 \\
 a_{13} &= (-0.030 \pm 0.002) m_\pi^{-3} = -0.085 \pm 0.006 \text{ fm}^3 \\
 a_{31} &= (-0.045 \pm 0.002) m_\pi^{-3} = -0.127 \pm 0.006 \text{ fm}^3 \\
 a_{33} &= (0.214 \pm 0.002) m_\pi^{-3} = 0.605 \pm 0.005 \text{ fm}^3
 \end{aligned} \tag{3-40}$$

The parameters for d- and f-waves are also known and for d-waves they are on the order of $5 \times 10^{-3} m_\pi^{-5}$ while the f-wave parameters are even less important. We neglect these contributions in the following.

The s- and p-waves dominate at low and intermediate energies so we can expand the scattering amplitude (3-29 with 3-32) retaining only the $\lambda = 0$ and $\lambda = 1$ terms and write

$$\begin{aligned}
 f(E_{\text{cm}}, \Theta) &= b_0 + b_1 \vec{\tau} \cdot \vec{t} + [c_0 + c_1 \vec{\tau} \cdot \vec{t}] \vec{q} \cdot \vec{q}' \\
 &\quad - i [d_0 + d_1 \vec{\tau} \cdot \vec{t}] \vec{\sigma} \cdot \vec{q} \times \vec{q}'
 \end{aligned} \tag{3-41}$$

where the six coefficients are in general complex and depend on the total center of mass energy of the system. The coefficients are related to the scattering parameters by [Er66]

$$\begin{aligned}
 b_0 &= \frac{1}{3} (a_1 + 2 a_3) \\
 b_1 &= \frac{1}{3} (a_3 - a_1) \\
 c_0 &= \frac{1}{3} (a_{11} + 2 a_{13} + 2 a_{31} + 4 a_{33}) \\
 c_1 &= \frac{1}{3} (-a_{11} - 2 a_{13} + a_{31} + 2 a_{33}) \\
 d_0 &= \frac{1}{3} (a_{11} - a_{13} + 2 a_{31} - 2 a_{33}) \\
 d_1 &= \frac{1}{3} (-a_{11} + a_{13} + a_{31} - a_{33})
 \end{aligned} \tag{3-42}$$

and thus have the values

$$\begin{aligned}
 b_0 &= (-0.010 \pm 0.003) m_\pi^{-1} = -0.014 \pm 0.004 \text{ fm} \\
 b_1 &= (-0.091 \pm 0.002) m_\pi^{-1} = -0.129 \pm 0.003 \text{ fm} \\
 c_0 &= (0.208 \pm 0.003) m_\pi^{-3} = 0.588 \pm 0.008 \text{ fm}^3 \\
 c_1 &= (0.175 \pm 0.002) m_\pi^{-3} = 0.495 \pm 0.006 \text{ fm}^3 \\
 d_0 &= (-0.190 \pm 0.002) m_\pi^{-3} = -0.537 \pm 0.006 \text{ fm}^3 \\
 d_1 &= (-0.069 \pm 0.002) m_\pi^{-3} = -0.195 \pm 0.006 \text{ fm}^3
 \end{aligned} \tag{3-43}$$

The most important parameters for low energy pion-nucleus interactions are the spin and isospin independent parameters b_0 and c_0 and the isospin dependent s-wave parameter b_1 . The parameters d_0 and d_1 on the other hand, are connected with spin-flip processes which

don't usually have an important role in the gross features of the pion-nucleus interaction.

3.5.2 Pion-Nucleus Interaction

We begin with the pion-nucleon scattering amplitude for s- and p-waves in the center of momentum (c.m.) frame (3-41) and neglect the spin dependent term. This scattering amplitude is transformed from the c.m. frame of the pion-nucleon system to the c.m. frame of the pion-nucleus system (the angle transformation) and the nuclear density is folded in to get the first order potential [Th76]:

$$2 \bar{\omega} V(r) = -4\pi [(1 + \epsilon) b_0 \rho(r) - \frac{c_0}{\pi^2} (\vec{\nabla} \cdot \rho(r) \vec{\nabla}) + \frac{\epsilon c_0}{2(1 + \epsilon)} \nabla^2 \rho(r)] \quad (3-44)$$

where $\epsilon = E_\pi/m_\pi$ is dimensionless, E_π is the total pion energy in the pion-nucleus center of momentum frame and the reduced energy is $\bar{\omega} = E_\pi / (1 + \epsilon / A)$. This form, first found by Kisslinger [Ki55], is explicitly nonlocal because of the p-wave contribution to the potential.

Second order corrections to the potential (3-44) arise from pion absorption processes requiring two or more nucleons, such as the process shown in figure 3-6.

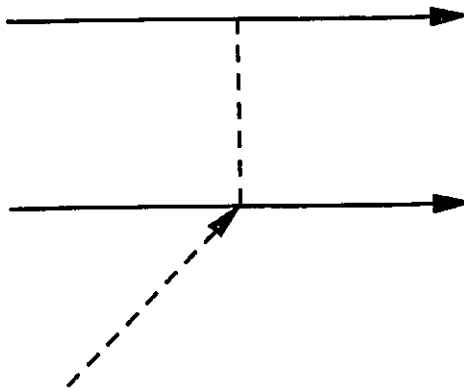


Figure 3-6. Diagram contributing to second order corrections in the pion-nucleus optical potential.

A phenomenological amplitude for these second order processes can be written as

$$f^{(2)}(E_{\text{cm}}, \Theta) = B_0 + C_0 \vec{q} \cdot \vec{q} \quad (3-45)$$

and the imaginary parts of the two complex coefficients can be calculated from a model

involving diagrams such as figure 3-6. The real parts of B_0 and C_0 are not determined by this model and are taken as the negative of their imaginary parts [Er66]. At energies above 50 MeV the real parts are set to zero [SMC79, SMC80]. Since the amplitude involves two nucleons the potential contains terms proportional to the square of the nuclear density

$$2 \bar{\omega} V^{(2)}(r) = -4\pi \left[\left(1 + \frac{\epsilon}{2}\right) B_0 \rho^2(r) - \frac{2C_0}{2+\epsilon} (\vec{\nabla} \cdot \rho^2(r) \vec{\nabla}) + \frac{\epsilon C_0}{4+2\epsilon} \nabla^2 \rho^2(r) \right] \quad (3-46)$$

Ericson and Ericson [Er66] have shown that when short range correlation effects between dipole scatterers are included, the p-wave part of the multiple scattering series can be summed, with the assumption that the pion wavelength is much larger than the average correlation length between nucleons. This results in the modification

$$4\pi c_0 \rho(r) \rightarrow \frac{4\pi c_0 \rho(r)}{1 + \frac{\xi^2}{2} 4\pi c_0 \rho(r)} \quad (3-47)$$

where ξ is the average correlation length between nucleons in the nucleus. A parameter λ is defined by

$$\lambda = \frac{A}{A-1} \frac{3\xi^2}{2} \quad (3-48)$$

and λ is adjusted to fit pion elastic scattering data. Going back to the language of optics this results in a nonlinear dependence of the index of refraction on the density of scatterers (the Lorentz-Lorenz effect [Ja75]).

The s-wave part of the multiple scattering series can be summed to second order to give a modification of the pion nucleon scattering parameter b_0

$$b_0 \rightarrow \bar{b}_0 = b_0 - (b_0^2 + 2b_1^2) \frac{3k_f}{2\pi} \quad (3-49)$$

where the Fermi momentum is $k_f = 1.4 \text{ fm}^{-1}$.

Putting these results together gives us the form of the pion-nucleus optical potential which has been used by Stricker, McManus and Carr [SMC79]. We write their potential, to emphasize the central plus gradient nature, as

$$2 \bar{\omega} V_{\text{opt}}(r) = g(r) + \vec{\nabla} \cdot h(r) \vec{\nabla} + 2 \bar{\omega} V_C(r) \quad (3-50)$$

where the radial functions $g(r)$ and $h(r)$ are:

$$\begin{aligned} g(r) &= -4\pi \left[b(r) + p_2 B_0 \rho^2(r) + \frac{p_1 - 1}{2} \nabla^2 c(r) + \frac{C_0 (p_2 - 1)}{2 p_2} \nabla^2 \rho^2(r) \right] \\ h(r) &= 4\pi \left[L(r) c(r) + \frac{C_0}{p_2} \rho^2(r) \right] \end{aligned} \quad (3-51)$$

where

$$\begin{aligned}
 v(r) &= p_1 [\bar{b}_0 \rho(r) - \epsilon_\pi b_1 \delta\rho(r)] \\
 c(r) &= \frac{1}{p_1} [c_0 \rho(r) - \epsilon_\pi c_1 \delta\rho(r)] \\
 L(r) &= [1 + \frac{4\pi}{3} \lambda \frac{A-1}{A} c(r)]^{-1}
 \end{aligned} \tag{3-52}$$

The density function $\delta\rho(r)$ is the difference between the neutron and proton densities. If the geometries of the densities are taken to be equal we have

$$\begin{aligned}
 \delta\rho(r) &= \rho_n(r) - \rho_p(r) \\
 &= \frac{N-Z}{A} \rho(r)
 \end{aligned} \tag{3-53}$$

ϵ_π is the charge of the incident pion, either ± 1 , ω and \vec{k} are the pion energy and wave vector in the pion-nucleus center of momentum frame, and ω_L and \vec{k}_L are the energy and wave vector of the pion in the laboratory frame. M is the atomic mass unit $M = 931 \text{ MeV}$, which we use to define the dimensionless quantities

$$\epsilon_0 = \frac{\omega_L}{M} \qquad \epsilon = \frac{\omega}{M} \tag{3-54}$$

We also need

$$p_1 = \frac{1 + \epsilon}{1 + \epsilon/A} \qquad p_2 = \frac{1 + \epsilon/2}{1 + \epsilon/A} \qquad \bar{\omega} = \frac{\omega}{1 + \epsilon/A} \tag{3-55}$$

where A is the atomic mass number.

Stricker, McManus and Carr [SMC79] have determined parameters for six incident pion energies: $T_\pi = 30, 40, 50, 116, 180$ and 220 MeV . In order to obtain a smooth energy dependence we perform a linear interpolation of the parameters provided by SMC. Singham and Tabakin [ST81] similarly provide parameter sets for a potential of the same form, with eight pion energies up to $T_\pi = 180 \text{ MeV}$, which we also linearly interpolate to get a smooth dependence on energy.

Laget has provided a set of parameters [La72] for a simple s-wave potential of the form

$$V_{\text{opt}} = (V_r + i V_i) \rho(r) \tag{3-56}$$

where $\rho(r)$ is the nuclear density normalized to the nuclear volume. The real and imaginary depths are tabulated in 20 MeV steps to a maximum pion kinetic energy of 300 MeV. The depths are deduced from pion-nucleon and pion-deuteron cross sections, and the potential is then used to calculate reaction and total pion-nucleus cross sections, and are found to provide general agreement with the data. This potential is not determined from elastic scattering angular distributions and is not expected to provide a good

description of differential cross sections. We include it to test the effect of a poorly determined pion wave function on our calculations.

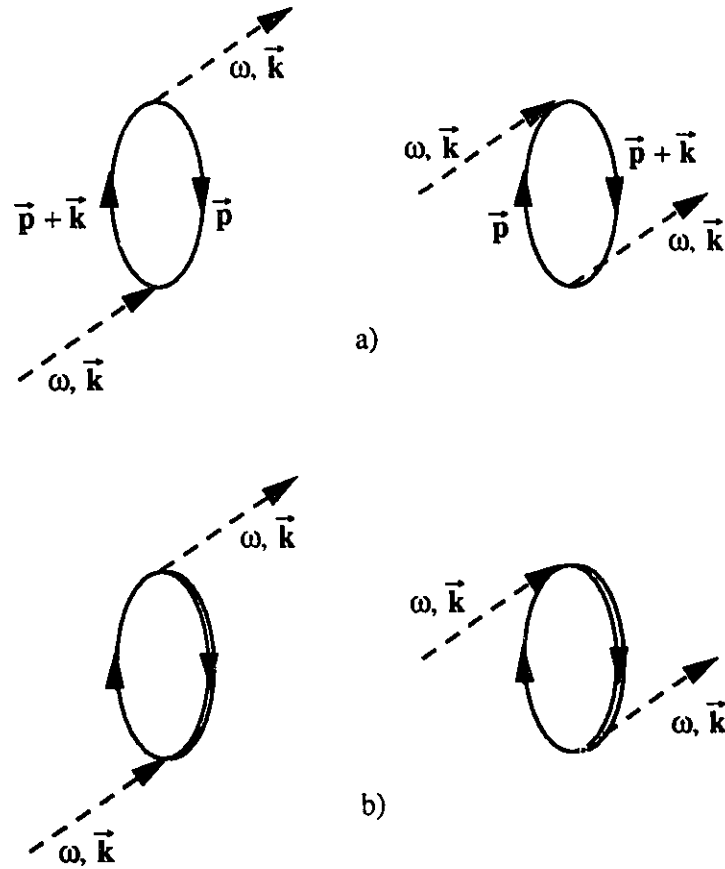


Figure 3-7. a) Nucleon-hole and b) Δ -hole intermediate states contributing to the pion self energy.

Oset and his coworkers [Ga88, Ni92] have calculated the pion self-energy, which is related to the optical potential by

$$\Pi(\omega, \rho) = 2\omega V_{opt} \quad (3-57)$$

where ω is the pion energy and ρ is the density of the target nucleus. The self-energy is calculated from consideration of nucleon-hole intermediate states and Δ -hole intermediate states, such as the diagrams shown in figure 3-7, which contribute in first order. The double line in the loop of figure 3-7b) indicates the delta isobar which has been created

through the excitation of the nucleon by interaction with a pion. Higher order terms are also included in their calculation of the optical potential, and their model results in a potential of the central plus gradient form (3-50), which we have seen before.

The Klein-Gordon equation with the pion-nucleus optical potential is

$$(-\nabla^2 + \mu^2 + 2\omega_\pi V_{\text{opt}}) \varphi = (\omega_\pi - V_C)^2 \varphi \quad (3-58)$$

If we take μ to be the rest mass of the pion and ignore the term involving the square of the Coulomb potential we have

$$[\nabla^2 + \vec{k}_\pi^2 - 2\omega_\pi (V_{\text{opt}} + V_C)] \varphi = 0 \quad (3-59)$$

which is the equation Stricker, McManus and Carr solve. Oset solves equation (3-58) taking μ as the pion-target reduced mass.

Figure 3-8 compares the four potentials described in a calculation of elastic scattering of π^- on ^{12}C at an incident pion kinetic energy of $T_\pi = 50$ MeV. The purely s-wave (local) potential of Laget give an angular distribution which doesn't describe the minimum at 70° or rise at backward angles, while the other potentials all describe the general features of the data.

3.5.3 Radial Equation for the Pion

For the sake of completeness, we now derive the radial equation for the pion wave function with the potential of equation (3-50).

We start with a Klein-Gordon equation with a potential $V(r)$

$$[\nabla^2 + \vec{k}_\pi^2 + V(r)] \varphi(\vec{r}) = 0 \quad (3-60)$$

where the potential has the Kisslinger form

$$V(r) = g(r) + \vec{\nabla} h(r) \cdot \vec{\nabla} \quad (3-61)$$

Recall:

$$\begin{aligned} \vec{\nabla} h(r) \cdot \vec{\nabla} \varphi(\vec{r}) &= \frac{\partial h(r)}{\partial r} \hat{r} \cdot \vec{\nabla} \varphi(\vec{r}) + h(r) \nabla^2 \varphi(\vec{r}) \\ \nabla^2 &= \frac{1}{r} \frac{\partial^2}{\partial r^2} r - \frac{\vec{L}^2}{r^2} \end{aligned} \quad (3-62)$$

Expand the pion wave function as

$$\varphi(\vec{r}) = 4\pi \sum_{LM} i^L v_L(r) Y_L^M(\Omega) Y_L^{M*}(\hat{k}_\pi) \quad (3-63)$$

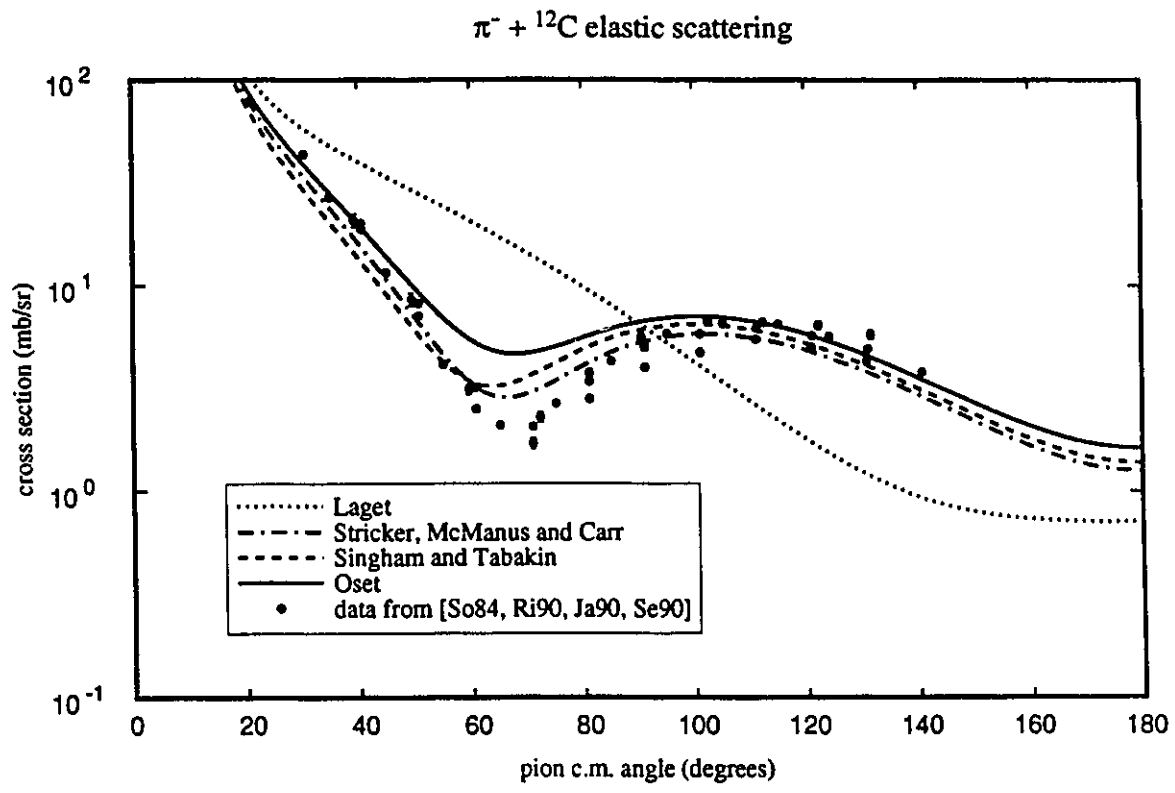


Figure 3-8. π^- elastic scattering from ${}^{12}\text{C}$ at an incident pion kinetic energy of $T_\pi = 50$ MeV. The curves are explained in the text. The data points are from four sources: [So84, Ri90, Ja90, Se90].

The radial equation is then

$$[1 + h(r)] \left[\frac{1}{r} \frac{\partial^2 v_L}{\partial r^2} - \frac{L(L+1)}{r^2} v_L \right] + [k^2 + g(r)] v_L + \frac{\partial h(r)}{\partial r} \frac{\partial v_L}{\partial r} = 0 \quad (3-64)$$

Now define $v_L(r) = \frac{y_L}{R}$ and let $R^2(r) = [1 + h(r)]$, then to get rid of the first derivative of v_L we introduce $z_L(r) = R(r) y_L(r)$ to get the radial equation in the form

$$z_L''(r) - \left[\frac{L(L+1)}{r^2} + f(r) \right] z_L(r) = 0 \quad (3-65)$$

with

$$f(r) = \frac{R''}{R} + \frac{2R'}{rR} - \frac{k^2 + g(r)}{R^2} \quad (3-66)$$

At this point we have an equation that looks like a Schrödinger equation which we can solve with our favorite Schrödinger equation solving algorithm. The Noumerov method [No24], modified by Thorlacius and Cooper [TC87] is the one that we will use. This method is discussed in detail in the Ph.D. thesis of Lotz [Lo89]. In the present case the radial wave functions are asymptotically normalized to Klein-Gordon Coulomb wave functions instead of the Dirac functions Lotz uses.

4 - Results for the Reaction $A(\gamma, \pi^- p)A-1$

In this chapter we explore the behaviour of our model for negative pion photoproduction on nuclei. We first consider the effect of changes in the description of the pion and proton wave functions, as well as the neutron bound state, on the cross section and spin observables. Next we look at the results of our model for kinematics which are very close to those of the free reaction, and compare the proton polarization and analyzing power calculated from our model with experimental data from the elementary process. The effect of increasing the energy of the incident photon while holding the angles of the detected particles fixed is considered, after which we fix the photon energy and vary the angles of the detected particles. Finally we compare the results of our model with the experimental data available to us.

4.1 Sensitivity to Changes in the Wave Functions

We consider first a photon incident on a ^{12}C nucleus. The incident photon has an energy of 380 MeV in the laboratory frame, and the direction of the photon momentum defines the z-axis. The momenta of the photon and the pion are used to define the x-z plane such that the pion momentum lies in the first quadrant at the spherical angle pair ($\theta_\pi = 120^\circ$, $\varphi_\pi = 0^\circ$). The proton is detected at an angle pair ($\theta_p = 20^\circ$, $\varphi_p = 180^\circ$) so we are considering a coplanar geometry. Having fixed the energy of the incoming particle and the position of the detectors we have one variable, which we choose to be the proton kinetic energy. All other quantities are then determined through energy and momentum conservation. We are looking at an exclusive reaction so we assume that we know the final state of the residual nucleus. The reaction takes place on a $1p_{3/2}$ neutron of carbon leaving the residual ^{11}C in its ground state with a $J = 3/2$ neutron hole. The separation energy of the valence neutron is $E_s = 18.721$ MeV [Aj85].

In figure 4-1 we consider some of the kinematic quantities relevant to this reaction as a function of proton kinetic energy. Figure 4-1a) shows an almost linear relation between the pion and proton energies, indicating that the energy of the recoil nucleus

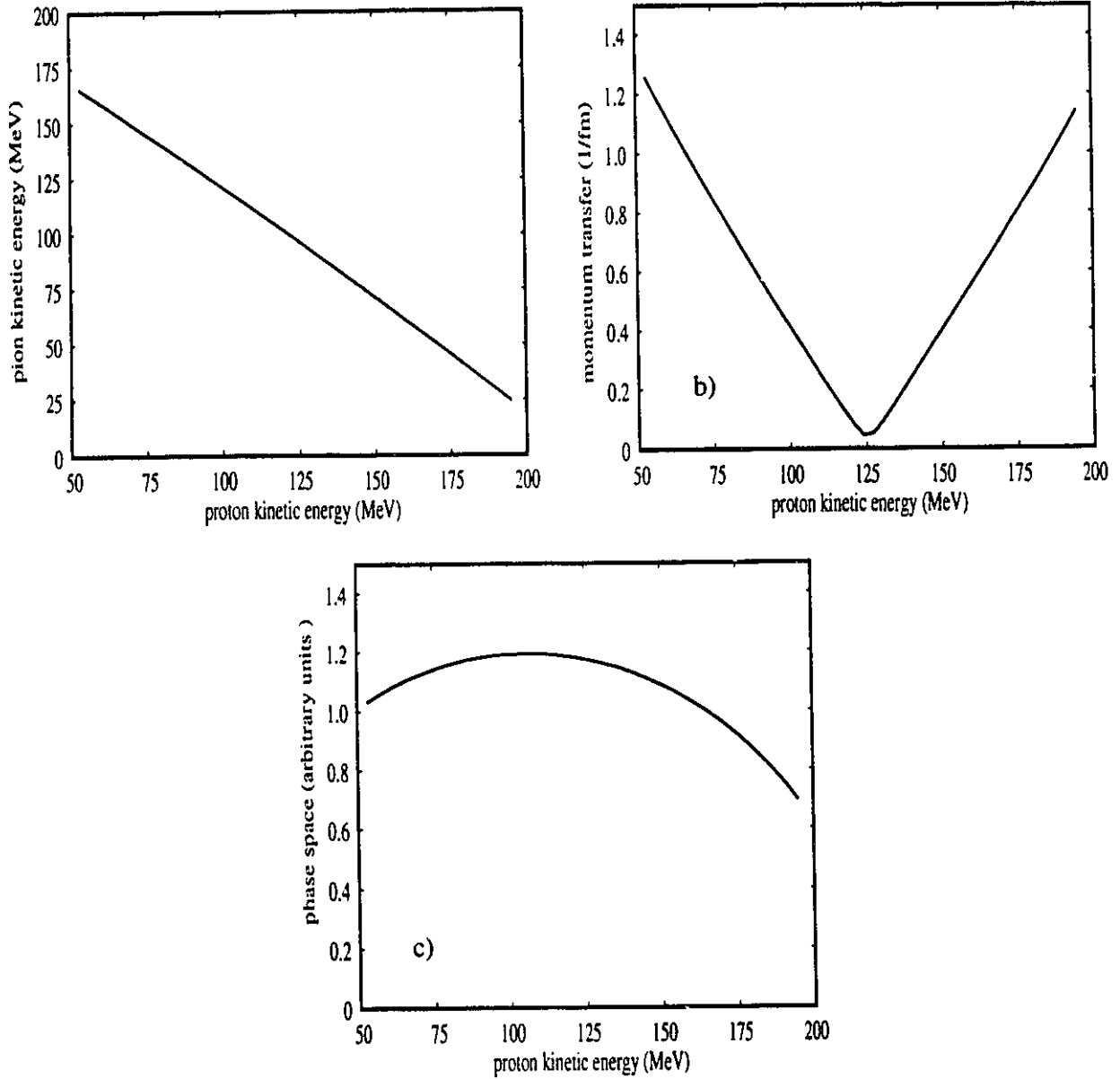
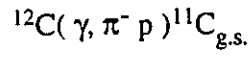


Figure 4-1. Variation in kinematic quantities for the experimental conditions:
 $E_\gamma = 380 \text{ MeV}$, $(\theta_p = 20^\circ, \varphi_p = 180^\circ)$ and $(\theta_\pi = 120^\circ, \varphi_\pi = 0^\circ)$, in the reaction
 $^{12}\text{C}(\gamma, \pi^- p)^{11}\text{C}_{\text{g.s.}}$

remains nearly constant. This means that the total energy of the pion-proton system is almost constant across the kinematic range. In figure 4-1b) we see the momentum transfer to the recoil nucleus as a function of the proton energy. The momentum transfer is very close to zero at a proton kinetic energy of 125 MeV and has a maximum of 1.3 fm^{-1} when the proton kinetic energy is 50 MeV. Figure 4-1c) shows the energy dependence in the phase space portion of the cross section, equation (2-113), to be quite weak, and any structure in the cross section will be governed by the matrix element.

The variation of the cross section with the addition of distortions to the wave functions of the final state particles is shown in figure 4-2. The dotted line shows the calculation using plane waves for both the proton and the pion. The bound state wave function is calculated using the Woods-Saxon binding potential of table 3-1. The s-matrix in this case can then be written in the form of equation (2-98) and the cross section is the square of the Fourier transform of the bound state wave function modified by some spin factors. The cross section goes to zero at $T_p = 125 \text{ MeV}$ where the momentum transfer to the residual nucleus is zero, as shown in figure 4-1b. This occurs because the momentum-space wave function for the $p_{3/2}$ bound state of carbon is zero when the momentum is zero, as can be seen in figure 3-4. The peaks in the cross section occur at $T_p = 90 \text{ MeV}$ and $T_p = 160 \text{ MeV}$ where the momentum transfer is $q=0.5 \text{ fm}^{-1}$. The cross section appears to be almost symmetric in momentum transfer about the $q=0$ point which we expect if we are Fourier transforming the bound state wave function.

The dot-dashed curve of figure 4-2 shows the effect of modifying the proton wave function by a distorting potential. The potential used is the global energy and mass dependent one of Cooper et al. [Co92] discussed in chapter 3. The addition of the potential reduces the magnitude of the peaks of the cross section by about one third and shifts the peaks and the minimum toward smaller proton energies by 3-4 MeV. The dashed line shows the effect of modifying the pion wave function with the distorting potential of Oset et al. [Ga88, Ni92]. The cross section in this case is shifted toward higher proton energy (lower pion energy), relative to the plane wave curve by $\sim 15 \text{ MeV}$, and the magnitudes of the peaks are reduced by approximately twenty per cent. The solid line has both the pion and proton described by distorted waves, and in this case the magnitude of the cross section is reduced to about one half of that of the plane wave

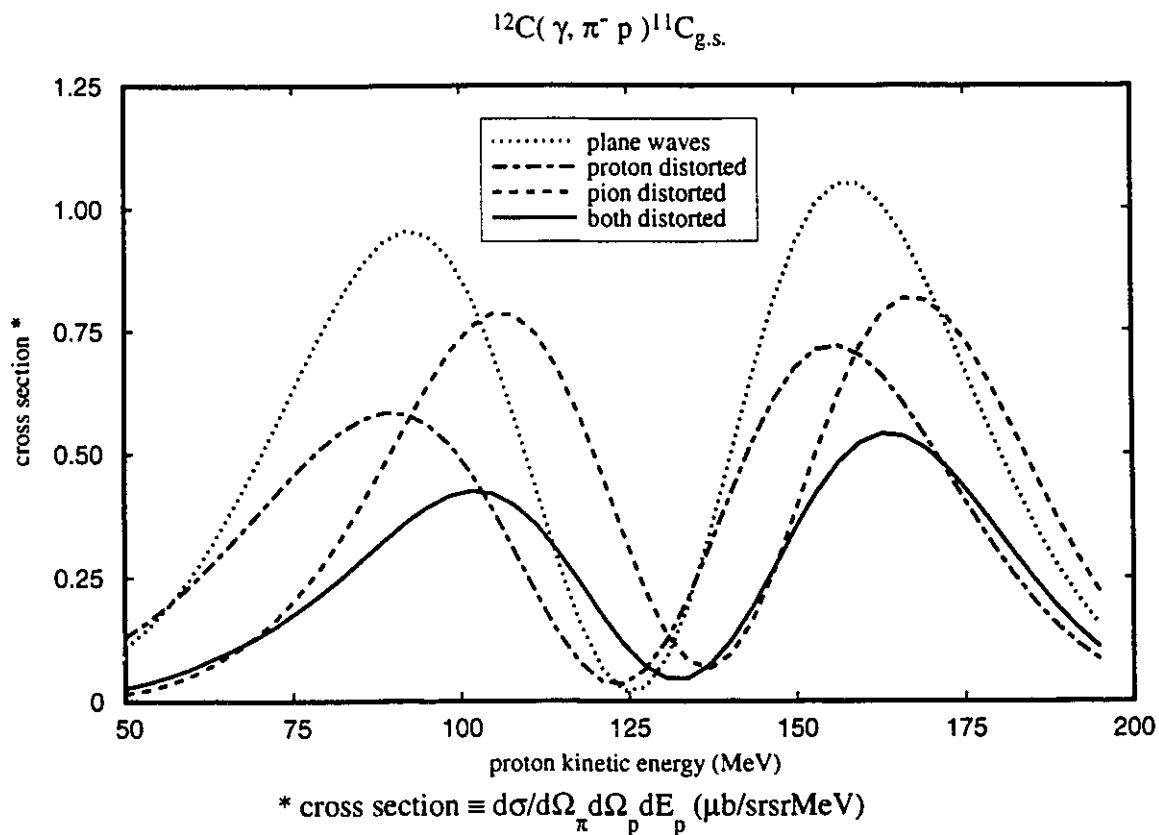


Figure 4-2. Dependence of the cross section on distortions of the final proton and pion. The kinematic conditions are $E_{\gamma} = 380$ MeV., ($\theta_p = 20^{\circ}$, $\varphi_p = 180^{\circ}$) and ($\theta_{\pi} = 120^{\circ}$, $\varphi_{\pi} = 0^{\circ}$). Dotted line - both proton and pion are plane waves. Dot-dashed line - proton is distorted by the global E and A dependent potential. Dashed line - pion is distorted by the potential of Oset. Solid line - both pion and proton are distorted.

calculations. The competing shifts in the proton energy have the result of moving the peaks and the minimum toward higher proton energy by ~ 10 MeV.

The effect of the addition of distortions on the polarization of the proton (equation (2-114)) and the analyzing power due to linearly polarized photons (equation (2-115)), is shown in figure 4-3. The dotted curves have plane waves describing both the pion and the proton. Note that the polarization of the proton is not zero even though there are no complex potentials in the wave equations. The polarization is nonzero due to the complex width of the delta resonance, which is included in the denominator of the delta propagator. When the width of the delta is set to zero the polarization is identically zero at all proton energies in the plane wave calculations. Addition of proton distortion only results in small changes from the plane wave results, except in the neighbourhood of the cross section minimum at $T_p = 125$ MeV, where both the proton polarization and analyzing power take rather drastic dips. The pion distortion alone has virtually no effect on the proton polarization and changes the analyzing power by less than 0.1. The inclusion of distortions for both the pion and the proton result in a reduction of approximately 0.1 in the proton polarization from the plane wave value for proton energies below 130 MeV, while above this energy the results for plane wave and distorted calculations are very close. The analyzing power results for plane wave and distorted calculations are significantly different only in the region of the cross section minimum. Note that the proton polarization and analyzing power, calculated using distorted waves for the proton and pion, are both positive over the entire range of proton kinetic energies.

Figure 4-4 shows the effects of changing the pion's distorting potential. The proton wave function is calculated with the E and A dependent global potential. We consider the four pion potentials discussed in chapter 3. The dotted curve is calculated using the s-wave pion potential of Laget [La72]. The dot-dashed curve results from using the potential of Stricker, McManus and Carr [SMC79, SMC80], while the dashed curve results from the potential of Singham and Tabakin [ST81]. The ST pion potential is similar to the SMC potential because Singham and Tabakin began with the potential parameters reported by SMC and made adjustments to improve the description of some data not included in the SMC analysis. The predictions from the SMC and ST potentials are very close to each other indicating that the modifications are not very significant here.

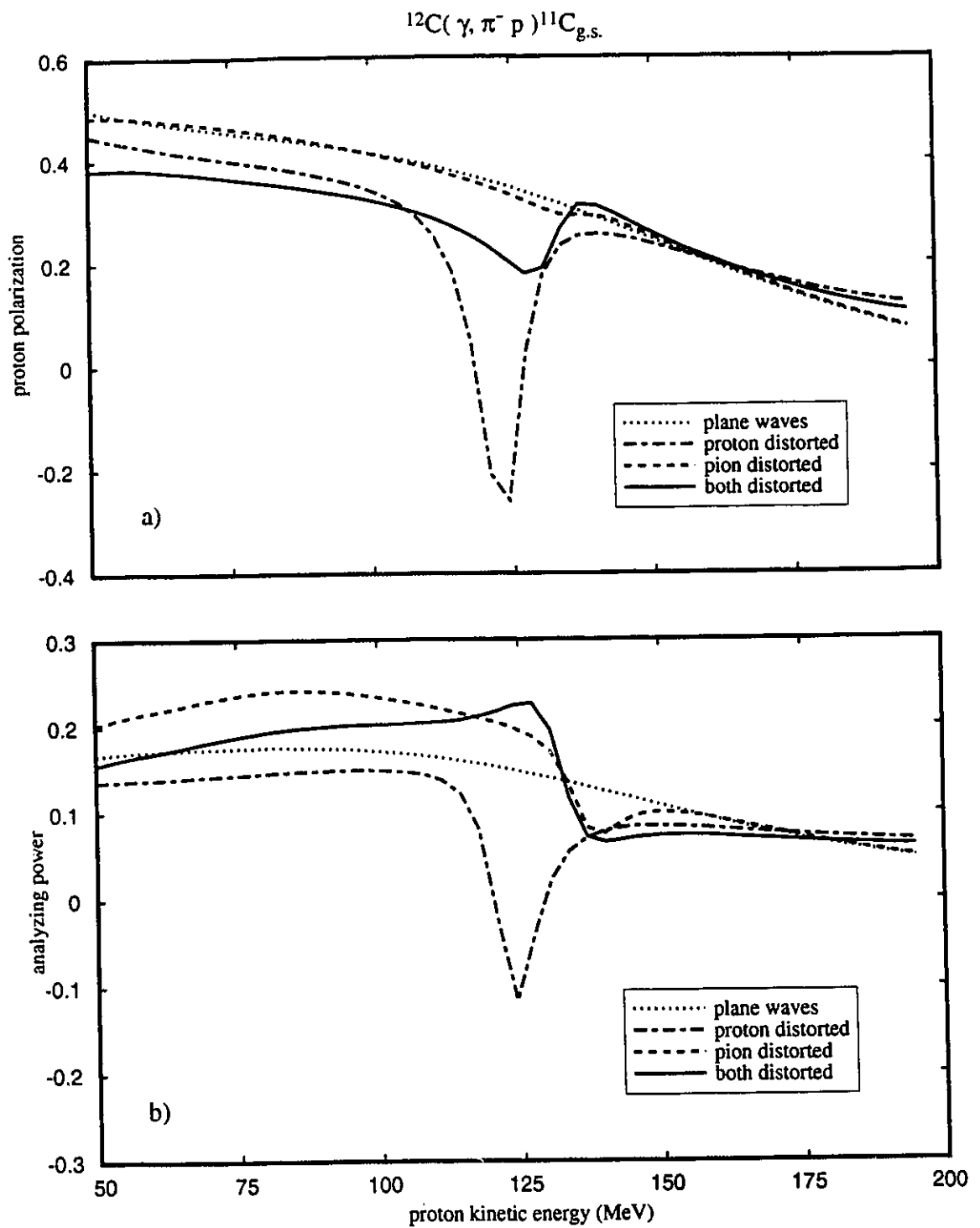


Figure 4-3. Dependence of the spin observables on distortions of the final proton and pion. Lines as for figure 4-2. a) polarization of the final proton and b) asymmetry due to initially linearly polarized photons.

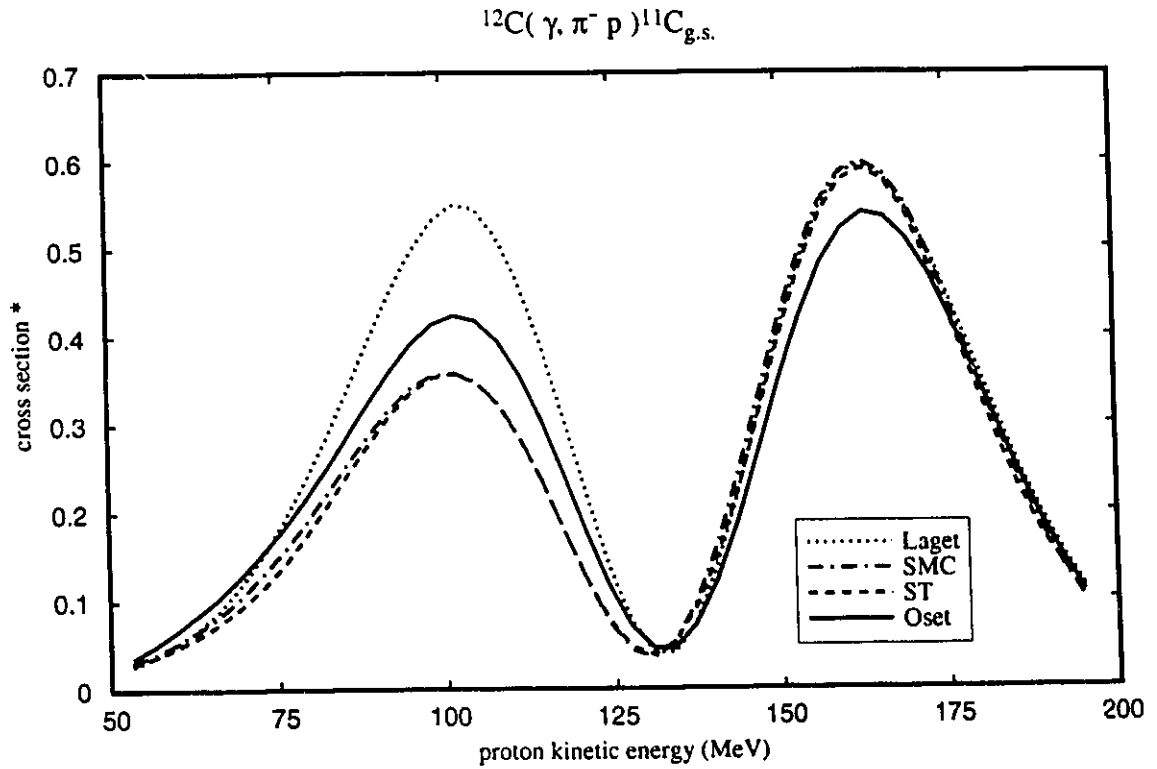


Figure 4-4. Dependence of the cross section on changes in pion distortion. The kinematic conditions are $E_{\gamma} = 380$ MeV., ($\theta_p = 20^{\circ}$, $\phi_p = 180^{\circ}$) and ($\theta_{\pi} = 120^{\circ}$, $\phi_{\pi} = 0^{\circ}$). The proton is distorted by the global E and A dependent potential in all the curves [Co92].
 Dotted line - Laget's pion potential [La72].
 Dot-dashed line - SMC pion potential [SMC79].
 Dashed line - Singham and Tabakin pion potential [ST81].
 Solid line - Oset's pion potential [Os91].

The solid curve is calculated from the pion optical potential of Oset et al. [Ga88, Ni92], obtained by calculating the pion self energy as shown in figure 3-9. We refer to these potentials simply as Laget, SMC, ST and Oset.

Figure 4-5 shows the effect on the spin observables of changing the pion distorting potentials. SMC and ST give very similar results, as they did for the cross section, while Oset gives basically the same shape as ST and SMC but varies from them for proton energies in the range 125 MeV to 150 MeV. Note that the minimum of the cross section in figure 4-4 lies in the range 130 MeV to 135 MeV and this is exactly where the largest sensitivity to the pion potential occurs. The three potentials just mentioned are all of basically the same form, i.e. the central plus gradient form of equation (3-50). The dotted curves of figure 4-5 show the results due to the Laget potential, which contains only the central (s-wave) portion of the potential. The results from Laget are quite close to those of the other potentials except in the neighbourhood of the cross section minimum. It is interesting to note that at $T_p = 100$ MeV, where the Laget pion potential results in the cross section being about a factor of 1.5 larger than SMC and ST and roughly 1.3 larger than Oset, the spin observables are all in reasonable agreement. The spin observable predictions from the different pion potentials are quite similar except in the region where the momentum transfer becomes small. SMC and ST are similar in this region as we would expect but Laget, Oset and (SMC, ST) can be distinguished in this region.

The reaction we are examining requires proton distortions which can be evaluated at any proton kinetic energy in the allowed kinematic region. Proton-nucleus elastic scattering data does not however exist for all nuclei at all proton kinetic energies of interest. We are fortunate that the Ohio group have taken the existing proton-nucleus elastic scattering data, and searching on the data, have determined optical potentials which are parametrized as functions of the proton kinetic energy in the range 65 MeV to 1 GeV and the atomic mass of the target nucleus in the range $A = 12$ to $A = 208$ [Co92]. They have also produced parameterizations particular to ^{12}C and ^{16}O which are functions of incident proton kinetic energy [Sh92].

The curves of figure 4-6 are calculated with the pion distortions of Oset et al. while the $1p_{3/2}$ neutron is described by the Woods-Saxon potential of table 3-1. The dotted line

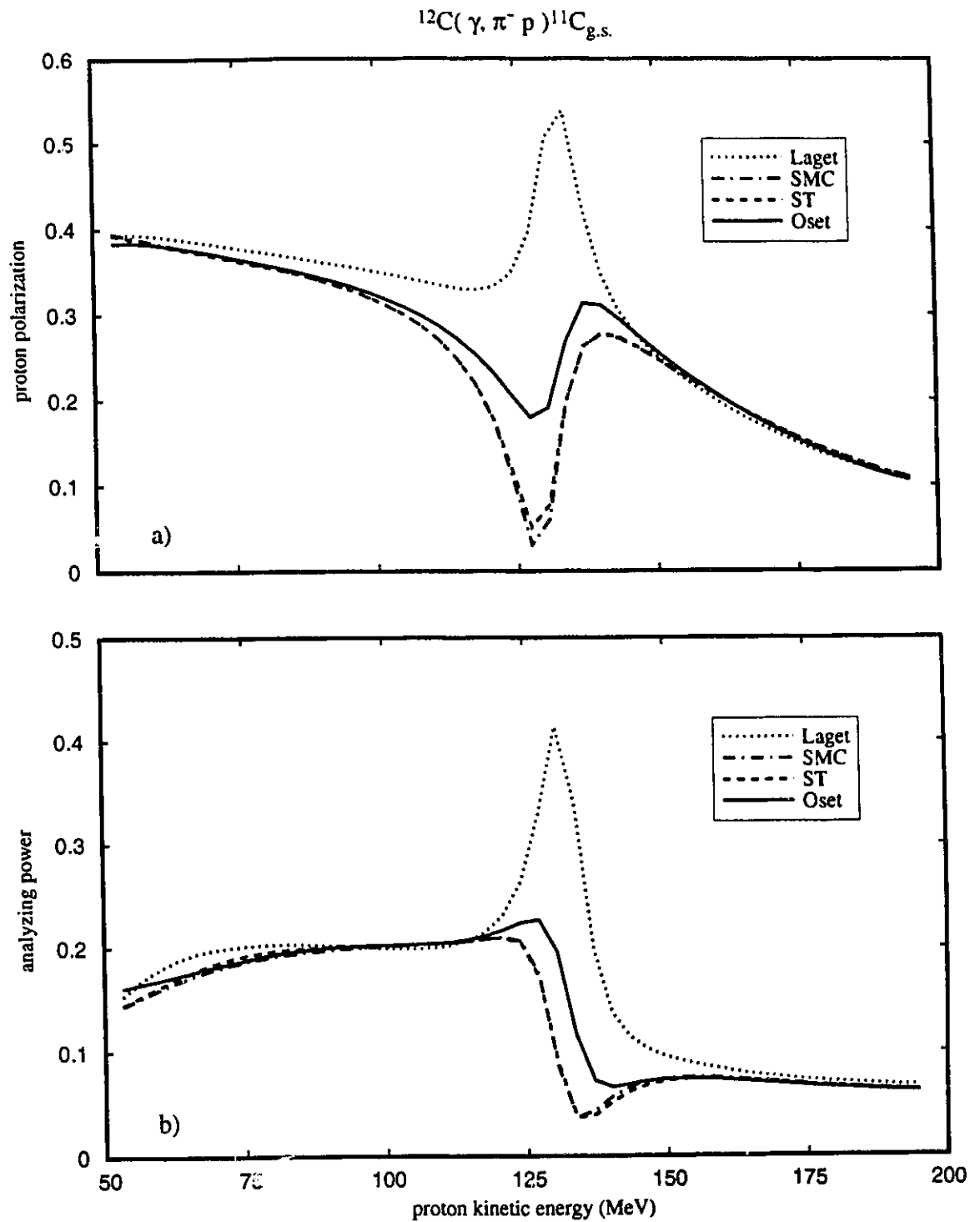


Figure 4-5. Dependence of the spin observables on changes in pion distortions. The proton is distorted by the global E and A dependent potential. a) polarization of the final proton and b) asymmetry due to linearly polarized photons. Lines as for figure 4-4.

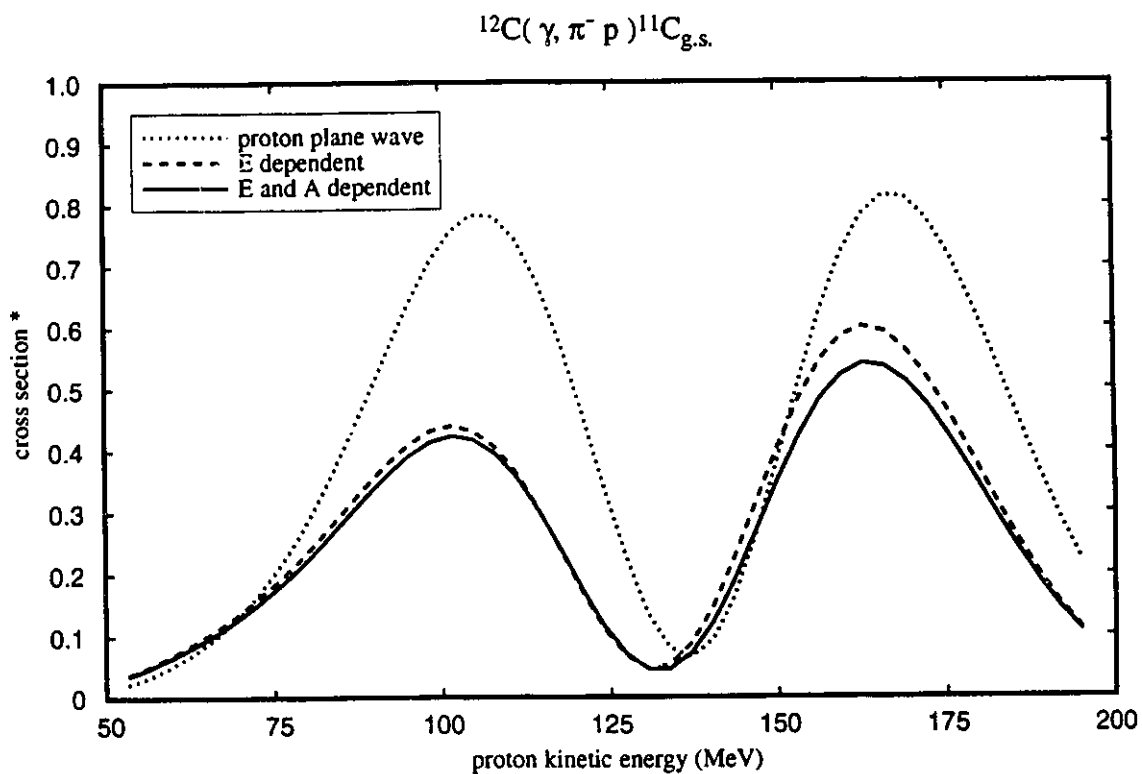


Figure 4-6. Dependence of the cross section on changes in proton distortion. The kinematic conditions are $E_{\gamma} = 380$ MeV., ($\theta_p = 20^{\circ}$, $\phi_p = 180^{\circ}$) and ($\theta_{\pi} = 120^{\circ}$, $\phi_{\pi} = 0^{\circ}$). The pion is distorted by the potential of Oset.

Dotted line - plane wave proton.

Dashed line - E dependent global potential for carbon.

Solid line - E and A dependent global potential.

results from describing the proton by a plane wave. The dashed line uses the E dependent parametrization for ^{12}C while the solid line uses the potential parametrized in both E and A. The addition of proton distortions reduces the cross section by one third to one half of the plane wave value, and the two different potential parameterizations result in differences of at most ten per cent in the resulting cross section.

The change in spin observables with proton distortion is shown in figure 4-7. The addition of proton distortion reduces the proton polarization by about 0.1 between $T_p = 50$ MeV and 135 MeV, while above $T_p = 135$ MeV proton distortions have little effect in changing the polarization from the plane wave value. The analyzing power is reduced by roughly 0.05 for small proton energies. The results for the two proton potentials follow each other quite closely except through the region where the momentum transfer to the nucleus becomes small. This also occurs for the different pion potentials as shown in figure 4-5. This amplification arises because small changes in the cross section become large relative changes at the minimum.

The effect of variations in the bound state wave function are shown in figures 4-8 and 4-9. The dotted curve results from a Dirac-Hartree binding potential [HS86] while the dashed and solid curves use a Woods-Saxon form for the binding potential. The dashed curve is calculated using the Woods-Saxon parameters of table 3-1 (WS1). These parameters provide a good description of (γ, p) data [Lo89], and so the bound state wave function calculated from these parameters reflects the high momentum transfer in that reaction. That is to say that the bound state wave function constrained by (γ, p) data should be better determined in the high momentum transfer region than a wave function whose sole constraint is fitting the binding energy. The WS potential used to calculate the solid curve uses the geometry parameters of table 3-1 but the depth of the vector potential was changed to $V_v = 400.0$ MeV and the scalar potential searched on to reproduce the binding energy. This yielded a scalar depth of $V_s = -477.9$ MeV and a potential which we refer to as WS2. The momentum transfer to the nucleus at the first cross section peak where $T_p = 100$ MeV is $q \approx 0.4 \text{ fm}^{-1}$, (see figure 4-1b), while at the other peak we have $T_p = 165$ MeV with $q \approx 0.6 \text{ fm}^{-1}$. We see from figure 3-4 that we are near the peak of the momentum space bound state wave functions. The distributions of the magnitude of the peaks of the cross sections reflects the distributions of the magnitude of the momentum

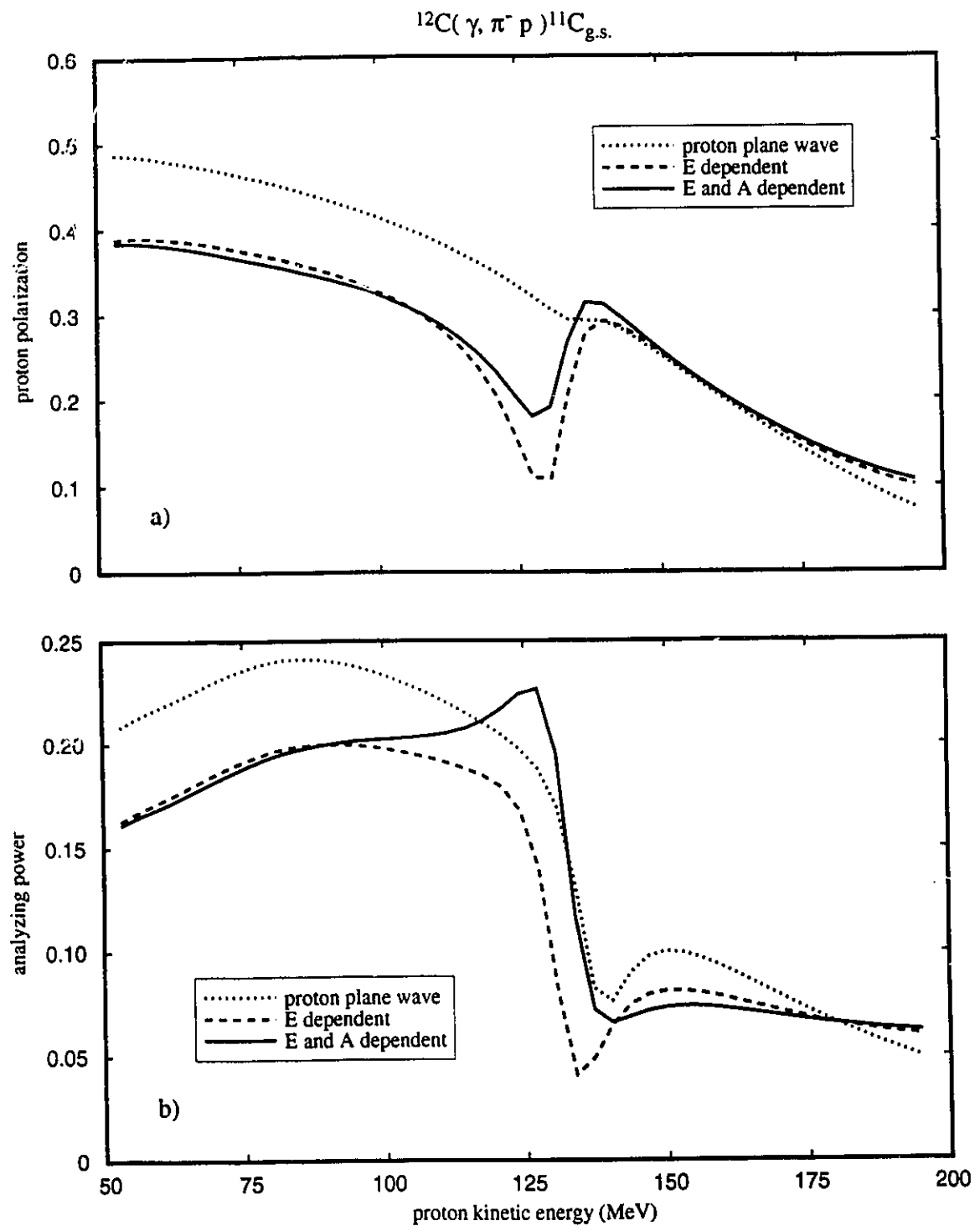


Figure 4-7. Dependence of the spin observables on changes in proton distortions. The pion is distorted by the potential of Oset. a) polarization of the final proton and b) analyzing power due to linearly polarized photons. Lines as for figure 4-6.

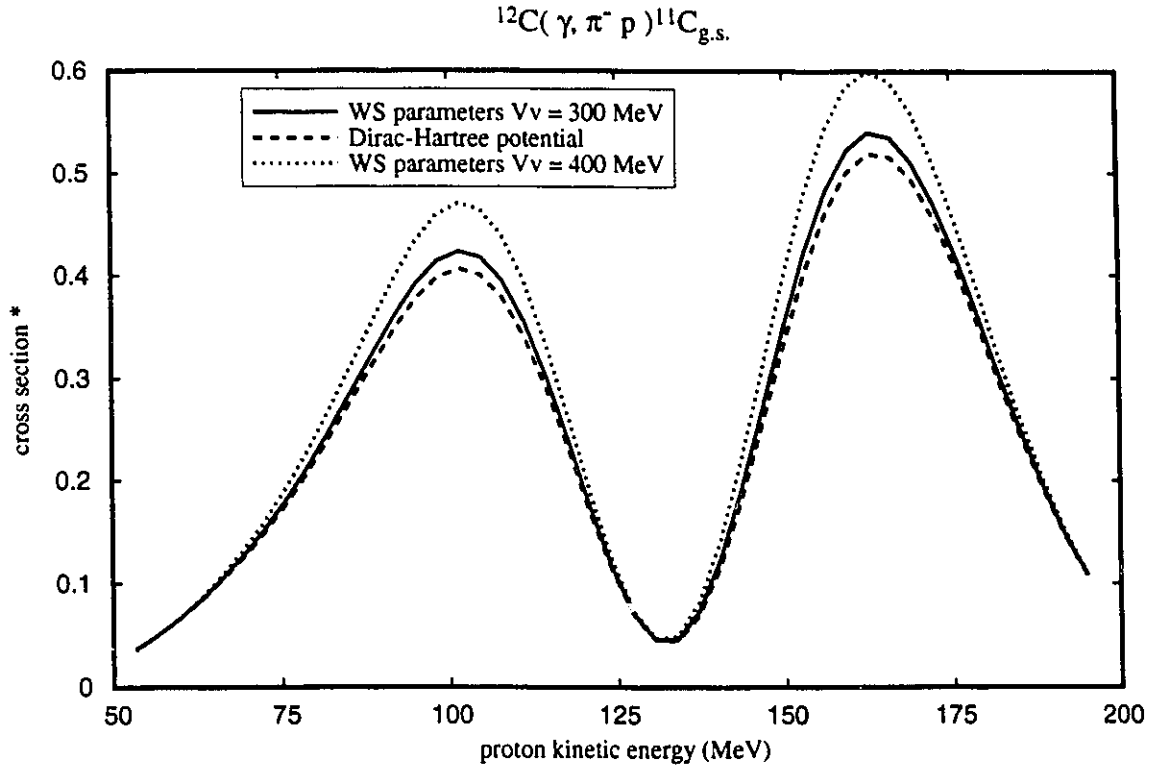


Figure 4-8. Sensitivity of the cross section to changes in the bound state wave function. The kinematic conditions are $E_{\gamma} = 380 \text{ MeV}$, $(\theta_p = 20^{\circ}, \phi_p = 180^{\circ})$ and $(\theta_{\pi} = 120^{\circ}, \phi_{\pi} = 0^{\circ})$. Pion is distorted by the potential of Oset and the proton is distorted by the global E and A dependent potential.
 Solid line - Woods-Saxon binding potential #1 with $V_v = 300 \text{ MeV}$.
 Dashed line - Dirac-Hartree binding potential.
 Dotted line - Woods-Saxon binding potential #2 with $V_v = 400 \text{ MeV}$.

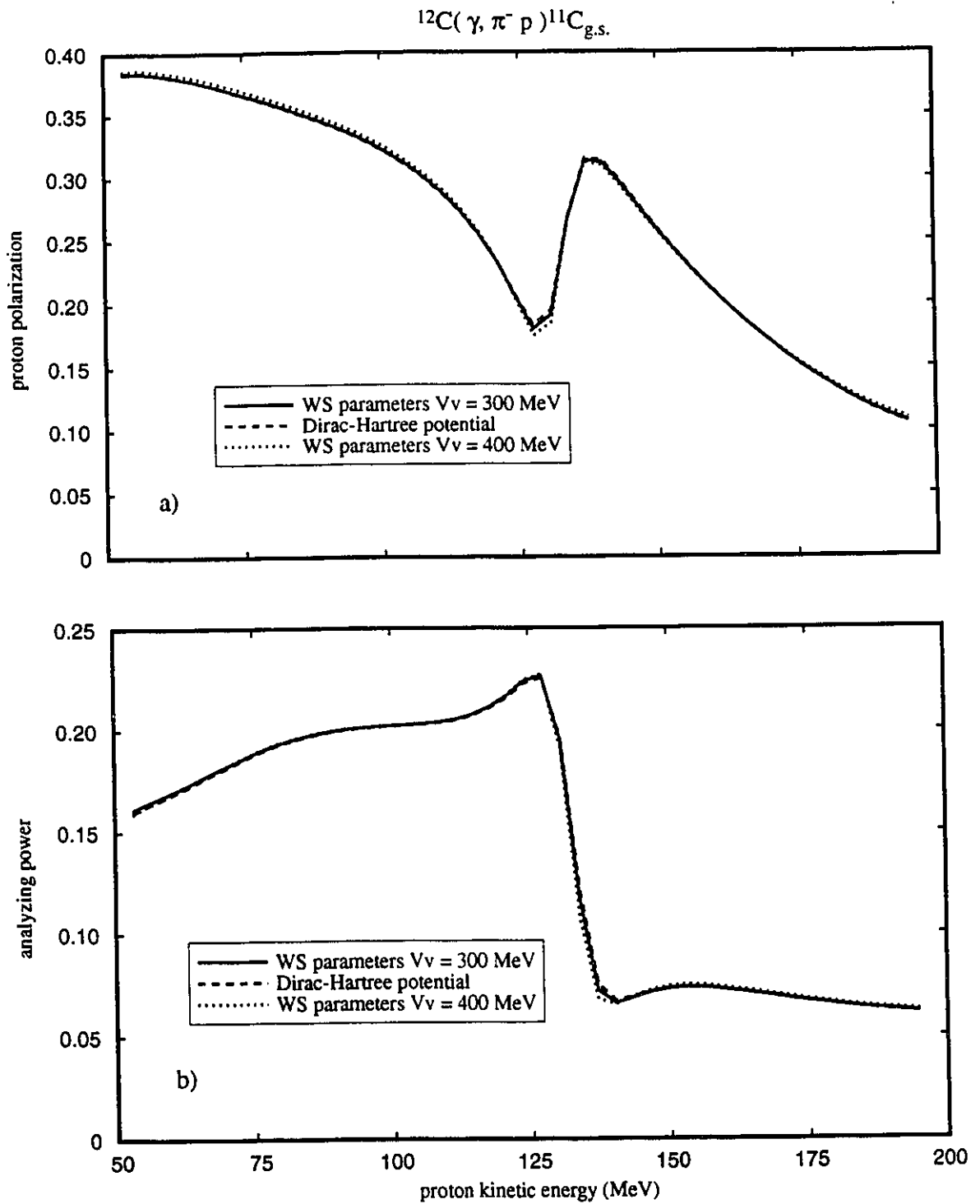


Figure 4-9. Sensitivity of the spin observables to changes in the bound state wave functions. a) polarization of the final proton and b) asymmetry due to linearly polarized photons. Lines as for figure 4-8.

space wave functions with the Hartree wave function having the smallest magnitude and the wave function calculated from WS2 having the largest. The cross section calculated with plane waves describing the pion and the proton has the same shape as the distorted wave cross section of figure 4-8 but is roughly a factor of two larger than the distorted wave result in this case.

The predicted polarization and analyzing power shown in figure 4-9 are extremely close for all three binding potentials and all show the rapid change as the momentum transfer to the nucleus passes through zero. The plane wave spin observables are the same as the dotted curves of figure 4-3. The plane wave curves resulting from the three bound state wave functions are indistinguishable on a graph.

In order to explore the sensitivity of our model to the bound state wave functions at high momentum transfer we changed the proton angle from $\theta_p = 20^\circ$ to $\theta_p = 70^\circ$ while holding the pion angle at $\theta_\pi = 120^\circ$. This changes the momentum transfer to lie in the range 2 fm^{-1} to 3 fm^{-1} as shown in figure 4-10. In this range of momentum transfer the momentum space wave functions of figure 3-6 become easily distinguishable. The cross section shown in figure 4-11 is calculated using plane waves for the proton and pion. The minima occur in the same order that the minima occur for the upper component momentum space wave functions, but the results are modified by the presence of the lower component of the bound state, which can be larger than the upper component wave function in this momentum range. The distorted wave cross sections are shown in figure 4-12. The addition of distortions washes out the minima and raises the cross sections for proton energies above 75 MeV by as much as an order of magnitude.

Spin observables calculated in the plane wave approximation are shown in figure 4-13. The interesting features (dips) in the results occur at the minima of the respective cross sections. The distorted wave calculations of the spin observables are shown in figure 4-14. The dips are gone as the distorted wave cross section did not exhibit this feature, and the curves follow each other closely.

We can change the bound state wave function by changing the separation energy, which we do in figure 4-15. The dashed curve is the cross section calculated with a bound state wave function determined by the Woods-Saxon potentials of table 3-1 with the

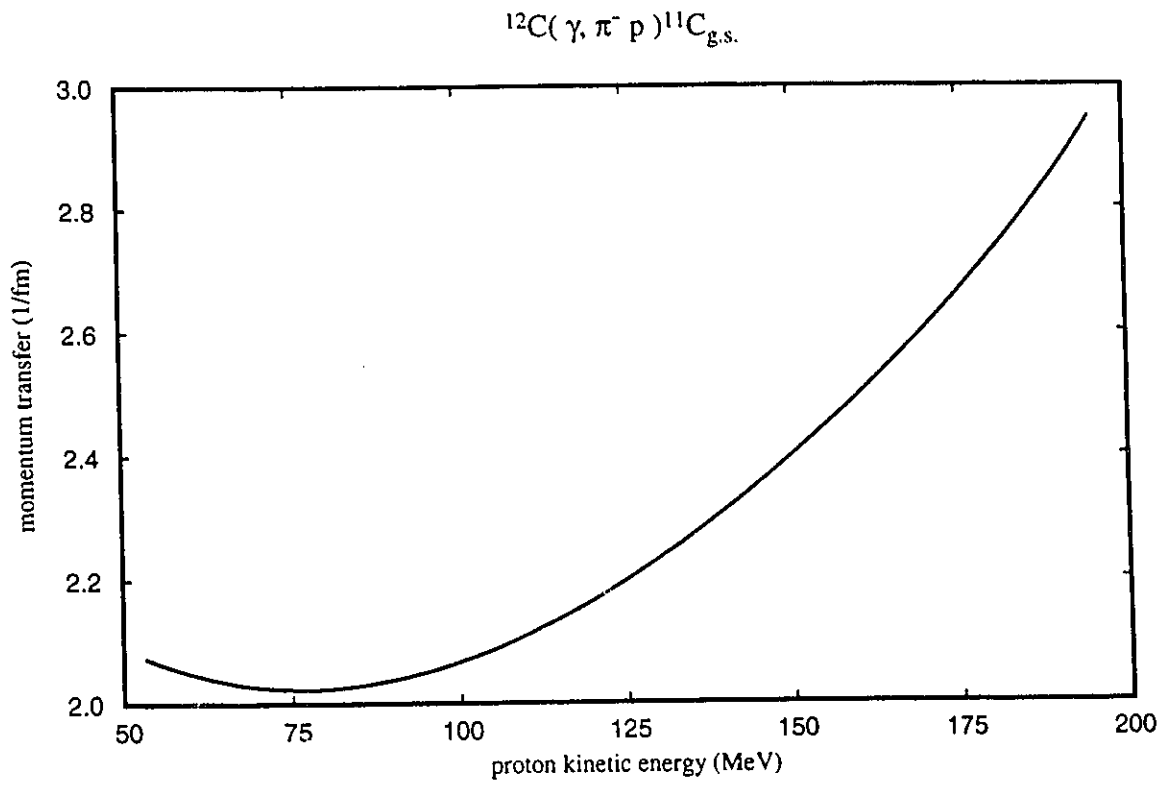


Figure 4-10. The kinematic conditions are $E_\gamma = 380 \text{ MeV}$, $(\theta_p = 70^\circ, \varphi_p = 180^\circ)$ and $(\theta_\pi = 120^\circ, \varphi_\pi = 0^\circ)$.

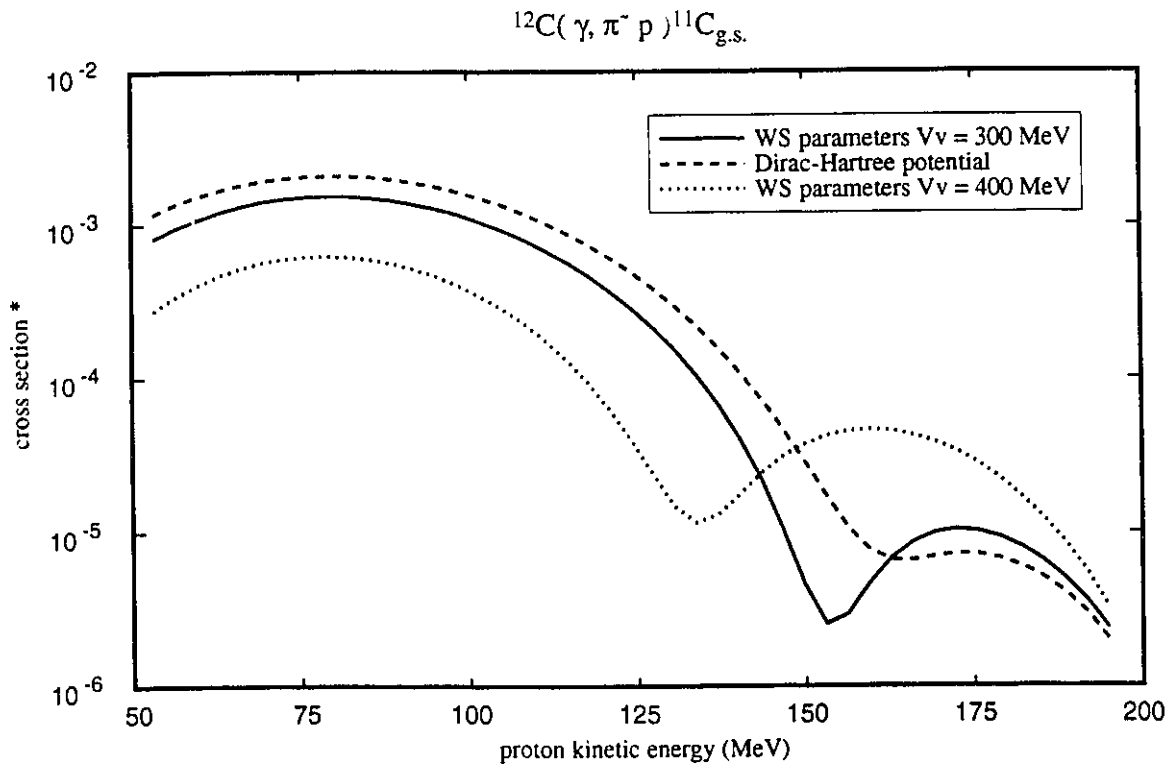


Figure 4-11. Sensitivity of the cross section to changes in the bound state wave function. The kinematic conditions are $E_{\gamma} = 380$ MeV., ($\theta_p = 70^{\circ}$, $\phi_p = 180^{\circ}$) and ($\theta_{\pi} = 120^{\circ}$, $\phi_{\pi} = 0^{\circ}$). The pion and the proton are described by plane waves.
 Solid line - Woods-Saxon binding potential #1 with $V_v = 300$ MeV.
 Dashed line - Dirac-Hartree binding potential.
 Dotted line - Woods-Saxon binding potential #2 with $V_v = 400$ MeV.

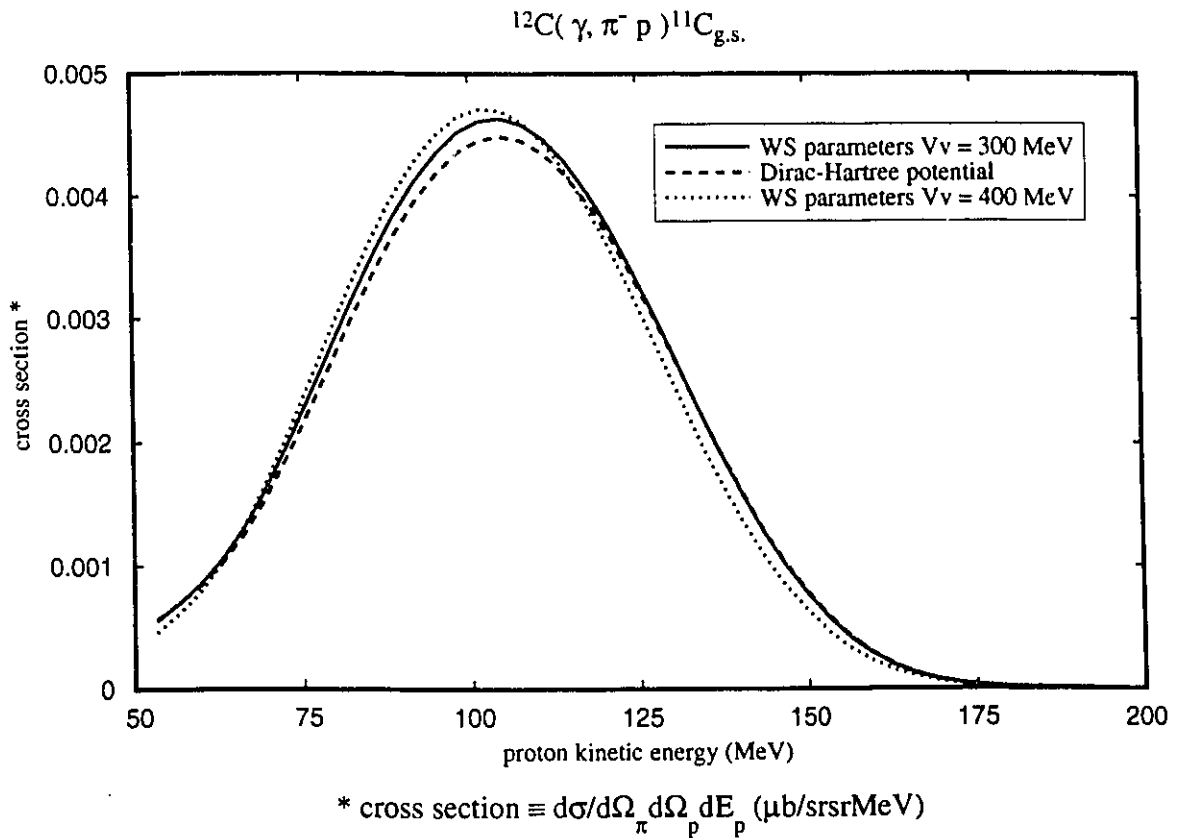


Figure 4-12. Sensitivity of the cross section to changes in the bound state wave function. The kinematic conditions are $E_{\gamma} = 380$ MeV., $(\theta_p = 70^{\circ}, \varphi_p = 180^{\circ})$ and $(\theta_{\pi} = 120^{\circ}, \varphi_{\pi} = 0^{\circ})$. Pion is distorted by the potential of Oset and the proton is distorted by the global E and A dependent potential.
Dashed line - Dirac-Hartree binding potential.
Solid line - Woods-Saxon binding potential #1 with $V_v = 300$ MeV.
Dotted line - Woods-Saxon binding potential #2 with $V_v = 400$ MeV.

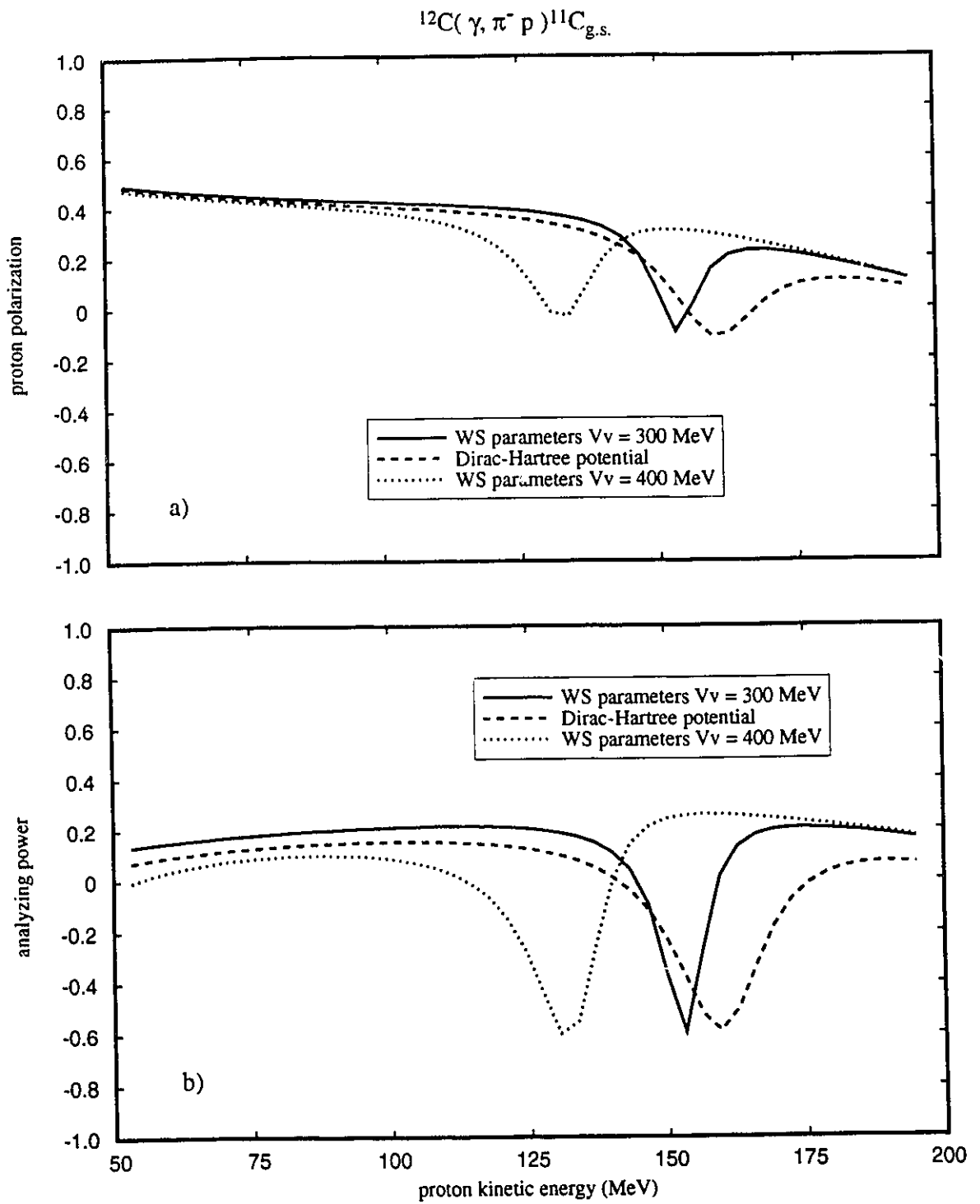


Figure 4-13. Sensitivity of the spin observables to changes in the bound state wave functions, with plane wave pion and proton. a) polarization of the final proton and b) analyzing power due to linearly polarized photons. Lines as for figure 4-11.

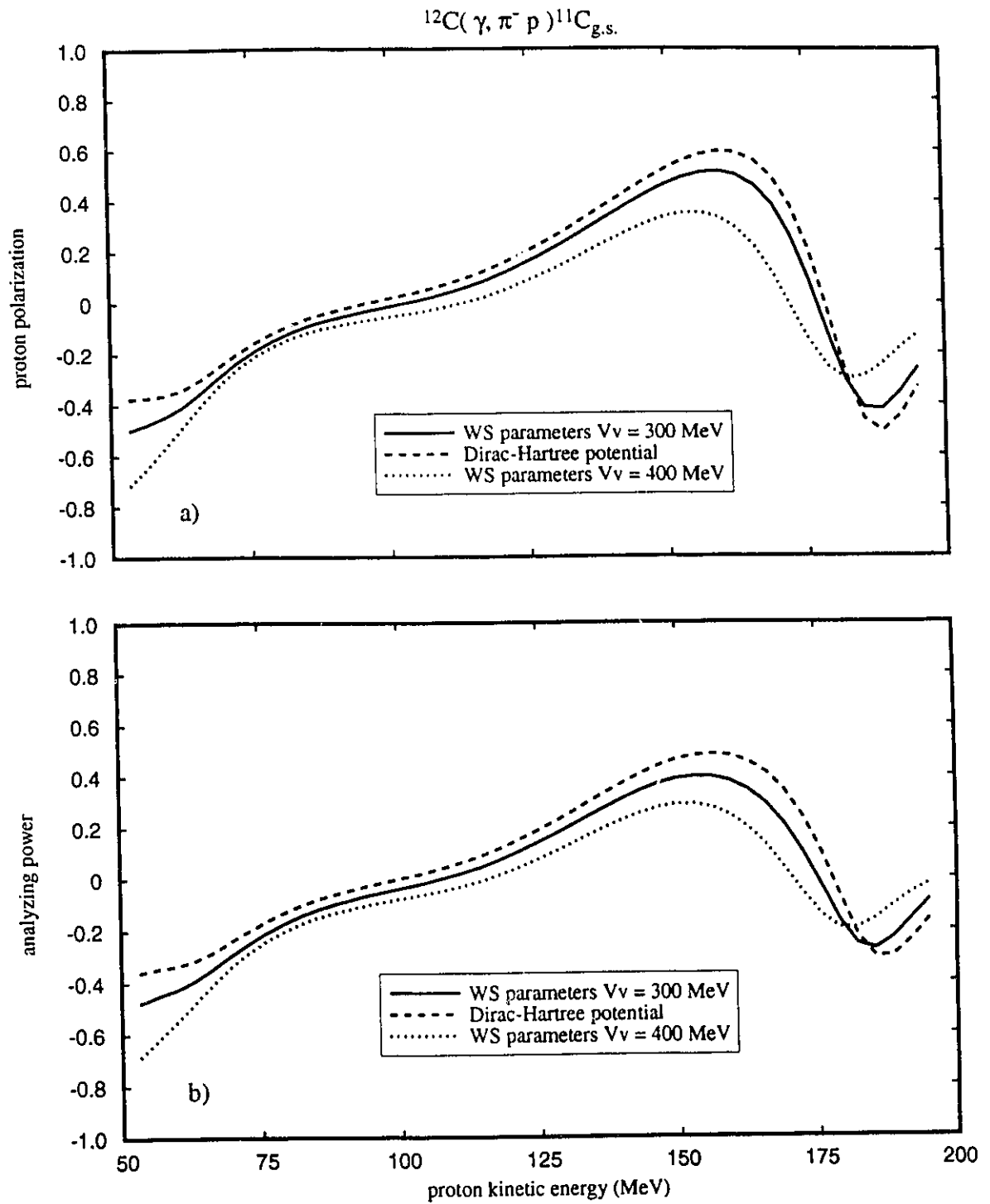


Figure 4-14. Sensitivity of the spin observables to changes in the bound state wave functions, with distorted pion and proton. a) polarization of the final proton and b) analyzing power due to initially linearly polarized photons. Lines as for figure 4-12.

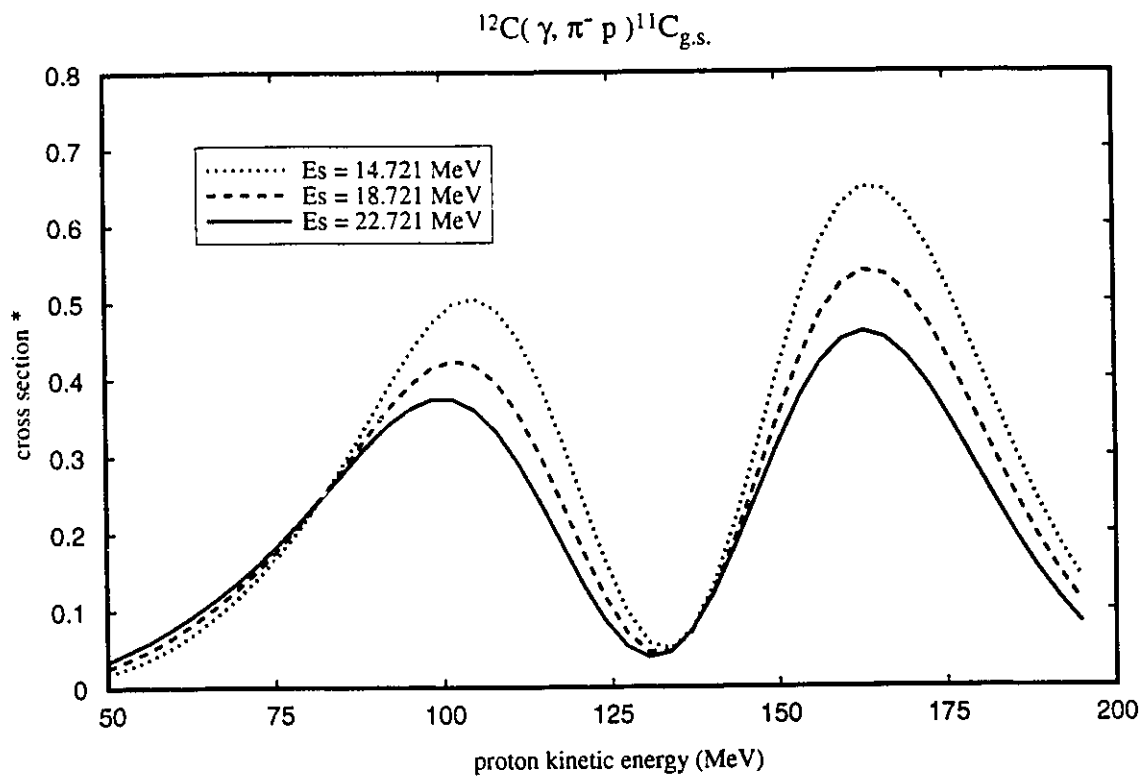


Figure 4-15. Sensitivity of the cross section to changes in the separation energy of the $1p_{3/2}$ neutron bound state wave function. The kinematic conditions are

$E_{\gamma} = 380 \text{ MeV}$, $(\theta_p = 20^{\circ}, \varphi_p = 130^{\circ})$ and $(\theta_{\pi} = 120^{\circ}, \varphi_{\pi} = 0^{\circ})$. Pion is distorted by the potential of Oset and the proton is distorted by the global E and A dependent potential. Dotted line - $E_s = 14.721 \text{ MeV}$.

Dashed line - $E_s = 18.721 \text{ MeV}$. Solid line - $E_s = 22.721 \text{ MeV}$.

measured value of the separation energy for the $1p_{3/2}$ neutron. The bound state for the dotted curve is determined by searching on the depth of the scalar potential of the parameter set of table 3-1 to fit a separation energy 4 MeV less than the experimental value, while the solid line has a bound state with a separation energy 4 MeV greater than the experimental value. As the binding energy is increased the rms radius of the bound state becomes smaller and the projectile has a smaller target resulting in a smaller cross section. An eight MeV increase in the separation energy from 14.721 MeV, reduces the cross section by almost thirty per cent.

The spin observables calculated from our different bound state wave functions of figure 4-15 are shown in figure 4-16. The three curves exhibit the same basic shape and the only significant change occurs for the proton polarization in the area of the cross section minimum where an eight MeV change in the separation energy can result in noticeable differences in the proton polarization.

To summarize, we have seen that including distortions in the pion and proton wave functions decreases the magnitude of the cross section by roughly a factor of two from the plane wave value in the cases considered. Addition of the proton distortion alone causes a large dip in the spin observables when the momentum transfer goes through zero, but when both pion and proton are distorted the results do not vary significantly from the plane wave ones. The results are not very sensitive to changes in the continuum wave function, or to different bound state wave functions; the latter is associated with the fact that distortions of the proton and pion wash out the differences observable in the plane wave calculation. We are most sensitive to differences in the pion optical potentials, which are probably the least well determined ingredients in our calculations.

The wave functions which we use in the present study are all determined from other sources: the pion and proton distorted waves are obtained through comparison with elastic scattering data, and the bound state wave function has the experimental binding energy as its eigenvalue in addition to providing the best description of the (γ, p) data in the thesis of G. Lotz. In what follows we use the E and A dependent potential for our proton distortion and either the potential of Singham and Tabakin or the potential of Oset for our pion distortion. The bound state is described by the Woods-Saxon parameter set of table 3-1.

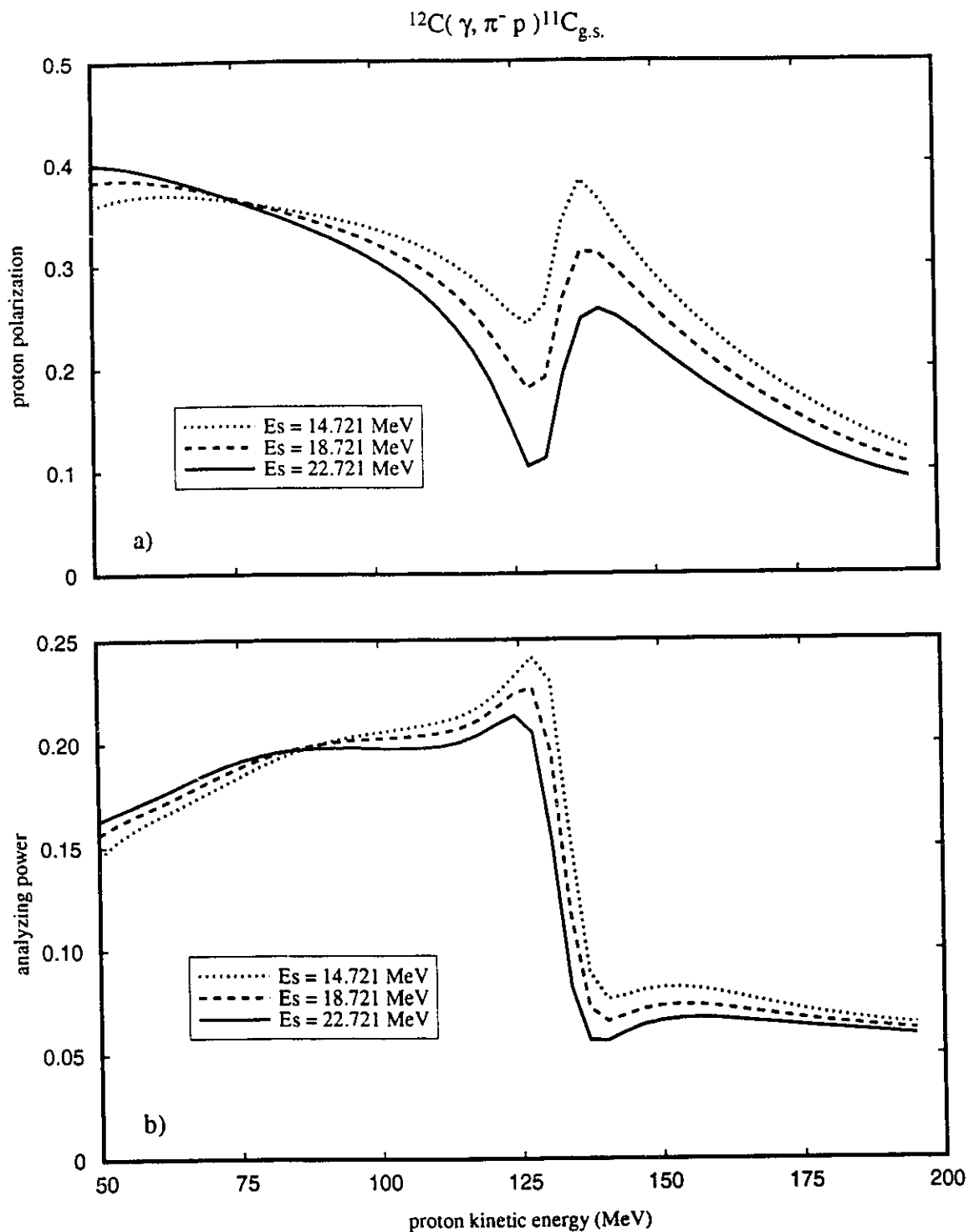


Figure 4-16. Sensitivity of the spin observables to changes in the separation energy of the $1p_{3/2}$ neutron bound state wave function. a) polarization of the final proton and b) analyzing power due to linearly polarized photons. Lines as for figure 4-15.

4.2 Nearly Free Kinematics

Our one nucleon model says that to a good approximation the pion photoproduction reaction occurring in the nucleus actually occurs on a single nucleon with the reaction products being ejected from the nucleus after the reaction occurs, without any significant contribution from other reaction mechanisms. If this picture is indeed valid we should be able to compare the results of our calculations with results of a model for the elementary process somehow, if we chose kinematics such that the momentum transfer to the residual nucleus is small.

The triple differential cross section of the DW is not directly comparable with the differential cross section for the elementary process, but we can in principle integrate the triple cross section over all possible proton energies and angles for a fixed pion angle to get a cross section which we can compare with the results of the elementary process

$$\frac{d\sigma}{d\Omega_\pi} = \int \frac{d\sigma}{d\Omega_\pi d\Omega_p dE_p} d\Omega_p dE_p \quad (4-1)$$

The only difficulty with doing this is the time required to do the numerical integration. The energy distribution of the triple cross section at a particular proton angle pair (θ , ϕ) requires between one and two hours on a Decstation 3100 depending on the accuracy asked for, and integration over the proton angles will require evaluation of the triple cross section over a web of angle pairs. A very coarse web could involve five θ s with five ϕ s at each, so the integration would require between 25 and 50 hours of cpu time per point in order to compare with the results of the elementary process. This is not a practical approach for us to take since to obtain reasonable accuracy would require a finer grid and hence more computer time. Fortunately the spin observables are more directly comparable between the free and the nuclear processes and these we will look at.

The kinematics in the two cases can never be exactly the same but we can force enough similarity that the differences become clear. We will look at three cases corresponding to pion angles of 45° , 90° and 135° in the center of momentum frame for the elementary process. The kinematics of the DW calculation are set so that the lab angles of the detected pion and proton are equal to the lab angles of the pion and proton

resulting from the elementary process. The pion is again placed in the first quadrant of the x-z plane, and the reaction must be coplanar to be consistent with the elementary process. We also force the proton which has been knocked out of the nucleus to have the same energy as the proton resulting from the elementary process. The kinematics of the nuclear process are now fixed and the energy of the pion, as well as the energy and direction of the recoil nucleus, can be calculated from energy and momentum conservation.

We begin by looking at a pion center of momentum angle of 45° for the free process. Figure 4-17 shows how the kinematic quantities change as a function of incident photon energy. Figure 4-17a) shows the proton kinetic energy in the laboratory frame as a function of photon lab energy, and figure 4-17c) shows the pion and proton lab angles as a function of photon energy. These quantities are forced to be the same in the DW calculation as they are for the elementary process. Figure 4-17b) shows the pion energy as a function of the photon energy. The dashed line is the pion energy for the elementary process while the solid line is the pion energy for the reaction on carbon. The kinetic energy of the pion resulting from the reaction on the nucleus is 20 MeV lower than the kinetic energy of the pion from the free process over the whole range of photon energies, because there is less energy available since the reacting neutron is bound by 18.721 MeV. The momentum transfer to the residual nucleus starts off at 0.16 fm^{-1} and quickly drops off to 0.11 fm^{-1} , which translates to the residual nucleus having a kinetic energy of about 0.02 MeV in the lab frame. Under these conditions the proton and pion are getting almost all the available energy in this reaction.

The triple differential cross section for these kinematics is shown in figure 4-18. The dotted curve is the result of the plane wave (PW) calculation of equation (2-98) while the dashed curve is the result of the distorted wave (DW) calculation of equation (2-103) with all the distorting potentials turned off. For these kinematics the two calculations agree quite well but start showing some small differences for photon energies larger than 500 MeV due to a slightly inadequate number of terms in the partial wave series of the DW calculations. The solid curve is the DW calculation using the global A and E dependent potential to distort the proton wave, and the potential of Singham and Tabakin to generate the pion wave function.

The DW cross section calculated from the Born terms alone is shown as the dotted

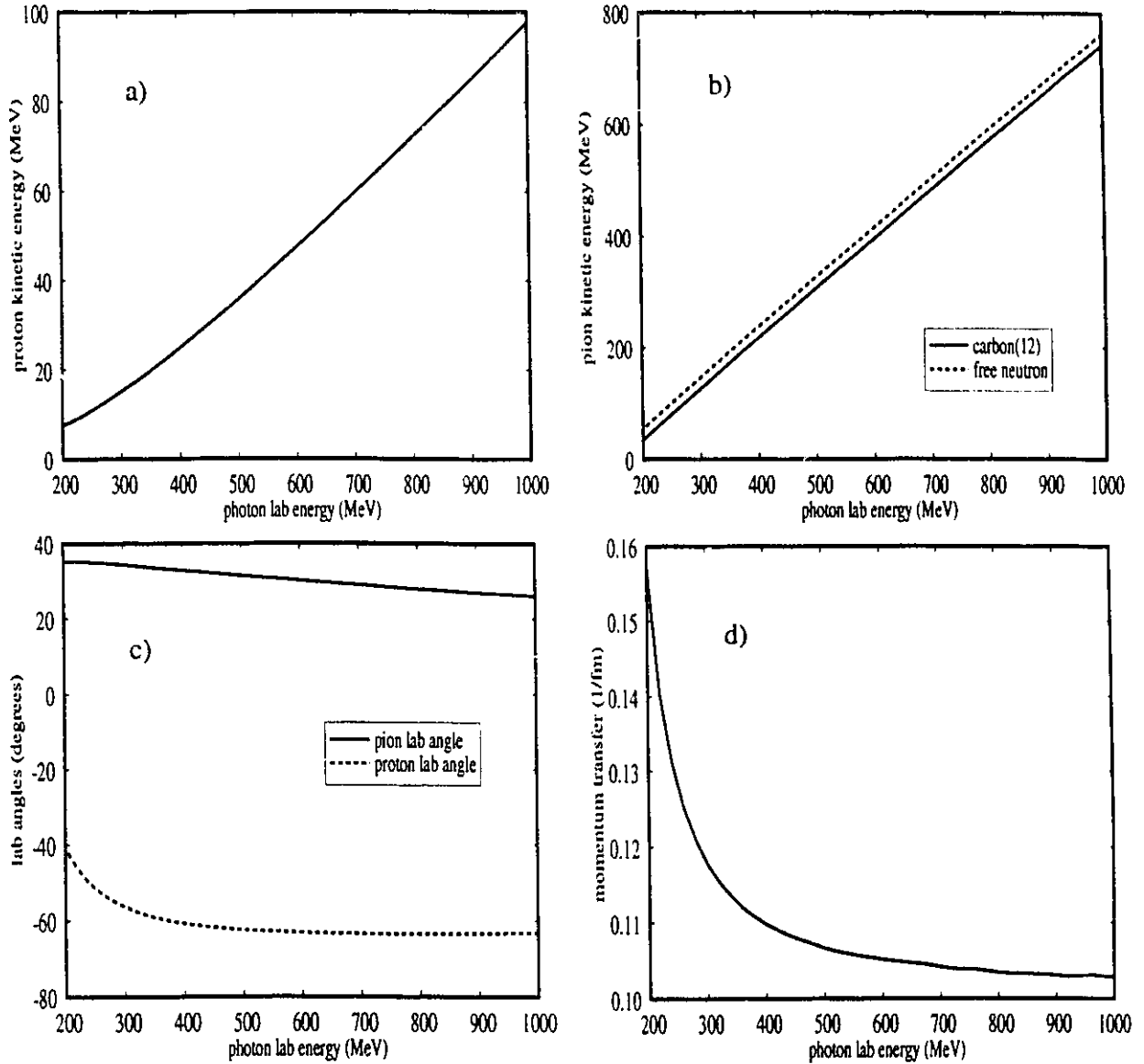
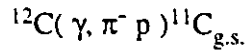


Figure 4-17. Variation in kinematic quantities for nearly free kinematics when the pion angle in the c.m. frame is fixed at $\theta_{\pi} = 45^{\circ}$, for the negative pion photoproduction reaction $^{12}\text{C}(\gamma, \pi^- p)^{11}\text{C}_{\text{g.s.}}$.

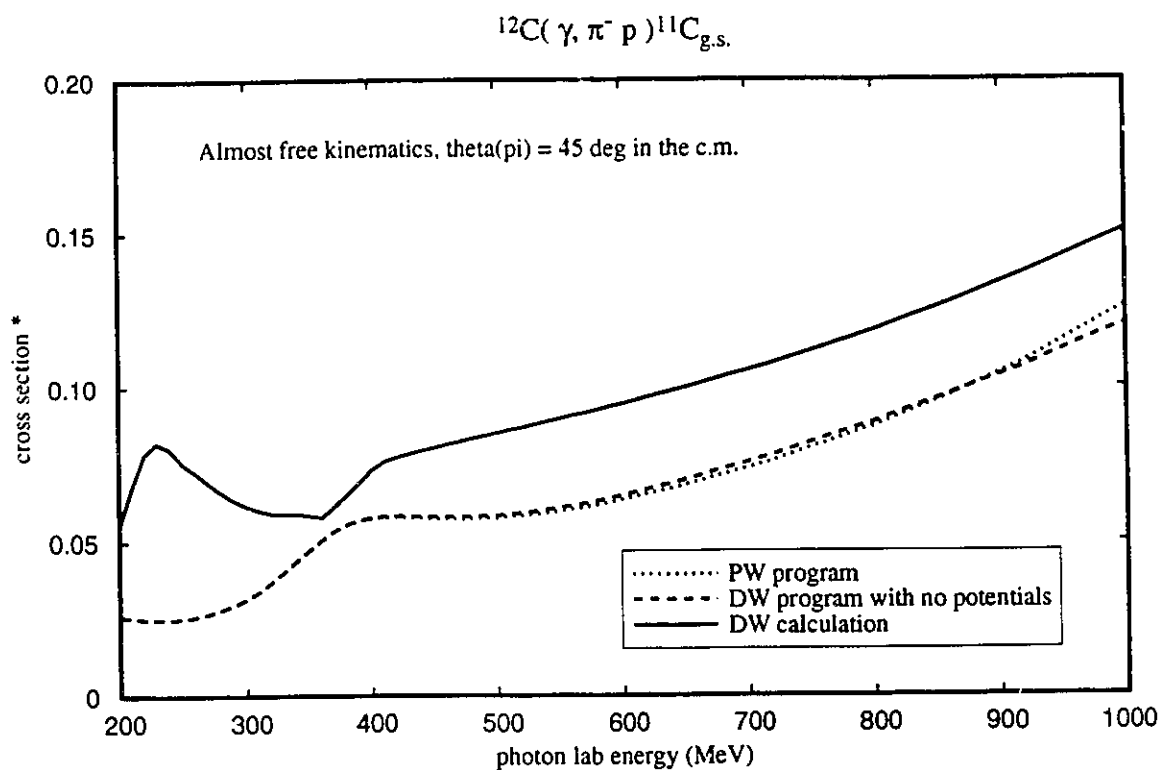


Figure 4-18. The cross section near free kinematics with the pion angle in the c.m. frame: $\theta_{\pi} = 45^{\circ}$. The pion and proton angles are fixed at their free values, as is the kinetic energy of the proton. The energy of the pion is then calculated. Dotted line - PW program. Dashed line - DW program with all distortions turned off. Solid line - DW calculation with the pion distorted by the potential of Singham and Tabakin, and proton distorted by the global A and E dependent potential.

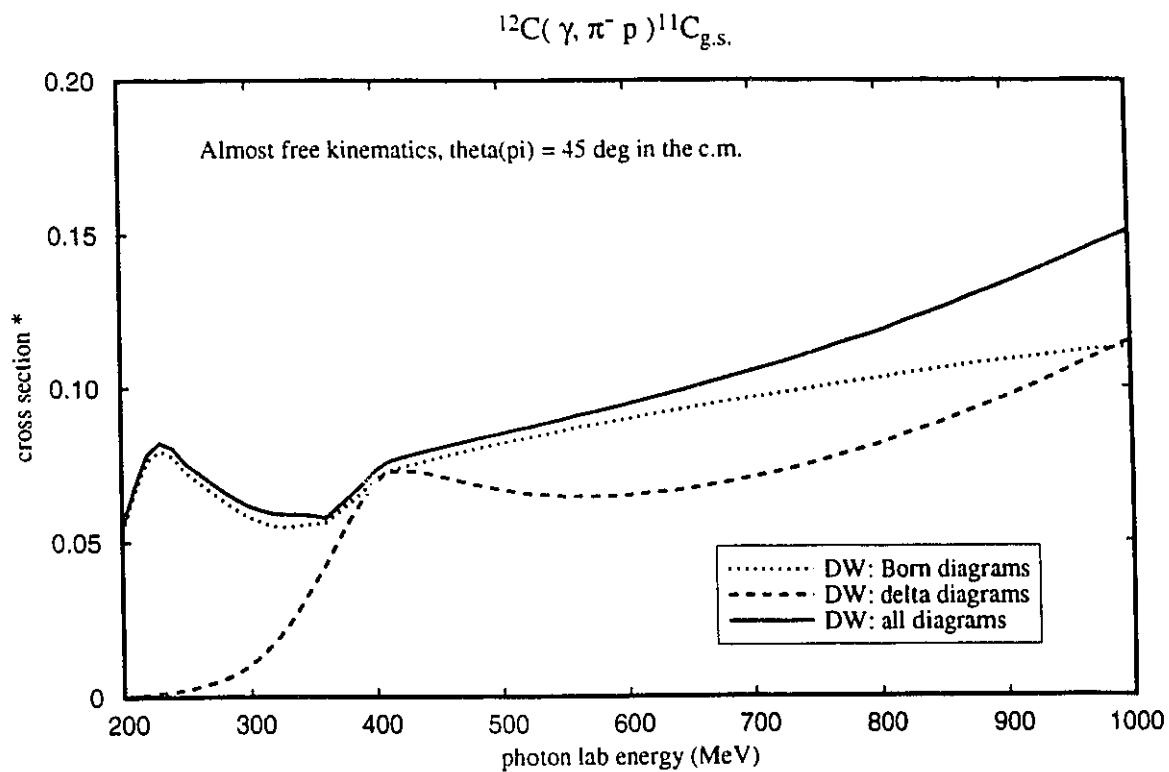


Figure 4-19. DW calculation of the cross section near free kinematics with the pion angle in the c.m. frame: $\theta_{\pi} = 45^{\circ}$, as discussed for figure 4-18.

Dotted line - Cross section calculated from Born terms only.

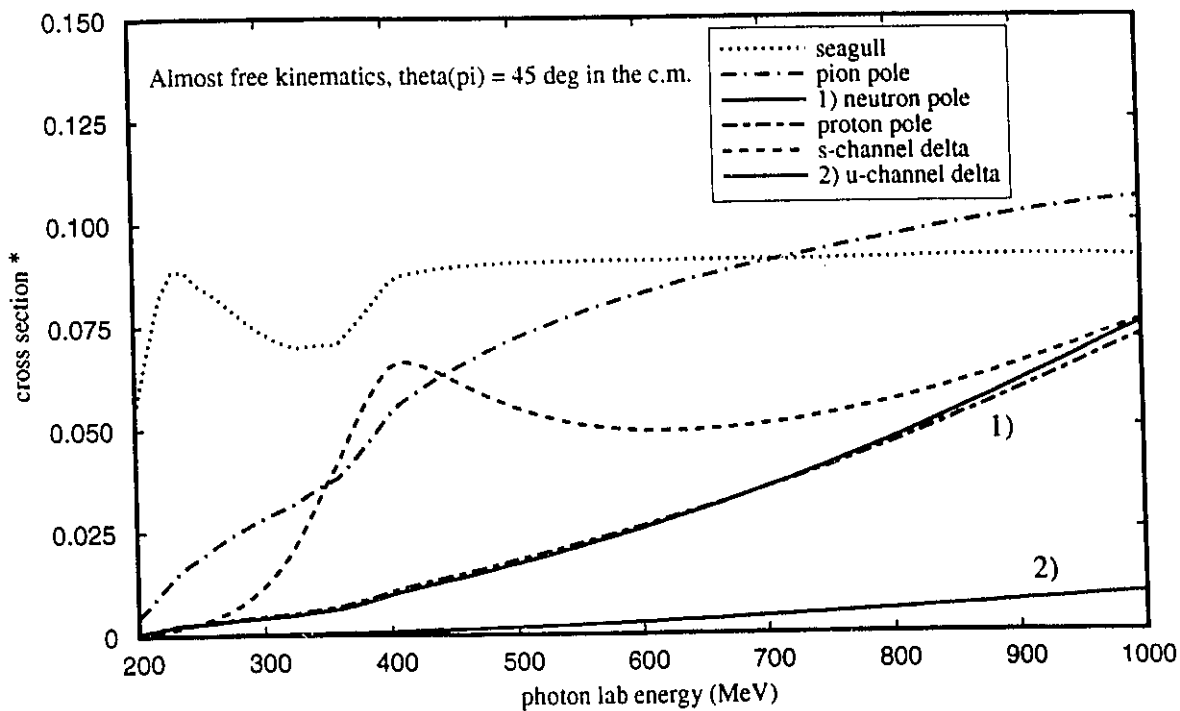
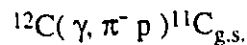
Dashed line - Cross section calculated from delta diagrams only.

Solid line - Cross section calculated from all diagrams.

curve of figure 4-19. The dashed curve shows the cross section calculated from the delta diagrams alone, and the solid curve shows the cross section calculated from the sum of all the diagrams. The cross section from the delta increases rapidly to a photon energy of 400 MeV but the total cross section changes from the cross section calculated from the Born terms by only a few per cent. The delta diagrams begin to influence the total cross section more for photon energies greater than 600 MeV.

The cross sections calculated for each of the contributing diagrams individually is shown in figure 4-20. The dotted line is the cross section calculated from the seagull diagram, and the dashed line is the cross section calculated from the s-channel delta. The dot-dashed curve is due to the pion pole and becomes a significant contributor to the cross section at roughly the same rate that the s-channel delta does below 450 MeV, while above 450 MeV the pion pole is a larger contributor than the s-channel delta, and even becomes larger than the seagull at 700 MeV. The behaviour of the triple cross section in the region of small momentum transfer is dominated by the fact that the bound state wave function for $\ell = 1$ is zero when the momentum transfer is zero. This does not radically change the relative importance of the contributing diagrams as shown in figure 4-20 from the contribution of the various diagrams to the free cross section, although there are some differences due to the different kinematics.

The spin observables are shown in figure 4-21, and this is where we can get a direct comparison between the elementary process and the nuclear reaction. The dot-dashed curve of figure 4-21a) is the polarization of the proton resulting from the free reaction. The dotted curve, which is overlapped by the dashed curve, is the polarization calculated from the PW expression (2-98), and the dashed curve is calculated from the DW expression (2-103) with the distorting potentials turned off. The solid curve is the result of the DW calculation with distorting potentials of figure 4-18 included. The free and plane-wave-nuclear calculations are quite close, which we would expect since the polarization of the proton arises from a complex part of the scattering amplitude, and the only contributing complex quantity is the width of the delta. The full distorted wave calculations include complex contributions from the distorting potentials of both the proton and the pion and for energies beyond 400 MeV the distortions change the polarization significantly from the free value. The polarization of the final proton in the



* cross section $\equiv d\sigma/d\Omega_{\pi} d\Omega_p dE_p$ ($\mu\text{b/sr sr MeV}$)

Figure 4-20. Contribution of each of the diagrams of figure 2-2 in the DW calculation of the cross section near free kinematics, with the pion angle in the c.m. frame: $\theta_{\pi} = 45^{\circ}$, as discussed for figure 4-18.

- Dotted curve - seagull diagram, figure 2-2a).
- Dot-dashed curve - pion pole, figure 2-2b).
- Solid curve 1) - neutron pole figure 2-2d).
- Short-dash long-dash curve - proton pole figure 2-2c).
- Dashed curve - s-channel delta diagram figure 2-2e).
- Solid curve 2) - u-channel delta diagram figure 2-2f).

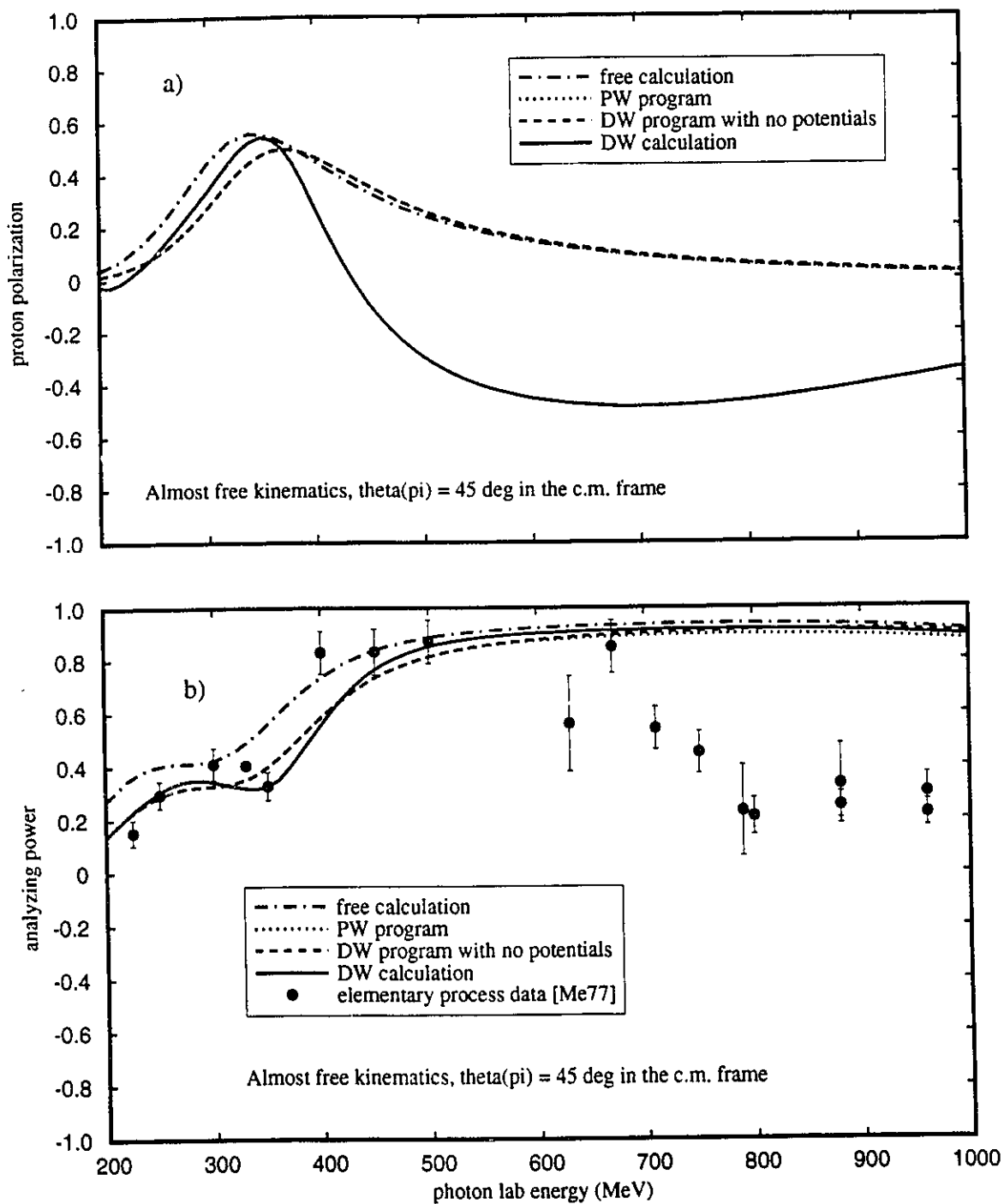
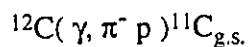


Figure 4-21. Spin observables near free kinematics with $\theta_\pi = 45^\circ$ in the c.m. frame.

Dot-dashed curve - negative pion photoproduction on a free neutron. Other curves as in figure 4-18. a) polarization of the final proton, and b) analyzing power due to linearly polarized photons.

neighbourhood of the delta resonance is nearly the same in all the calculations; the fact that the initial neutron is bound in a nucleus, or that the proton and the pion are interacting with a nucleus in the final state do not change the polarization of the final proton appreciably for photon energies in the range $E_\gamma = 200$ to 400 MeV.

The analyzing power due to linear photon polarization is calculated in figure 4-21b), and the curves are labelled as for the polarization calculations. The nuclear calculations show some shift in energy from the the free calculation for low photon energies and at high energies the calculations all seem to converge. This is an interesting feature of the analyzing power. The data points are from the compilation of free pion photoproduction data of Menze, Pfeil and Wilcke [Me77]. All the calculations seem to be in reasonable agreement with the data for photon energies in the region of the delta resonance. At higher energies other resonances and meson exchanges must be included. We therefore do not expect our present model to describe the data in this energy region.

The important point is that our model is consistent with the free calculations. The free data are described reasonably well by all three calculations in the region of the delta resonance and the free and plane wave calculations show the same behaviour at high energies. When $\theta_\pi = 45^\circ$ in the center of momentum frame, and the momentum transfer is very small, the analyzing power and the polarization of the proton are modified only slightly when the target neutron is part of a nucleus.

We play the same game at two other center of momentum pion angles, namely 90° and 135° . The pion and proton angles, as well as the proton energy are again fixed at the values from the elementary process and the pion energy calculated. The pion energy in both cases is 20 MeV less for the reaction on a nucleus than for the free reaction as can be seen in figures 4-22b) and 4-27b). The momentum transfer to the nucleus is small in both cases and the kinetic energy of the recoil nucleus is well below 0.1 MeV.

The cross section for nearly free kinematics at a free process angle of $\theta_\pi = 90^\circ$ in the center of momentum frame is shown in figure 4-23. the PW calculation (dotted curve) and the DW calculation without distorting potentials (dashed curve) begin to diverge above 650 MeV because of the numerical limitations of our DW program (the calculation needs more proton partial waves for the sums to converge). The addition of distortions

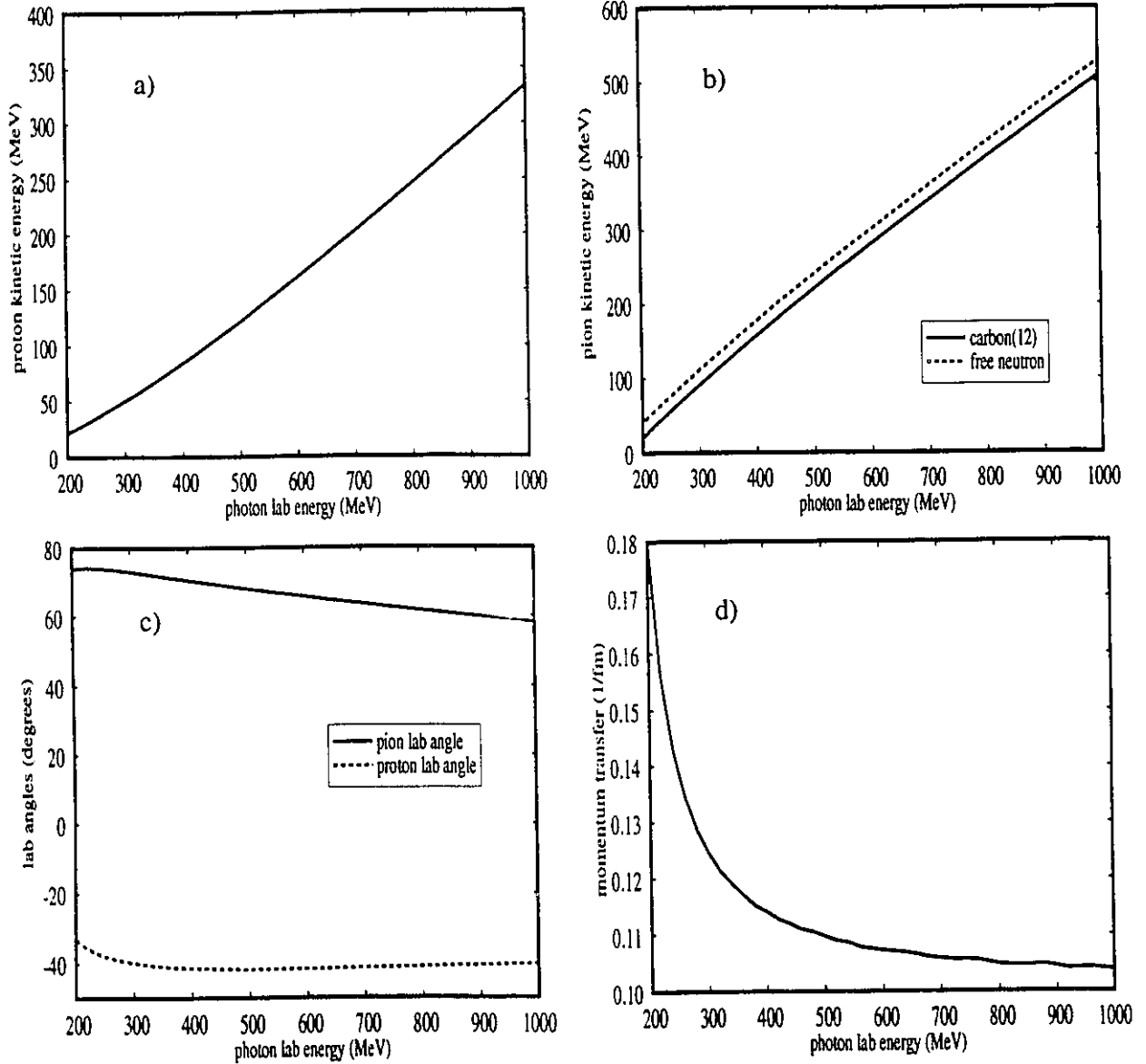
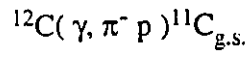


Figure 4-22. Variation in kinematic quantities for nearly free kinematics when the pion angle in the c.m. frame is fixed at $\theta_{\pi} = 90^{\circ}$, for the negative pion photoproduction reaction $^{12}\text{C}(\gamma, \pi^- p)^{11}\text{C}_{\text{g.s.}}$.

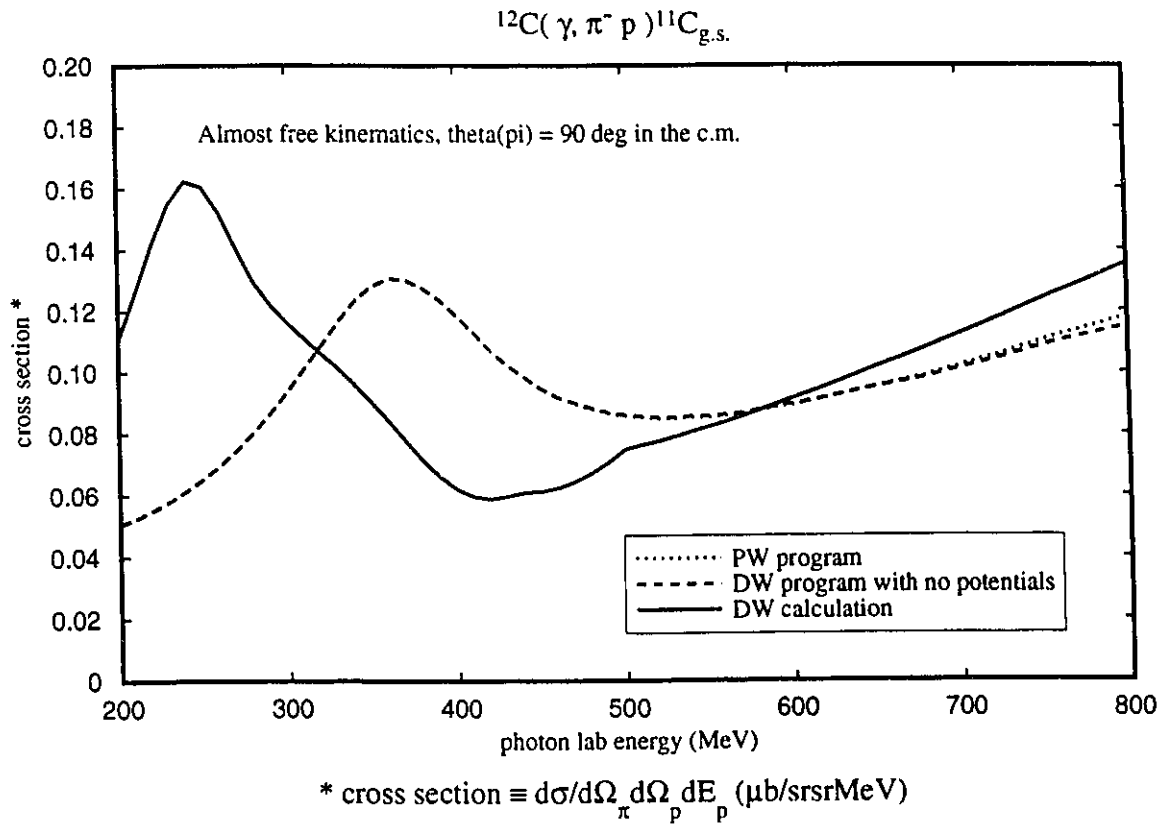


Figure 4-23. The cross section near free kinematics with the pion angle in the c.m. frame: $\theta_{\pi} = 90^{\circ}$. The pion and proton angles are fixed at their free values, as is the kinetic energy of the proton. The energy of the pion is then calculated. Dotted line - PW program. Dashed line - DW program with all distortions turned off. Solid line - DW calculation with the pion distorted by the potential of Singham and Tabakin, and proton distorted by the global A and E dependent potential.

(solid curve) shifts the peak and the minimum toward lower photon energies by 100 MeV. At first sight the peak might be attributed to the delta isobar, however the calculation of the DW cross section due to the Born terms alone (dotted curve of figure 4-24) shows that they are responsible for the peak at 250 MeV. An even more detailed consideration (figure 4-25) shows peaks at 250 MeV in the cross sections calculated from both the seagull diagram (dotted curve) and the pion pole diagram (dot-dashed curve), while the s-channel delta (dashed curve) shows the resonance bump peaking at about 400 MeV. In this kinematic region the amplitudes of the Born terms interfere in such a way that the cross section calculated from the sum of all the diagrams above 400 MeV is less than the cross section calculated from either the Born terms or the delta diagrams alone.

In figure 4-26 we look at the spin observables for a pion center of mass angle of $\theta_\pi = 90^\circ$. As for the $\theta_\pi = 45^\circ$ calculations, the free calculation (dot-dashed curve) and the PW calculation (dotted curve) have close to the same shape but are shifted slightly in photon energy. The PW calculation and the DW calculation without potentials overlap each other. Even though the cross section calculations in PW and DW diverge for photon energies above 650 MeV, the sums are sufficiently converged for the spin observable calculations. The inclusion of distortions for the pion and proton (solid curve) does not change the proton polarization much in the delta region, but causes a significant change away from the free calculation above 400 MeV. We show data for both the free reaction [Me77] and the reaction on ^{12}C [Go71]. Our free model doesn't agree with the free data, which isn't surprising since there are many resonances above 400 MeV which we have not included in the model. Also the free data agree with the nuclear data so the important processes should be the same. Therefore the fact that our polarization calculation seems to agree with the data above 400 MeV is purely an accident and other resonances and meson exchanges must be included before we can claim to describe the data.

The addition of distortions in the analyzing power calculation of figure 4-26b) damps the analyzing power from the free value through the delta region between 300 MeV to 400 MeV. All the calculations converge above 500 MeV. Note that the PW calculation and the DW calculation without potentials diverge slightly above 800 MeV, but are still very close.

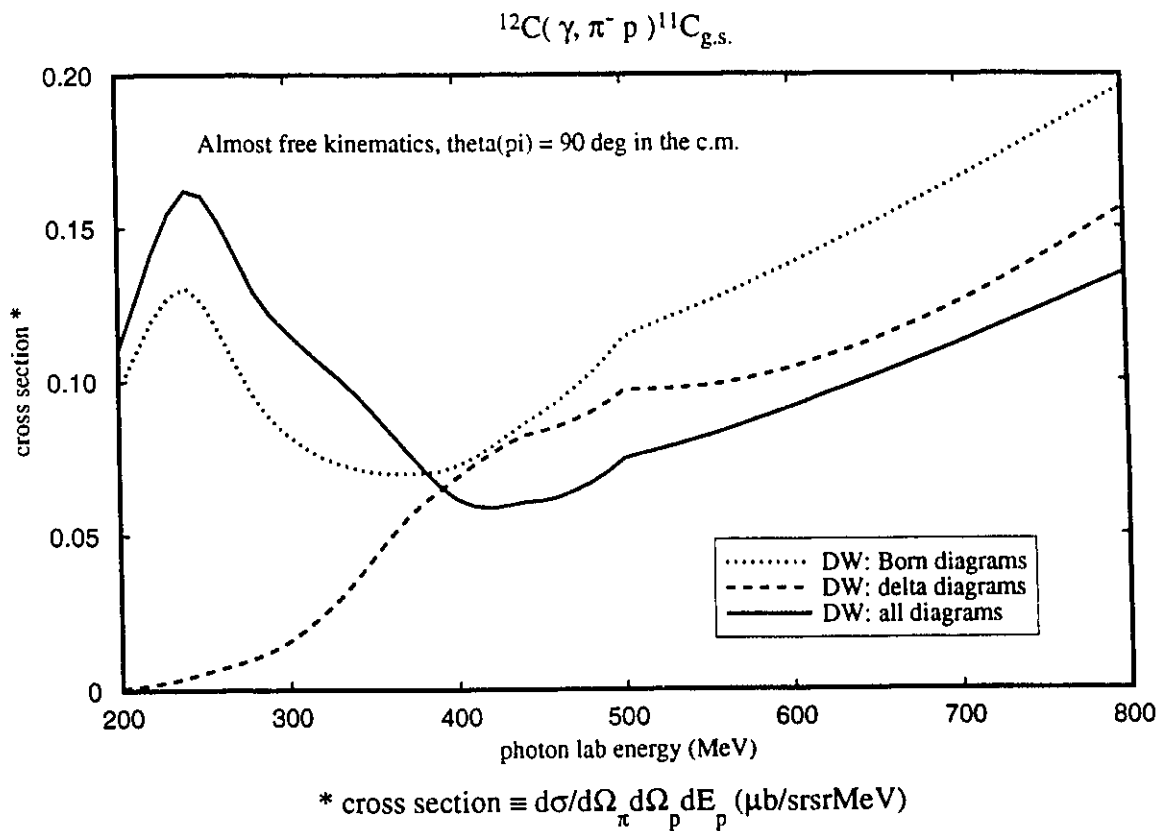


Figure 4-24. DW calculation of the cross section near free kinematics with the pion angle in the c.m. frame: $\theta_{\pi} = 90^{\circ}$, as discussed for figure 4-23.

- Dotted line - Cross section calculated from Born terms only.
- Dashed line - Cross section calculated from delta diagrams only.
- Solid line - Cross section calculated from all diagrams.

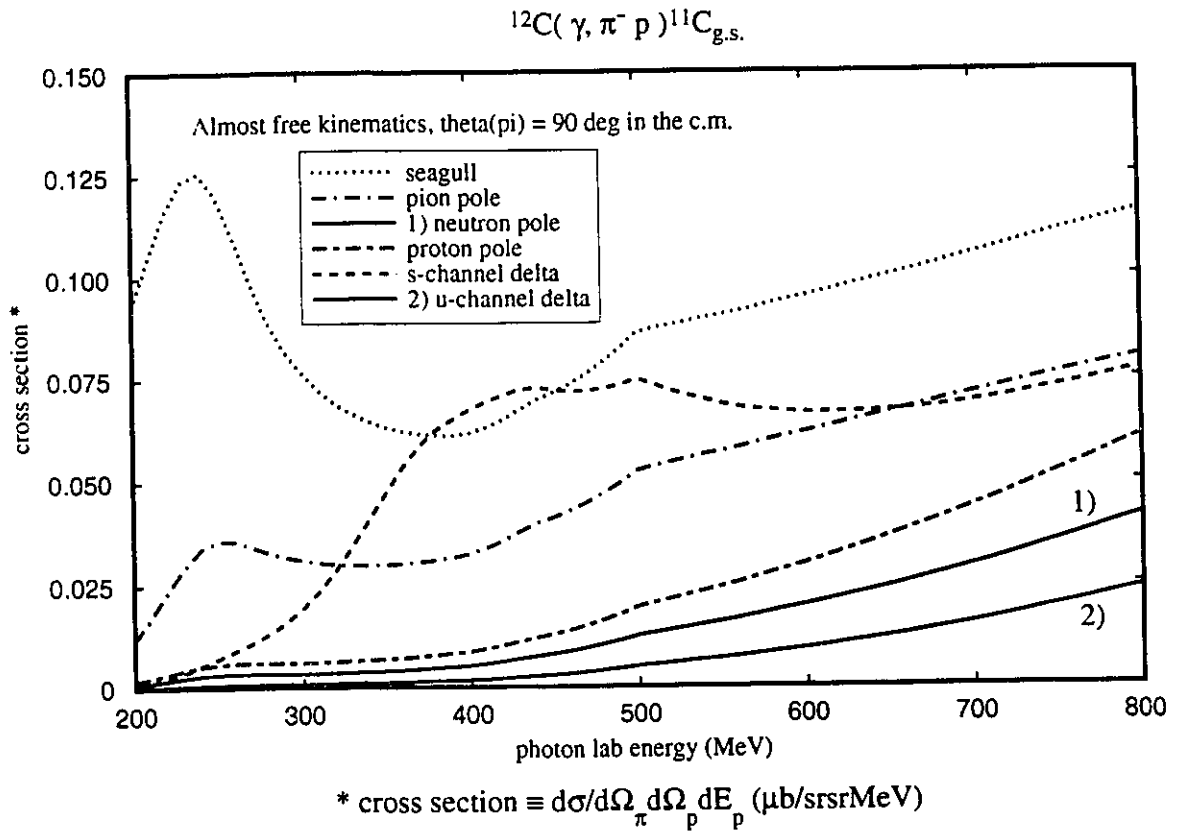


Figure 4-25. Contribution of each of the diagrams of figure 2-2 in the DW calculation of the cross section near free kinematics, with the pion angle in the c.m. frame: $\theta_{\pi} = 90^{\circ}$, as discussed for figure 4-23.

- Dotted curve - seagull diagram, figure 2-2a).
- Dot-dashed curve - pion pole, figure 2-2b).
- Solid curve 1) - neutron pole figure 2-2d).
- Short-dash long-dash curve - proton pole figure 2-2c).
- Dashed curve - s-channel delta diagram figure 2-2e).
- Solid curve 2) - u-channel delta diagram figure 2-2f).

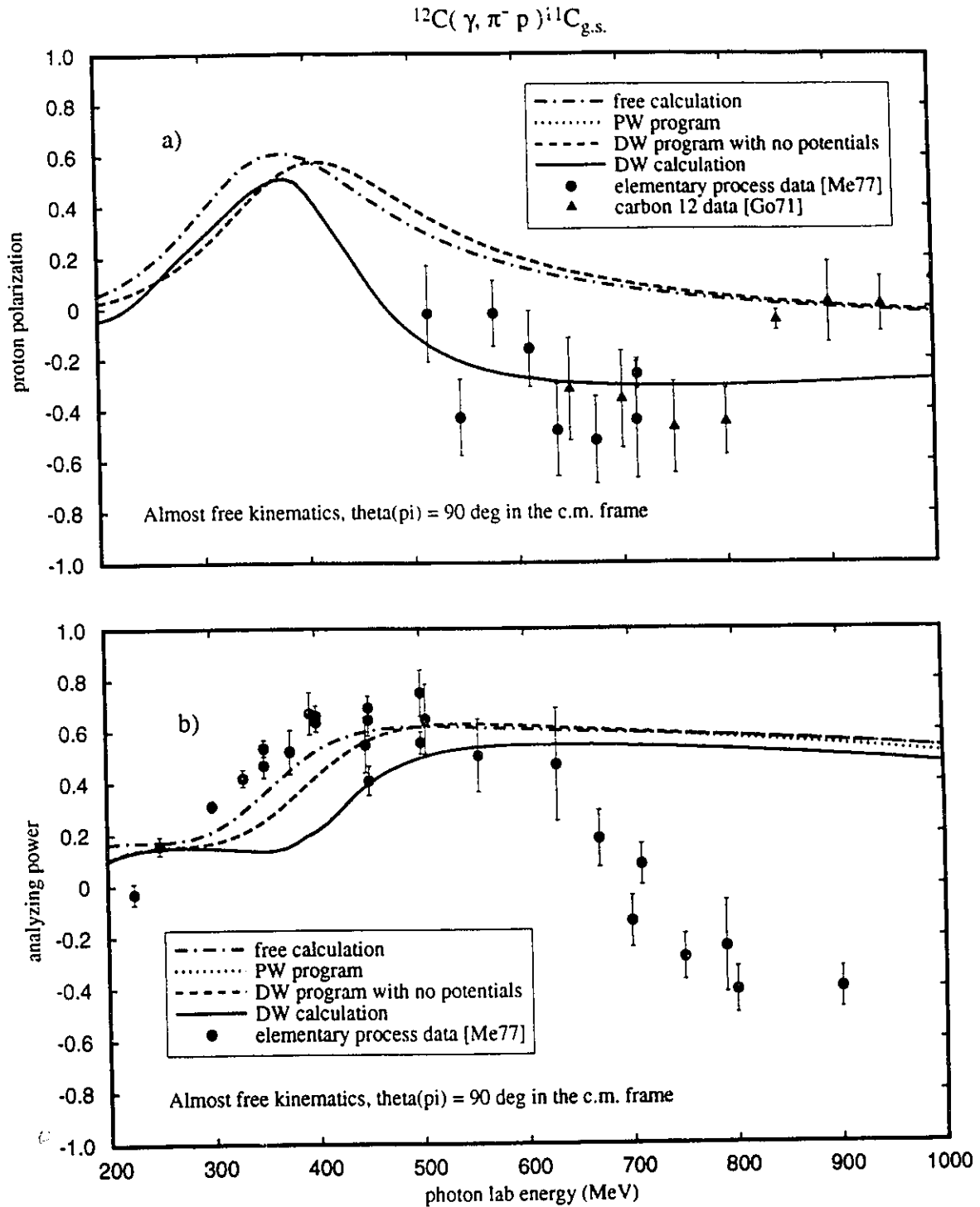


Figure 4-26. Spin observables near free kinematics with $\theta_{\pi} = 90^{\circ}$ in the c.m. frame.

Dot-dashed curve - negative pion photoproduction on a free neutron. Other curves as in figure 4-23. a) polarization of the final proton, and b) analyzing power due to linearly polarized photons.

The last nearly free situation we consider has $\theta_\pi = 135^\circ$ in the center of momentum frame. The cross section as a function of photon energy is shown in figure 4-28. The PW calculation (dotted curve) and the DW calculation without potentials (dashed curve) now diverge at 450 MeV. The pronounced peak in the PW calculation at 350 MeV is shifted to 250 MeV when the pion and proton distortions are turned on (solid curve). We calculate the cross section due to the Born diagrams and the delta diagrams separately in figure 4-29. The peak is due to the Born terms (dotted curve), while the cross section due to delta diagrams (dashed curve) is monotonically increasing, showing no resonance peak at all. Calculation of the cross section due to the individual diagrams, as shown in figure 4-30, shows that the seagull diagram is the dominant contributor and the other diagrams, including the s-channel delta, have become much less important for low photon energies than at $\theta_\pi = 90^\circ$.

The spin observables are shown in figure 4-31. The free calculations and the PW show similar behaviour except for a shift in photon energy. The PW and DW without distorting potentials overlap each other once again, even though the differences in the cross section calculation are large at this pion angle. The addition of pion and proton distortions causes the proton polarization to become 0.2 to 0.3 more negative than in the free or PW calculations. The addition of distortions in the analyzing power calculation causes the analyzing power to become very close to zero from a value of 0.2 at 400 MeV, but at high photon energies all the calculations converge.

In this section we have seen that a PW calculation of pion photoproduction on a nucleus is consistent with a model for the elementary process, and agrees with the free data reasonably well. For these kinematics the picture of the reaction taking place on a single neutron in the nucleus with minor modifications due to binding seems to be valid. The interaction of the final state pion and proton with the residual nucleus does not change the polarization of the proton appreciably near the isobar region, but above 400 MeV the polarization becomes significantly more negative than the free reaction model predicts. The analyzing powers predicted by the three calculations are very close at high photon energies. In the delta region the three calculations yield analyzing powers which are very similar for $\theta_\pi = 45^\circ$, are shifted by about 70 MeV at $\theta_\pi = 90^\circ$ and even have a

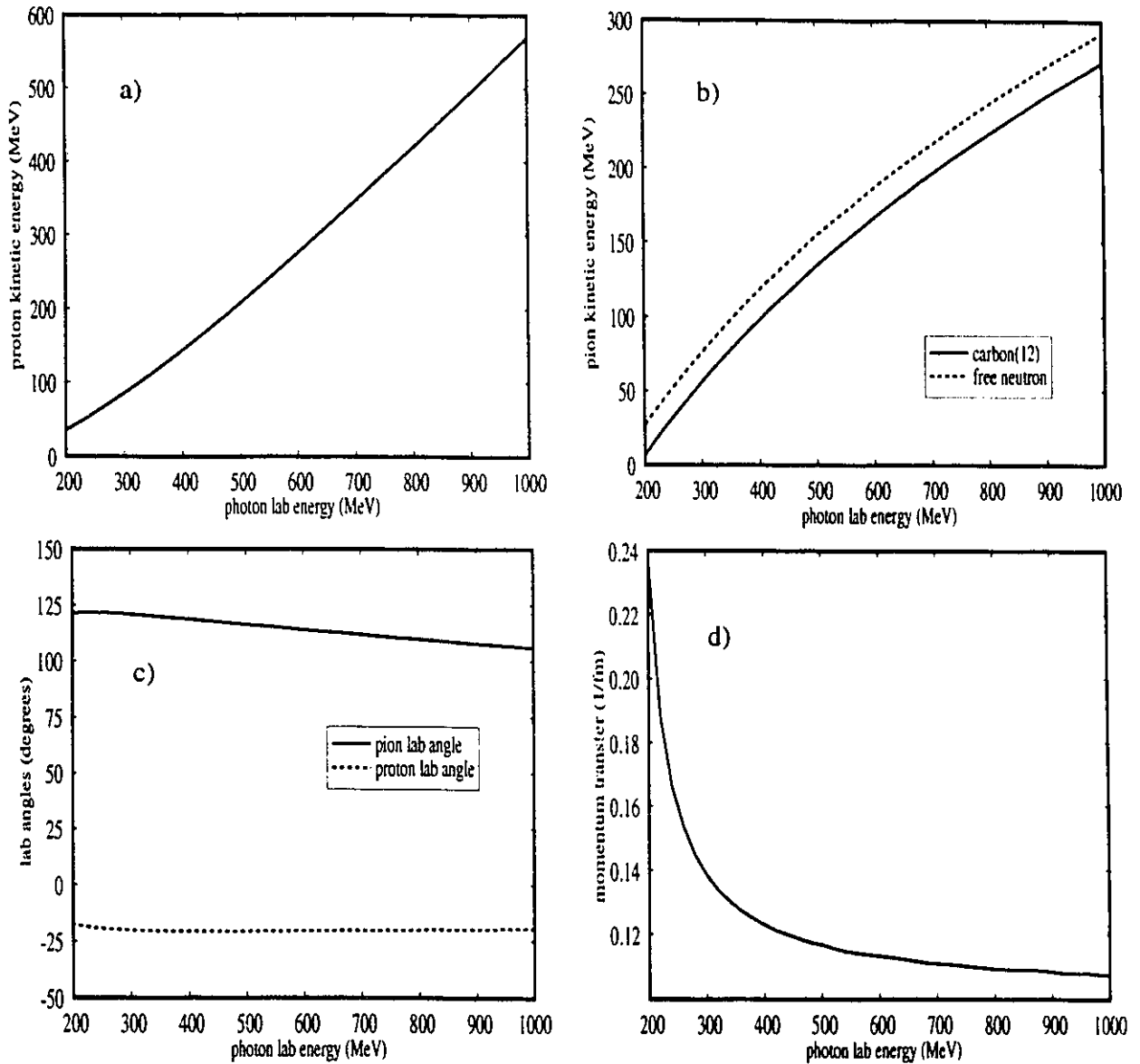
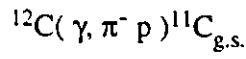
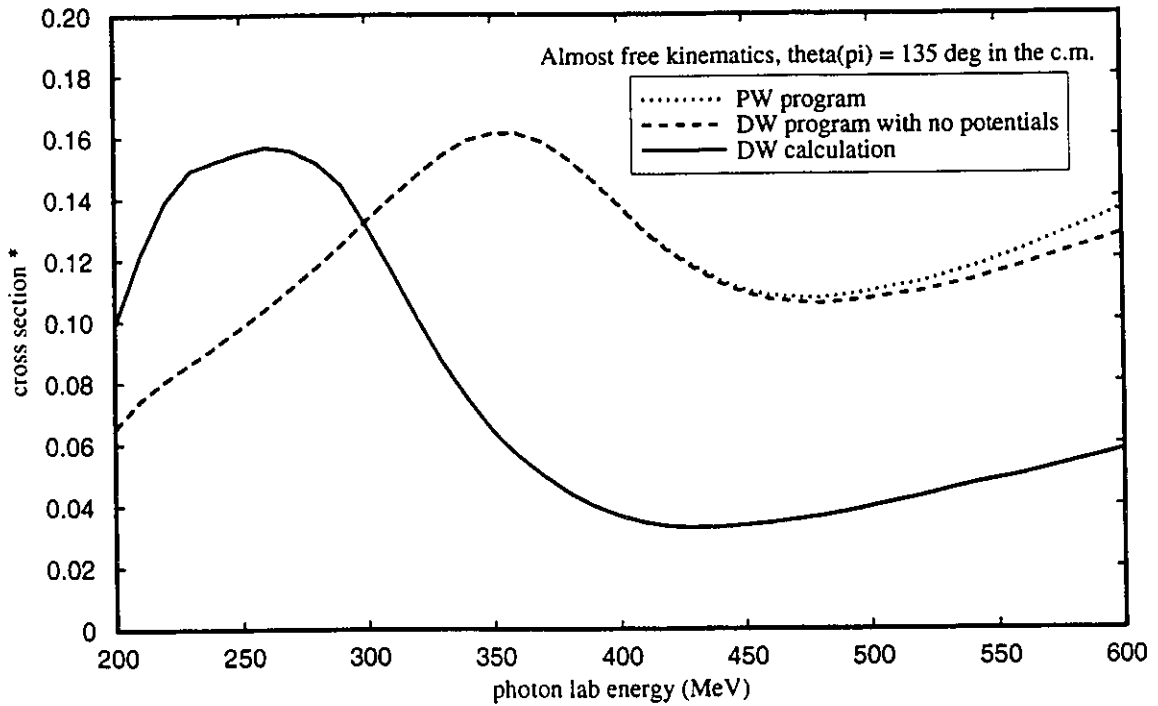
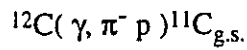


Figure 4-27. Variation in kinematic quantities for nearly free kinematics when the pion angle in the c.m. frame is fixed at $\theta_{\pi} = 135^{\circ}$, for the negative pion photoproduction reaction $^{12}\text{C}(\gamma, \pi^- p)^{11}\text{C}_{\text{g.s.}}$.



* cross section $\equiv d\sigma/d\Omega_{\pi} d\Omega_p dE_p$ ($\mu\text{b/sr sr MeV}$)

Figure 4-28. The cross section near free kinematics with the pion angle in the c.m. frame: $\theta_{\pi} = 135^{\circ}$. The pion and proton angles are fixed at their free values, as is the kinetic energy of the proton. The energy of the pion is then calculated. Dotted line - PW program. Dashed line - DW program with all distortions turned off. Solid line - DW calculation with the pion distorted by the potential of Singham and Tabakin, and proton distorted by the global A and E dependent potential.

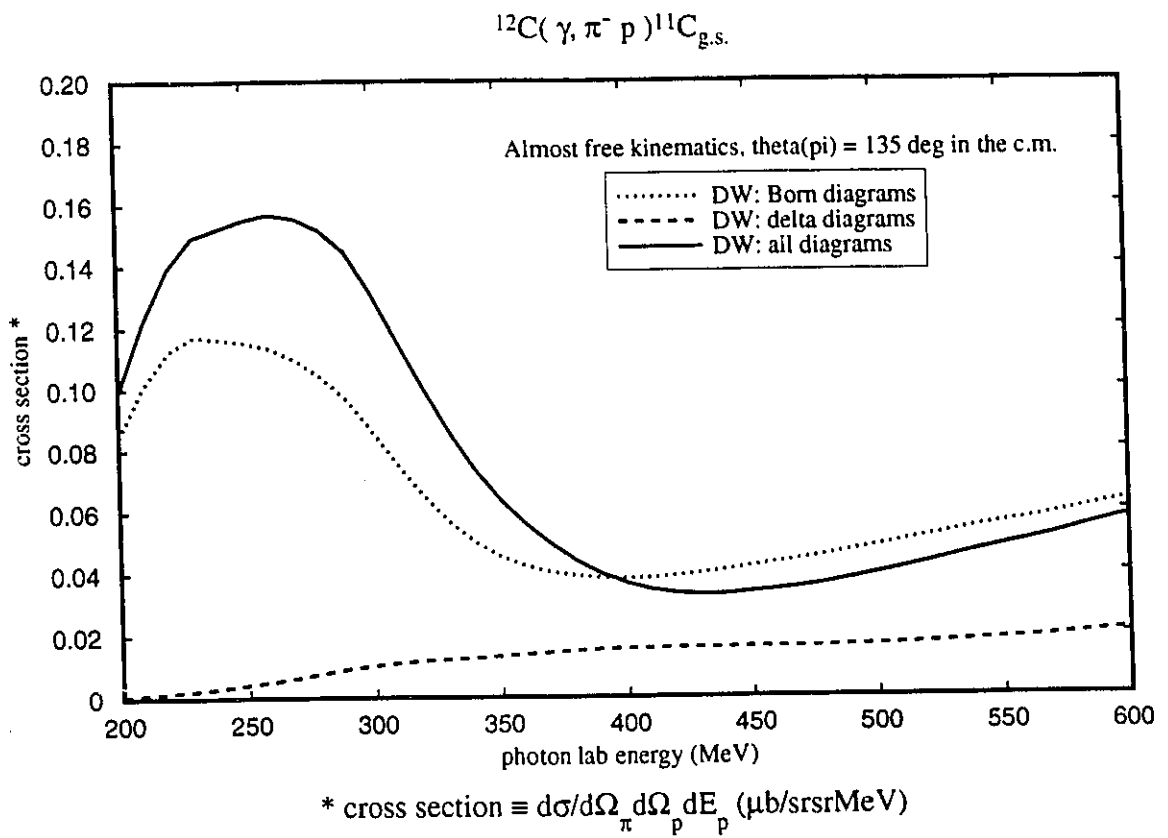


Figure 4-29. DW calculation of the cross section near free kinematics with the pion angle in the c.m. frame: $\theta_{\pi} = 135^{\circ}$, as discussed for figure 4-28.

Dotted line - Cross section calculated from Born terms only.

Dashed line - Cross section calculated from delta diagrams only.

Solid line - Cross section calculated from all diagrams.

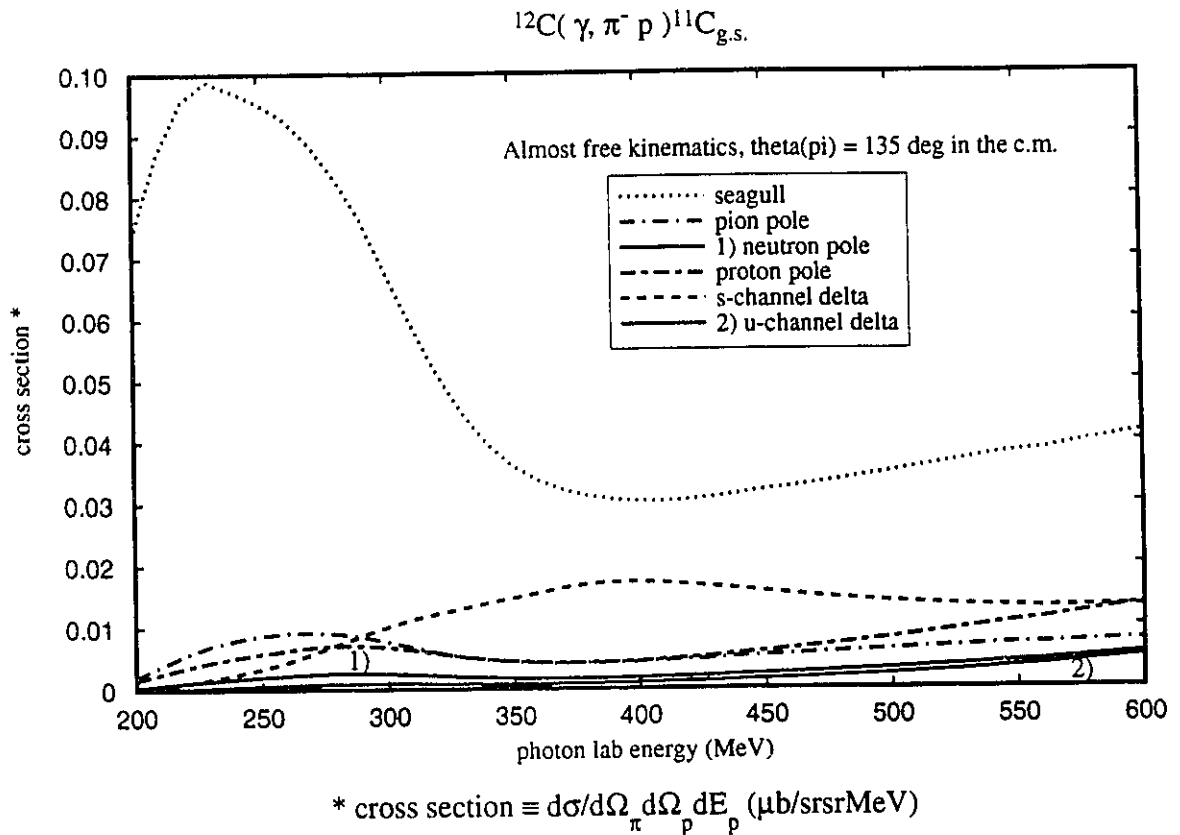


Figure 4-30. Contribution of each of the diagrams of figure 2-2 in the DW calculation of the cross section near free kinematics, with the pion angle in the c.m. frame: $\theta_{\pi} = 135^{\circ}$, as discussed for figure 4-28.

- Dotted curve - seagull diagram, figure 2-2a).
- Dot-dashed curve - pion pole, figure 2-2b).
- Solid curve 1) - neutron pole figure 2-2d).
- Short-dash long-dash curve - proton pole figure 2-2c).
- Dashed curve - s-channel delta diagram figure 2-2e).
- Solid curve 2) - u-channel delta diagram figure 2-2f).

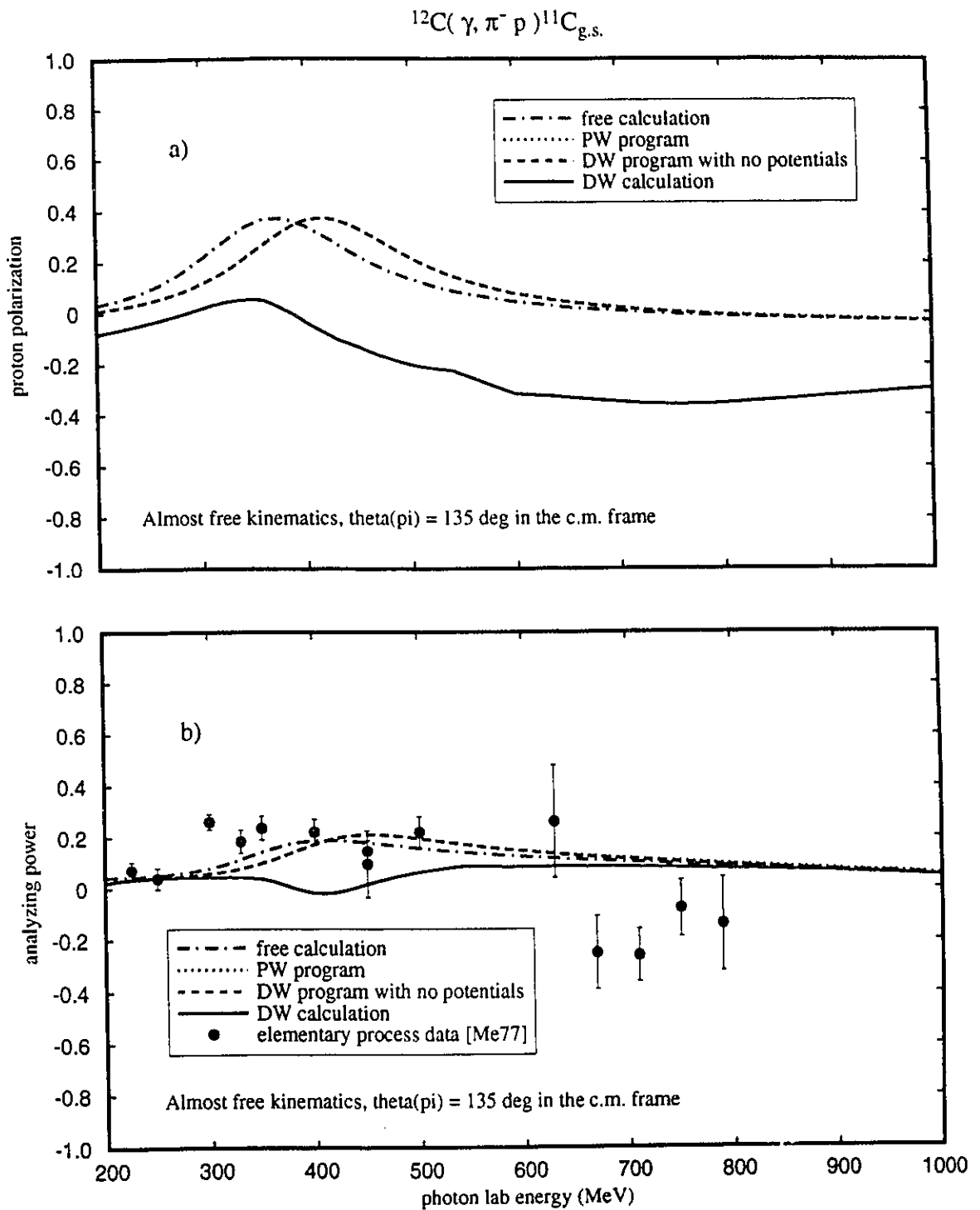


Figure 4-31. Spin observables near free kinematics with $\theta_{\pi} = 135^{\circ}$ in the c.m. frame.

Dot-dashed curve - negative pion photoproduction on a free neutron. Other curves as in figure 4-28. a) polarization of the final proton, and b) analyzing power due to linearly polarized photons.

different shape at $\theta_\pi = 135^\circ$, indicating that the distortions are having a more pronounced effect at larger pion angles.

The polarization of the final proton calculated from the DW model, when the neutron is bound in the nucleus, is not significantly different from that of the proton resulting from the elementary process for pion angles of $\theta_\pi = 45^\circ$ and $\theta_\pi = 90^\circ$ in the region of the delta resonance. At $\theta_\pi = 135^\circ$ a proton polarization from the elementary process of 0.2 is reduced to almost zero when the neutron is bound. The polarization of the proton therefore doesn't seem to be very interesting in this kinematic region. At $\theta_\pi = 45^\circ$ the analyzing power also shows only a small difference in results between having a free or a bound neutron. At $\theta_\pi = 90^\circ$ however the the analyzing power at $E_\gamma = 400$ MeV has been reduced from 0.6 for the free neutron to 0.2 for the bound neutron, and judging from the error bars on the data this is clearly a measurable change.

The important point is that our model is consistent with the free calculation when the momentum transfer to the residual nucleus is small. The free data are described reasonably well by all three calculations in the region of the delta resonance. The free and PW calculations show very similar behaviour at all energies except for a shift in the photon energy due to the different kinematics of the bound and free neutron. This is exactly what we would expect because the ingredients in the two calculations are the same except for the modification of the energy of the bound neutron through binding. Thus our model has really incorporated the elementary process into a reaction in a nucleus. The question of the range of validity of this model can only be answered through comparison with experimental data, which we will do later in the chapter.

We also note that the relative importance of the various diagrams is dependent on the kinematics considered. The seagull diagram is the dominant contributor at small photon energies and even around the delta region, when the photon has an energy in the range 300 MeV to 400 MeV, the seagull diagram is comparable in its contribution to the s-channel delta when the center of momentum pion angle is $\theta_\pi = 90^\circ$, as we see in figure 4-25, and remains slightly greater than the s-channel delta when the pion angle is either $\theta_\pi = 45^\circ$ or 135° . The pion pole diagram can also be a significant contributor, as we see in figure 4-20 for a pion center of momentum angle of $\theta_\pi = 45^\circ$, where the pion pole is actually larger than the s-channel delta everywhere except around 400 MeV. Of course

the situation is not that simple to interpret since we do not add the cross sections calculated from the individual diagrams, but must add the amplitudes and then calculate the observables. The interference between the various amplitudes thus makes it difficult to give credit to a specific process or diagram for the results obtained. The best we can do is try to include everything essential to the process until we have a complete description, in agreement with experiment.

4.3 Behaviour Under Kinematic Changes

We now examine the question of how the model behaves under different kinematic conditions. In particular we vary the incident photon energy while holding the pion and proton angles constant and then hold the photon energy fixed while changing the proton and pion angles. The pion wave function is distorted through the potential of Oset while the proton distortion is the global A and E dependent fit of Cooper et al. [Co92]. The bound state potential is the Woods-Saxon parametrization of table 3-1. We consider a photon incident on a ^{12}C nucleus and the residual ^{11}C is left in its ground state.

First we look at the effect of increasing the energy of the incident photon while holding the angles at which we detect the proton and the pion constant at ($\theta_p = 20^\circ$, $\phi_p = 180^\circ$) and ($\theta_\pi = 120^\circ$, $\phi_\pi = 180^\circ$). The cross sections calculated for incident photon energies ranging from $E_\gamma = 220$ MeV to $E_\gamma = 420$ MeV in steps of 40 MeV are shown in figures 4-32 to 4-34. The dotted line in each graph shows the cross section calculated from the Born terms alone while the dashed line shows the cross section calculated from the delta diagrams only. The solid line is the cross section calculated from the sum of all the diagrams included in our model. In figure 4-32a) the incident photon energy is $E_\gamma = 220$ MeV and the cross section from the delta diagrams alone is only a few per cent of the cross section calculated from the Born terms. Even at this relatively low energy however, the interference between the Born and delta diagrams causes the total cross section to be twenty to twenty-five per cent larger than the cross section due to the Born terms alone. At an incident photon energy of $E_\gamma = 260$ MeV (figure 4-32b) the cross section calculated from the delta diagrams alone is still only fifteen per cent of the cross section due to the

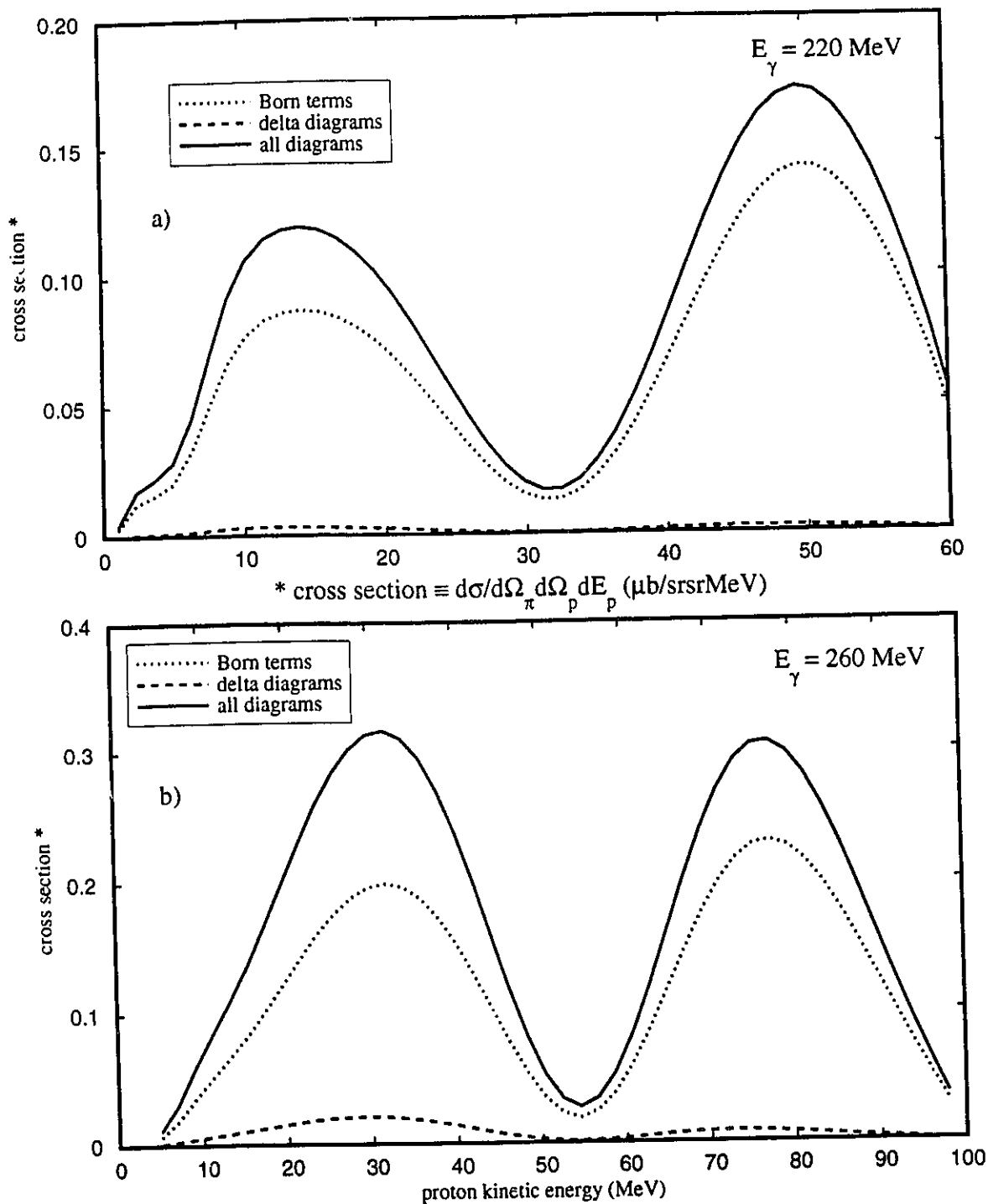
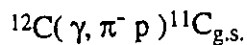


Figure 4-32. Born and delta diagram contributions to the cross section. The kinematic conditions are: $(\theta_p = 20^\circ, \varphi_p = 180^\circ)$ and $(\theta_\pi = 120^\circ, \varphi_\pi = 0^\circ)$. a) photon energy is $E_\gamma = 220 \text{ MeV}$, b) photon energy is $E_\gamma = 260 \text{ MeV}$.

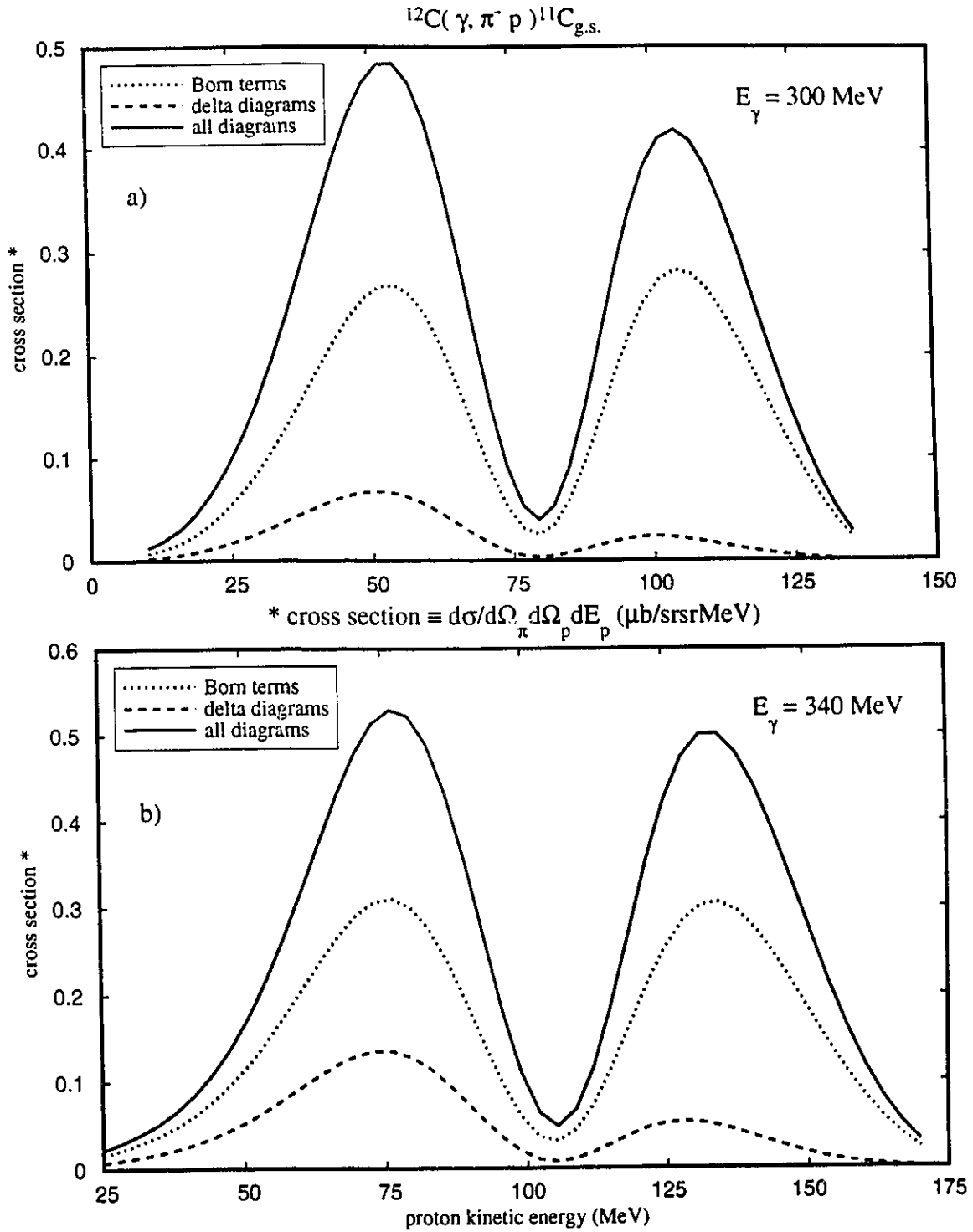


Figure 4-33. Born and delta diagram contributions to the cross section. The kinematic conditions are: $(\theta_p = 20^\circ, \varphi_p = 180^\circ)$ and $(\theta_\pi = 120^\circ, \varphi_\pi = 0^\circ)$. a) photon energy is $E_\gamma = 300 \text{ MeV}$, b) photon energy is $E_\gamma = 340 \text{ MeV}$.

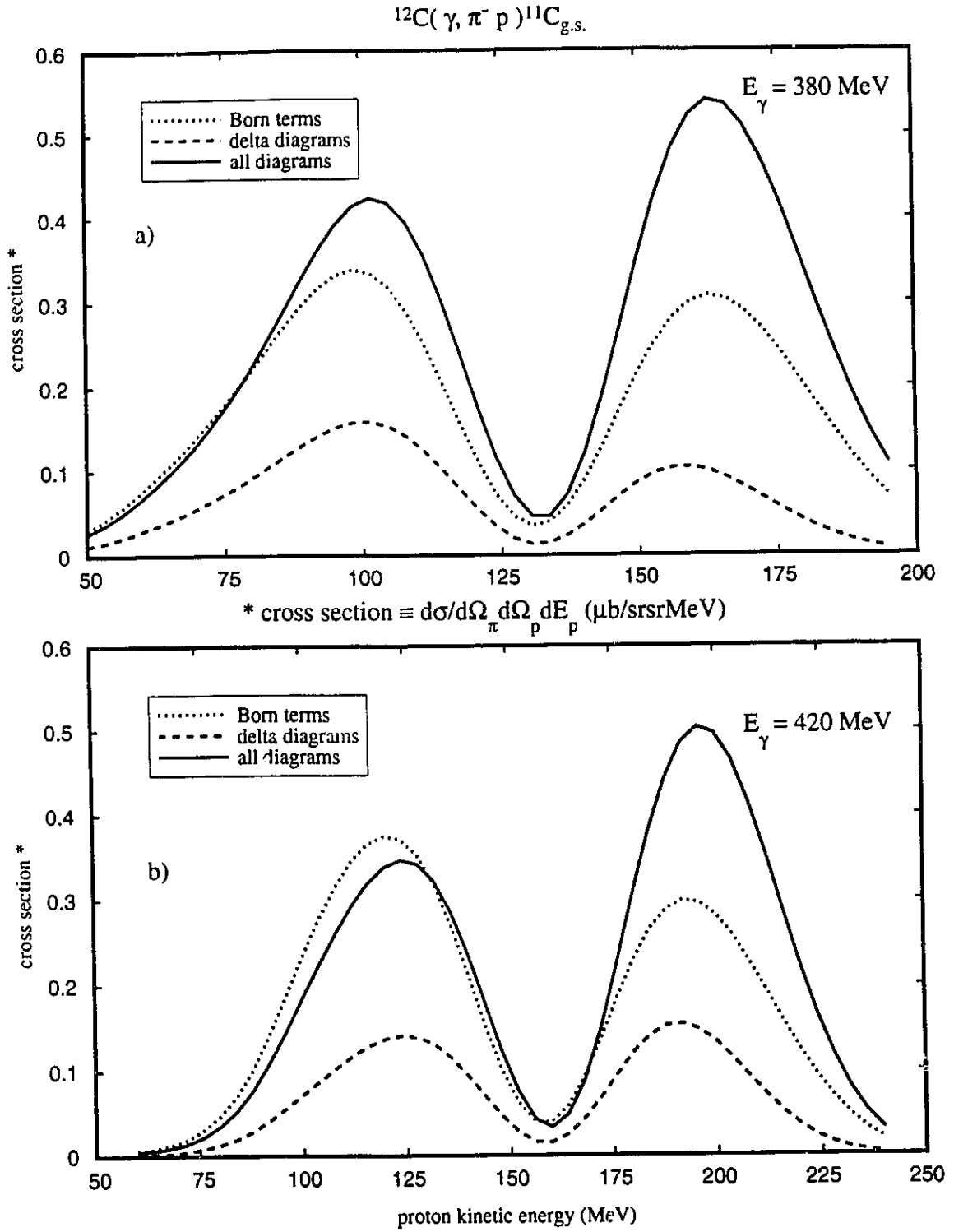


Figure 4-34. Born and delta diagram contributions to the cross section. The kinematic conditions are: $(\theta_p = 20^\circ, \phi_p = 180^\circ)$ and $(\theta_\pi = 120^\circ, \phi_\pi = 0^\circ)$. a) photon energy is $E_\gamma = 380 \text{ MeV}$, b) photon energy is $E_\gamma = 420 \text{ MeV}$.

Born terms but the total cross section is about fifty per cent larger than the cross section calculated from the Born terms alone. At $E_\gamma = 300$ MeV the delta cross section is up to one third that of the Born cross section while the total cross section is almost double that of the Born cross section. Past this photon energy the magnitude of the cross section calculated from the delta diagrams continues to increase relative to the Born cross section but the magnitude of the total cross section decreases relative to the Born cross section, until at $E_\gamma = 420$ MeV the delta actually makes the total cross section slightly smaller than the cross section calculated from the Born terms alone for some proton energies. The contribution of the delta resonance to the total cross section is most important at a photon energy of approximately $E_\gamma = 300$ -350 MeV, but even at 220 MeV the effect should be detectable experimentally.

The calculation of the spin observables of equations (2-114) and (2-115), the proton polarization and analyzing power respectively, involves a numerator calculated from the t-matrix and a denominator which gives the cross section calculated from that t-matrix. Calculation of spin observables in this fashion does not indicate the relative importance of the various diagrams, so we take as the denominator the total cross section calculated from the sum of all the contributing diagrams. This provides us with an indication of the relative importance of the terms we are trying to compare.

In figures 4-35 to 4-40 we show the polarization of the final proton and the analyzing power for six incident photon energies covering the range $E_\gamma = 220$ MeV to $E_\gamma = 420$ MeV in steps of 40 MeV. The delta terms by themselves contribute only marginally to the polarization of the proton and the analyzing power at incident photon energies of $E_\gamma = 220$ and 260 MeV, figures 4-35 and 4-36. At $E_\gamma = 300$ MeV (figure 4-37) the proton polarization calculated from the Born terms is generally slightly negative and the addition of the delta diagrams brings the polarization to a positive value between 0.1 and 0.2. At $E_\gamma = 340, 380$ and 420 MeV, figures 4-38, 4-39 and 4-40, the proton polarization shows the most sensitivity to the addition of the delta. For these energies the delta diagrams can contribute to a proton polarization of more than 0.3. Using the Born terms only results in the proton polarization being generally small and negative over the photon energy range from 220 MeV to 420 MeV, with a rapid change as the momentum transfer to the nucleus passes through zero. The delta contribution to the polarization

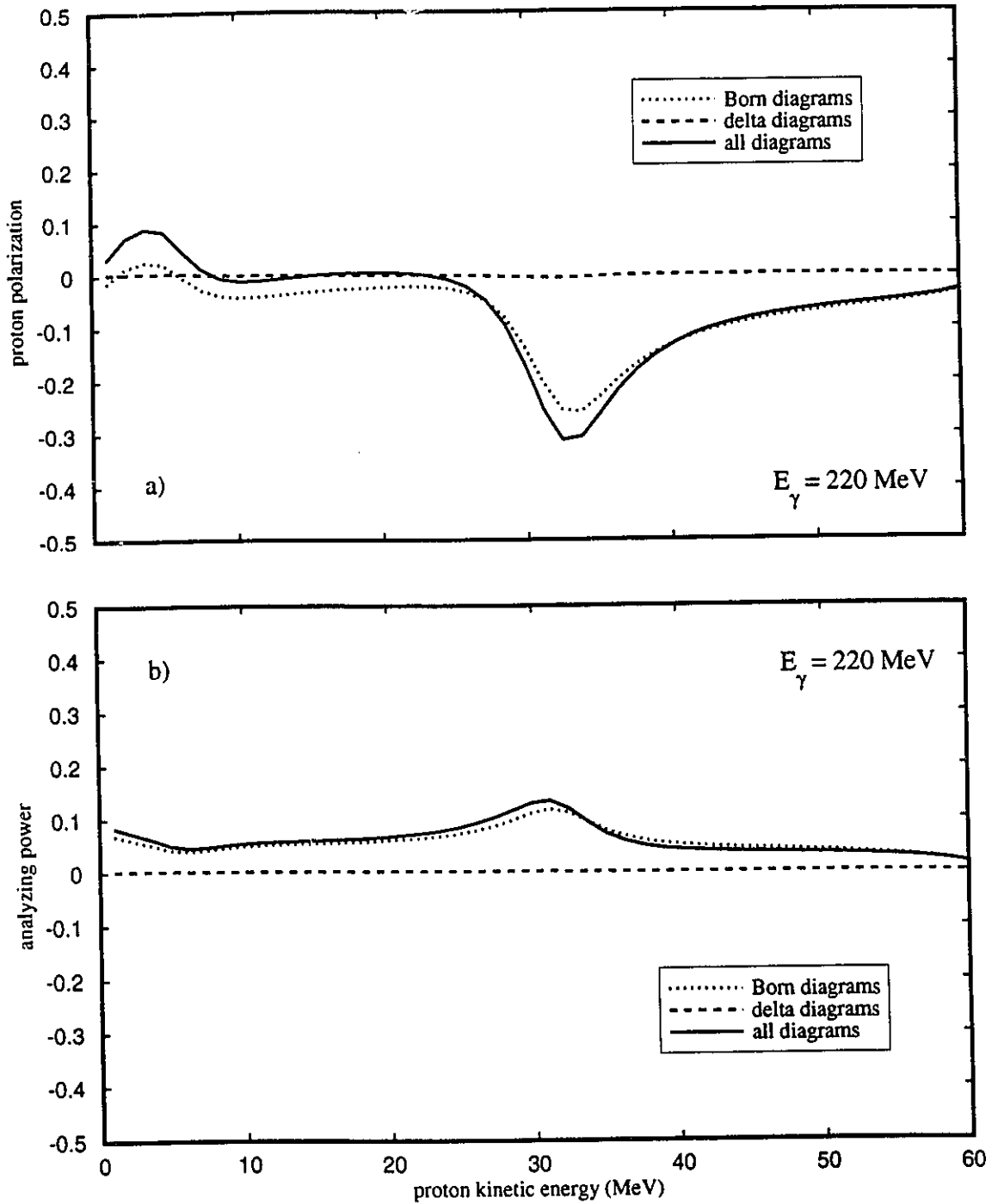
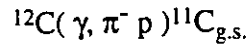


Figure 5-35. Born and delta diagram contributions to the spin observables. The incident photon energy is $E_\gamma = 220$ MeV and the proton and pion angles are $(\theta_p = 20^\circ, \varphi_p = 180^\circ)$ and $(\theta_\pi = 120^\circ, \varphi_\pi = 0^\circ)$.

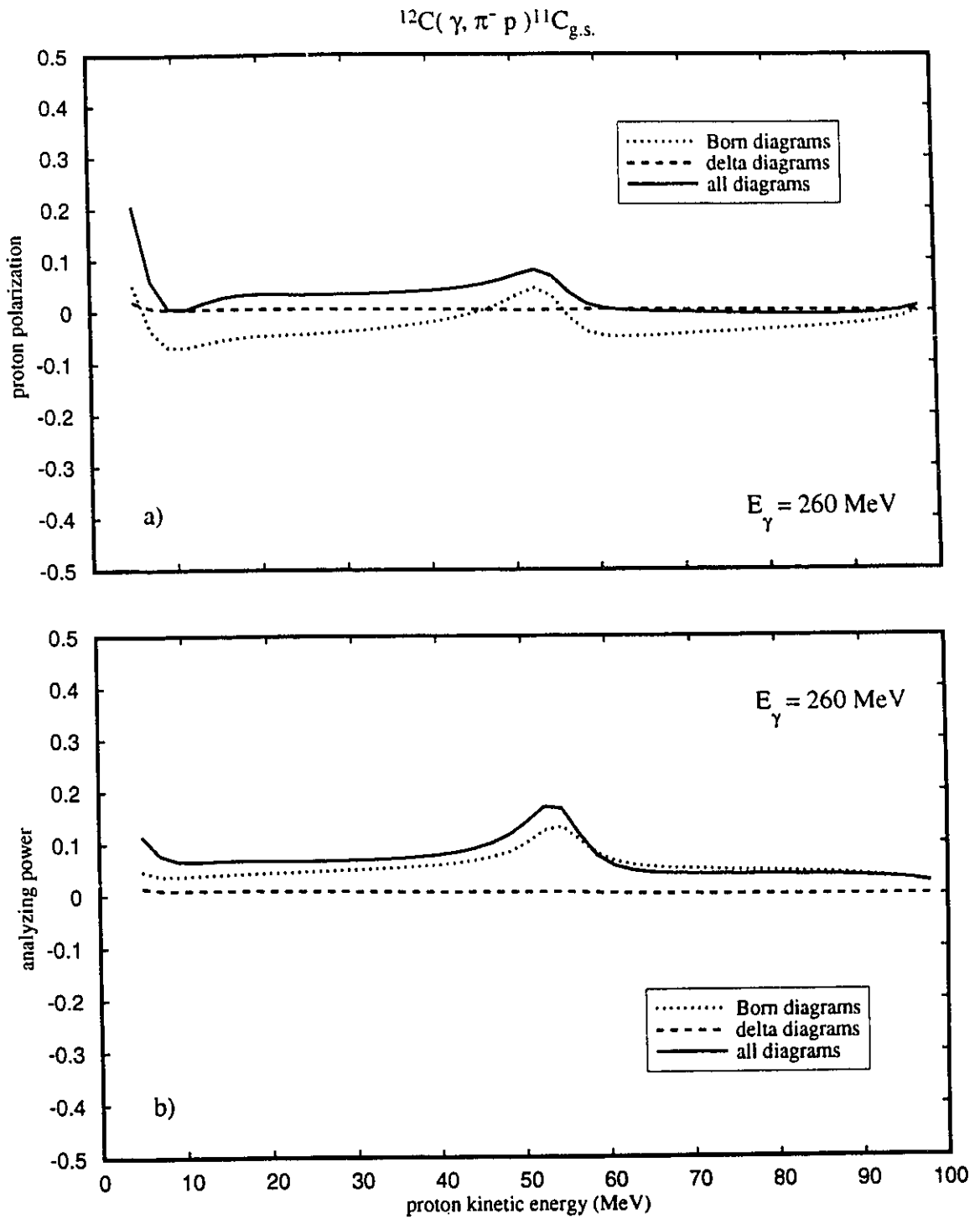


Figure 4-36. Born and delta diagram contributions to the spin observables. The incident photon energy is $E_\gamma = 260$ MeV and the proton and pion angles are $(\theta_p = 20^\circ, \varphi_p = 180^\circ)$ and $(\theta_\pi = 120^\circ, \varphi_\pi = 0^\circ)$.

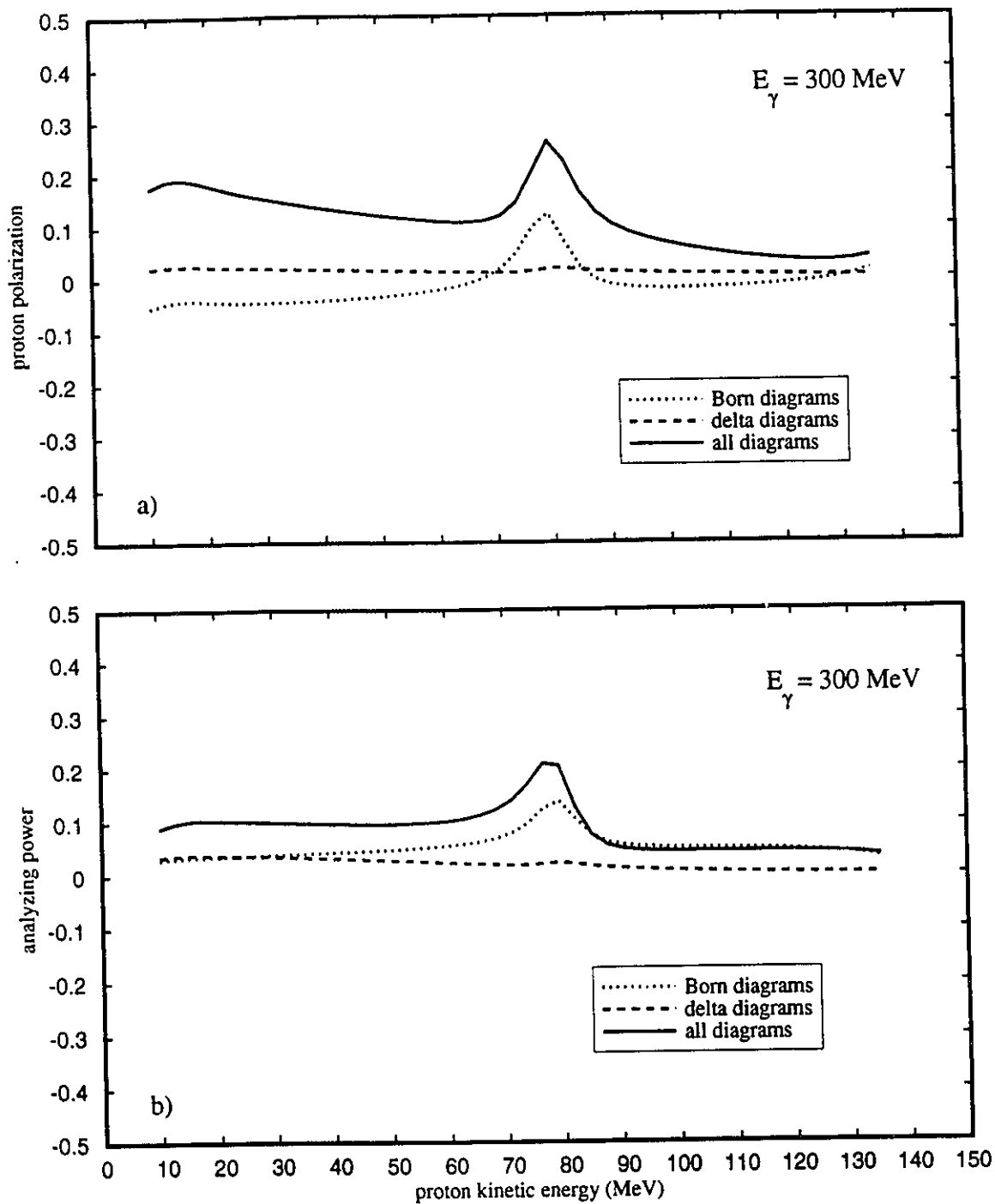
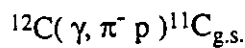


Figure 4-37. Born and delta diagram contributions to the spin observables. The incident photon energy is $E_\gamma = 300$ MeV and the proton and pion angles are $(\theta_p = 20^\circ, \phi_p = 180^\circ)$ and $(\theta_\pi = 120^\circ, \phi_\pi = 0^\circ)$.

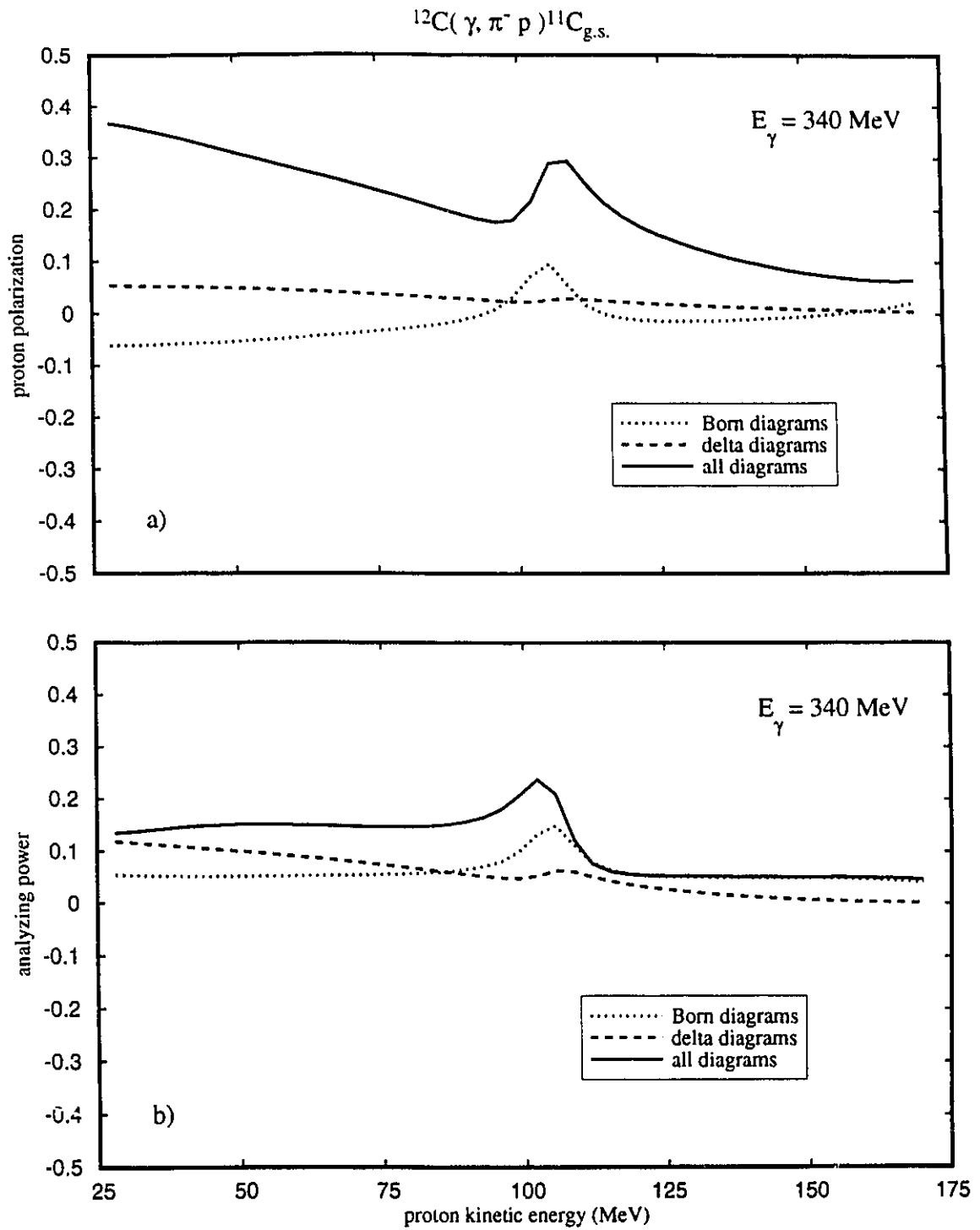


Figure 4-38. Born and delta diagram contributions to the spin observables. The incident photon energy is $E_\gamma = 340 \text{ MeV}$ and the proton and pion angles are $(\theta_p = 20^\circ, \varphi_p = 180^\circ)$ and $(\theta_\pi = 120^\circ, \varphi_\pi = 0^\circ)$.

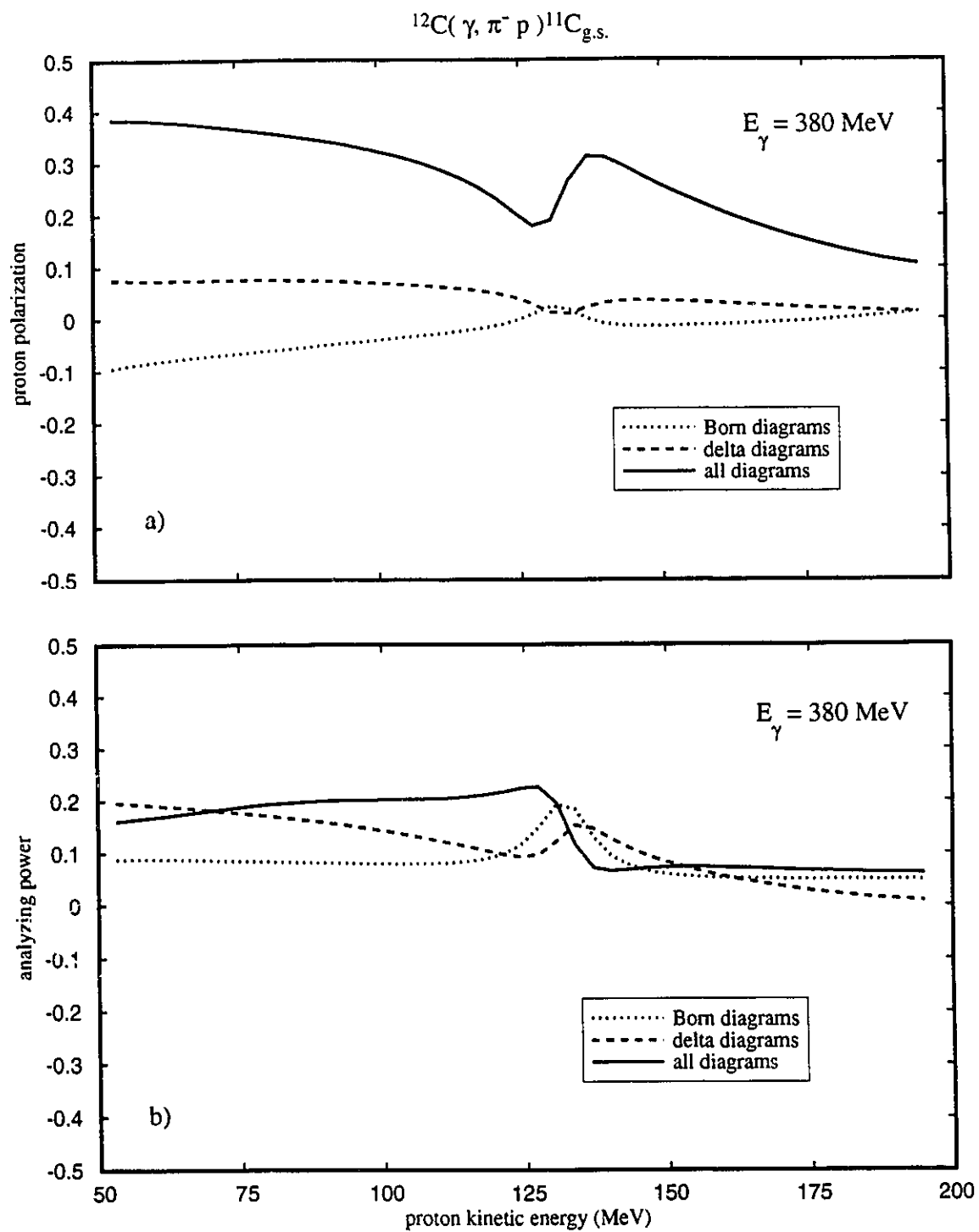


Figure 4-39. Born and delta diagram contributions to the spin observables. The incident photon energy is $E_\gamma = 380 \text{ MeV}$ and the proton and pion angles are $(\theta_p = 20^\circ, \varphi_p = 180^\circ)$ and $(\theta_\pi = 120^\circ, \varphi_\pi = 0^\circ)$.

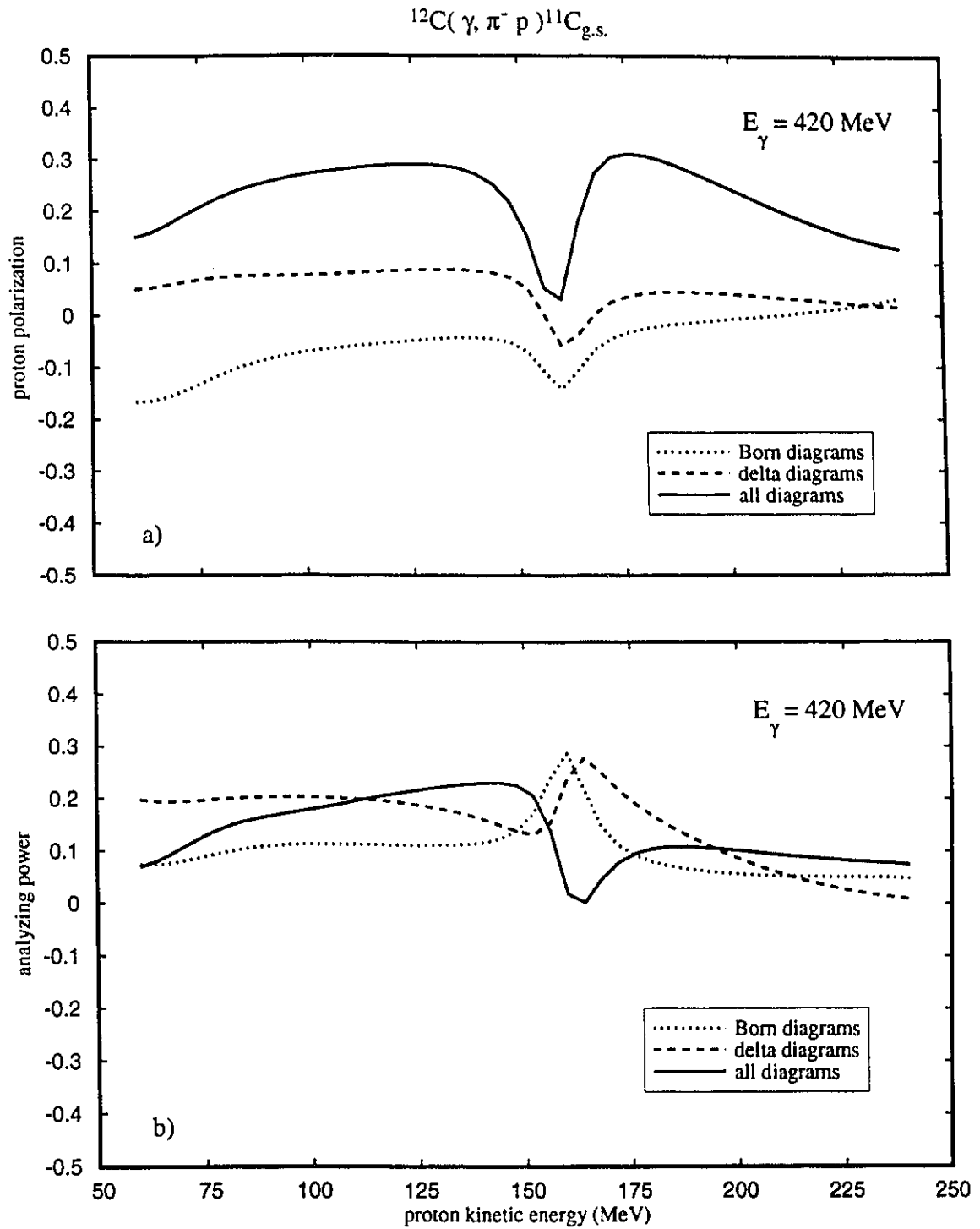


Figure 4-40. Born and delta diagram contribution to the spin observables. The incident photon energy is $E_\gamma = 420$ MeV and the proton and pion angles are $(\theta_p = 20^\circ, \varphi_p = 180^\circ)$ and $(\theta_\pi = 120^\circ, \varphi_\pi = 0^\circ)$.

becomes very important above 300 MeV. It must be noted that the polarization calculated from the delta diagrams or the Born terms alone is quite small and it is the interference between the Born and delta diagrams which produces the bulk of the protons polarization. The analyzing power is also affected by the delta diagrams but the effect is not as noticeable as for the polarization.

Now we consider the effect of changing the angles of the detected pion and proton while fixing the incident photon energy at $E_\gamma = 380$ MeV.

The cross sections are largest for forward proton angles, either 20° or 40° , with pions away from the z-axis, in the range 60° to 120° . The cross section peaks for these angles lie in the range 0.4 to 0.7 $\mu\text{b/sr sr MeV}$. For larger proton angles the peak cross sections diminish steadily, by roughly a factor of two for every 20° increase in the proton angle, to 0.04 $\mu\text{b/sr sr MeV}$ at $\theta_p = 120^\circ$ with $\theta_\pi = 20^\circ$. In figures 4-41 to 4-46 we show theoretical predictions for the observables in a number of cases for which the cross sections are larger than 0.2 $\mu\text{b/sr sr MeV}$, for three forward proton angles $\theta_p = 20^\circ, 40^\circ$ and 60° . The cross sections are shown in figures 4-41, 4-43 and 4-45 for the pion angles which have cross sections larger than 0.2 $\mu\text{b/sr sr MeV}$. When the proton angle is the most forward at $\theta_p = 20^\circ$ the peak cross sections are larger than 0.6 $\mu\text{b/sr sr MeV}$ for two pion angles $\theta_\pi = 80^\circ, 100^\circ$. When the energy of the detected proton is in the range $T_p = 50$ MeV to 175 MeV, where the cross section should be measurable, the momentum transfer covers the range from $q = 1 \text{ fm}^{-1}$ to 1.4 fm^{-1} . The polarization of the final proton (figure 4-42a) is as much as 0.5, while the analyzing power (figure 4-42b) goes up to 0.3. Note that the low energy peaks are due to the vanishingly small cross section and are of no practical consequence.

When the proton angle is increased by 20° to $\theta_p = 40^\circ$ (figure 4-43a), we find a very wide range of pion angles for which the cross section is greater than 0.2 $\mu\text{b/sr sr MeV}$. In fact when the pion angle lies in the range $\theta_\pi = 40^\circ$ to 120° the peak cross sections lie between 0.3 and 0.45 $\mu\text{b/sr sr MeV}$. The range of momentum transfer covered here (figure 4-43b) is similar to that of the previous proton angle, going from almost zero to 1.4 fm^{-1} . The polarization of the final proton (figure 4-44a) now goes up to 0.7 with most of the values lying around 0.4 to 0.5. The analyzing power (figure 4-44b) is as much as 0.5

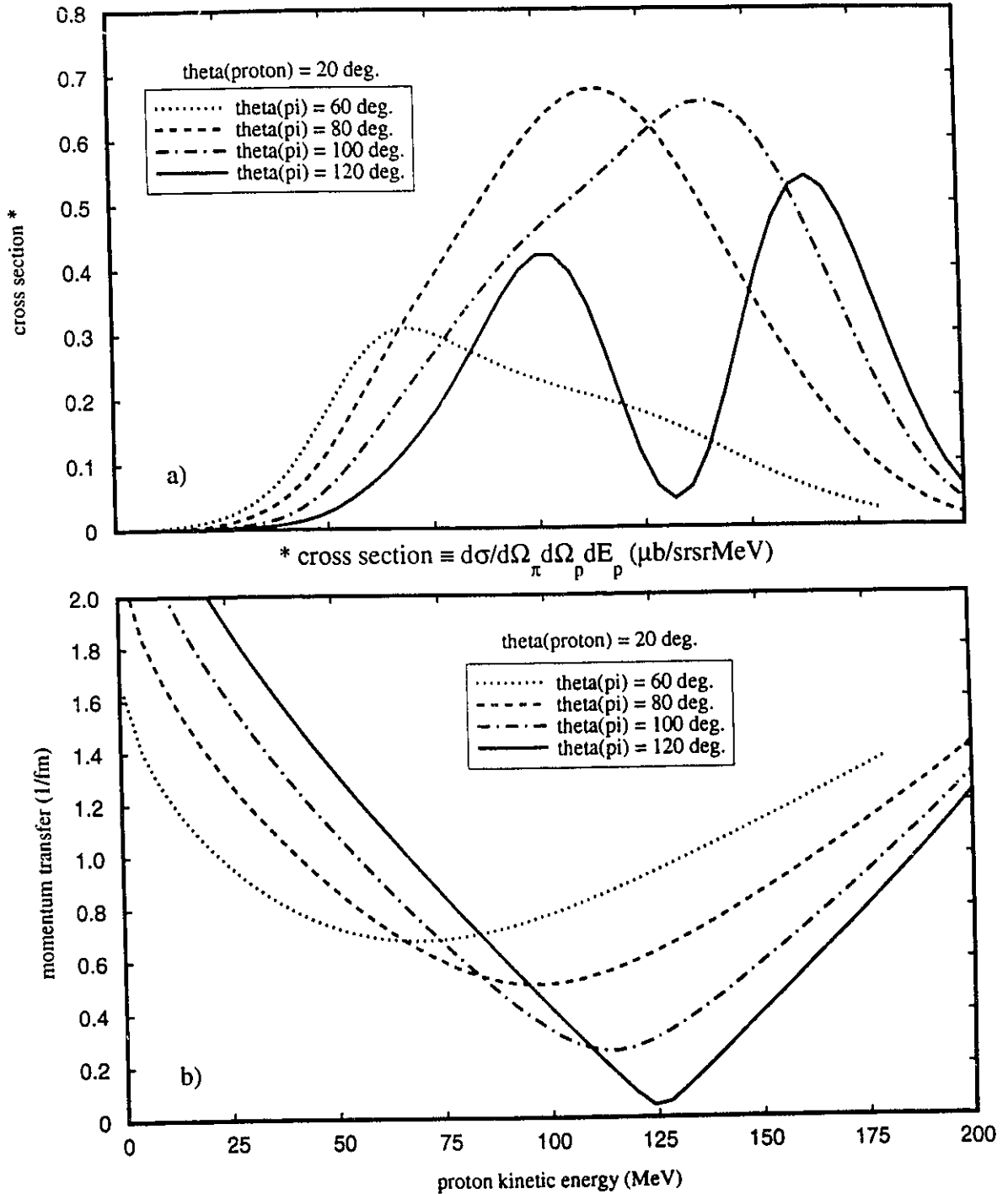
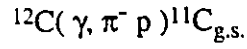


Figure 4-41. a) the cross section and b) the momentum transfer, vary as the pion angle varies, as indicated in the legend. The proton angle is held fixed at ($\theta_p = 20^\circ$, $\phi_p = 180^\circ$) with a photon energy of $E_\gamma = 380$ MeV.

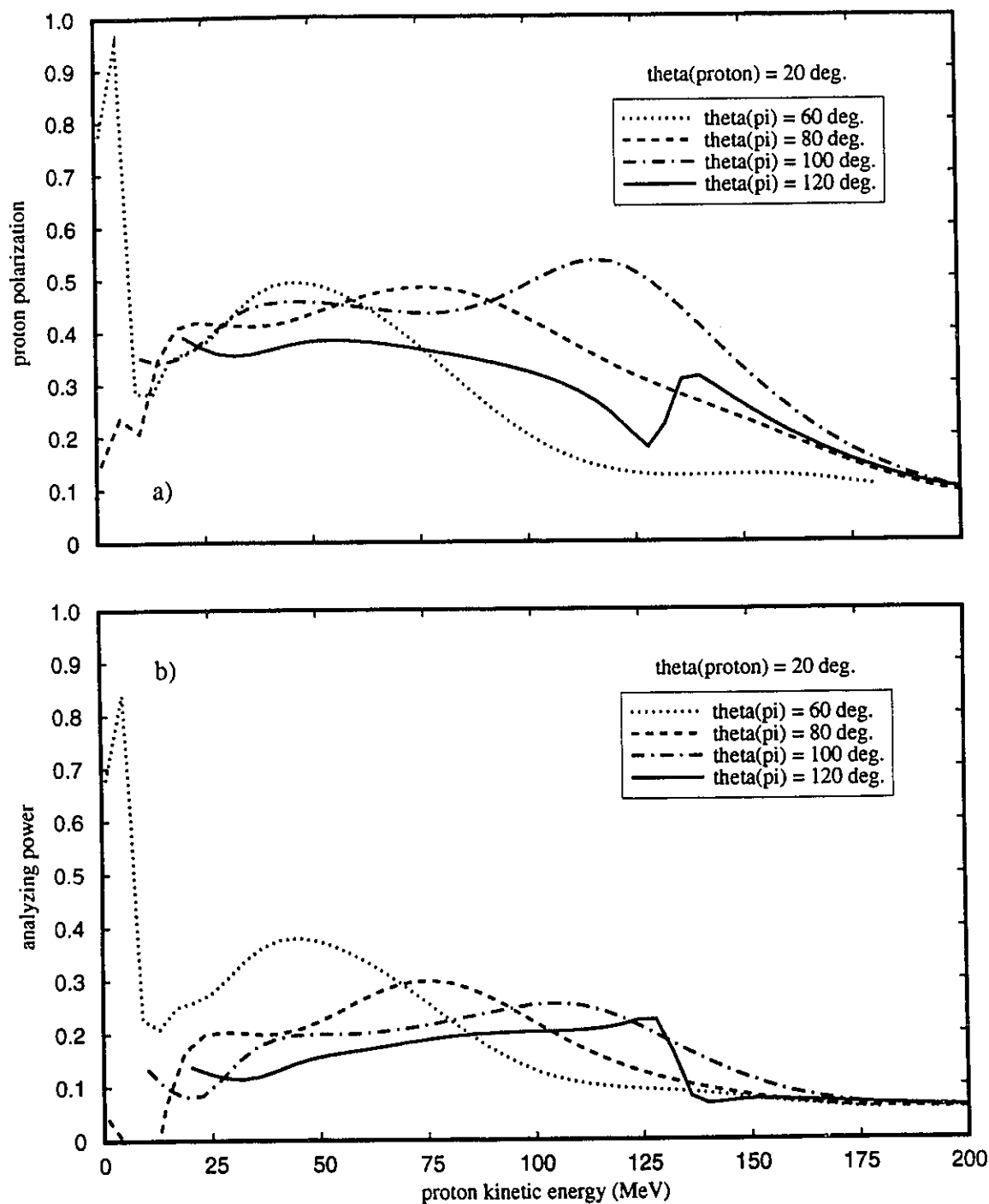
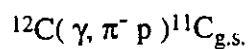


Figure 4-42. a) proton polarization and b) the analyzing power, vary as the pion angle varies, as indicated in the legend. The proton angle is held fixed at $(\theta_p = 20^\circ, \phi_p = 180^\circ)$ with a photon energy of $E_\gamma = 380$ MeV.

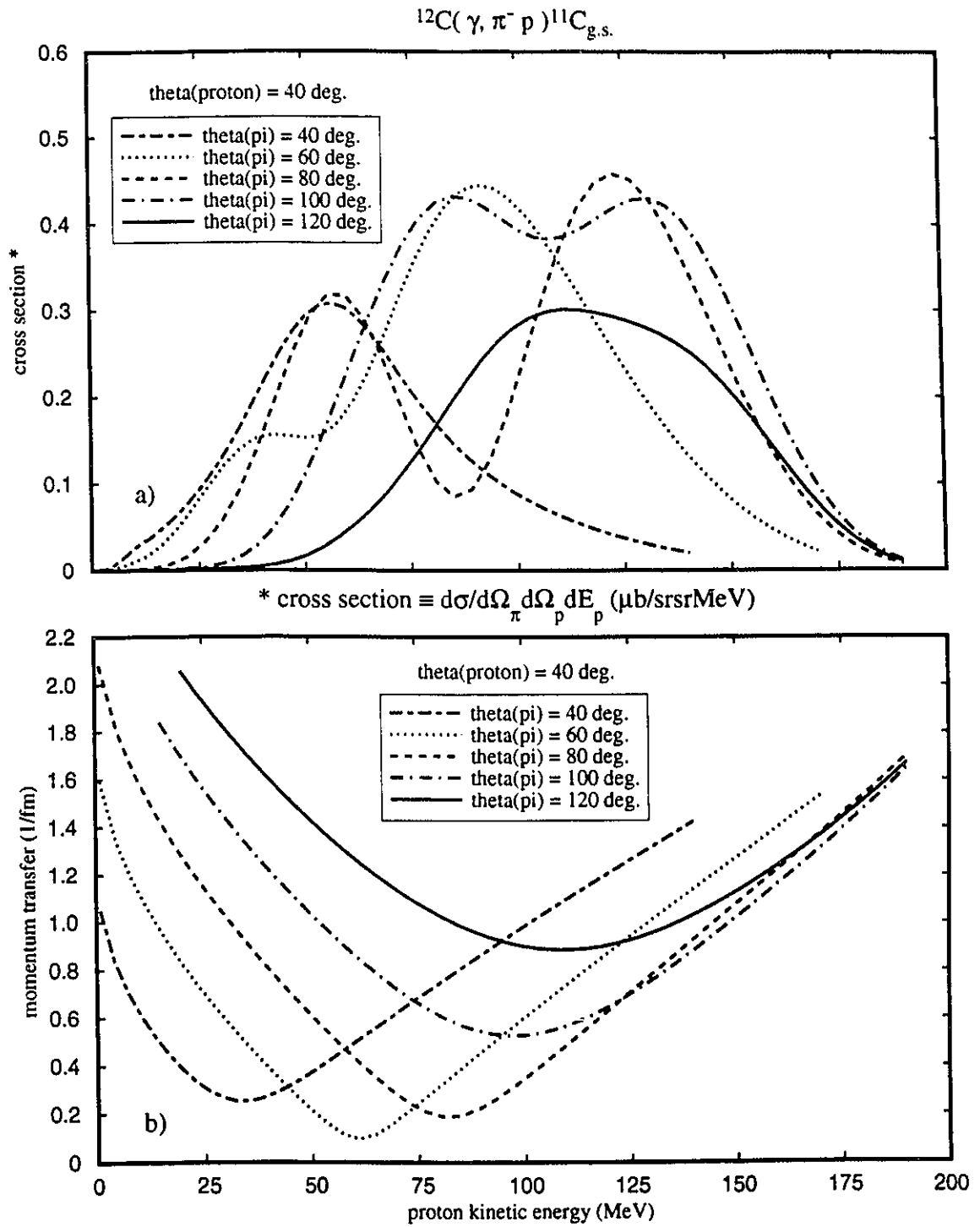


Figure 4-43. a) the cross section and b) the momentum transfer, vary as the pion angle varies, as indicated in the legend. The proton angle is held fixed at ($\theta_p = 40^\circ$, $\phi_p = 180^\circ$) with a photon energy of $E_\gamma = 380$ MeV.

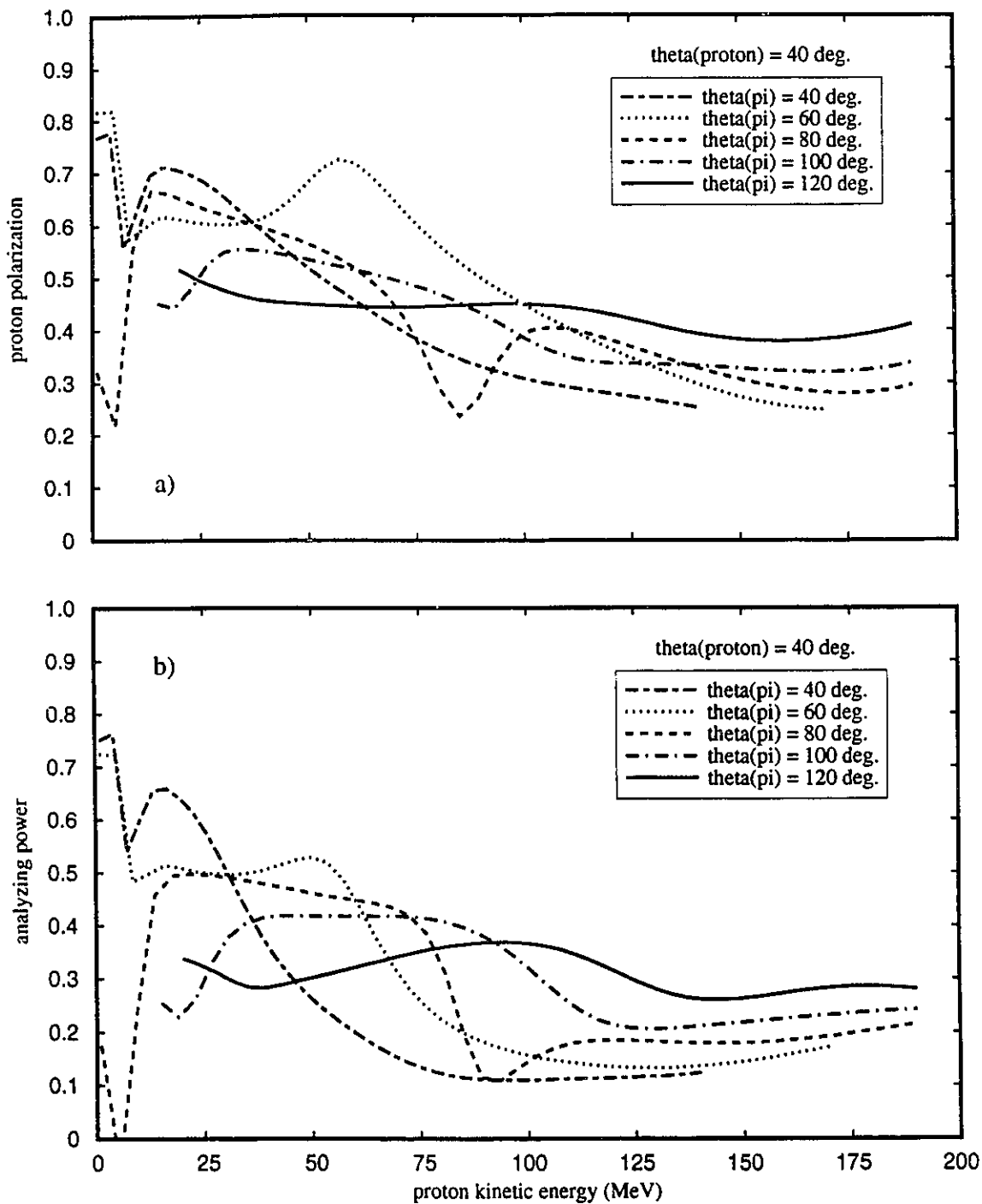
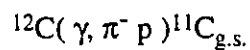


Figure 4-44. a) the proton polarization and b) the analyzing power, vary as the pion angle varies, as indicated in the legend. The proton angle is held fixed at $(\theta_p = 40^\circ, \varphi_p = 180^\circ)$ with a photon energy of $E_\gamma = 380$ MeV.

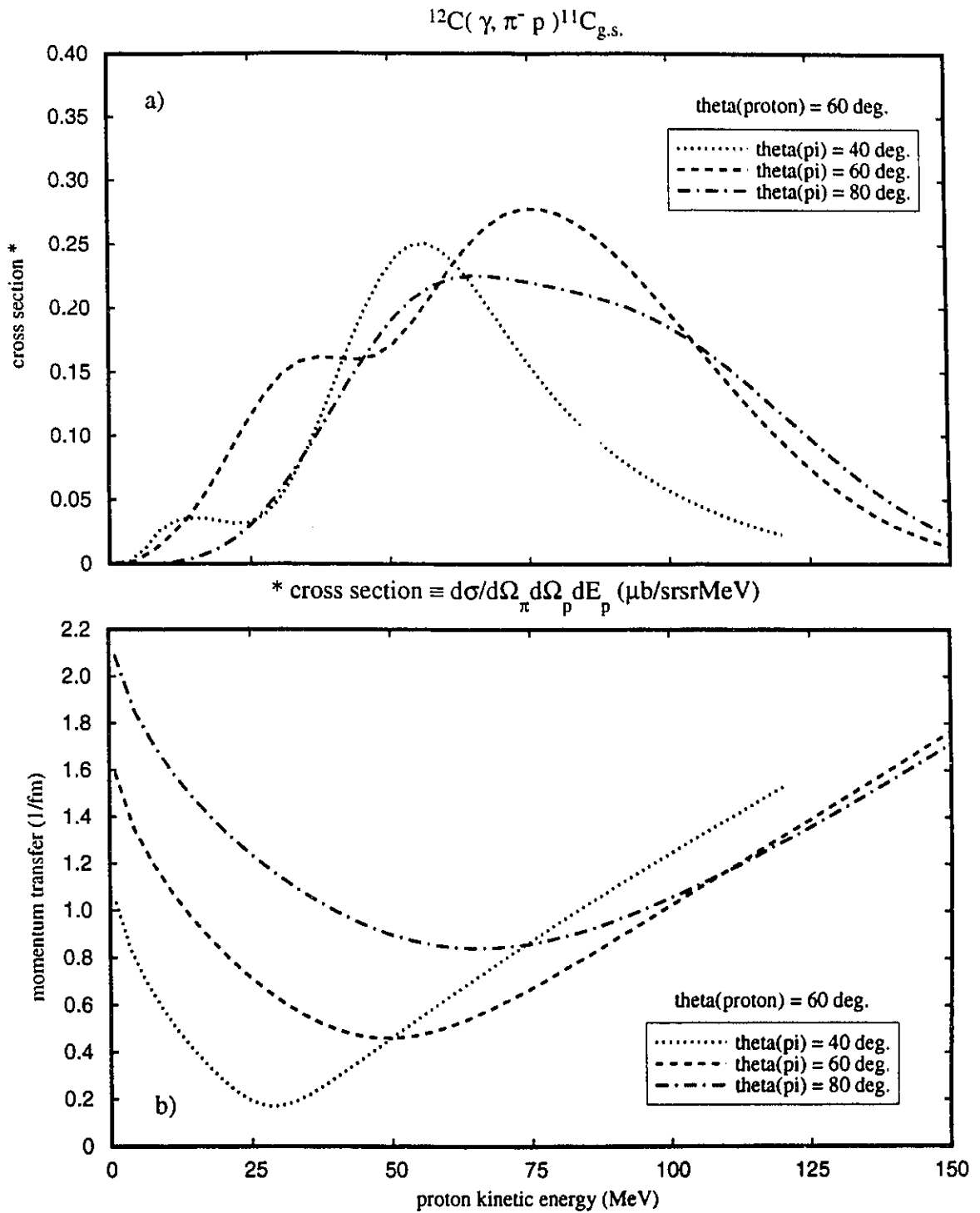


Figure 4-45. a) the cross section and b) the momentum transfer, vary as the pion angle varies, as indicated in the legend. The proton angle is held fixed at $(\theta_p = 60^\circ, \varphi_p = 180^\circ)$ with a photon energy of $E_\gamma = 380 \text{ MeV}$.

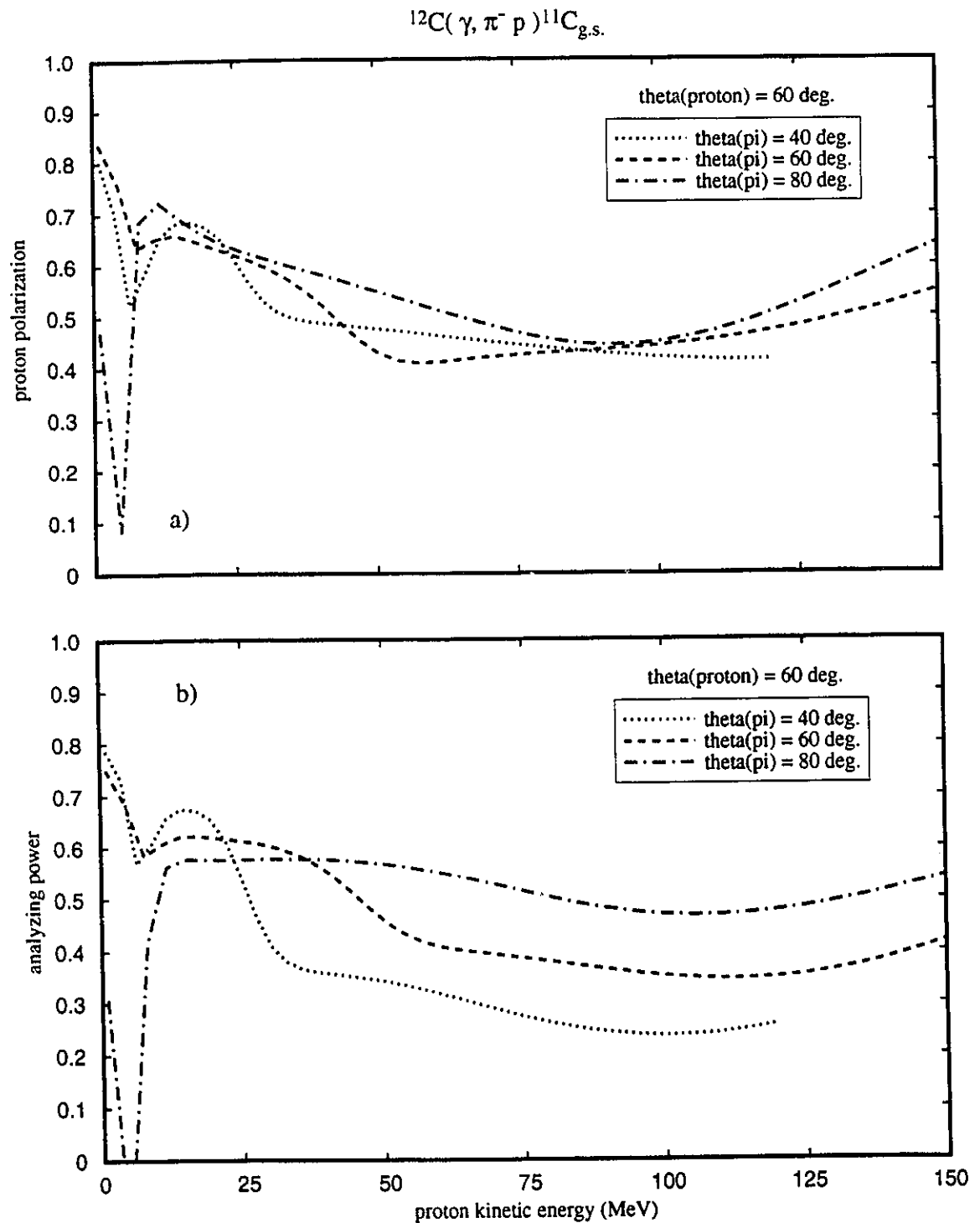


Figure 4-46. a) the proton polarization and b) the analyzing power, vary as the pion angle varies, as indicated in the legend. The proton angle is held fixed at $(\theta_p = 60^\circ, \varphi_p = 180^\circ)$ with a photon energy of $E_\gamma = 380$ MeV.

with most of the values in the range 0.1 to 0.3.

Increasing the proton angle again to $\theta_p = 60^\circ$ we see that the range of pion angles for which we have a cross section larger than $0.2 \mu\text{b/sr srMeV}$ has narrowed considerably so that for pions with angles in the range $\theta_\pi = 40^\circ$ to 80° we have cross section peaks in the range 0.2 to $0.3 \mu\text{b/sr srMeV}$. Here the range of momentum transfer (figure 4-45b) has narrowed slightly to lie between 0.2 and 1.3 fm^{-1} . The final proton polarization lies in the range 0.4 to 0.6 , while the analyzing power (figure 4-46b) is between 0.3 and 0.6 .

Here we see that we can find situations where the cross section is measurable (cross sections as small as $0.1 \mu\text{b/sr srMeV}$ have been measured at the Tomsk synchrotron [GS79a, AG90]) over a fairly large range of proton and pion angles. The angles are such that the detectors would not interfere with the beam. The range of momentum transfer explored is from 0 fm^{-1} to about 1.4 fm^{-1} , a very nice complement to the high momentum transfer reactions such as (γ, p) and (p, π) , which look at momentum transfers of 2 fm^{-1} or more. The polarization of the final proton and the analyzing power due to a linearly polarized incident photon have values up to 0.6 , which should be measurable at the new generation of high duty-factor electron accelerators. With these new machines we could perhaps even measure cross sections an order of magnitude smaller than those discussed here expanding further the kinematic range which could be explored.

4.4 Comparison With Experimental Data

We compare the results of this model with the data available from the three experiments which have studied negative pion photoproduction on a nucleus; two experiments performed at Tomsk and one at MIT.

4.4.1 The Tomsk 1979 Experiment

I.V. Glavanakov and V.N. Stibunov reported a measurement of differential cross section for the reaction $^{12}\text{C}(\gamma, \pi^- p)^{11}\text{C}$ in 1979 [GS79]. The proton and pion were detected in a coplanar geometry with the laboratory angle pairs $(\theta_p = 20^\circ, \phi_p = 180^\circ)$ and $(\theta_\pi = 120^\circ, \phi_\pi = 0^\circ)$ in our coordinate system. They didn't have sufficient energy

resolution to discern the final state of the residual nucleus so they divided the data into two ranges of residual nucleus excitation energy: 0-10 MeV and 10-40 MeV. The 0-10 MeV data were interpreted as corresponding to states arising from the removal of a $1p_{3/2}$ neutron and mostly leaving the residual nucleus in its ground state, while the 10-40 MeV data correspond to states arising from the removal of a $1s_{1/2}$ neutron from the target nucleus, leaving a clean $1s_{1/2}$ hole for the most part. The data for an incident photon energy of $E_\gamma = 380$ MeV were presented again by Glavanakov in 1989 [G189]. We read the data from figure 4 of the 1989 paper. The data from the low excitation energy case (knockout of a p-shell neutron) changed slightly between the two papers without any explanation.

Figure 4-47 shows the data from [G189] in which the nucleus is (mostly) left in the ground state when a $1p_{3/2}$ neutron is knocked out of the nucleus. The curve is the result of our Dirac based DW calculation. The proton is distorted with the A and E dependent potential of Cooper et al. [Co92] while the pion distortion is that of Oset et al. The calculation shows the symmetry in the momentum transfer which we would expect if we were simply taking the Fourier transform of the bound state wave function as in the PW calculation. The DW calculation reduces the cross section from the plane wave value by a factor of two, as shown in figure 4-2, and shifts the minimum and maxima to higher proton energies by 10 MeV without changing the relative size of the peaks appreciably. The factor of three difference in the magnitude of the two peaks is not easy to understand from our model. Glavanakov and Stibunov [GS79] did a nonrelativistic impulse approximation calculation, in which proton and pion distortions were included in the eikonal approximation and the bound states were described by harmonic oscillator wave functions. They concluded that the strong energy dependence of the pion-nucleus and proton-nucleus interactions is responsible for producing the asymmetry in the cross section, an effect which is not as prominent in the present DW model.

Figure 4-48 shows the data of Glavanakov and Stibunov [GS79] for the case in which the residual nucleus is (mostly) left in an excited state resulting from the removal of a $1s_{1/2}$ neutron. We could not find a precise value for the separation energy of the neutron so we used $E_s = 35$ MeV, which corresponds to the separation energy of the $1p_{3/2}$

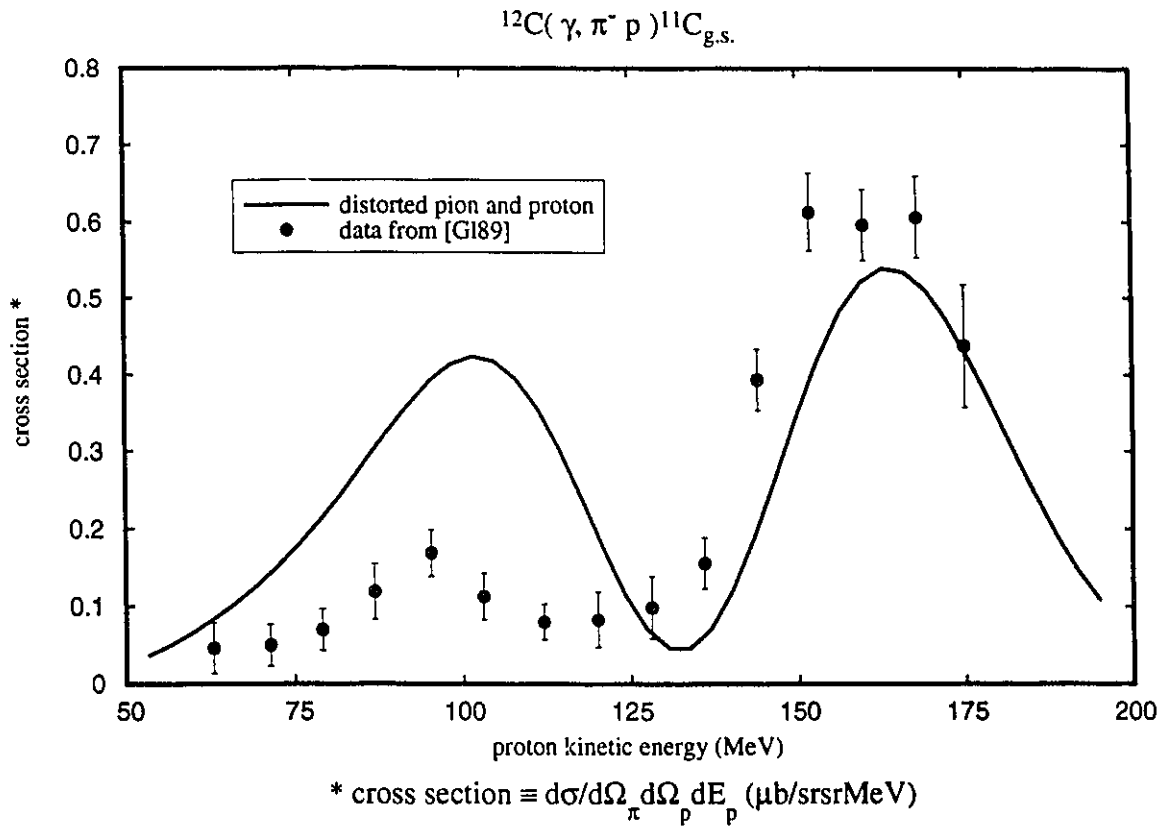


Figure 4-47. Cross section as a function of proton kinetic energy.

The kinematic conditions are $E_{\gamma} = 380$ MeV., ($\theta_p = 20^{\circ}$, $\varphi_p = 180^{\circ}$) and

($\theta_{\pi} = 120^{\circ}$, $\varphi_{\pi} = 0^{\circ}$).

Solid line - pion distorted by the potential of Oset and proton distorted by the global E and A dependent potential. The data points are from [G189].

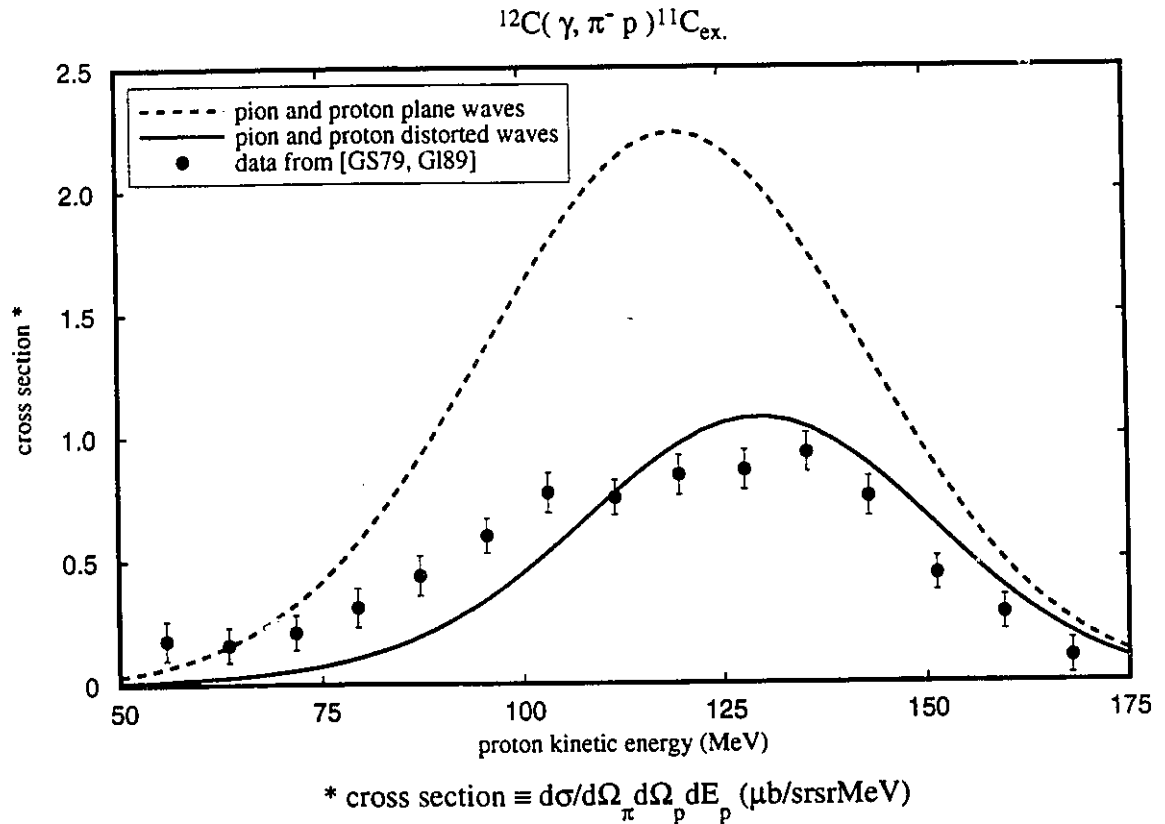


Figure 4-48. Cross section as a function of proton kinetic energy. A $1s_{1/2}$ neutron is knocked out of the target nucleus leaving a hole with excitation energy approx. 16 MeV above the ground state of ^{11}C . The kinematic conditions are $E_{\gamma} = 380$ MeV., ($\theta_p = 20^{\circ}$, $\phi_p = 180^{\circ}$) and ($\theta_{\pi} = 120^{\circ}$, $\phi_{\pi} = 0^{\circ}$). The separation energy of the $1s_{1/2}$ neutron of ^{12}C was taken to be $E_s = 35$ MeV. Dashed curve - proton and pion plane waves. Solid line - The proton is distorted by the global E and A dependent potential while the pion is distorted by the potential of Oset. Data points from Glavanakov [GS79, G189].

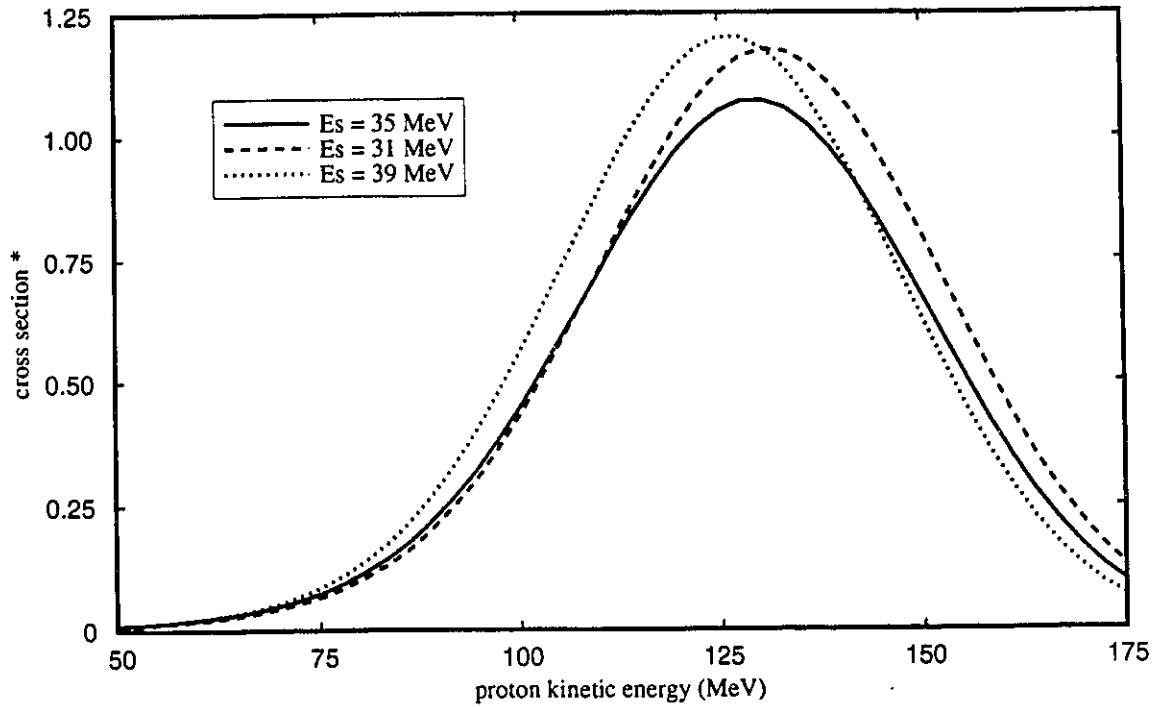
neutron (18.721 MeV) plus an excitation energy, to move a $1s_{1/2}$ neutron to the $1p_{3/2}$ level, of approximately 16 MeV. The dashed curve is the PW calculation while the solid curve has the same proton and pion distortions that we used in figure 4-47.

Our description of the data for knockout of both the s- and p-shell neutron is not as good as that obtained by Glavanakov and Stibunov [GS79] or by Glavanakov [G189]. It should be pointed out that our calculations contain no parameters which we adjust to improve the description of the data. In particular we can not understand the asymmetry in the cross section data for the knockout of a $1p_{3/2}$ neutron. The DW calculations for both the ground state (figure 4-47) and the excited state (figure 4-48) also seem to be shifted toward higher proton energies by about 10 MeV relative to the data, another effect that we have no explanation for. The dependence of the cross section for the knockout of a $1s_{1/2}$ neutron on the binding energy is shown in figure 4-49. The description of the data would be improved by using a slightly higher separation energy.

4.4.2 The Tomsk 1990 Experiment

P.S. Anan'in and I.V. Glavanakov recently reported the results of another pion photoproduction experiment on ^{12}C [AG90], in which the angle of the detected proton was changed from the previous experiment to ($\theta_p = 40^\circ$, $\varphi_p = 180^\circ$), while the pion angle was kept at the same value as the previous experiment, namely ($\theta_\pi = 120^\circ$, $\varphi_\pi = 0^\circ$) in our coordinate system. This changes the range of momentum transfers covered in the experiment to higher values than examined previously. Note that they did not have the energy resolution to detect the final state of the residual nucleus so they *assumed* that the ^{11}C nucleus was in its ground state. The relevant kinematic quantities are shown in figure 4-50. The momentum transfer, shown in figure 4-50b), lies in the range 0.8 fm^{-1} to 1.6 fm^{-1} .

Figure 4-51 shows data at an incident photon energy of $E_\gamma = 340 \pm 23 \text{ MeV}$. The dashed curve is the PW calculation, and the solid curve has the global A and E dependent proton distortions while the pion distortions are those of Oset et al. These data have very small error bars and the DW calculation describes the data quite well. The nonrelativistic calculation of Glavanakov [G189] yielded a plane wave calculation a few per cent larger



* cross section $\equiv d\sigma/d\Omega_{\pi} d\Omega_p dE_p$ ($\mu\text{b/sr sr MeV}$)

Figure 4-49. Dependence of the cross section on the separation energy of the $1s_{1/2}$ neutron. The kinematic conditions are $E_{\gamma} = 380 \text{ MeV}$,

($\theta_p = 20^\circ$, $\varphi_p = 180^\circ$) and ($\theta_{\pi} = 120^\circ$, $\varphi_{\pi} = 0^\circ$).

The proton is distorted by the global E and A dependent potential while the pion is distorted by the potential of Oset. Dotted line - $E_s = 31 \text{ MeV}$,

Dashed line - $E_s = 35 \text{ MeV}$. Solid line - $E_s = 39 \text{ MeV}$.

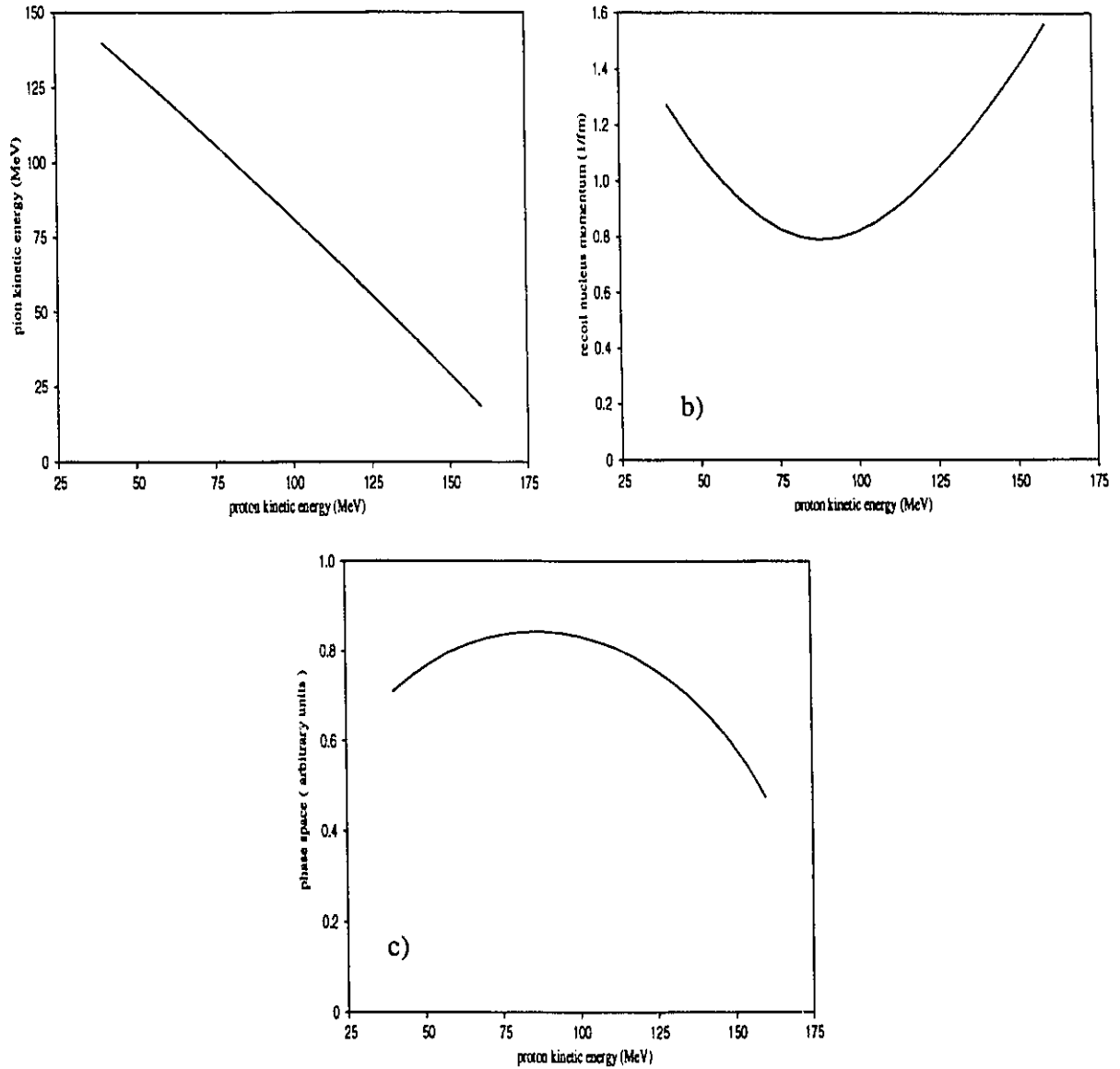


Figure 4-50. Variation in kinematic quantities for the experimental conditions: $E_\gamma = 340 \text{ MeV}$, $(\theta_p = 40^\circ, \varphi_p = 180^\circ)$ and $(\theta_\pi = 120^\circ, \varphi_\pi = 0^\circ)$, in the reaction $^{12}\text{C}(\gamma, \pi^- p)^{11}\text{C}_{g.s.}$.

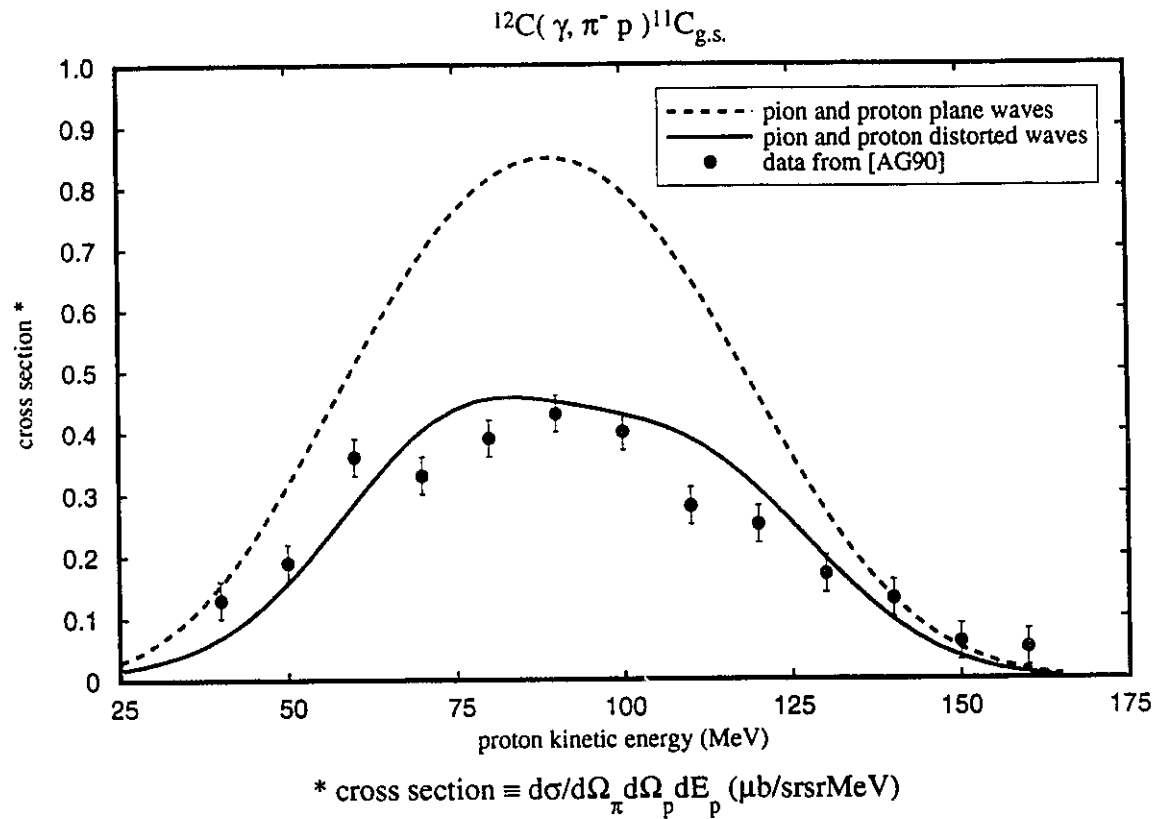


Figure 4-51. Cross section as a function of proton kinetic energy. The kinematic conditions are $E_{\gamma} = 340$ MeV., $(\theta_p = 40^{\circ}, \varphi_p = 180^{\circ})$ and $(\theta_{\pi} = 120^{\circ}, \varphi_{\pi} = 0^{\circ})$. Dashed curve - pion and proton plane waves. Solid line - pion distorted by the potential of Oset and proton distorted by the global E and A dependent potential. The data points are from [AG90].

than our PW (dashed curve) of figure 4-51, while his distorted wave calculation yielded a curve roughly twenty per cent smaller than our DW calculation (solid curve), and passing below all the data. The distortion of the nonrelativistic final state wave functions is included through an optical potential in the eikonal approximation. The pion potential is then of the s-wave form of the Laget potential, while the nonrelativistic proton potential is a simple Woods-Saxon. These potentials do not provide a good a description of elastic scattering as the potentials which we use in our model (see for example figure 3-10 to compare results for the pion potentials).

The bulk of the data from this experiment were reported for fixed energy of the final state pion. We show the momentum transfer as a function of proton energy for the ten pion energies for which the data are reported in figure 4-52. The momentum transfer here covers the range 0.55 fm^{-1} to 1.5 fm^{-1} . The pion kinetic energy is fixed so the energy of the photon must change to allow the proton energy to change. In figure 4-53 we show the energy of the incident photon as a function of the proton kinetic energy for all the pion energies. The pion energies are incremented in roughly 10 MeV steps and the photon energies show parallel trajectories for all ten pion energies, covering a photon energy range of 200 MeV to 450 MeV.

Figures 4-54 to 4-58 show the cross sections calculated for each of the ten pion energies for which data are reported. The dashed curves are the PW calculations and the solid curves are the DW calculations. The quality of agreement with data overall is difficult to judge for these data due to the large error bars and the high degree of scatter in the data points. The PW calculation for a pion kinetic energy of $T_{\pi} = 33.2 \text{ MeV}$, shown in figure 4-54, passes through the error bars of 9 out of 13 points, while the DW calculation passes through 7. The calculations seem to have a reasonable shape, but it is difficult to say. The next three graphs, for pion kinetic energies of $T_{\pi} = 44.3 \text{ MeV}$, 54.9 MeV and 65.5 MeV , have the data roughly a factor of two above the DW calculation, and even slightly above the plane wave calculation. Examination of figure 4-53 shows that the momentum transfer where the data has the largest value of the cross section for these pion energies, at a proton kinetic energy of 60 MeV, is in the range 0.6 fm^{-1} to 0.7 fm^{-1} . This is the lowest momentum transfer examined in this data set.

The last six graphs have the PW calculation above most of the data while the DW

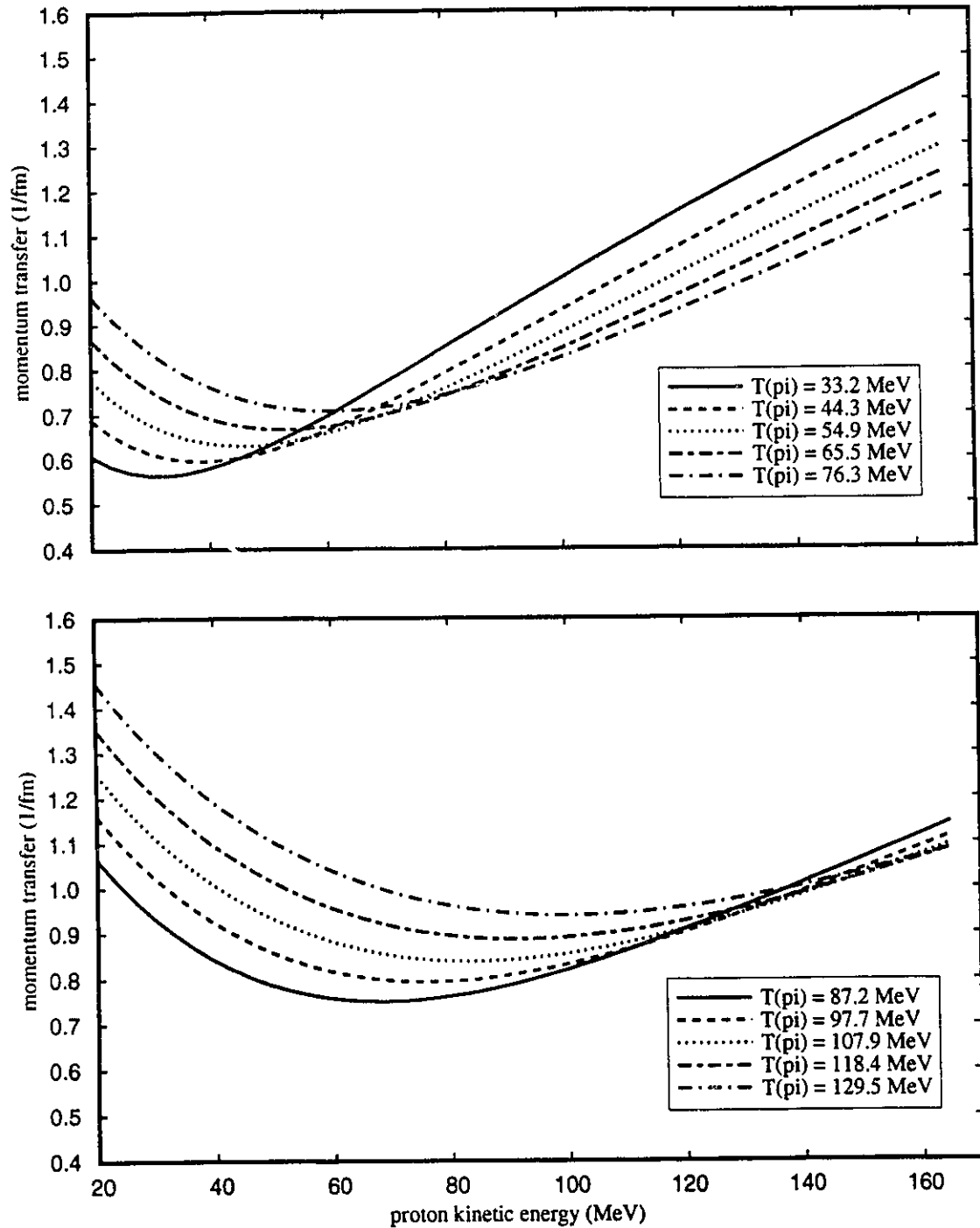
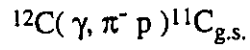


Figure 4-52. Momentum transfer as a function of proton kinetic energy for different pion kinetic energies corresponding to the data sets of [AG90]. The kinematic conditions are $(\theta_p = 40^\circ, \varphi_p = 180^\circ)$ and $(\theta_\pi = 120^\circ, \varphi_\pi = 0^\circ)$.

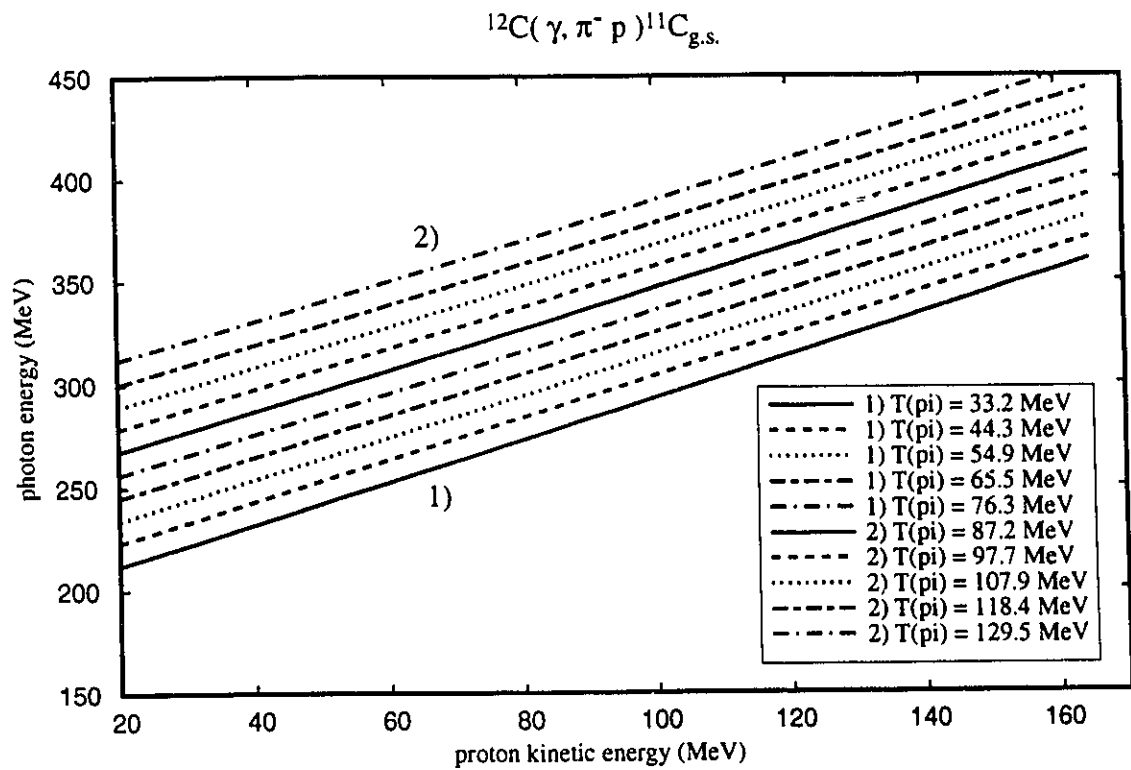


Figure 4-53. Incident photon energy as a function of proton kinetic energy for different pion kinetic energies corresponding to the data sets of [AG90]. The kinematic conditions are $(\theta_p = 40^\circ, \varphi_p = 180^\circ)$ and $(\theta_\pi = 120^\circ, \varphi_\pi = 0^\circ)$.

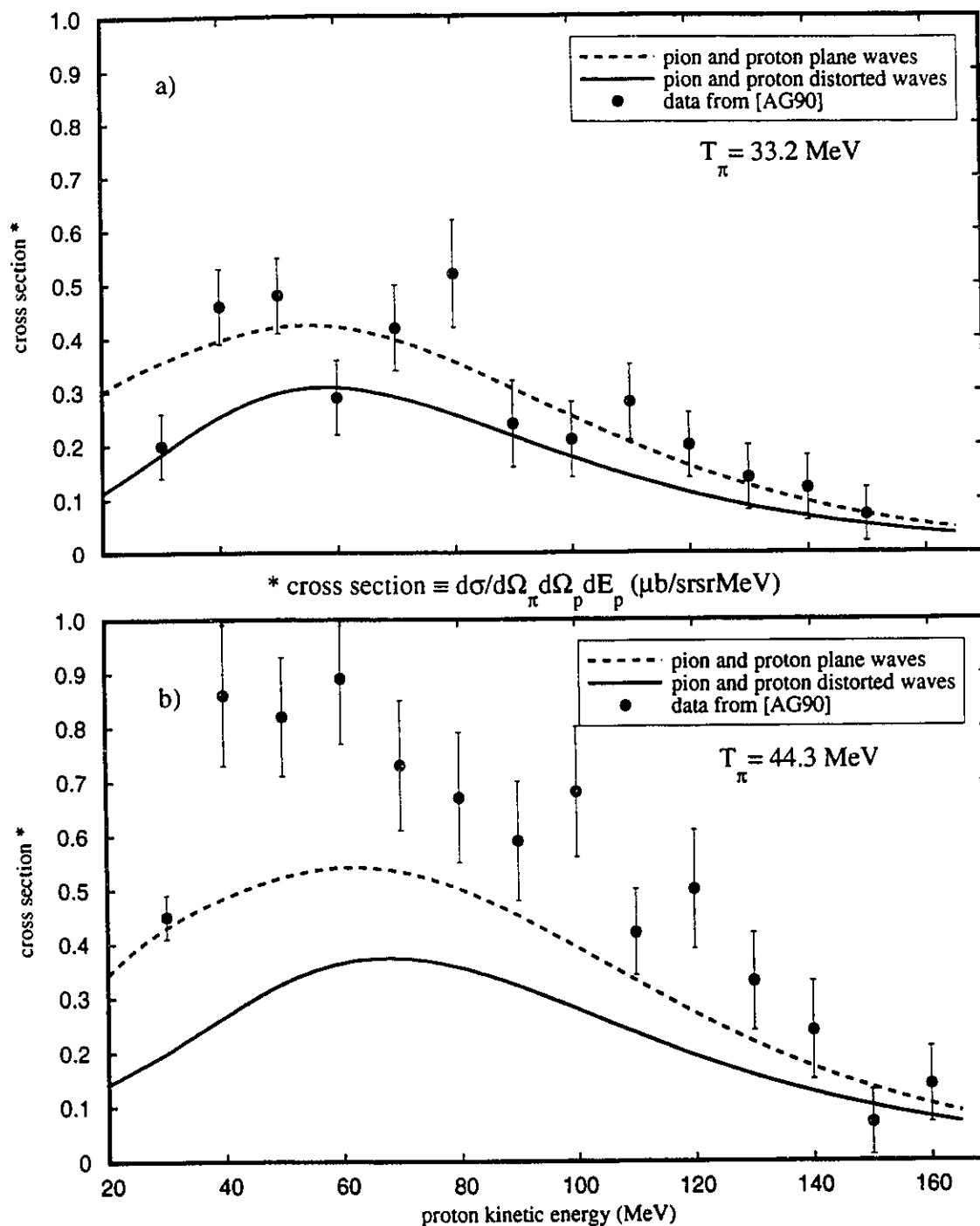
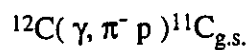


Figure 4-54. Cross section versus proton kinetic energy with pion kinetic energy held constant at a) $T_{\pi} = 33.2 \text{ MeV}$ and b) $T_{\pi} = 44.3 \text{ MeV}$. The kinematic conditions are $(\theta_p = 40^\circ, \phi_p = 180^\circ)$ and $(\theta_{\pi} = 120^\circ, \phi_{\pi} = 0^\circ)$. Dashed curves - proton and pion plane waves. Solid curves - pion distorted by the potential of Oset and proton distorted by the global E and A dependent potential. The data points are from [AG90].

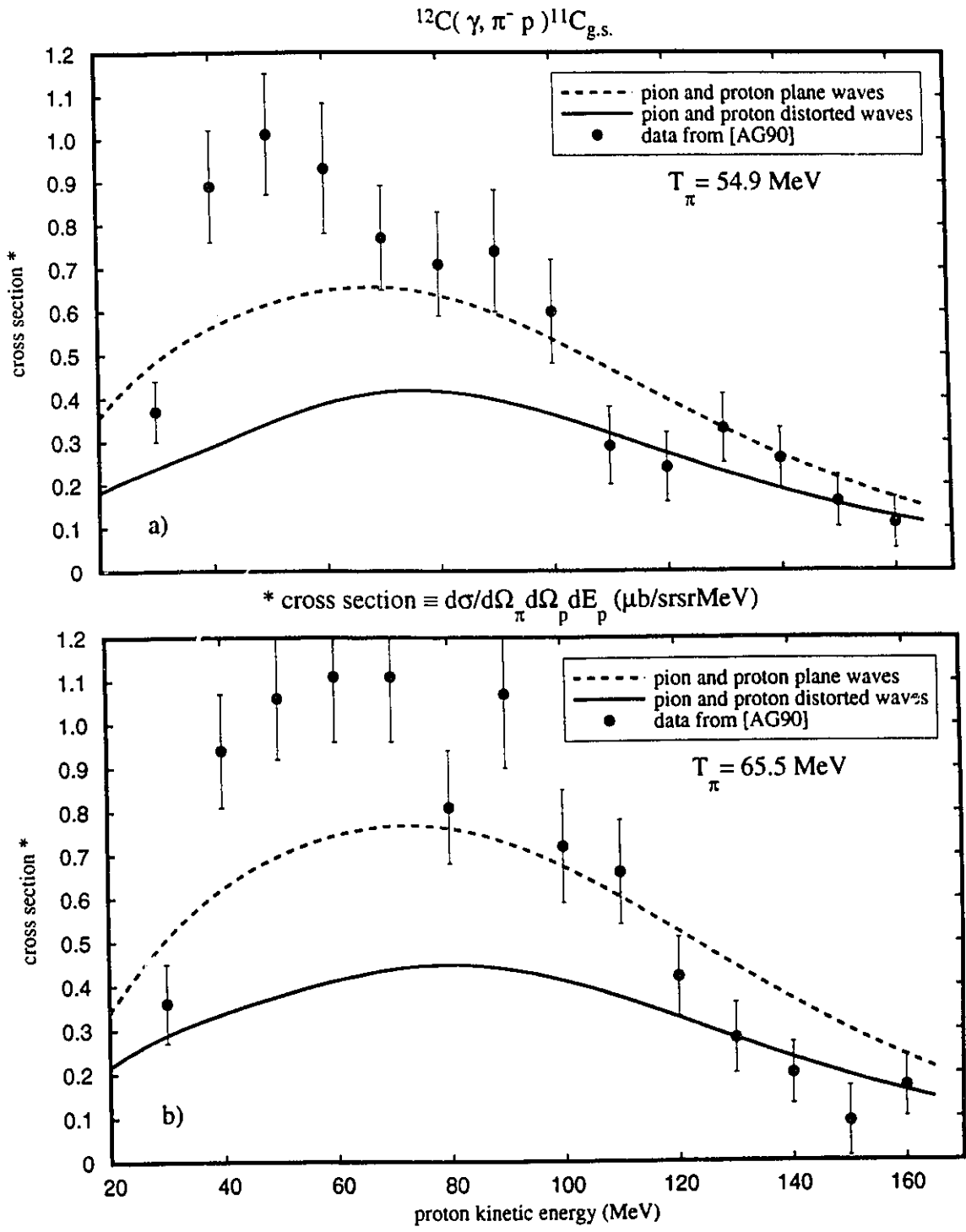


Figure 4-55. Cross section versus proton kinetic energy with pion kinetic energy held constant at a) $T_{\pi} = 54.9$ MeV and b) $T_{\pi} = 65.5$ MeV. The kinematic conditions are $(\theta_p = 40^{\circ}, \varphi_p = 180^{\circ})$ and $(\theta_{\pi} = 120^{\circ}, \varphi_{\pi} = 0^{\circ})$. Dashed curves - proton and pion plane waves. Solid curves - pion distorted by the potential of Oset and proton distorted by the global E and A dependent potential. The data points are from [AG90].

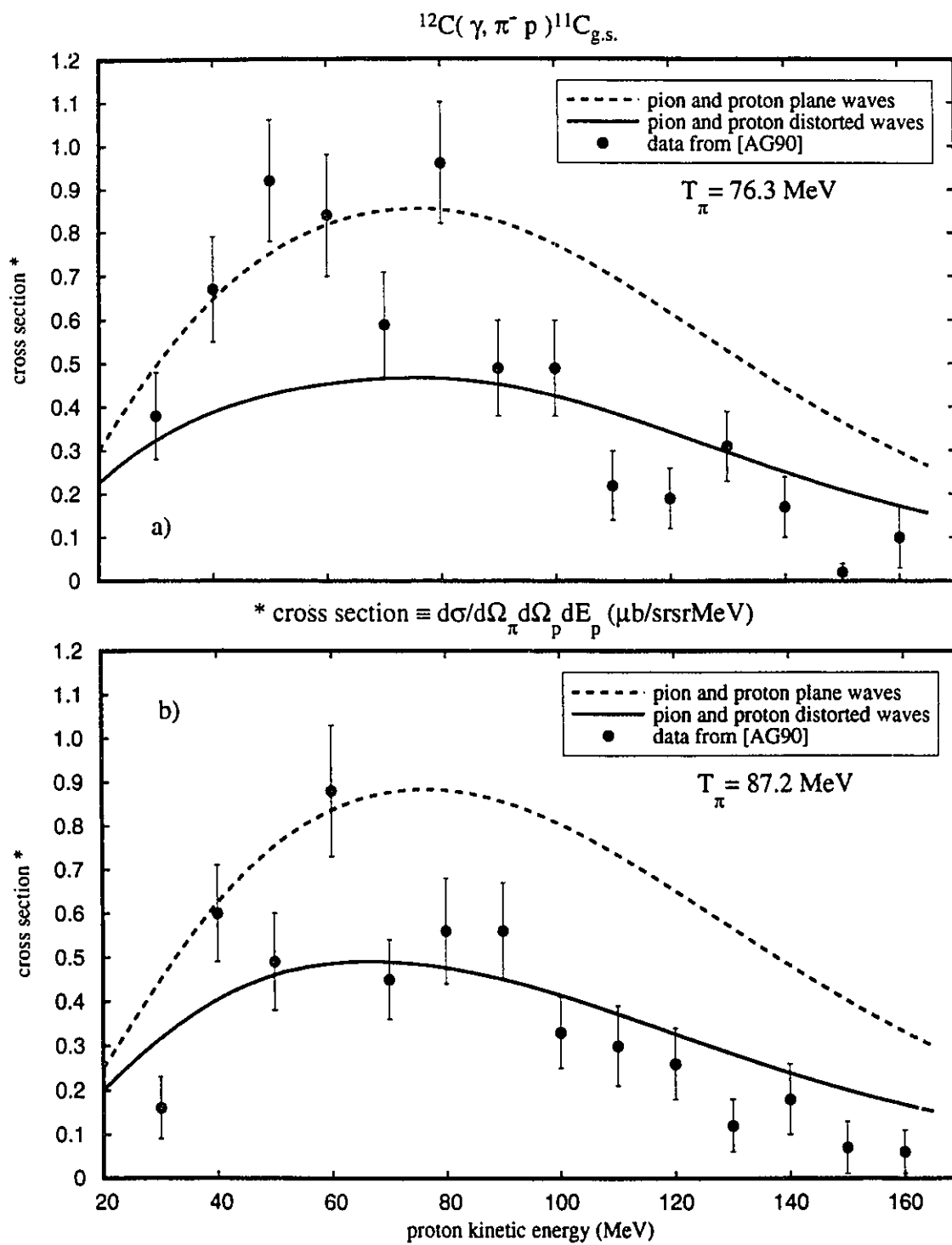


Figure 4-56. Cross section versus proton kinetic energy with pion kinetic energy held constant at a) $T_{\pi} = 76.3$ MeV and b) $T_{\pi} = 87.2$ MeV. The kinematic conditions are $(\theta_p = 40^{\circ}, \varphi_p = 180^{\circ})$ and $(\theta_{\pi} = 120^{\circ}, \varphi_{\pi} = 0^{\circ})$. Dashed curves - proton and pion plane waves. Solid curves - pion distorted by the potential of Oset and proton distorted by the global E and A dependent potential. The data points are from [AG90].

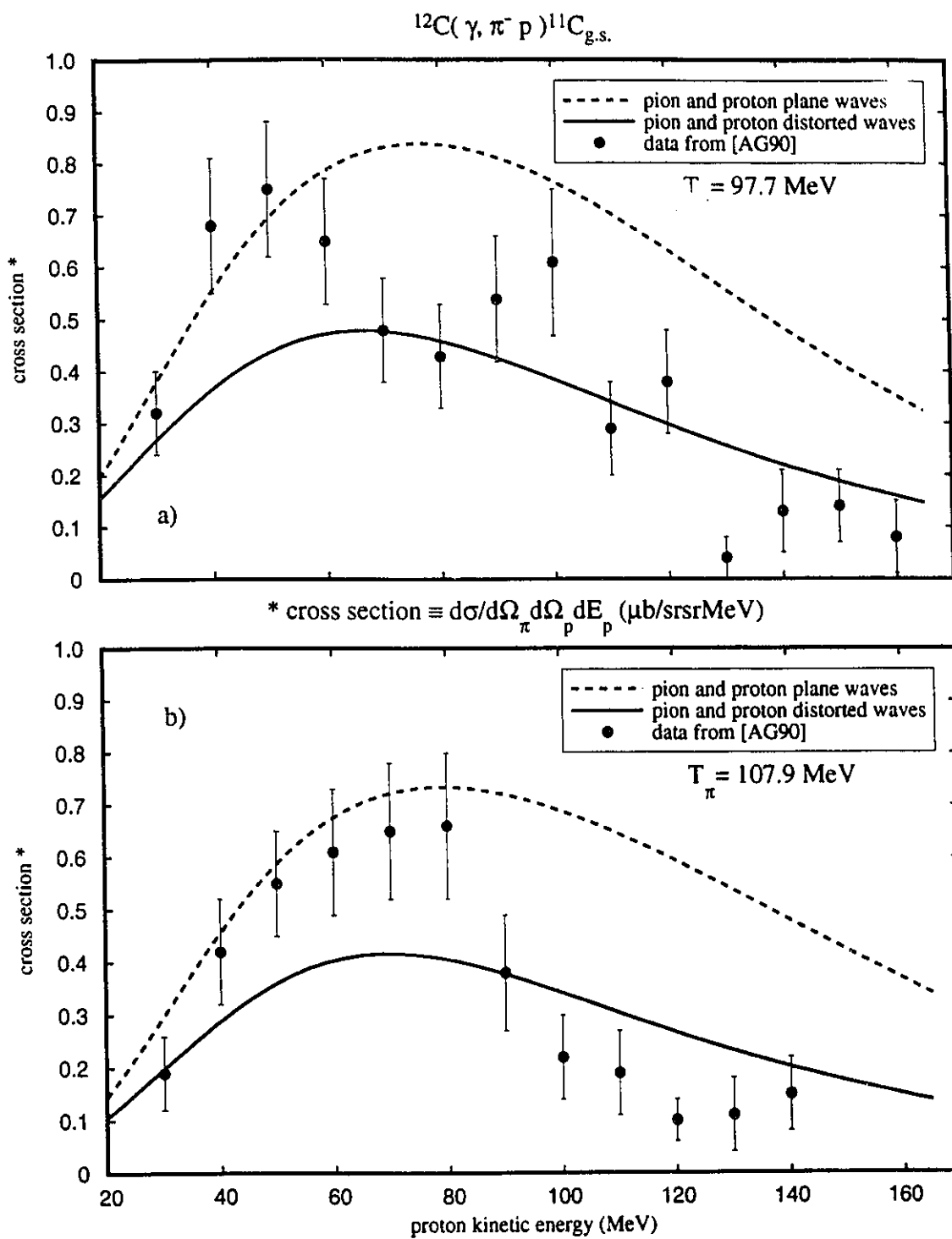


Figure 4-57. Cross section versus proton kinetic energy with pion kinetic energy held constant at a) $T_{\pi} = 97.7$ MeV and b) $T_{\pi} = 107.9$ MeV. The kinematic conditions are $(\theta_p = 40^{\circ}, \varphi_p = 180^{\circ})$ and $(\theta_{\pi} = 120^{\circ}, \varphi_{\pi} = 0^{\circ})$. Dashed curves - proton and pion plane waves. Solid curves - pion distorted by the potential of Oset and proton distorted by the global E and A dependent potential. The data points are from [AG90].

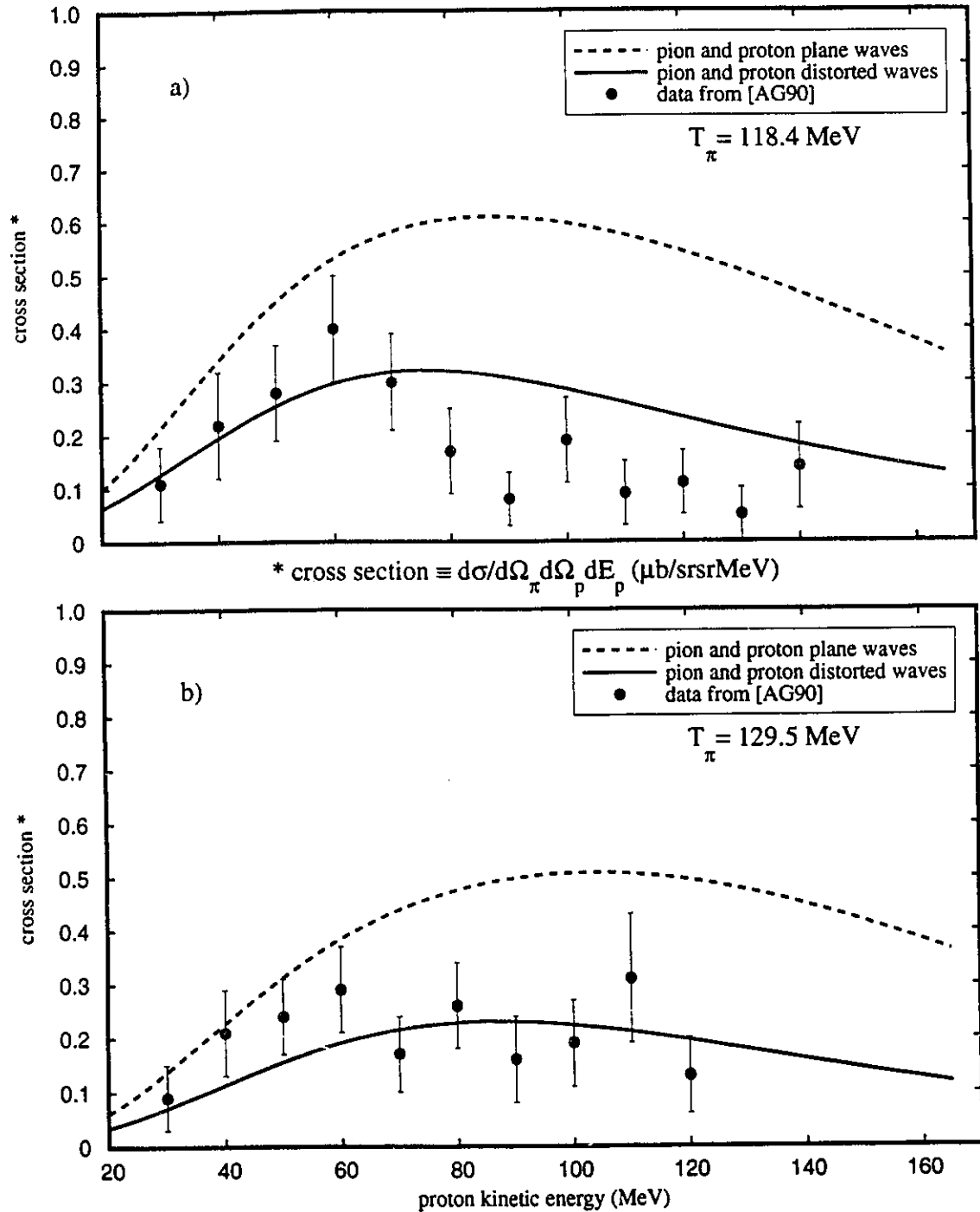
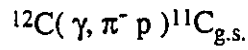


Figure 4-58. Cross section versus proton kinetic energy with pion kinetic energy held fixed at a) $T_\pi = 118.4 \text{ MeV}$ and b) $T_\pi = 129.5 \text{ MeV}$. The kinematic conditions are $(\theta_p = 40^\circ, \varphi_p = 180^\circ)$ and $(\theta_\pi = 120^\circ, \varphi_\pi = 0^\circ)$. Dashed curves - proton and pion plane waves. Solid curves - pion distorted by the potential of Oset and proton distorted by the global E and A dependent potential. The data points are from [AG90].

calculation passes through the data in an average sort of way which is difficult to make conclusions about. The shapes of the curves are not unreasonable, showing a weak maximum around a proton kinetic energy of 60 to 80 MeV which seems consistent with the data.

The data from this experiment were compared to the model of Glavanakov [G189]. His plane wave impulse approximation calculation yields cross sections which are larger than our PW calculations by a factor of about 1.8 for small pion kinetic energies, and decreasing to be smaller than our PW calculations by a factor of 0.9 for the largest pion energy $T_\pi = 129.5$ MeV. In addition his distorted wave results are larger than our DW calculation by a factor of about 1.4 for the small pion energies, and diminish relative to our model until his results are a factor of 0.6 smaller than ours at the largest pion energy. The difference between plane and distorted wave results is about forty to fifty per cent larger in the nonrelativistic analysis of Glavanakov than in our model, indicating that his model is more sensitive to distortions of the pion and proton than ours.

Anan'in and Glavanakov have made the statement [AG90] "At a photon energy ~ 300 MeV the main mechanism of production of pions in $[\gamma + n \rightarrow p + \pi^-]$ is photoexcitation of the $\Delta(1232)$ resonance." An examination of appendix F, in which we discuss the free reaction, shows that this is not true. The delta diagrams do not contribute more to the cross section than the Born terms do. This behaviour is carried over to the kinematically more complicated reaction on a nucleus, and we have not seen a situation in negative pion photoproduction where the cross section for the reaction is currently measurable, and the major contribution comes from the excitation of the delta.

4.4.3 The MIT Experiment

We now consider the results of the pion photoproduction experiment performed by the group at MIT [Ph89, Ph92] on ^{16}O . They state several times in their paper [Ph92] that they have measured an exclusive reaction, but in the same paper they state that they were not able to resolve the ground state and the 6.2 MeV excited state in the residual ^{15}O nucleus.

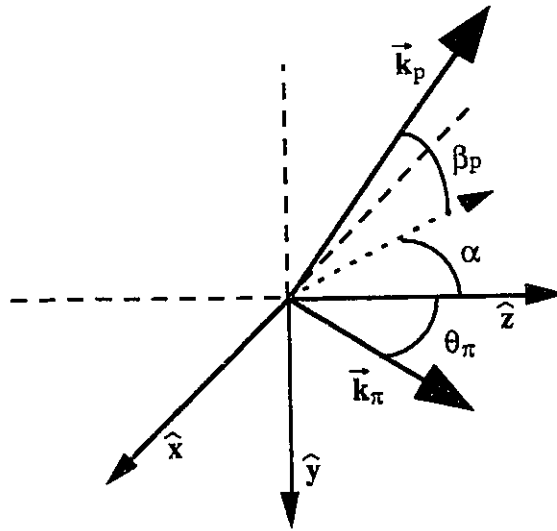


Figure 4-59. Kinematics for the MIT experiment.

The kinematics for the MIT experiment $^{16}\text{O}(\gamma, \pi^- p)^{15}\text{O}$ [Ph92] are shown in figure 4-59. The momentum directions of the photon and pion define the x-z plane. The protons are detected in a vertical array of plastic scintillator counter telescopes located at an angle α from the z-axis in the x-z plane and the cross section is measured as a function of the out-of-plane-angle β_p , the angle from the x-z plane to the proton momentum. Measurements were taken at two pion angles with several proton out-of-plane angles β measured for the proton at each pion angle. One pion angle, $\theta_\pi = 64^\circ$, corresponds to a center of momentum pion angle of 90° in the elementary reaction, while the other pion angle, $\theta_\pi = 120^\circ$, corresponds to a center of momentum pion angle of 135° in the elementary process. For $\theta_\pi = 64^\circ$ ($\alpha_p = 40^\circ$) the pion spectrometer (Bigbite) was able to detect pions with momenta in the range [Ho92]

$$195 \text{ MeV}/c \leq p_\pi \leq 281 \text{ MeV}/c \quad \text{at} \quad \theta_\pi = 64^\circ$$

which translates to a pion kinetic energy range of

$$100 \text{ MeV} \leq T_\pi \leq 174 \text{ MeV} \quad \text{at} \quad \theta_\pi = 64^\circ.$$

The kinematically allowed proton energies from this range of pion energies then vary slightly with the out-of-plane angle and we have the extreme values

$$94 \text{ MeV} \geq T_p \geq 20 \text{ MeV} \quad \text{at} \quad \theta_\pi = 64^\circ, \beta_p = 0^\circ$$

$$92 \text{ MeV} \geq T_p \geq 19 \text{ MeV} \quad \text{at} \quad \theta_\pi = 64^\circ, \beta_p = 40^\circ.$$

For the other pion angle $\theta_\pi = 120^\circ$ ($\alpha_p = 20^\circ$), we have similar limitations on the pion momentum

$$144 \text{ MeV}/c \leq p_\pi \leq 207 \text{ MeV}/c \quad \text{at} \quad \theta_\pi = 120^\circ$$

which we translate as before to a pion kinetic energy range of

$$61 \text{ MeV} \leq T_\pi \leq 110 \text{ MeV} \quad \text{at} \quad \theta_\pi = 120^\circ.$$

The kinematically allowed proton energies from this range of pion energies again vary slightly with the out-of-plane angle and we have the extreme values

$$134 \text{ MeV} \geq T_p \geq 84 \text{ MeV} \quad \text{at} \quad \theta_\pi = 120^\circ, \beta_p = 0^\circ$$

$$130 \text{ MeV} \geq T_p \geq 81 \text{ MeV} \quad \text{at} \quad \theta_\pi = 120^\circ, \beta_p = 40^\circ.$$

The proton detectors were sensitive to protons with kinetic energy in the range [Ph89]

$$30 \text{ MeV} \leq T_p \leq 110 \text{ MeV}$$

and the range of energies in which correlated p- π pairs are detectable is limited to the overlapping energy region of the two detectors.

The bound state is described with a Woods-Saxon potential with the parameters shown in table 4-1, obtained from the Ph.D. thesis of Lotz [Lo89].

Vector potential:	$V_v = 367.37 \text{ MeV}$	$r_v = 1.0739 \text{ fm}$	$a_v = 0.5728 \text{ fm}$
Scalar potential:	$V_s = -451.13 \text{ MeV}$	$r_s = 1.0734 \text{ fm}$	$a_s = 0.6258 \text{ fm}$

Table 4-1. Woods-Saxon binding potential parameters for ^{16}O

The parameters for this binding potential are determined from a search algorithm which gives the best fit to (γ, p) data and describes the $1p_{1/2}$ proton. The coefficient of fractional parentage of the bound state wave function was taken to be 1.0 so the $1p_{1/2}$ proton was assumed to be in an ideal shell model state, an approximation which should be good for the doubly magic ^{16}O nucleus. We use these parameters and adjust the depth of the scalar potential slightly in order to reproduce the separation energy of the $1p_{1/2}$ neutron $E_s = 15.664 \text{ MeV}$ [Aj82], and get the scalar depth $V_s = -451.534 \text{ MeV}$. The

proton wave function is distorted by the global A and E dependent potential of Cooper et al. [Co92] while the pion wave function is distorted by the potential of Oset et al [Ga88, Ni92].

The triple differential cross section as a function of proton kinetic energy for four proton out-of-plane angles, at the backward pion angle $\theta_\pi = 120^\circ$, is shown in figure 4-60. The dip in the curve for $\beta_p = 0^\circ$ (solid) at $T_p = 110$ MeV corresponds to the point where the momentum transfer goes to zero as shown in figure 4-61. At this point the momentum space wave function for the $1p_{1/2}$ neutron is zero just like the $1p_{3/2}$ neutron wave function in ^{12}C shown in figure 3-6. At $\beta_p = 10^\circ$ (small dash - large dash curve) the momentum transfer over the observable region has increased to roughly 0.5 fm^{-1} , moving toward the peak of the bound state wave function. The cross section at this point has a bell shape which it maintains through larger values of the out-of-plane angle, and hence momentum transfer, while the magnitude of the peak cross section decreases by nearly a factor of ten between $\beta_p = 10^\circ$ and $\beta_p = 30^\circ$.

The vertical dotted lines indicate the minimum and maximum kinetic energies of protons detectable by the telescope array. The vertical dashed lines indicate the minimum and maximum proton kinetic energies corresponding to the limits of pion momentum detectable by the MIT pion spectrometer Bigbite. The overlapping range, indicated by the arrow, is the range of proton kinetic energies over which correlated pion-proton pairs are detectable by their apparatus. The lower limit is set by the lower limit of the pion detector and the upper limit is defined by the upper limit of the proton array.

Figure 4-62 shows the cross section as a function of proton kinetic energy for four proton out-of-plane angles at the forward pion angle $\theta_\pi = 64^\circ$. The shoulder at $T_p = 40$ MeV occurs because of the small-momentum behaviour of the bound state wave function, as we have seen before. The vertical dotted lines in the figure indicate the limits of proton momentum from the proton detector while the vertical dashed lines indicate the limits from the pion detector. The range of detectable correlated π -p pairs is indicated by the horizontal arrow. Here the lower limit is set by the lower limit of the proton detector while the upper limit is defined by the upper limit of the pion spectrometer.

The momentum transfer corresponding to the cross section curves for the out-of-plane angles of figure 4-62, is shown in figure 4-63 along with the limits imposed by the

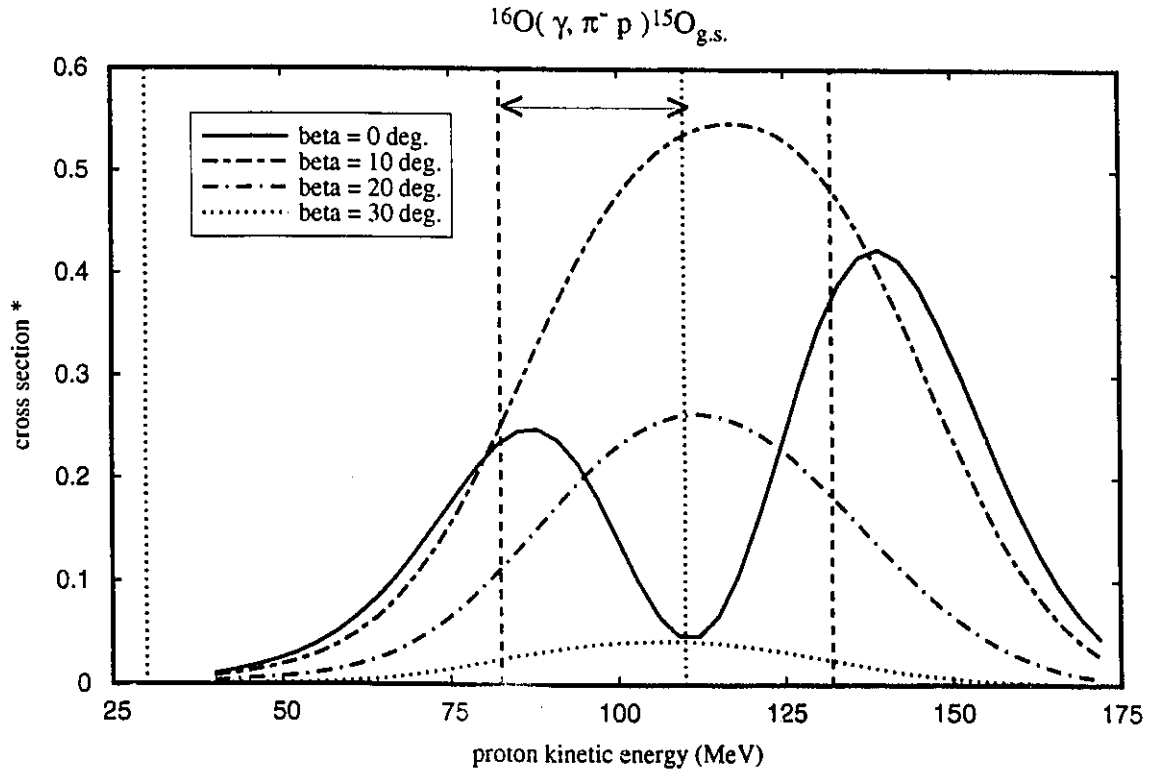


Figure 4-60. Cross section versus proton kinetic energy for four out-of-plane angles. The kinematic conditions are $E_{\gamma} = 350 \text{ MeV}$, ($\alpha_p = 20^\circ$, β_p varies) and ($\theta_{\pi} = 120^\circ$, $\phi_{\pi} = 0^\circ$). Pion distorted by the potential of Oset and proton distorted by the global E and A dependent potential. Curves as indicated in the legend for out-of-plane angles: $\beta_p = 0^\circ, 10^\circ, 20^\circ, 30^\circ$. Vertical dotted lines - proton detector limits and vertical dashed lines - proton energy range determined by pion detector limits.

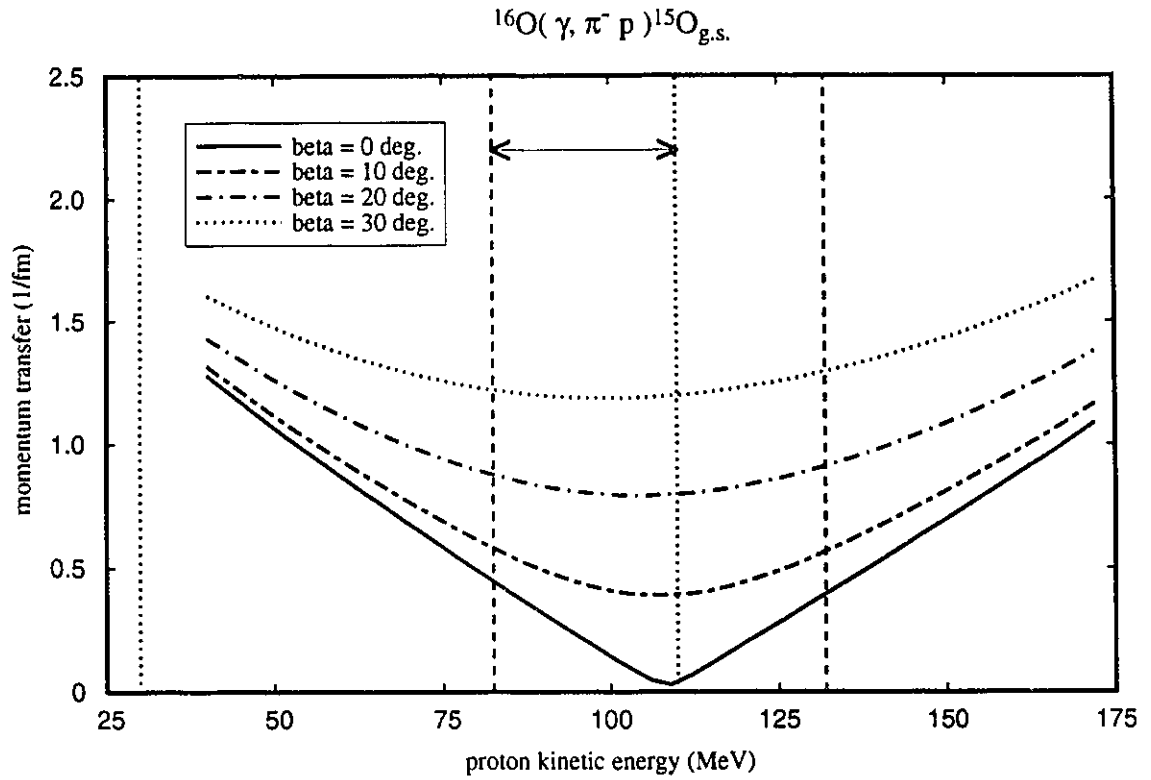


Figure 4-61. Change in momentum transfer to the nucleus as the out of plane angle is varied. The kinematic conditions are $E_{\gamma} = 350 \text{ MeV}$,

($\alpha_p = 20^\circ$, β_p varies) and ($\theta_{\pi} = 120^\circ$, $\phi_{\pi} = 0^\circ$). Curves as indicated in the legend for out-of-plane angles: $\beta_p = 0^\circ, 10^\circ, 20^\circ, 30^\circ$.

Vertical dotted lines - proton detector limits and vertical dashed lines - proton energy range determined by pion detector limits.

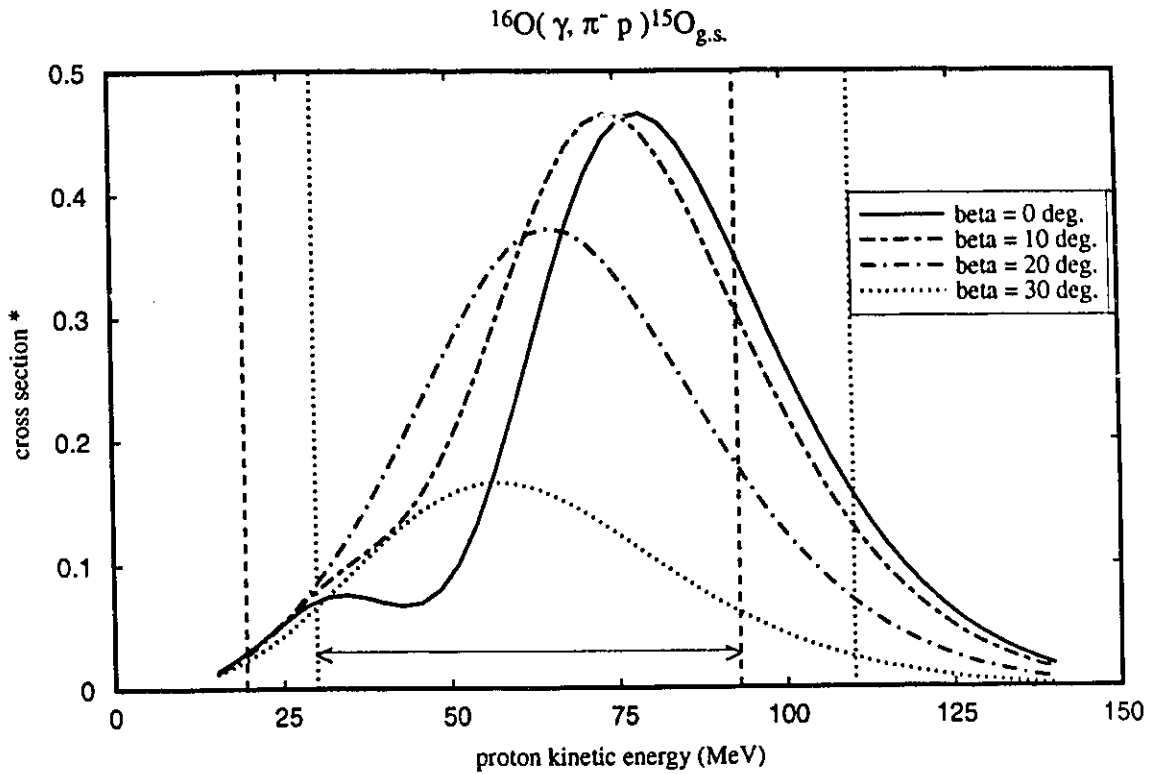


Figure 4-62. Cross section versus proton kinetic energy for four out-of-plane angles. The kinematic conditions are $E_{\gamma} = 350$ MeV., ($\alpha_p = 40^{\circ}$, β_p varies) and ($\theta_{\pi} = 64^{\circ}$, $\varphi_{\pi} = 0^{\circ}$). Pion distorted by the potential of Oset and proton distorted by the global E and A dependent potential. Curves are as indicated in the legend for proton out-of-plane angles: $\beta_p = 0^{\circ}, 10^{\circ}, 20^{\circ}, 30^{\circ}$. Vertical dotted lines - proton detector limits and vertical dashed lines - proton energy range set by pion detector limits.

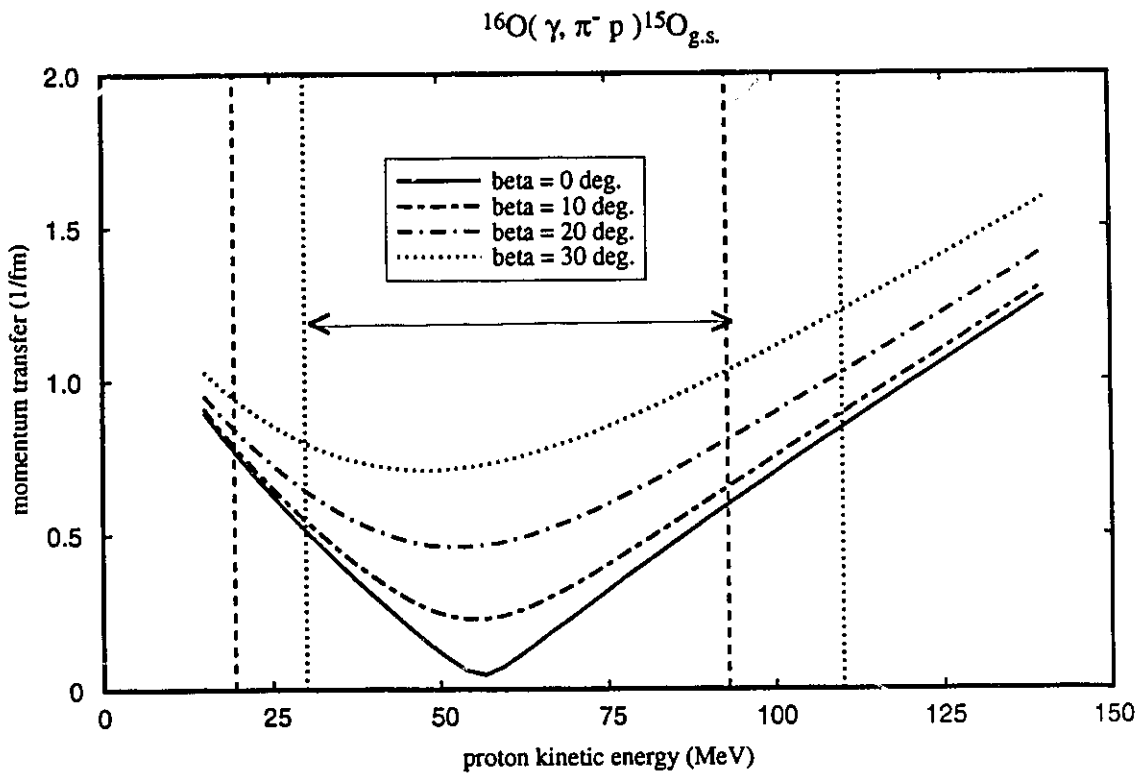


Figure 4-63. Change in momentum transfer to the nucleus as the out of plane angle is varied. The kinematic conditions are $E_{\gamma} = 350 \text{ MeV}$,

($\alpha_p = 40^\circ$, β_p varies) and ($\theta_{\pi} = 64^\circ$, $\varphi_{\pi} = 0^\circ$). Curves are as indicated in the legend for proton out-of-plane angles: $\beta_p = 0^\circ, 10^\circ, 20^\circ, 30^\circ$.

Vertical dotted lines - proton detector limits and vertical dashed lines - proton energy limits defined by pion detector limits.

detectors. The momentum transfer varies by 0.5 fm^{-1} or less over the detectable range of proton energies for each of the out-of-plane angles in both figure 4-61 and 4-63.

The spin observables for the out-of-plane cross sections are shown in figures 4-64 and 4-65. The polarization shown in figure 4-64a) shows a rapid change as the momentum transfer passes through zero for the case when the proton is detected in the plane, while the cases which are out of the plane follow each other quite closely. The rapid change through the zero of momentum transfer is also apparent in the analyzing power calculation of figure 4-64b). The analyzing power, unlike the polarization, does show a fairly strong variation with the out-of-plane angle, changing by up to forty per cent when beta changes from 0° to 30° . We see essentially the same behaviour in figure 4-65. The polarization here doesn't vary much with out-of-plane angle, while for proton kinetic energies less than 50 MeV the analyzing power shows a fairly strong variation with out-of-plane angle.

In figure 4-66 we compare the experimental data from MIT [Ph92] for the forward pion angle $\theta_\pi = 64^\circ$, with our calculations. the solid curve is the result of integrating triple cross sections such as those shown in figure 4-63 over the allowed range of proton energies indicated by the arrow. Similarly in figure 4-67 we compare the data at the backward pion angle $\theta_\pi = 120^\circ$ with the cross sections obtained by integrating the triple cross sections of figure 4-60 over the allowed proton kinetic energy range. The calculation at the forward pion angle is two to three times larger than the data while for the backward angle the calculations are in relatively better agreement with the data. At neither pion angle does the shape of the data set agree with that of the calculation. The data are peaked at $\beta_p = 0^\circ$ and fall off with increasing β_p while the calculation has peaks at out-of-plane angles of $\beta_p = 11^\circ$ - 12° around a minimum at $\beta_p = 0^\circ$. The shape of the calculated curve is readily understandable by looking at the triple cross sections of figures 4-60 and 4-63. The integrated cross section for $\beta_p = 0^\circ$ is smaller than that at $\beta_p = 10^\circ$ because at small β_p the shape of the triple cross section is strongly affected by the low momentum behaviour of the bound state wave function.

The dotted curves of figures 4-66 and 4-67 show the cross section calculated from the Born terms only, while the dashed lines are the cross section calculated from the delta

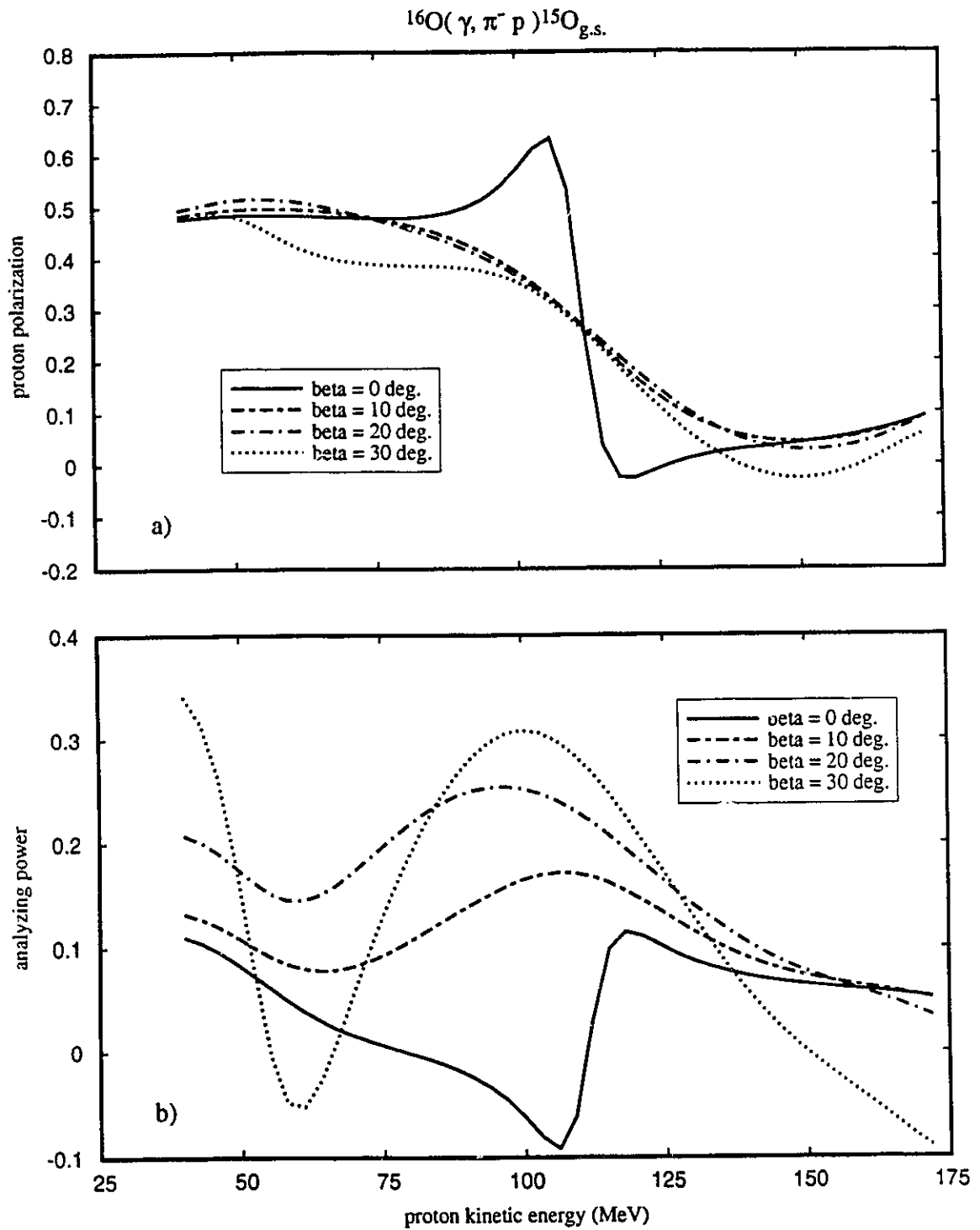


Figure 4-64. Change in spin observables as the out-of-plane angle β is varied. Pion distorted by the potential of Oset and proton distorted by the global E and A dependent potential. Lines as for figure 4-60.

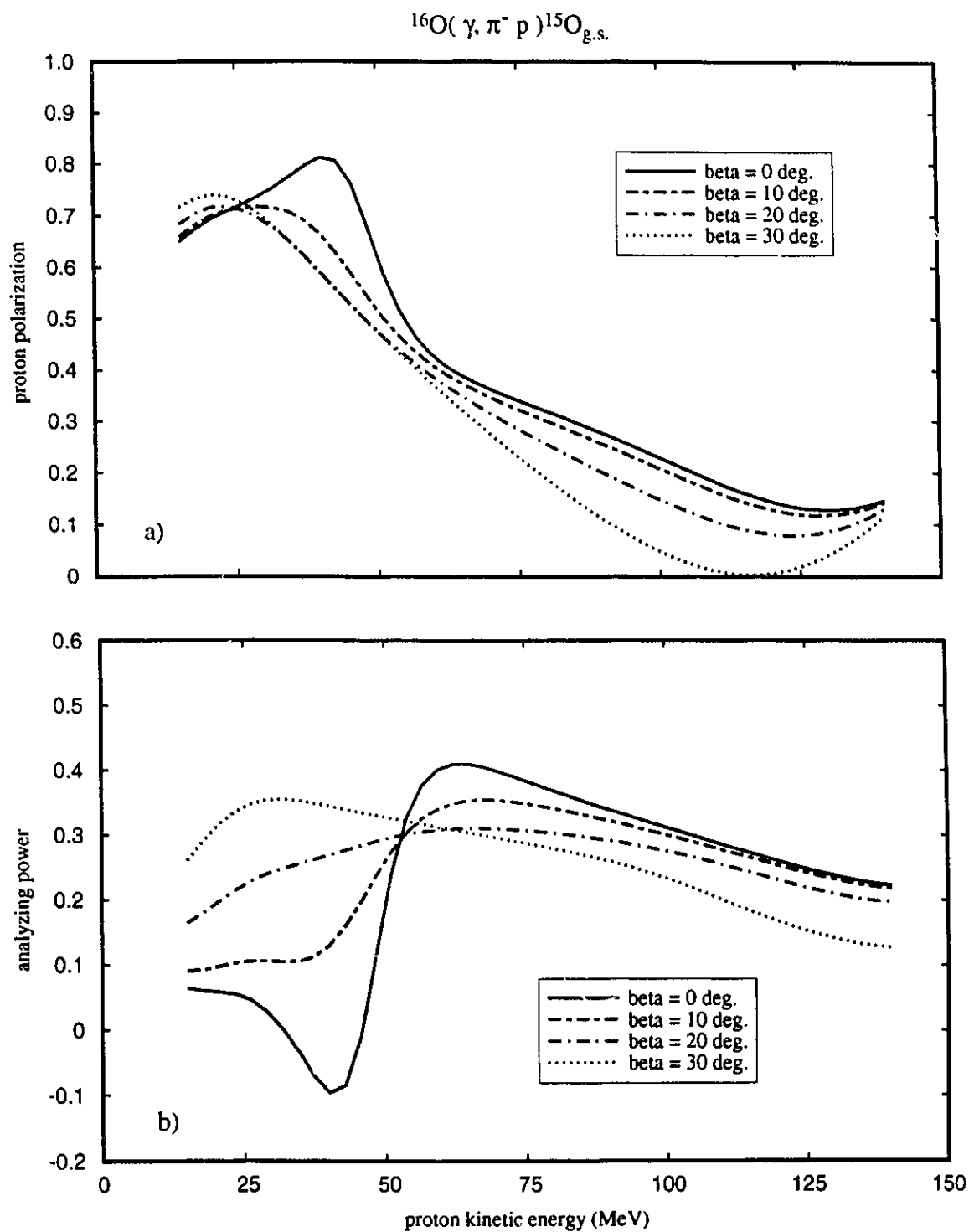
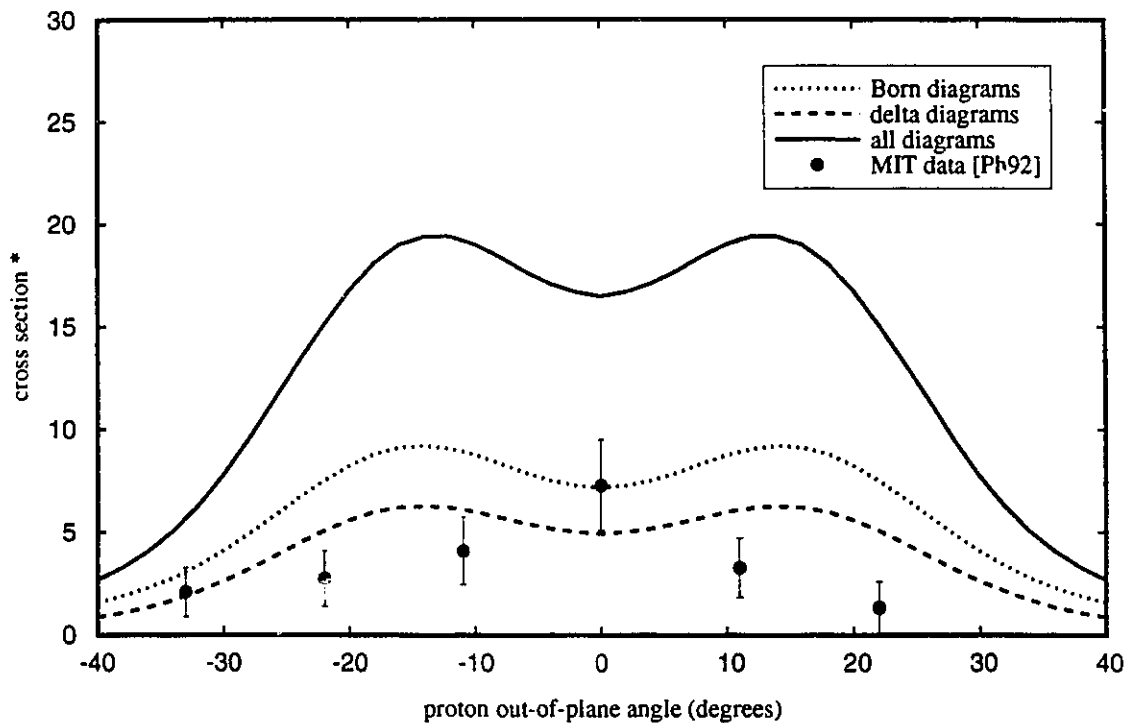


Figure 4-65. Change in spin observables as the out-of-plane angle β is varied. Pion distorted by the potential of Oset and proton distorted by the global E and A dependent potential. Lines as for figure 4-63.

$^{16}\text{O}(\gamma, \pi^- p)^{15}\text{O}_{\text{g.s.}}$



* cross section $\equiv d\sigma/d\Omega_{\pi} d\Omega_p$ ($\mu\text{b/sr sr}$)

Figure 4-66. Cross section versus proton out-of-plane angle. The kinematic conditions are $E_{\gamma} = 350 \text{ MeV.}$, ($\alpha_p = 40^\circ$, β_p varies) and ($\theta_{\pi} = 64^\circ$, $\phi_{\pi} = 0^\circ$). Pion distorted by the potential of Oset and proton distorted by the global E and A dependent potential. Data points are from [Ph92]. Dotted line - Born terms only. Dashed line - delta diagrams only. Solid line - sum of all diagrams.

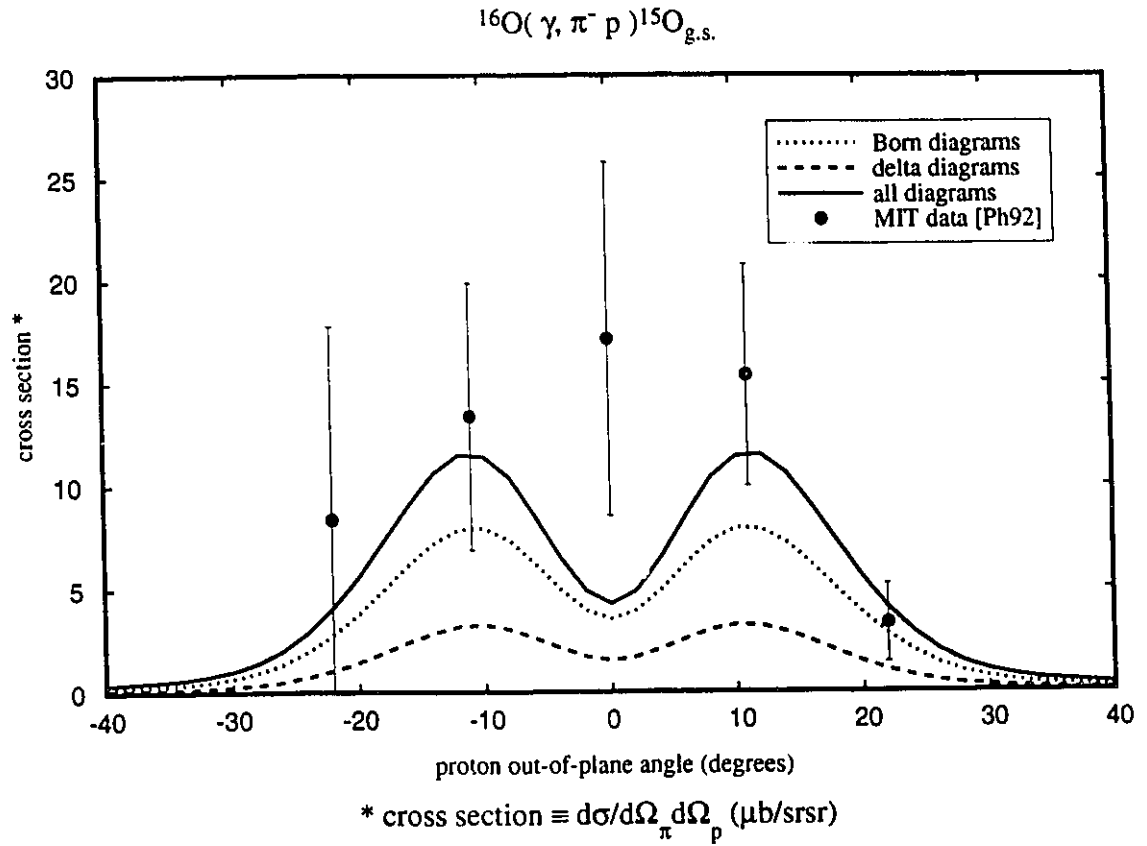


Figure 4-67. Cross section versus proton out-of-plane angle. The kinematic conditions are $E_{\gamma} = 350 \text{ MeV.}$, ($\alpha_p = 20^\circ$, β_p varies) and ($\theta_{\pi} = 120^\circ$, $\phi_{\pi} = 0^\circ$). Pion distorted by the potential of Oset and proton distorted by the global E and A dependent potential. Data points are from [Ph92]. Dotted line - Born terms only. Dashed line - delta diagrams only. Solid line - sum of all diagrams.

diagrams only. Note that the Born terms are the major contributors in both calculations, but at the forward pion angle the magnitude of the delta cross section is two thirds that of the Born cross section while the cross section calculated from the sum of all the diagrams is twice that of the Born cross section. At the backward pion angle the magnitude of the delta cross section is slightly less than one half that of the Born cross section and the total cross section is about 1.5 times that of the Born cross section. The delta diagrams are larger contributors to the cross section at the forward pion angle than at the backward angle, and the delta contribution is certainly important to obtain the final cross section but the delta is not the most important contributor here. This result is contrary to the analysis of Pham [Ph89], and we next examine their analysis in more detail.

The dotted curve of figure 4-68 shows the factorized nonrelativistic distorted wave calculation of Pham for the backward pion angle, which we read from figure 5.10 of his thesis [Ph89]. The triple differential cross section was integrated over the momentum acceptance of the pion detector (see page 170 of his thesis [Ph89], or the model calculations section of the paper [Ph92]), corresponding to integration between the dashed vertical lines of figure 4-60. The dashed curve of figure 4-68 shows our calculation using the momentum limits of the pion detector. The solid curve of figure 4-68 shows the result of our calculation when we use the integration limits as set by the combination of detectors. This reduces the cross section by about a factor of two because the proton detector lowers the upper limit of detectable proton energy from 130 MeV to 110 MeV as shown in figure 4-60, resulting in a significant reduction of the total cross section.

In figure 4-69 we show Pham's calculation for the forward pion angle, from figure 5.9 of his thesis. Again the integration limits are set by the pion detector only, corresponding to integration between the vertical dashed lines of figure 4-63. The dashed curve shows our calculations with limits set by the pion detector, while the solid curve shows the calculations using the limits set by both detectors. In this case the reduction in the cross section is only a few per cent because the proton detector changes the lower limit of the detectable proton energy from 20 MeV to 30 MeV, and the cross section in this range is quite small as can be seen in figure 4-63.

In order to gauge the importance of the delta isobar in the reaction, Pham [Ph89]

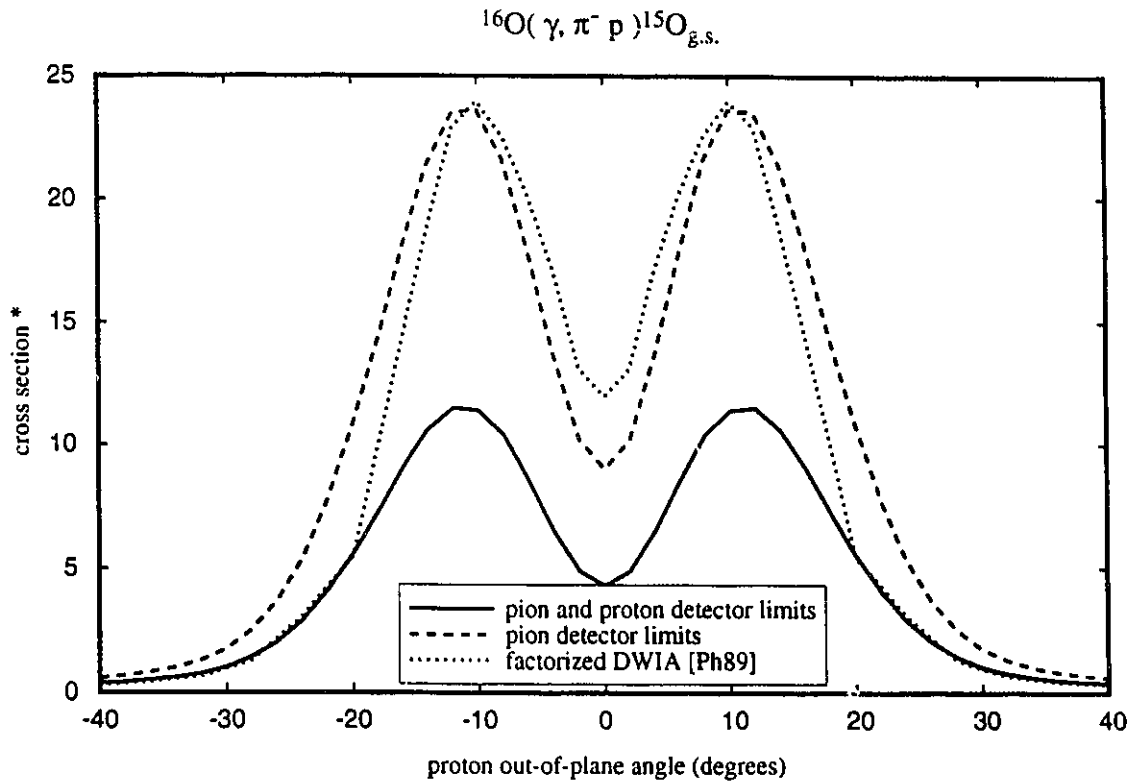


Figure 4-68. DW calculations with different integration limits. The kinematic conditions are $E_{\gamma} = 350 \text{ MeV.}$, ($\alpha_p = 20^\circ$, β_p varies) and ($\theta_{\pi} = 120^\circ$, $\phi_{\pi} = 0^\circ$).

Pion and proton distorted waves.

Dotted line - Pham's factorized DWIA calculation.

Dashed line - Our DW calculation with the pion distorted by the potential of Oset, and the proton distorted by the global E and A dependent potential.

Integration limits set by pion and proton detectors. Solid line - Our calculation with integration limits set by the pion detector alone.

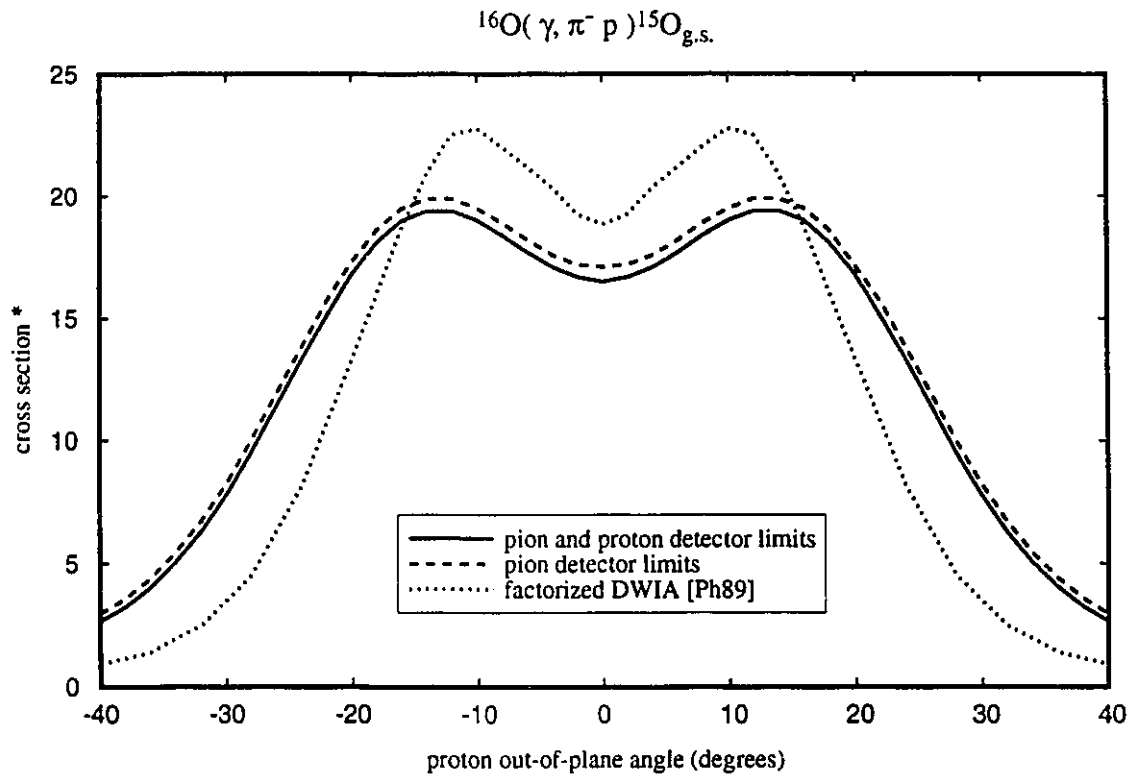


Figure 4-69. DW calculations with different integration limits. The kinematic conditions are $E_{\gamma} = 350 \text{ MeV.}$, ($\alpha_p = 40^{\circ}$, β_p varies) and ($\theta_{\pi} = 64^{\circ}$, $\phi_{\pi} = 0^{\circ}$).

Pion and proton distorted waves.

Dotted line - Pham's factorized DWIA calculation.

Dashed line - Our DW calculation with the pion distorted by the potential of Oset and the proton distorted by the global E and A dependent potential.

Integration limits set by pion and proton detectors. Solid line - Our calculation with integration limits set by the pion detector alone.

calculated the cross section without the delta diagrams (Born terms only), and again with all the diagrams except the seagull. The cross section for the backward pion angle is shown in figure 4-70. The dashed line shows the cross section calculated with the Born diagrams only while the dotted line is the cross section calculated from the delta diagrams only. The solid line is the cross section calculated from the sum of all the diagrams. The cross section calculated from the sum of all the diagrams except the seagull is the dot-dashed line. Pham noted that the calculation with no delta (dashed) is larger than the calculation with no seagull (dot-dashed) and concluded that the seagull contribution is the most important at this angle.

We can take a closer look at the contributions of the various diagrams by calculating the cross section from each diagram individually, which we have done in figure 4-71. The seagull diagram gives the largest cross section while the s-channel delta gives a cross section about two thirds of the magnitude of the seagull. The proton pole and the pion pole give cross sections roughly one quarter of that of the seagull, while the neutron pole and the u-channel delta give cross sections less than ten per cent of that of the seagull. So it seems that the seagull contribution is the most important at this angle.

The cross section calculated for the forward pion angle are shown in figure 4-72, and the curves are labelled as they are in figure 4-70. Here the calculation with no seagull (dot-dashed) is larger than the calculation with no delta (dashed), which led Pham to conclude that the delta contribution is the most important at this angle. This would be true if we only had contributions from the seagull and the delta.

Figure 4-73 shows the cross section calculated for each of the contributing diagrams at the forward pion angle. The seagull diagram gives the largest cross section, as it did for the backward pion angle and the s-channel delta gives a cross section which has increased to about 75% of the seagull cross section. The cross section due to the pion pole is now almost two-thirds of the seagull cross section, and is much more important than it was at the backward pion angle. The other diagrams give cross sections that are about ten per cent or less of the seagull cross section. Note that for both the forward and backward pion angles, the cross section calculated from the Born terms alone (dashed) is larger than the cross section calculated from the delta diagrams alone (dotted), and while the delta contribution is larger relative to the Born contribution at the forward pion angle, the

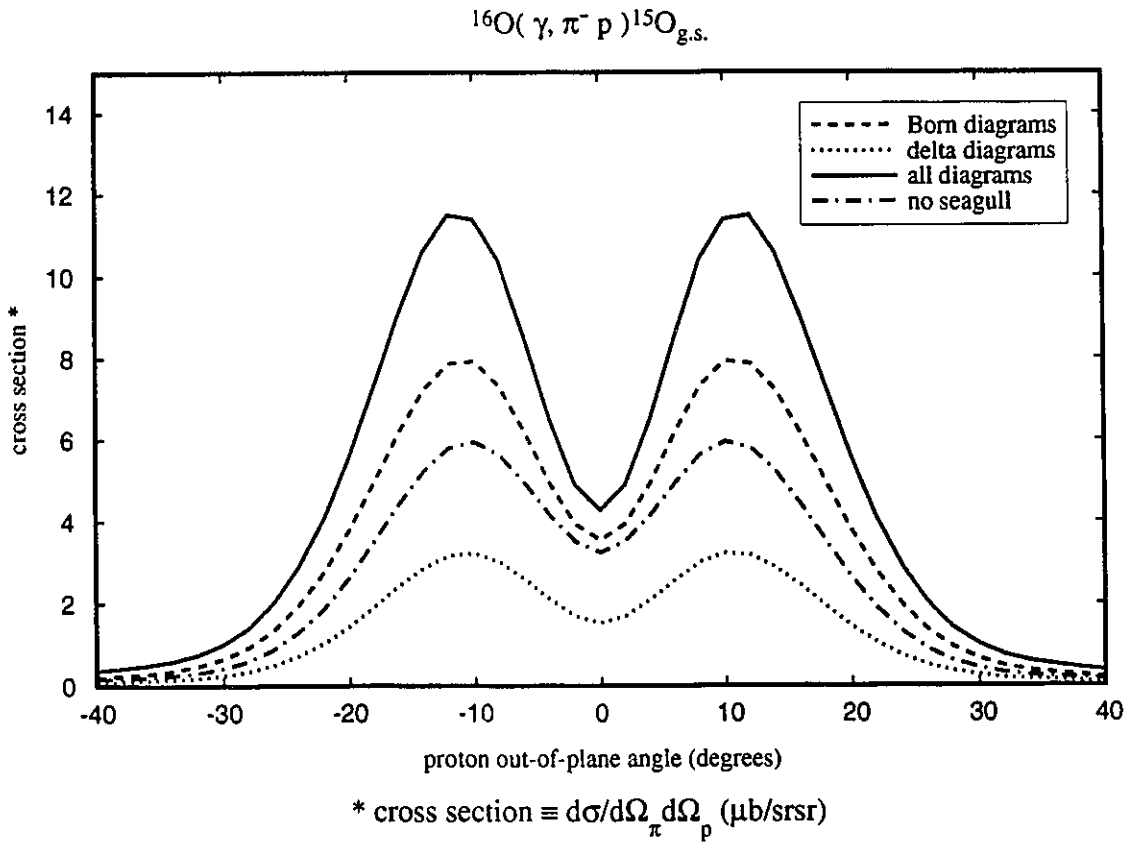


Figure 4-70. Cross section versus proton out-of-plane angle. The kinematic conditions are $E_{\gamma} = 350 \text{ MeV.}$, ($\alpha_p = 20^\circ$, β_p varies) and ($\theta_{\pi} = 120^\circ$, $\phi_{\pi} = 0^\circ$). Pion distorted by the potential of Oset and proton distorted by the global E and A dependent potential. Dashed line - Born terms only. Dotted line - delta diagrams only. Solid line - sum of all diagrams. Dot-dashed line - all diagrams except seagull.

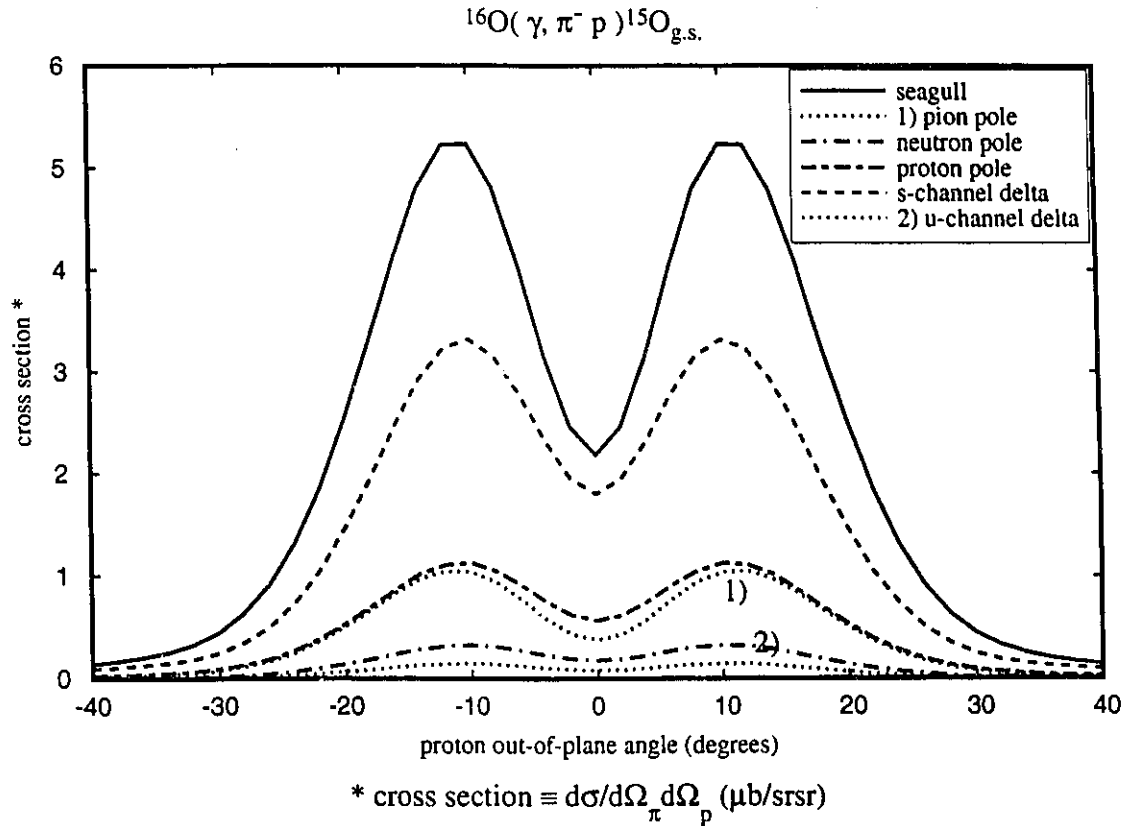


Figure 4-71. Cross section calculated from the s-matrix of the individual diagrams. The kinematic conditions are $E_{\gamma} = 350 \text{ MeV.}$, ($\alpha_p = 20^\circ$, β_p varies) and ($\theta_{\pi} = 120^\circ$, $\varphi_{\pi} = 0^\circ$). Pion distorted by the potential of Oset and proton distorted by the global E and A dependent potential. The curves are discussed in the text.

$^{16}\text{O}(\gamma, \pi^- p)^{15}\text{O}_{\text{g.s.}}$

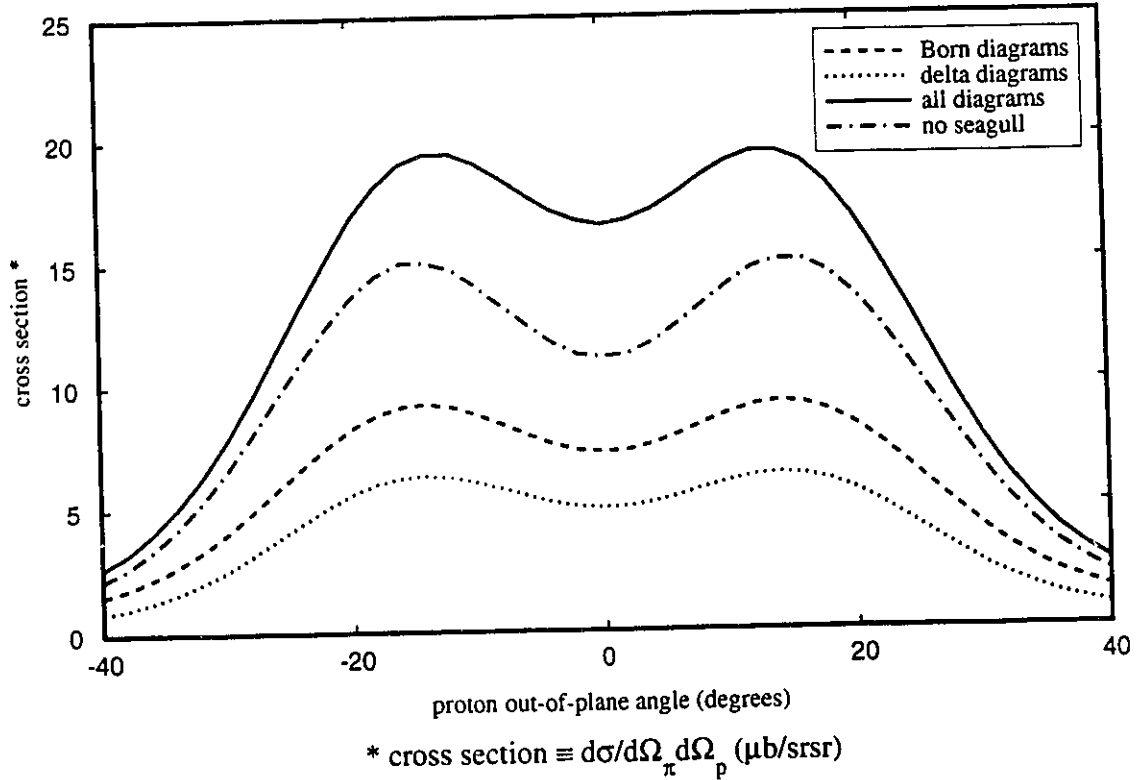


Figure 4-72. Cross section versus proton out-of-plane angle. The kinematic conditions are $E_{\gamma} = 350 \text{ MeV.}$, ($\alpha_p = 40^\circ$, β_p varies) and ($\theta_{\pi} = 64^\circ$, $\varphi_{\pi} = 0^\circ$). Pion distorted by the potential of Oset and proton distorted by the global E and A-dependent potential. Dashed line - Born terms only. Dotted line - delta diagrams only. Solid line - sum of all diagrams. Dot-dashed line - all diagrams except seagull.

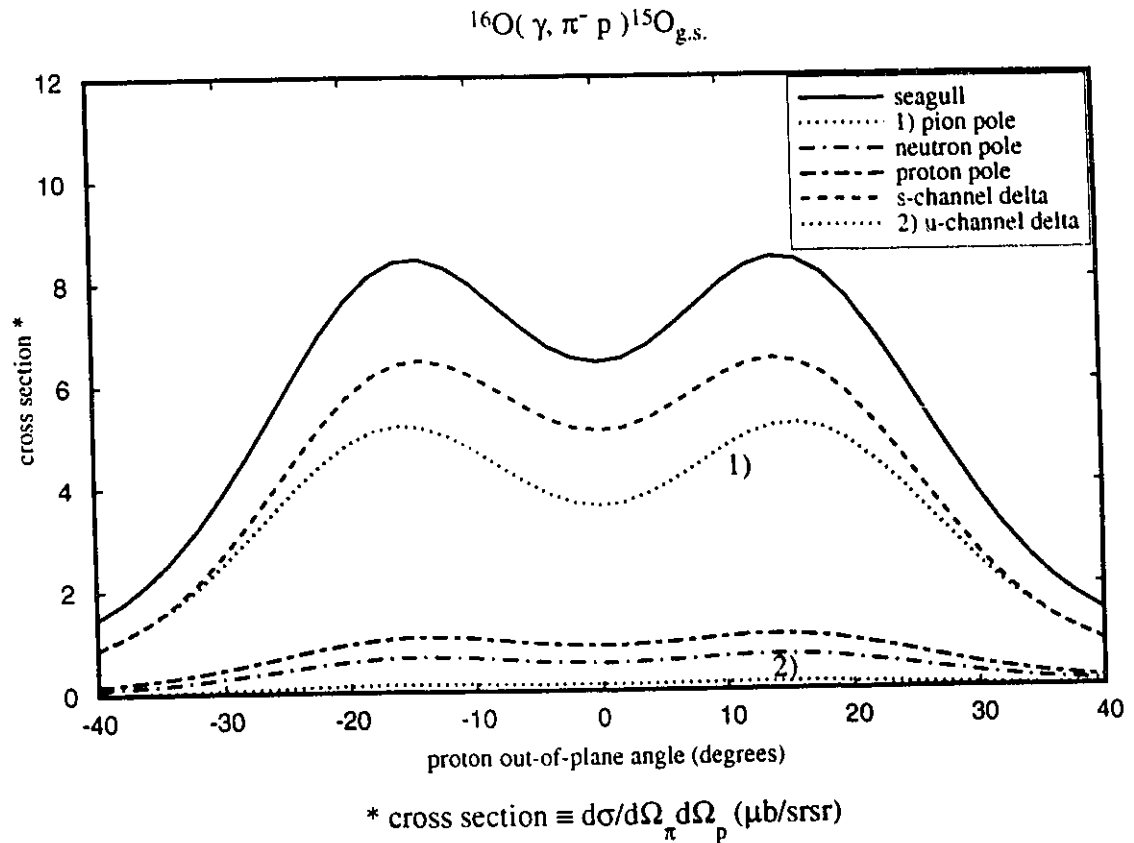


Figure 4-73. Cross section calculated from the s-matrix of the individual diagrams. The kinematic conditions are $E_{\gamma} = 350 \text{ MeV}$, ($\alpha_p = 40^\circ$, β_p varies) and ($\theta_{\pi} = 64^\circ$, $\phi_{\pi} = 0^\circ$). Pion distorted by the potential of Oset and proton distorted by the global E and A dependent potential. The curves are discussed in the text.

statement that the delta is 'the most important at this angle' is not supported. The reason the cross section calculated with no seagull diagram is larger than that calculated for no delta at the forward pion angle, is that the pion pole diagram has become an important contributor to the cross section and interferes with the the delta and the seagull in such a way that the pion pole plus the delta yields a larger cross section than the pion pole plus the seagull (ignoring the other three diagrams) for the forward pion angle.

We therefore find that at the backward pion angle our calculation is close to the data, while at the forward pion angle our calculation is a factor of two to three above the data. We have no explanation for the discrepancy but do make two observations about the data.

First both measurements were performed near free kinematics where the elementary process occurring on a single bound neutron should be a good approximation. Our model yields triple differential cross sections with peaks of about $0.5 \mu\text{b/srMeV}$ for both pion angles within the range of proton energies allowed by the detectors. Integration over the allowed range results in the integrated cross section being about twice as large for the forward pion angle as the backward angle. The data however are twice as large for the backward angle as for the forward. This would seem to imply some mechanism for the forward angle, corresponding to a pion center of momentum angle of 90° in the free process, which reduces the cross section relative to the DW cross section of our one nucleon model. It might be argued that mechanisms involving the diagrams containing propagating particles, such as non-locality and interaction in the propagators or the effects of changing the Δ mass, could reduce the magnitude of the contribution of the corresponding diagrams, but it is difficult to imagine that they could reduce the cross section to the size of the cross section calculated from the seagull diagram alone, which is what would be required. Alternatively, distortion effects of the proton and pion or different prescriptions for the bound state wave function might be thought to affect the seagull diagram as well as the other diagrams. These wave functions are obtained from other sources, are very well determined and have no parameters which we can adjust in order to improve the description of the data. Other reaction mechanisms would probably increase the total cross section over that obtained from the one nucleon model, and so

can't provide the necessary reduction.

Secondly, the cross section in the neighbourhood of zero momentum transfer must be strongly affected by the behaviour of the momentum space bound state wave function, an effect which is clear in our calculations but is not reflected in the data. As we have seen, Glavanakov et al. have measured the pion photoproduction cross section from carbon at $\theta_\pi = 120^\circ$ with $\theta_p = 20^\circ$ [GS79, G189], i.e. at the same angles as the MIT experiment, although the Russian experiment had an incident photon energy of 380 MeV instead of 350 MeV. Glavanakov et al. did observe the cross section becoming small when the momentum transfer became zero, consistent with the behaviour of our one nucleon model. The MIT data provide no indication that the momentum dependence of the p-shell neutron is affecting the cross section. The most noticeable effect would come in the backward pion angle data according to the one nucleon model, but these data have very large error bars and conclusive statements are not possible.

We have obtained good agreement with the existing experimental data in some cases, and in other cases the model disagrees with the data. The comparisons are not convincing however due to the uncertainties in the data. The Tomsk data are not truly exclusive as the final state of the residual nucleus could not be resolved, and the cross sections contain some events in which the residual nucleus is left in an excited state. These events were estimated to be less than twenty per cent of the total in the 1979 experiment [GS79a], and less than ten per cent in the 1990 experiment [AG90]. The MIT data are presented as exclusive data but they couldn't resolve the ground state from the 6.2 MeV excited state, and the error bars are quite large due to the small number of events recorded. We need high quality data, with a large number of recorded events and a well resolved state of the final nucleus, before we can make any strong statements about the limits of applicability of our model in this reaction.

Chapter 5 - A One Nucleon Model for the Reaction $A(\pi^+, \gamma p)A-1$

In the $(\pi^+, \gamma p)$ reaction, the incident positively charged pion interacts with a bound neutron through some process denoted by the blob in figure 5-1. A proton and photon are produced and are detected experimentally and the residual nucleus is left in a definite state. We treat this reaction along the same lines as the $(\gamma, \pi^- p)$ reaction discussed in chapters 3 and 5. The wave functions for the initial neutron and final proton are, as before, solutions of the Dirac equation with appropriate scalar and vector potentials; these describe the interactions of the particles with the initial and final nuclei. The pion wave function is a solution of the Klein-Gordon equation with an appropriate optical potential for the pion-nucleus system. We include contributions to the interaction blob by the diagrams shown in figure 5-2. The four diagrams, (5-2a) to 5-2d), are the Born terms, and the diagrams 5-2e) and 5-2f) are the s-channel and u-channel Δ diagrams. Note that in figure 5-2d) the photon can couple to the proton through both the electric charge and the anomalous magnetic moment of the proton, while in figure 5-2c) the photon can only couple to the neutron through the anomalous magnetic moment.

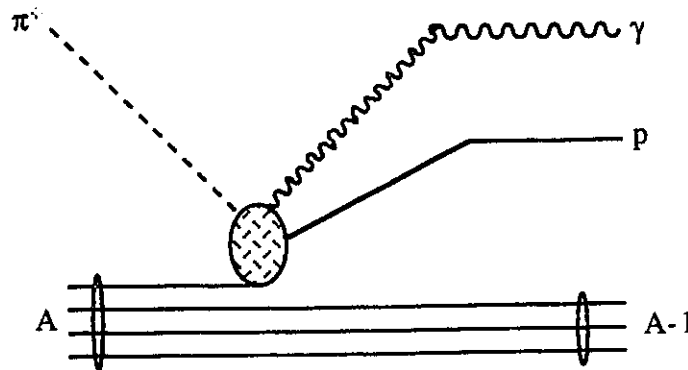


Figure 5-1. The one nucleon model for $A(\pi^+, \gamma p)A-1$

The lagrangian density we use is that described in chapter 3 for the pion photoproduction reaction. The difference between the two reactions is that we now have a positive pion incident on the target, while the photon appears in the final state. This will

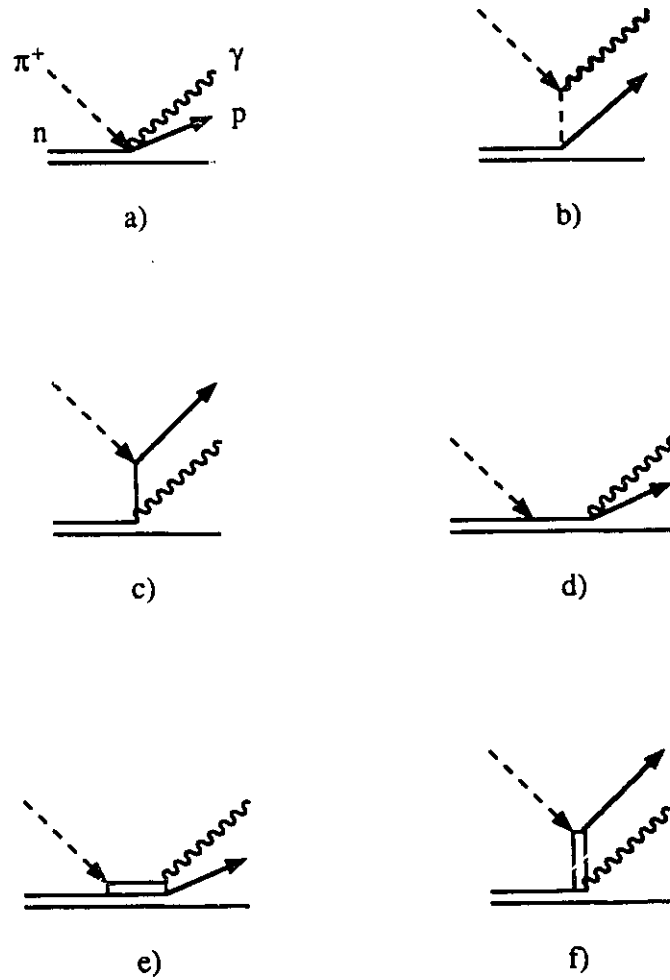


Figure 5-2. Diagrams contributing to pion-induced photon production on a nucleus. a-d) the Born terms, e) the s-channel Δ diagram, and f) the u-channel Δ diagram.

change some of the details of the calculations but the techniques are the same as we have seen before. We will simply highlight the differences and quote the results leaving the derivations to the interested reader.

5.1 The Reaction Amplitude

For the reaction $A(\pi^+, \gamma p)A-1$ the initial state $|i\rangle$ contains a positively charged pion and a nucleus with A nucleons, while the final state $|f\rangle$ contains a photon, a proton ejected from the initial nucleus and a final nucleus with $A-1$ nucleons. In this one nucleon model for $(\pi^+, \gamma p)$ we can write the initial and final states using creation and annihilation operators as we did in chapter 3 for the $(\gamma, \pi^- p)$ reaction. We write the initial state as [Ja71]:

$$|i\rangle = b_{\pi}^{\dagger}(\vec{k}_{\pi}) \sum_{J_B M_B} (J, J_B; M, M_B | J_i, M_i) \mathcal{J}_{J_i J} (J_B) b_{J_B M_B}^{\dagger} |\phi_J^M\rangle \quad (5-1)$$

where $b_{\pi}^{\dagger}(\vec{k}_{\pi})$ creates a positively charged pion with momentum \vec{k}_{π} while $b_{J_B M_B}^{\dagger}$ creates a bound nucleon with angular momentum J_B and projection M_B bound to the core $|\phi_J^M\rangle$. $\mathcal{J}_{J_i J} (J_B)$ is the coefficient of fractional parentage which we have seen in equation (2-17).

The final state is

$$|f\rangle = a_p^{\dagger}(\vec{k}_{\gamma}) b_{s_f}^{\dagger}(\vec{k}_p) |\phi_{J_f}^{M_f}\rangle \quad (5-2)$$

where $a_p^{\dagger}(\vec{k}_{\gamma})$ creates a photon with momentum \vec{k}_{γ} and polarization p , $b_{s_f}^{\dagger}(\vec{k}_p)$ creates a nucleon with momentum \vec{k}_p and angular momentum projection s_f while the state $|\phi_{J_f}^{M_f}\rangle$ describes the residual nucleus with angular momentum J_f and projection M_f .

Using the interaction lagrangians (2-4) and (2-10), as well as the fields (2-20), (2-21) and (2-22) we calculate the Fock space matrix elements. Then using the form of the propagators as discussed in appendix B we can do the integration at one vertex. Finally we do the time integration to leave a three dimensional space integral, and we have the S -matrix in the form:

$$S_{fi} = \sqrt{2} e^{\frac{f_{\pi}}{m_{\pi}}} (2\pi)^{-7/2} \delta(E_p + E_{\gamma} - E_B - E_{\pi}) \left(\frac{m}{E_p} \frac{1}{2\omega_{\pi}} \frac{1}{2\omega_{\gamma}} \right)^{1/2} \quad (5-3)$$

$$\times \sum_{J_B M_B} (J_f, J_B; M_f, M_B | J_i, M_i) \mathcal{J}_{J_i J_f} (J_B)$$

$$\times \int d^3x \psi_{s_f}^{\dagger}(k_p, \vec{x}) \Gamma_{\text{total}} \psi_{J_B M_B}(\vec{x}) \phi_{\pi}(k_{\pi}, \vec{x}) e^{-i\vec{k}_{\gamma} \cdot \vec{x}}$$

where the 4x4 matrix operator between the nucleon spinors is the sum of operators from each of the contributing diagrams

$$\Gamma_{\text{total}} = \sum_i \Gamma_i \quad (5-4)$$

The Γ matrices from the various diagrams are:

$$\Gamma_{\text{seagull}} = \gamma_0 \gamma_5 \not{\epsilon}_p \quad (5-5)$$

$$\Gamma_{\text{pion}} = -2 \frac{\epsilon_p \cdot k}{k^2 - m_\pi^2} \gamma_0 \gamma_5 \not{k} \quad \text{with } k = k_\pi - k_\gamma \quad (5-6)$$

$$\Gamma_{\text{proton}}^e = -\gamma_0 \not{\epsilon}_p \frac{k + m_p}{k^2 - m_p^2} \gamma_5 \not{k}_\pi \quad \text{with } k = k_p + k_\gamma \quad (5-7)$$

$$\Gamma_{\text{proton}}^\mu = -\frac{\kappa_p}{4m_p} \gamma_0 [k_\gamma, \not{\epsilon}_p] \frac{k + m_p}{k^2 - m_p^2} \gamma_5 \not{k}_\pi \quad \text{with } k = k_p + k_\gamma \quad (5-8)$$

$$\Gamma_{\text{neutron}} = -\frac{\kappa_n}{4m_p} \gamma_0 \gamma_5 \not{k}_\pi \frac{k + m_n}{k^2 - m_n^2} [k_\gamma, \not{\epsilon}_p] \quad \text{with } k = k_p - k_\pi \quad (5-9)$$

$$\begin{aligned} \Gamma_{\Delta-s} &= \frac{f_{\gamma N \Delta} f_{\pi N \Delta}}{3 f_\pi m_\pi} \gamma_0 \gamma_5 [k^\gamma \epsilon_{\mu p} - k_\mu^\gamma \not{\epsilon}_p] \frac{\not{p}_\Delta + m_\Delta}{p_\Delta^2 - m_\Delta^2 + i m_\Delta \Gamma_\Delta} \\ &\quad \times [g^{\mu\nu} - \frac{1}{3} \gamma^\mu \gamma^\nu - \frac{1}{3 m_\Delta} (\gamma^\mu p_\Delta^\nu - \gamma^\nu p_\Delta^\mu) - \frac{2}{3 m_\Delta^2} p_\Delta^\mu p_\Delta^\nu] k_\nu^\gamma \\ &\quad \text{with } p_\Delta = k_p + k_\gamma \end{aligned} \quad (5-10)$$

$$\begin{aligned} \Gamma_{\Delta-u} &= -\frac{f_{\gamma N \Delta} f_{\pi N \Delta}}{3 f_\pi m_\pi} \gamma_0 \frac{\not{p}_\Delta + m_\Delta}{p_\Delta^2 - m_\Delta^2 + i m_\Delta \Gamma_\Delta} \\ &\quad \times k_\mu^\pi [g^{\mu\nu} - \frac{1}{3} \gamma^\mu \gamma^\nu - \frac{1}{3 m_\Delta} (\gamma^\mu p_\Delta^\nu - \gamma^\nu p_\Delta^\mu) - \frac{2}{3 m_\Delta^2} p_\Delta^\mu p_\Delta^\nu] \\ &\quad \times [k_\gamma \epsilon_{\nu p} - k_\nu^\gamma \not{\epsilon}_p] \gamma_5 \\ &\quad \text{with } p_\Delta = k_p - k_\pi \end{aligned} \quad (5-11)$$

The momentum of the intermediate particle is calculated from the momenta of two of the external particles as indicated in equations (5-5) to (5-11).

As in chapter 3, we must specify the wave functions describing the continuum and bound nucleons as well as the initial state pion, if we wish to go further with our calculation. We first do the calculation using plane waves for both the pion and the proton and obtain an expression for the s-matrix which is straightforward to evaluate. We then consider distorted waves for the pion and proton, which results in a more complicated form for the s-matrix but in the absence of distorting potentials must yield the same results as the plane wave calculation.

5.2 Plane Waves

We neglect the final state interactions of the pion and proton with the final nucleus. The pion wave function is a solution of the free Klein-Gordon equation and is simply

$$\varphi_{\pi}(\vec{k}_{\pi}, \vec{x}) = e^{i\vec{k}_{\pi} \cdot \vec{x}} \quad (5-12)$$

The positive energy solution of the free Dirac equation with spin projection s_f and momentum \vec{k}_p is [BD64] written as in equation (2-91), while the bound state neutron wave function is written in equation (2-93). We write the complex 4x4 operator Γ in terms of complex 2x2 matrix operators as in equation (2-97) and some straightforward algebra yields for the s-matrix

$$\begin{aligned} S_{fi} = & \sqrt{2} e^{\frac{f_{\pi}}{m_{\pi}}} (2\pi)^{-7/2} \delta(E_p + E_{\gamma} - E_B - E_{\pi}) \left[\frac{E_p + m}{2E_p} \frac{1}{2\omega_{\pi}} \frac{1}{2\omega_{\gamma}} \right]^{1/2} \\ & \times \sum_{J_B M_B} (J_f, J_B; M_f, M_B | J_i, M_i) \mathcal{J}_{J_i J_f}(J_B) \\ & \times \int d^3x e^{i\vec{q} \cdot \vec{x}} \{ f_B(r) \langle 1/2, s_f | \Gamma_f | \mathcal{Y}_{L_B 1/2 J_B}^{M_B} \rangle \\ & \quad + i g_B(r) \langle 1/2, s_f | \Gamma_g | \mathcal{Y}_{L_B 1/2 J_B}^{M_B} \rangle \} \end{aligned} \quad (5-13)$$

where the momentum transfer to the nucleus is $\vec{q} = \vec{k}_{\pi} - \vec{k}_{\gamma} - \vec{k}_p$ and we have defined the 2x2 matrices

$$\Gamma_f = \Gamma_{11} + \frac{\vec{\sigma} \cdot \vec{k}_p}{E_p + m} \Gamma_{21} \quad \Gamma_g = \Gamma_{12} + \frac{\vec{\sigma} \cdot \vec{k}_p}{E_p + m} \Gamma_{22} \quad (5-14)$$

This expression for the s-matrix is the same as equation (2-98), except for two small changes. The photon and pion momenta have changed signs in the calculation of the momentum transfer, and the pion and photon energies have changed signs in the delta function. Both of these changes occur because the two reactions interchange the roles of the pion and photon.

5.3 Distorted Waves

We now allow the pion to interact with the target nucleus, and the proton to interact with the residual nucleus by introducing appropriate potentials into the wave equation describing the motion of the particle. The proton is described by a solution of the Dirac

equation with scalar and vector potentials as written in equation (2-100). The pion wave function is expanded similarly as

$$\varphi_{\pi}(\mathbf{k}_{\pi}, \vec{\mathbf{x}}) = 4\pi \sum_{L_{\pi} M_{\pi}} i^{L_{\pi}} v_{L_{\pi}}(k_{\pi}r) Y_{L_{\pi}}^{M_{\pi}}(\Omega) Y_{L_{\pi}}^{M_{\pi}*}(\hat{\mathbf{k}}_{\pi}) \quad (5-15)$$

In the limit that the pion potentials are zero the radial functions become exactly spherical Bessel functions and the pion wave function is exactly the plane wave function (5-12) [Ja75]. The potentials describing proton and pion elastic scattering from a nucleus are discussed in chapter 4.

As before we choose the photon momentum to lie along the z-axis such that the photon momentum vector is $\vec{\mathbf{k}}_{\gamma} = (0, 0, k_{\gamma})$. The details of the coordinate system are shown in figure 5-3. For the case of coplanar geometry both the pion and proton momenta lie in the first quadrant of the x-z plane so the azimuthal angles are zero. For non-coplanar geometry we hold the pion momentum in the x-z plane and let the proton momentum come out of the plane. The photon polarization vector has components in the x and y directions as discussed on page 37. The photon is described by

$$\begin{aligned} e^{-i \vec{\mathbf{k}}_{\gamma} \cdot \vec{\mathbf{x}}} &= e^{i k_{\gamma} z} \\ &= \sqrt{4\pi} \sum_{L_{\gamma}} i^{-L_{\gamma}} (2L_{\gamma} + 1)^{1/2} j_{L_{\gamma}}(k_{\gamma}r) Y_{L_{\gamma}}^0(\Omega) \end{aligned} \quad (5-16)$$

Using these expansions for the wave functions describing the continuum particles, the form (2-93) for the bound state wave function and writing the Γ operator in terms of 2x2 complex matrices as in (2-97) the s-matrix can be written as

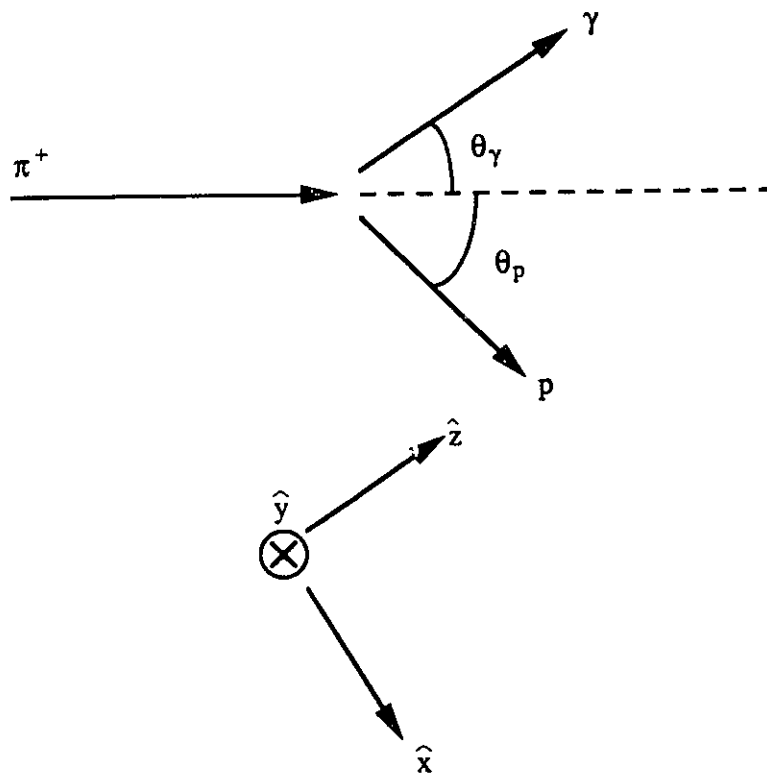


Figure 5-3. Coordinate system for the reaction $A(\pi^+, \gamma p)A-1$. The z-axis is chosen along the photon momentum and the pion momentum lies in the first quadrant of the x-z plane.

$$\begin{aligned}
S_{fi} = & \frac{\sqrt{2}}{\pi} e \frac{f_{\pi}}{m_{\pi}} \left(\frac{E_p + m}{E_p \omega_{\pi} \omega_{\gamma}} \right)^{1/2} \delta(E_p + E_{\gamma} - E_B - E_{\pi}) \\
& \times \sum_{J_B M_B} (J_f, J_B; M_f, M_B | J_i, M_i) \mathcal{J}_{J_i, J_f}(J_B) \\
& \times \sum_{L J L_{\pi} L_{\gamma}} i^{L_{\pi} - L - L_{\gamma}} (2L_{\gamma} + 1)^{1/2} \\
& \times \sum_{M M_{\pi}} Y_L^{M - s_f}(\hat{\mathbf{k}}_p) Y_{L_{\pi}}^{M_{\pi} *}(\hat{\mathbf{k}}_{\pi}) (L, \frac{1}{2}; M - s_f, s_f | J, M) \\
& \times \left\{ R_{ff}[\kappa \kappa_B L_{\pi} L_{\gamma}] A_{11} \begin{bmatrix} \kappa & \kappa_B & L_{\pi} & L_{\gamma} & \xi \\ M & M_B & M_{\pi} & & \end{bmatrix} \right. \\
& \quad + R_{gg}[\kappa \kappa_B L_{\pi} L_{\gamma}] A_{22} \begin{bmatrix} \kappa' & \kappa_B' & L_{\pi} & L_{\gamma} & \xi \\ M & M_B & M_{\pi} & & \end{bmatrix} \\
& \quad + i R_{fg}[\kappa \kappa_B L_{\pi} L_{\gamma}] A_{12} \begin{bmatrix} \kappa & \kappa_B' & L_{\pi} & L_{\gamma} & \xi \\ M & M_B & M_{\pi} & & \end{bmatrix} \\
& \quad \left. - i R_{gf}[\kappa \kappa_B L_{\pi} L_{\gamma}] A_{21} \begin{bmatrix} \kappa' & \kappa_B & L_{\pi} & L_{\gamma} & \xi \\ M & M_B & M_{\pi} & & \end{bmatrix} \right\} \tag{5-17}
\end{aligned}$$

where the radial integrals are defined [with $\kappa = (L - J)(2J + 1)$ and $L' = 2J - L$] as they were in chapter 3 equation (2-104), and the angular integrals are those of equation (2-105). The differences between equations (2-103) and (5-17) are the change in sign of the pion and photon energies in the delta function, and the change in sign of the pion and photon angular momenta in the exponent of i . The latter change corresponds to the change of signs of pion and photon momenta which we saw in the plane wave result (5-13).

We calculate the energies and momenta of the final particles using the constraints provided by conservation of energy and momentum. These are not enough to fix the kinematics of the outgoing particles since the final state has three particles, so we set the directions of two particles and the energy of one of the particles; the kinematics for the reaction are then well determined.

5.4 Gauge invariance

We test for gauge invariance, as we did in section 2.5, by making the replacement

[BD64]

$$\epsilon_{\mu p} \rightarrow k_{\mu} \quad (5-18)$$

and if the calculation is gauge invariant the result will be zero. The anomalous magnetic moment diagrams and the two diagrams due to the delta are all gauge invariant in both the plane and distorted wave calculations.

The remaining diagrams have the photon coupling to a particle through the electric charge. To check that the sum of the Γ matrices for the three diagrams given in equations (5-5), (5-6) and (5-7) is gauge invariant, make the substitution (5-18) into the sum as we did in equation (2-110). We again find that in the plane wave approximation the combination of the three Born terms is gauge invariant, but when the proton wave function is a solution of an equation with potentials, the s-matrix is no longer gauge invariant, and as before we continue on with a calculation that is gauge invariant in the limit of vanishing potentials.

5.5 Observables for $A(\pi^+, \gamma p)A^{-1}$

Following section 2.6 we can obtain the expressions for the observables most easily by writing the s-matrix in a more concise form

$$S_{fi} = \frac{\sqrt{2}}{\pi} e \frac{f_{\pi}}{m_{\pi}} \left(\frac{E_p + m}{E_p E_{\pi} E_{\gamma}} \right)^{1/2} \delta(E_p + E_{\gamma} - E_B - E_{\pi}) \quad (5-19)$$

$$\times \sum_{J_B M_B} (J_f, J_B; M_f, M_B | J_i, M_i) \mathcal{J}_{J_i J_f}(J_B) Z_{M_B}^{s_r \xi}$$

where $Z_{M_B}^{s_r \xi}$ is a function of the polarization of the photon, the spin projection of the final proton and the projection of the nuclear bound state. $Z_{M_B}^{s_r \xi}$ contains the radial and angular integrals and the sums over all the angular momenta. The exact form for $Z_{M_B}^{s_r \xi}$ can be obtained by comparing with (5-13) for the plane wave calculation or (5-17) for the distorted wave calculation.

The cross section is then calculated through the usual procedure [BD64] of squaring the s-matrix to get a transition probability, multiplying by the number of available final states and dividing by the incident flux. We finally average over initial spin projections and sum over final spin projections to get (appendix D)

$$\frac{d\sigma}{d\Omega_\pi d\Omega_p dE_p} = 8 (4\pi)^2 \frac{1}{\hbar c} \frac{\alpha \beta}{m_\pi^2 c^4} (E_p + mc^2) E_\gamma \frac{P_p}{P_\pi} \sum_{J_B M_B} \frac{J_{J_i J_r}(J_B)}{2J_B + 1} |Z_{M_B}^{s_r \xi}|^2 \quad (5-20)$$

The polarization of the final proton is the same as it was in chapter 3, except for the slight change of notation of the z-matrix, namely

$$P = -2 \frac{\text{Im} \sum_{\xi M_B} Z_{M_B}^{1/2 \xi} [Z_{M_B}^{-1/2 \xi}]^*}{\sum_{s_r \xi M_B} Z_{M_B}^{s_r \xi} [Z_{M_B}^{s_r \xi}]^*} \quad (5-21)$$

5.6 Results for the $A(\pi^+, \gamma p)A-1$ Reaction

There are currently no published data for this reaction. There has been an experiment at TRIUMF to perform a measurement on ^{16}O , experiment 550. Data was taken at two incident pion energies, $T_\pi = 163.7$ MeV and $T_\pi = 218.6$ MeV. At each of these pion energies data was taken at two photon angles, each with four proton angles. The angles and energies for which triple differential cross section data will become available in the future are:

$$T_\pi = 163.7 \text{ MeV:}$$

$$\begin{aligned} \theta_\gamma = 77.4^\circ & \quad \text{with} \quad \theta_p = 15.7^\circ, 28.7^\circ, 41.7^\circ, 54.7^\circ \\ \theta_\gamma = 125.4^\circ & \quad \text{with} \quad \theta_p = 15.7^\circ, 28.7^\circ, 41.7^\circ, 54.7^\circ \end{aligned}$$

$$T_\pi = 218.6 \text{ MeV:}$$

$$\begin{aligned} \theta_\gamma = 75.2^\circ & \quad \text{with} \quad \theta_p = 15.7^\circ, 28.7^\circ, 41.7^\circ, 54.7^\circ \\ \theta_\gamma = 123.5^\circ & \quad \text{with} \quad \theta_p = 15.7^\circ, 28.7^\circ, 41.7^\circ, 54.7^\circ \end{aligned}$$

where the angles are defined with respect to the pion momentum as shown in figure 5-3. We have calculated the cross sections and proton polarizations for these kinematics and show results for the forward photon angle in the following diagrams.

We begin with the low pion energy, $T_\pi = 163.7$ MeV, where the photon angle is θ_γ

$= 77.4^\circ$. Figure 5-4 shows the cross sections calculated for the four proton angles. The proton is distorted by the global A and E dependent potential while the pion potential is that of Oset. The largest cross section occurs for the largest proton angle, corresponding to a small momentum transfer as shown in figure 5-5. The cross sections calculated with plane waves describing the pion and proton are shown in figure 5-6. The reduction in the peak cross section when distortions are added is roughly a factor of two, as we have seen for the reaction $(\gamma, \pi^- p)$ which we looked at in chapter 4. The polarization of the final proton is shown in figure 5-7. These curves correspond to the DW cross sections of figure 5-4. The cross section peaks occur at a proton energy of about $T_p = 70$ MeV, where the proton polarization is 0.4 for all four detected proton angles.

In figure 5-8 we show the DW cross section for the proton angle which has the largest cross section, namely $\theta_p = 54.7^\circ$. The dotted curve is the cross section calculated from the Born terms only, the dashed curve is calculated from the delta diagrams and the solid curve is the cross section when all the diagrams have been included. The cross section calculated from the delta diagrams is two thirds of the magnitude of the Born cross section at the peak, while the total cross section is fifty per cent larger than the Born cross section. Figure 5-9 shows the change in the cross section when distortion effects for both the pion and proton are included, for the kinematics of figure 5-8. The peak cross section is reduced by a factor of two, and the left-hand peak of the plane wave cross section is removed completely when distortions are included. The polarization for these kinematics is shown in figure 5-10. The dashed curve results when the pion and proton are described by plane waves, and the solid curve has distortions included. Near the peak of the cross section the polarization has a value of 0.6 and is very nearly the same in either the PW or DW calculations.

The other pion energy considered is $T_\pi = 218.6$ MeV. The photon angle is changed slightly at this energy from the previous case to $\theta_\gamma = 75.2^\circ$, but the four associated proton angles are the same as before. In figure 5-11 we show the DW differential cross sections calculated for the four proton angles. The largest cross section is again associated with the largest proton angle, $\theta_p = 54.7^\circ$. The momentum transfers corresponding to the cross section curves are shown in figure 5-12. The plane wave cross section is shown in figure 5-13. In this case the magnitude of the peak cross section is decreased by a factor of four when the distortions are included in the pion and proton wave functions. The polarization

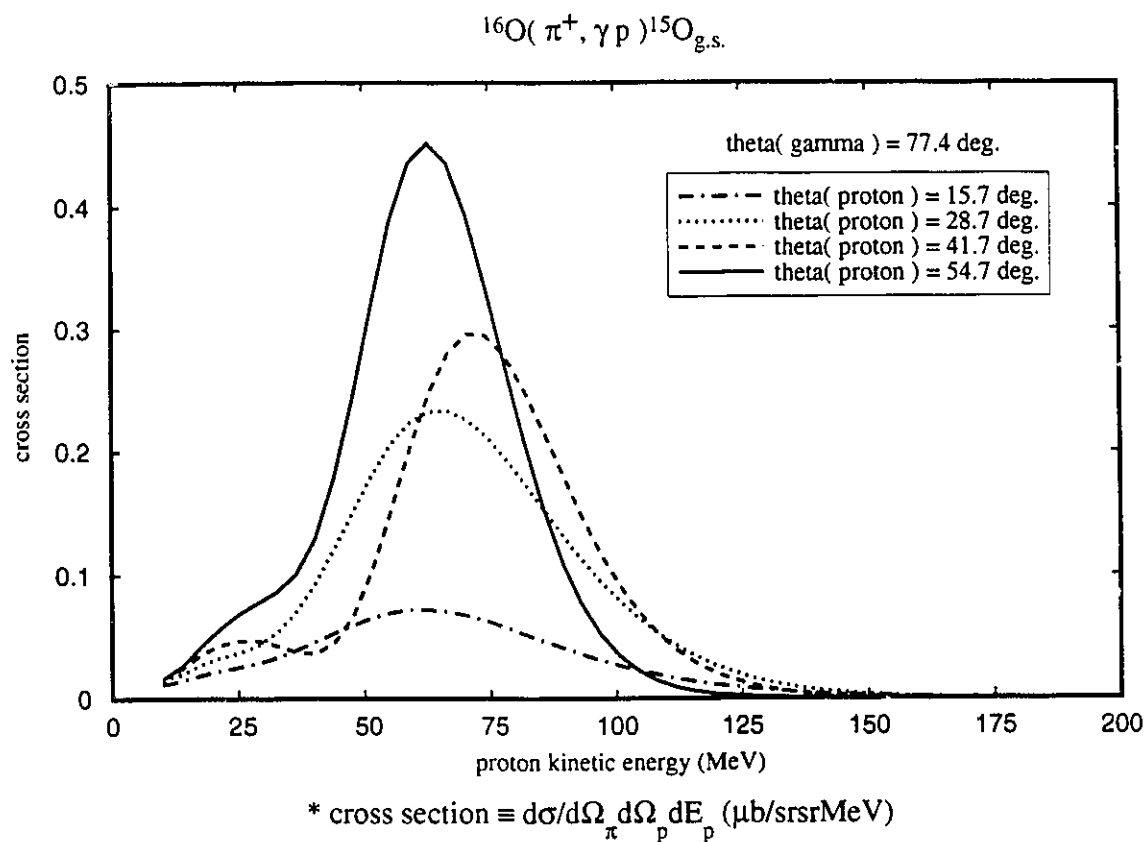


Figure 5-4. Cross section as a function of proton energy for four proton angles. The kinematic conditions are $T_{\pi} = 163.7$ MeV with $\theta_{\gamma} = 77.4^{\circ}$. Proton is distorted by the global E and A dependent potential, while the pion is distorted by the potential of Oset. Dotdashed curve - $\theta_p = 15.7^{\circ}$, dotted curve - $\theta_p = 28.7^{\circ}$, dashed curve - $\theta_p = 41.7^{\circ}$, solid curve - $\theta_p = 54.7^{\circ}$.

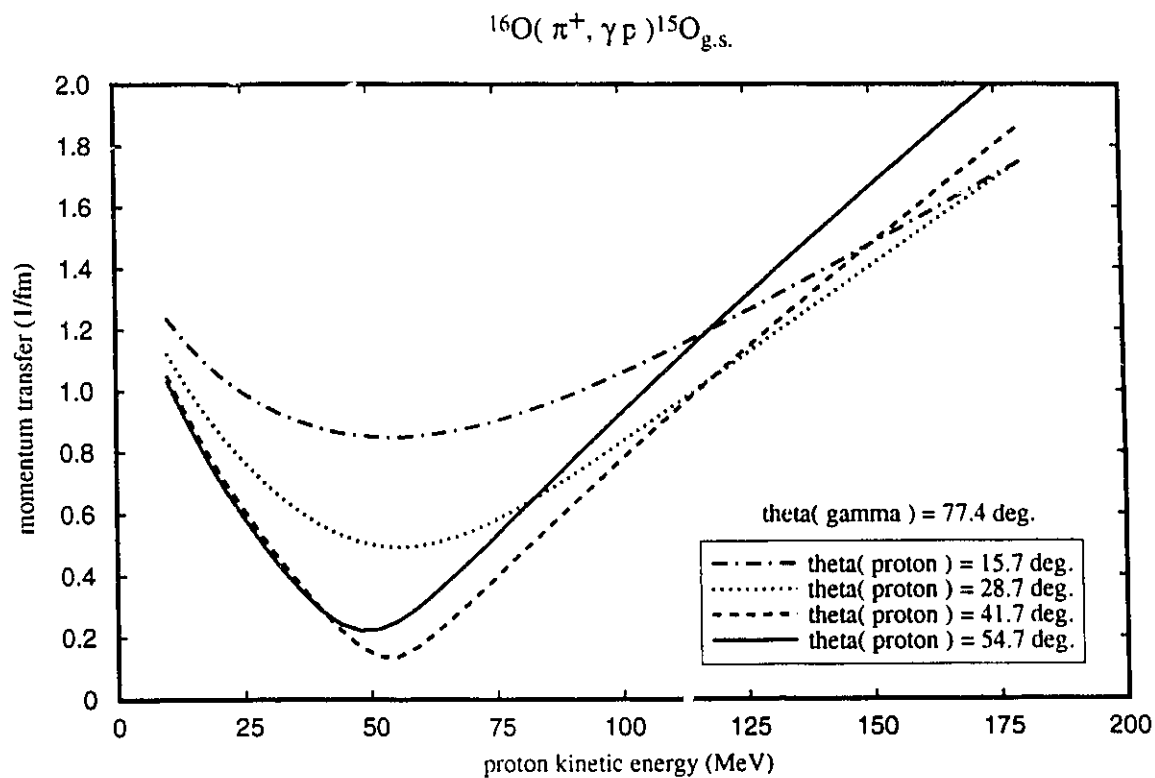


Figure 5-5. Momentum transfer as a function of proton energy for four proton angles. The kinematic conditions are $T_{\pi} = 163.7$ MeV with $\theta_{\gamma} = 77.4^{\circ}$.

Dotdashed curve - $\theta_p = 15.7^{\circ}$, dotted curve - $\theta_p = 28.7^{\circ}$,

dashed curve - $\theta_p = 41.7^{\circ}$, solid curve - $\theta_p = 54.7^{\circ}$.

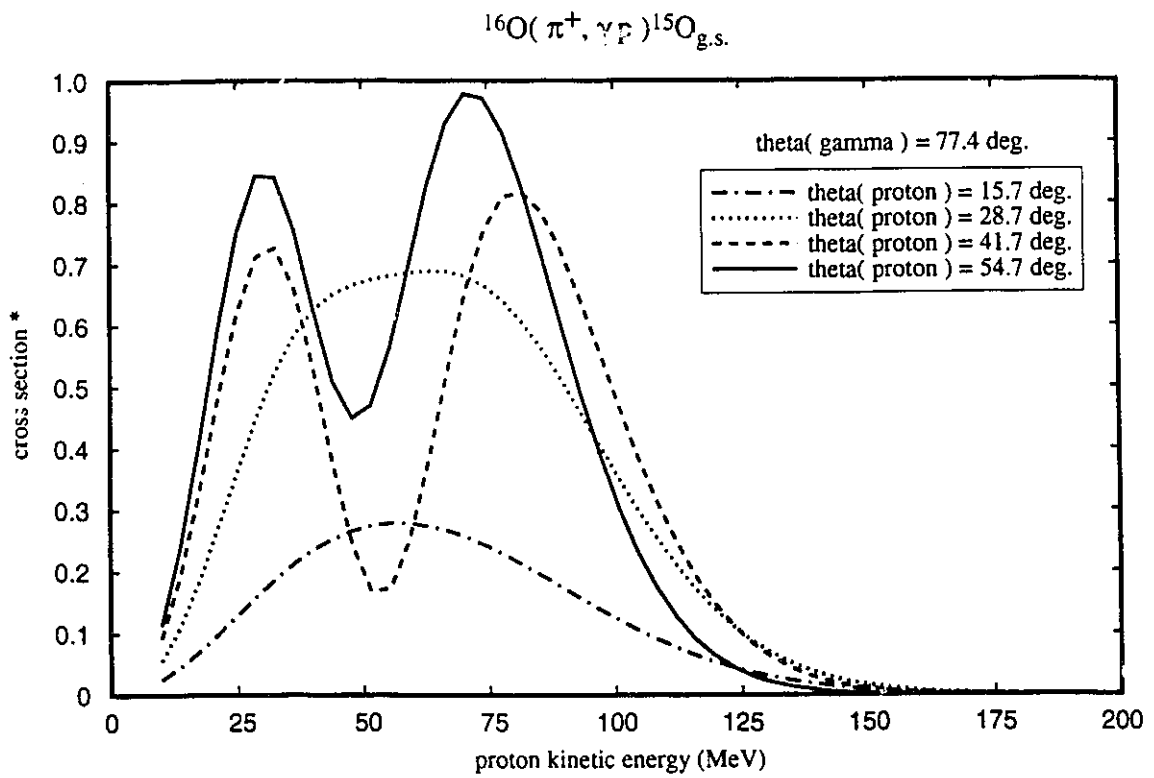


Figure 5-6. Cross section as a function of proton energy for four proton angles. The kinematic conditions are $T_{\pi} = 163.7$ MeV with $\theta_{\gamma} = 77.4^{\circ}$. Proton and pion are described by plane waves.

Dotdashed curve - $\theta_p = 15.7^{\circ}$, dotted curve - $\theta_p = 28.7^{\circ}$,

dashed curve - $\theta_p = 41.7^{\circ}$, solid curve - $\theta_p = 54.7^{\circ}$.

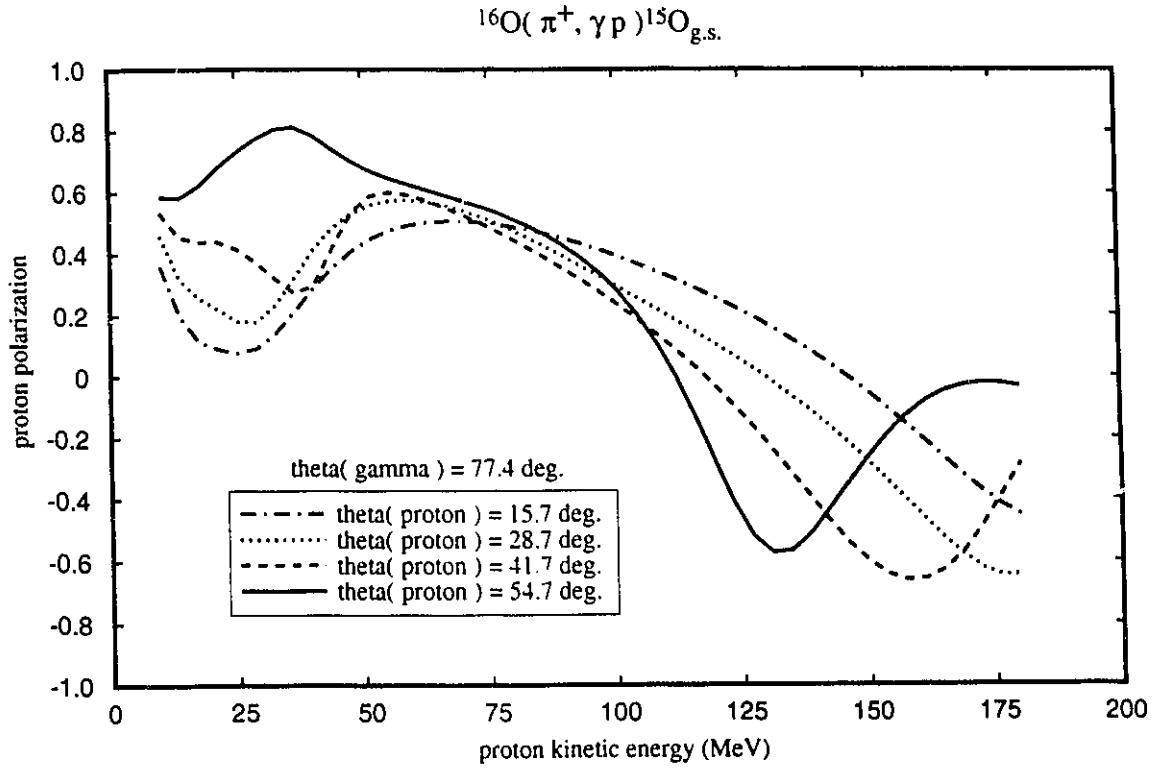


Figure 5-7. Proton polarization as a function of proton energy for four proton angles. The kinematic conditions are $T_\pi = 163.7$ MeV with $\theta_\gamma = 77.4^\circ$. Proton is distorted by the global E and A dependent potential, while the pion is distorted by the potential of Oset. Dotdashed curve - $\theta_p = 15.7^\circ$, dotted curve - $\theta_p = 28.7^\circ$, dashed curve - $\theta_p = 41.7^\circ$, solid curve - $\theta_p = 54.7^\circ$.

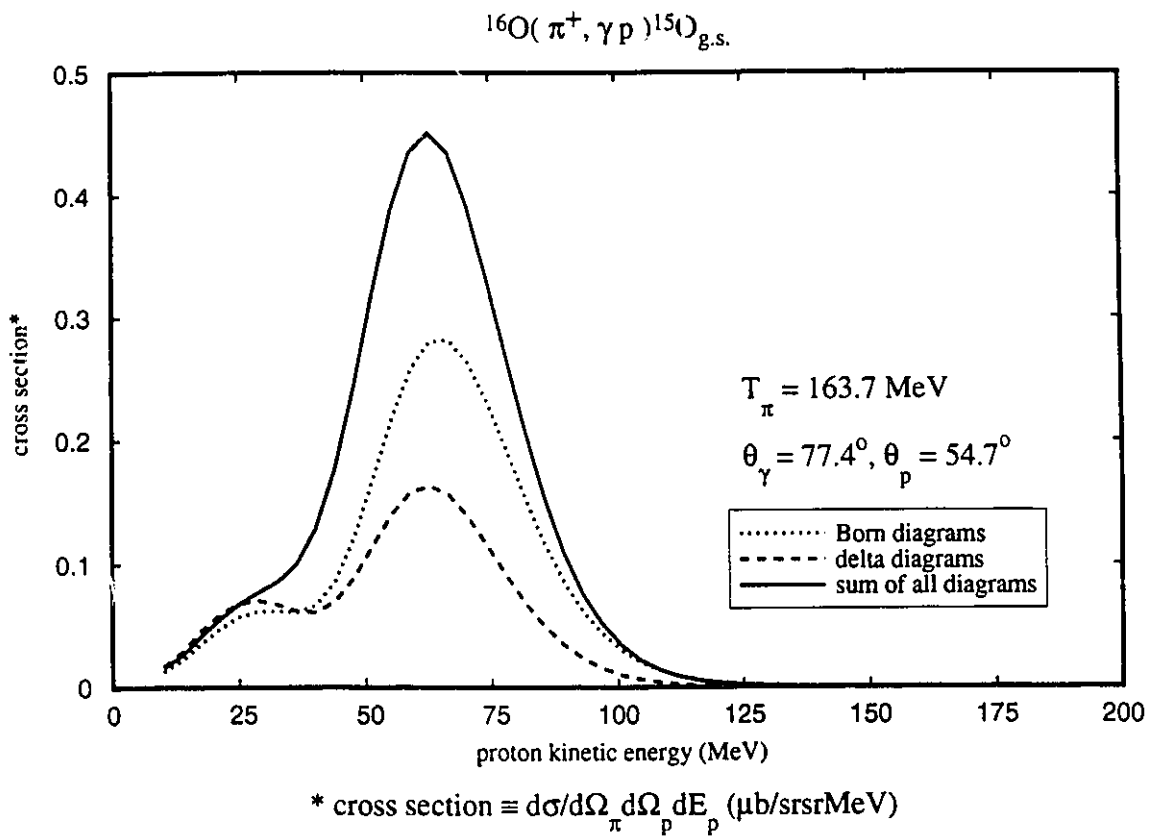


Figure 5-8. Cross section as a function of proton energy. The kinematic conditions are $T_{\pi} = 163.7$ MeV with $\theta_{\gamma} = 77.4^{\circ}$. Proton is distorted by the global A and E dependent potential, while the pion is distorted by the potential of Oset. Dotted curve - Born diagrams, dashed curve - delta diagrams, solid curve - sum of all diagrams.

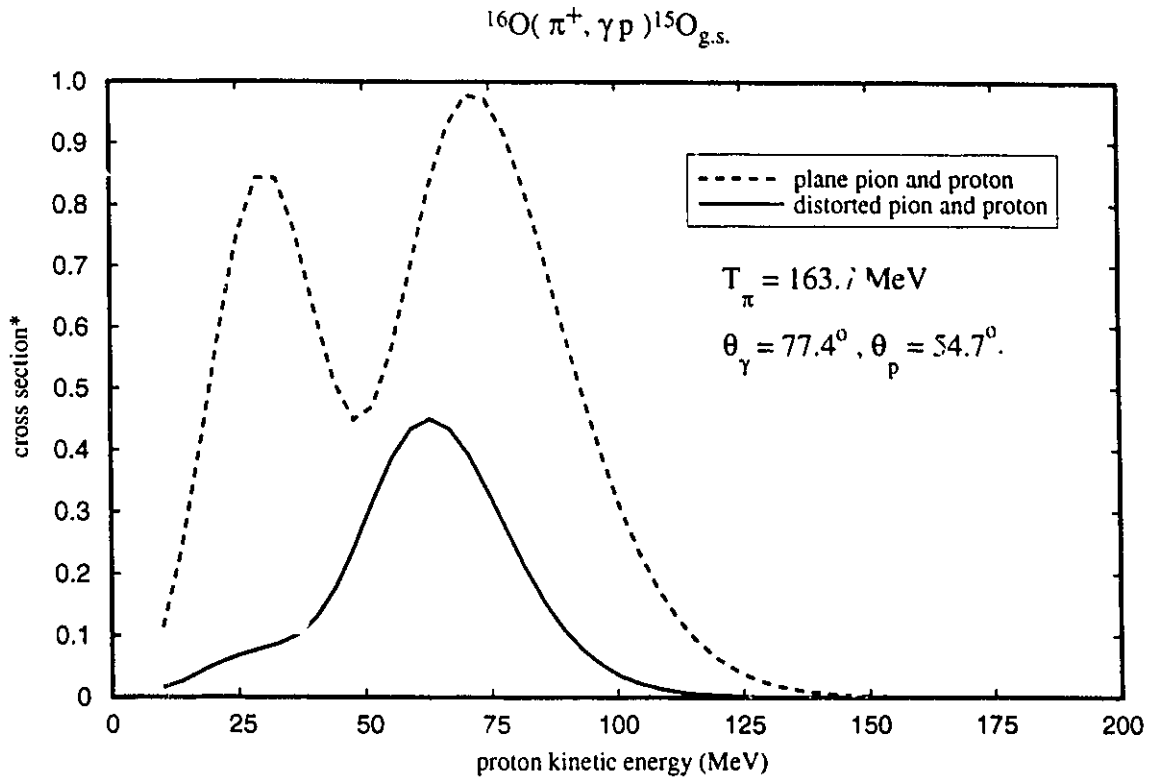


Figure 5-9. Cross section as a function of proton energy. The kinematic conditions are $T_{\pi} = 163.7$ MeV with $\theta_{\gamma} = 77.4^{\circ}$ and $\theta_p = 54.7^{\circ}$. Dashed curve - pion and proton plane waves, solid curve - proton distorted by the global E and A dependent potential, while the pion is distorted by the potential of Oset.

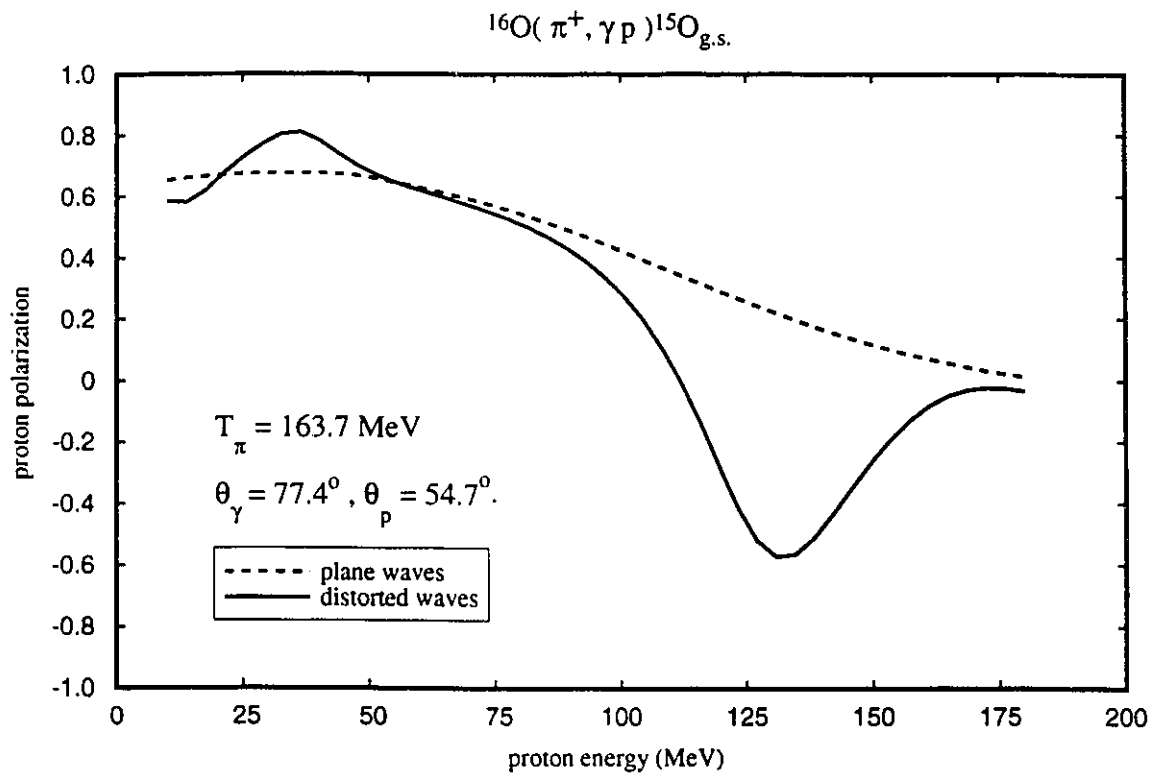


Figure 5-10. Proton polarization as a function of proton energy. The kinematic conditions are $T_\pi = 163.7$ MeV with $\theta_\gamma = 77.4^\circ$ and $\theta_p = 54.7^\circ$.

Dashed curve - pion and proton plane waves,
 solid curve - proton distorted by the global E and A dependent potential, while the pion is distorted by the potential of Oset.

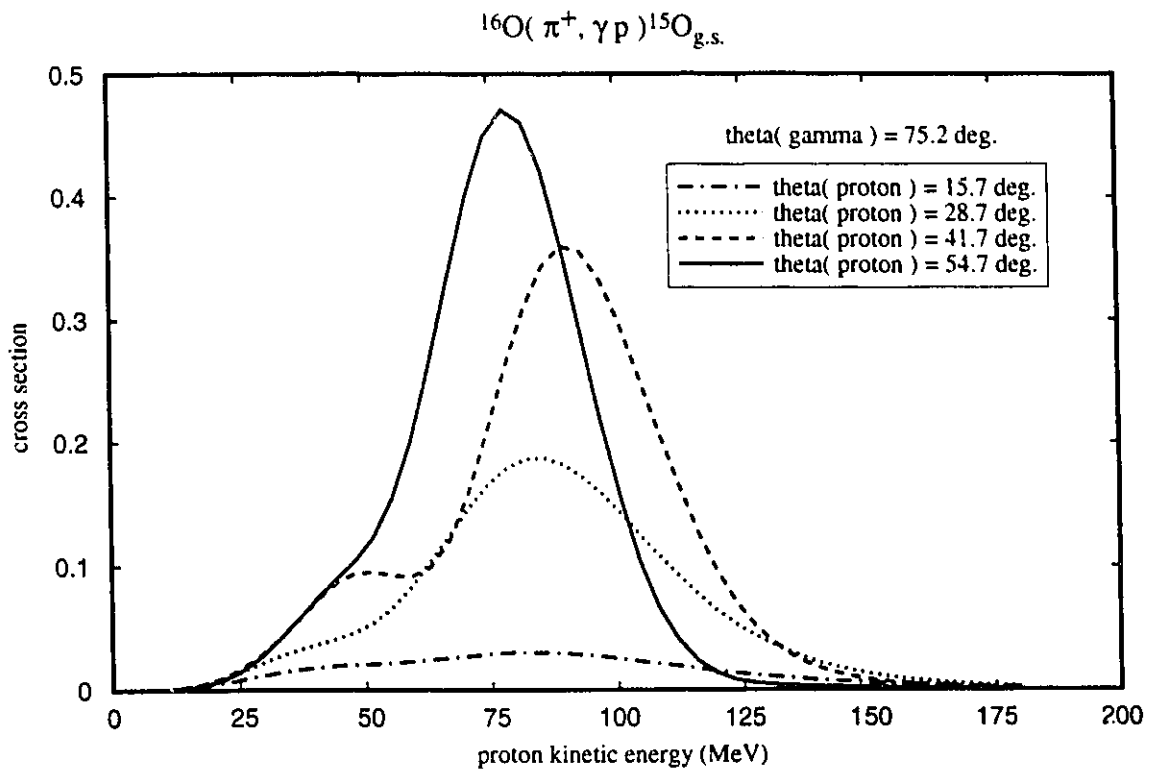


Figure 5-11. Cross section as a function of proton energy for four proton angles. The kinematic conditions are $T_{\pi} = 218.6$ MeV with $\theta_{\gamma} = 75.2^{\circ}$. Proton is distorted by the global E and A dependent potential, while the pion is distorted by the potential of Oset. Dotdashed curve - $\theta_p = 15.7^{\circ}$, dotted curve - $\theta_p = 28.7^{\circ}$, dashed curve - $\theta_p = 41.7^{\circ}$, solid curve - $\theta_p = 54.7^{\circ}$.

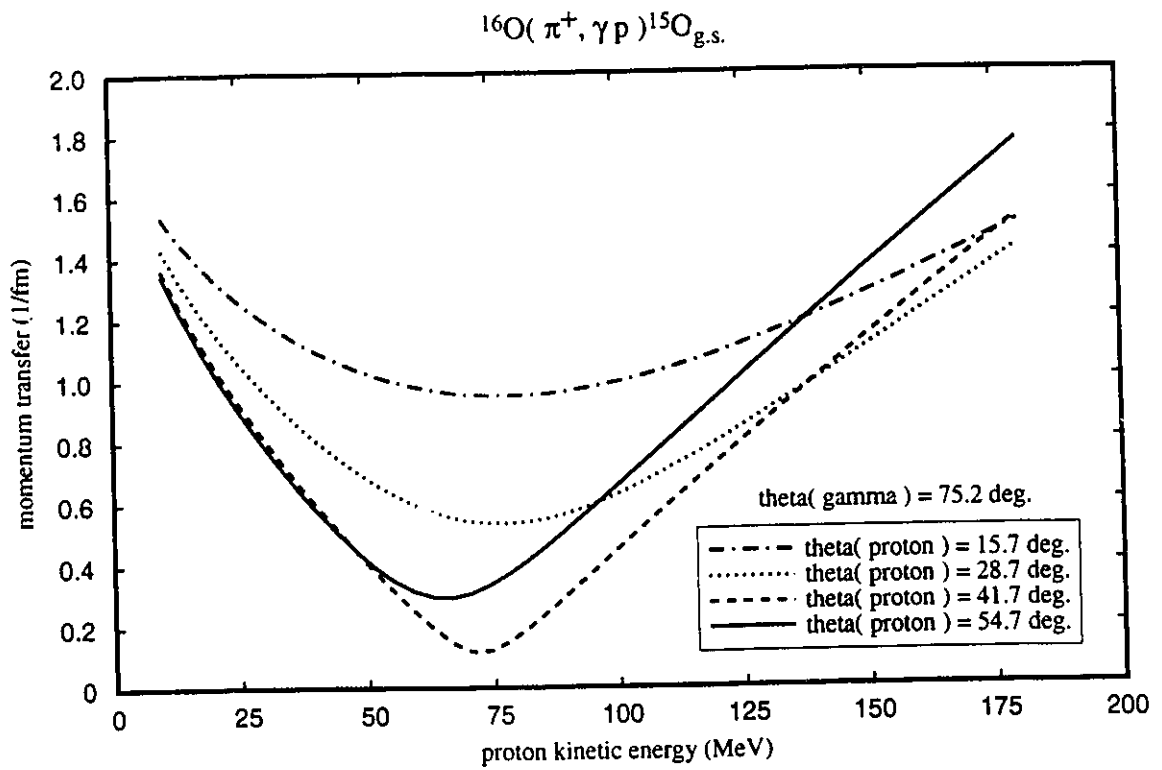


Figure 5-12. Momentum transfer as a function of proton energy for four proton angles. The kinematic conditions are $T_{\pi} = 218.6$ MeV with $\theta_{\gamma} = 75.2^{\circ}$. Proton is distorted by the global E and A dependent potential, while the pion is distorted by the potential of Oset. Dotted curve - $\theta_p = 15.7^{\circ}$, dashed curve - $\theta_p = 28.7^{\circ}$, dash-dot curve - $\theta_p = 41.7^{\circ}$, solid curve - $\theta_p = 54.7^{\circ}$.

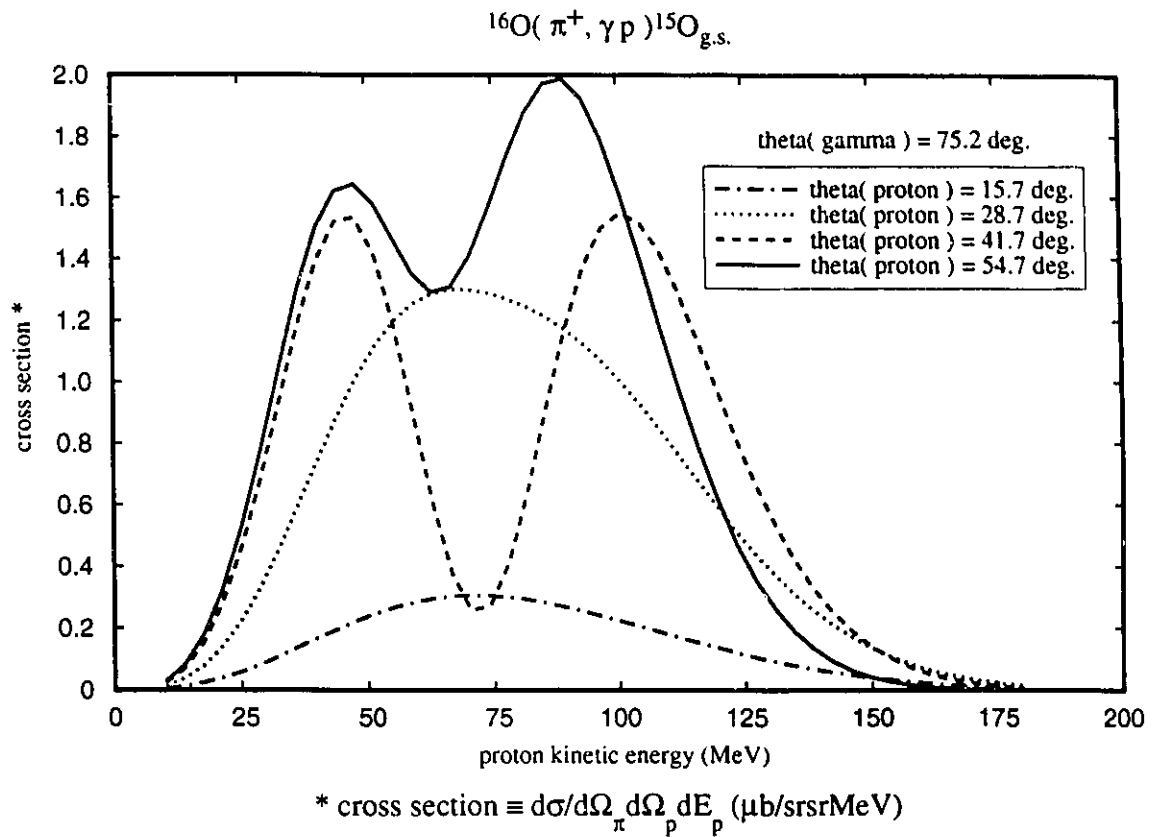


Figure 5-13. Cross section as a function of proton energy for four proton angles. The kinematic conditions are $T_{\pi} = 218.6$ MeV with $\theta_{\gamma} = 75.2^{\circ}$. Proton and pion are described by plane waves. Dotdashed curve - $\theta_p = 15.7^{\circ}$, dotted curve - $\theta_p = 28.7^{\circ}$, dashed curve - $\theta_p = 41.7^{\circ}$, solid curve - $\theta_p = 54.7^{\circ}$.

of the proton for all four proton angles is shown in figure 5-14. The polarization is fairly constant in the proton kinetic energy range $30 \text{ MeV} \leq T_p \leq 100 \text{ MeV}$, with a value of about 0.5.

The DW cross section for a proton angle of $\theta_p = 54.7^\circ$ is shown in figure 5-15. The dotted curve is the cross section calculated from the Born diagrams, the dashed curve is calculated from the delta diagrams and the sum of all the diagrams yields the solid curve. The delta cross section is fifty per cent larger than the cross section calculated from the Born terms, and the total cross section about three times as large as the Born cross section. This is the one case that we have seen where the delta diagrams are the dominant contributor to the total cross section. The cross section calculated with and without distortions for the pion and proton is shown in figure 5-16. The distortions reduce the magnitude of the peak of the cross section by about a factor of four in this case. The polarization of the outgoing proton is shown in figure 5-17 calculated with and without distortions. The dashed curve results when the pion and proton are described by plane waves, while the solid curve has potentials for both the pion and the proton. The polarization is not affected very strongly by inclusion of the interaction potentials, and where the cross section is the largest the polarization is fairly constant at about 0.6.

We have had the opportunity to compare one set of preliminary data for a pion kinetic energy of $T_\pi = 218.6 \text{ MeV}$, with photon and proton angles $\theta_\gamma = 75.2^\circ$ and $\theta_p = 28.7^\circ$ [Fa93]. Our distorted wave calculation is shown as the dotted curve of figure 5-11. The normalization of the data has not been fixed as yet, but the shape of the data is consistent with the results of our model. We do not show a comparison as the data are not yet finalized. The rest of the data is expected to become available for comparison in the near future.

The cross sections for the reactions $A(\gamma, \pi^- p)A-1$ and $A(\pi^+, \gamma p)A-1$ are in the neighbourhood of one microbarn/srMeV. These are measurable with existing machines, but better energy resolution and higher intensity that will become available with the new generation of electron accelerators in the near future will provide much better data. We will then be able to clarify the question of how well we understand the mechanism of charged pion photoproduction on nuclei.

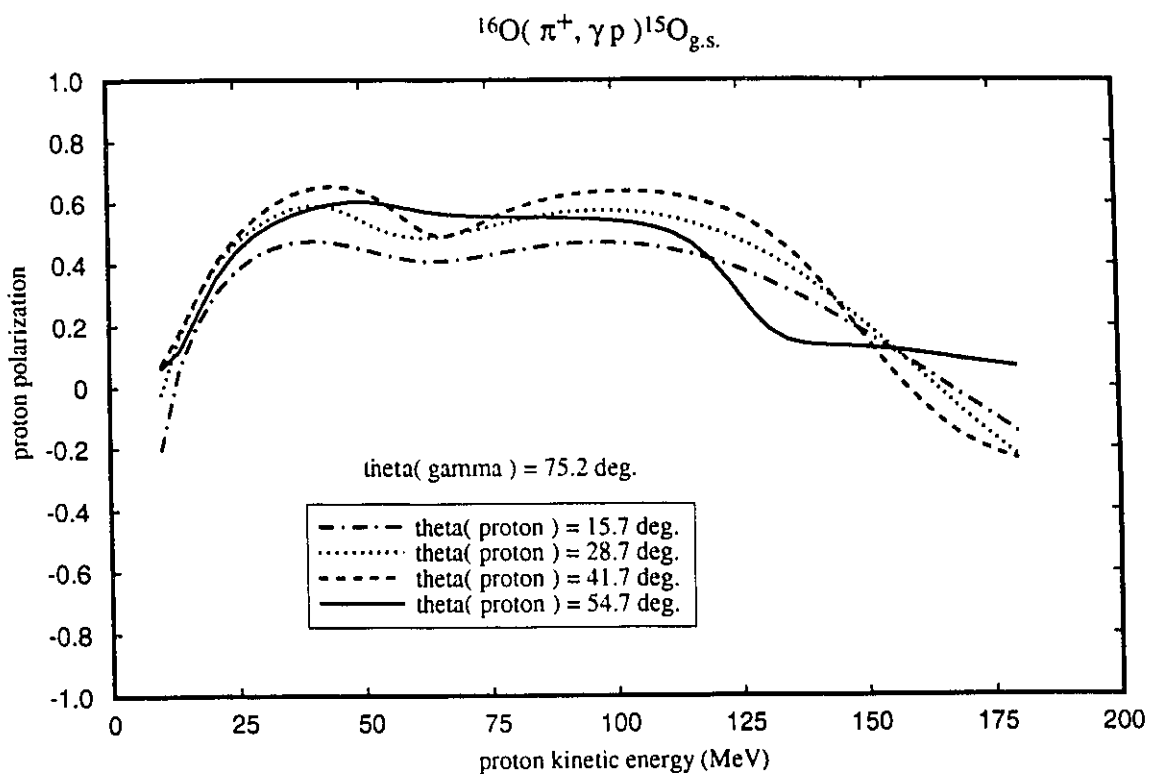


Figure 5-14. Proton polarization as a function of proton energy for four proton angles. The kinematic conditions are $T_{\pi} = 218.6$ MeV with $\theta_{\gamma} = 75.2^{\circ}$. Proton is distorted by the global E and A dependent potential, while the pion is distorted by the potential of Oset. Dotdashed curve - $\theta_p = 15.7^{\circ}$, dotted curve - $\theta_p = 28.7^{\circ}$, dashed curve - $\theta_p = 41.7^{\circ}$, solid curve - $\theta_p = 54.7^{\circ}$.

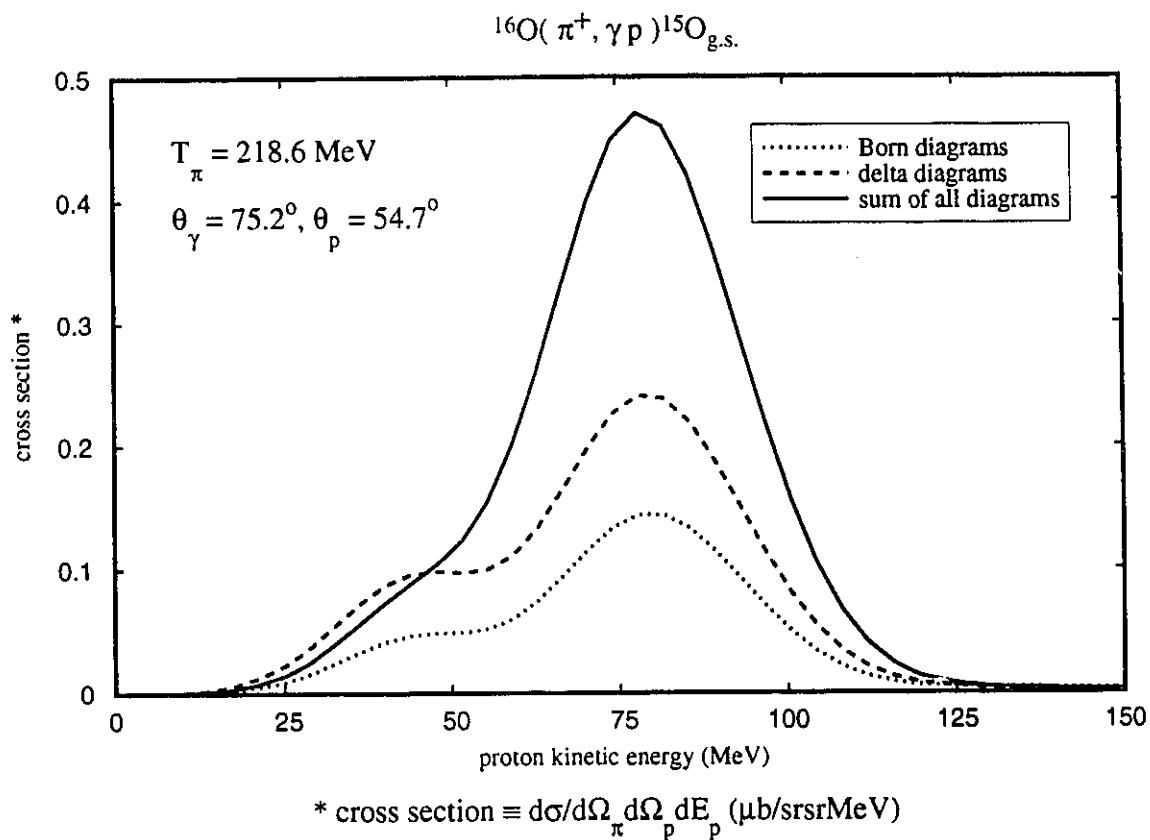


Figure 5-15. Cross section as a function of proton energy. The kinematic conditions are $T_{\pi} = 218.6$ MeV with $\theta_{\gamma} = 75.2^{\circ}$ and $\theta_p = 54.7^{\circ}$. Proton is distorted by the global A and E dependent potential, while the pion is distorted by the potential of Oset. Dotted curve - Born diagrams, dashed curve - delta diagrams, solid curve - sum of all diagrams.

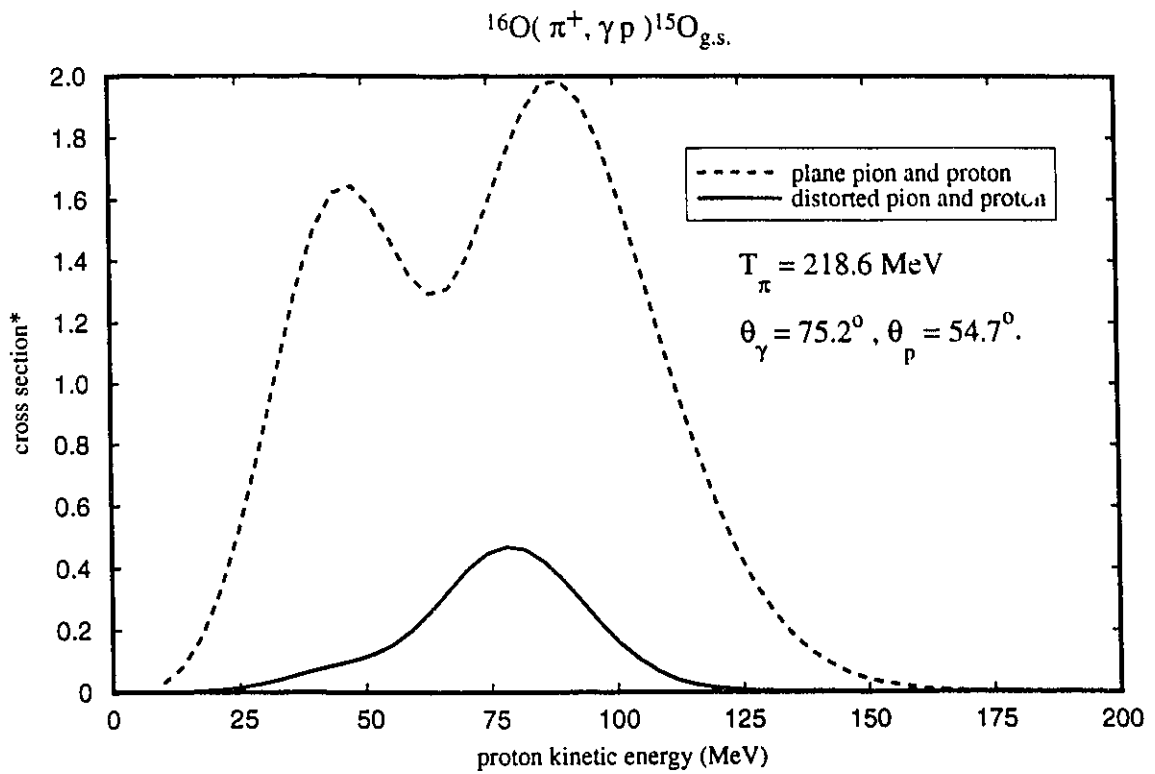
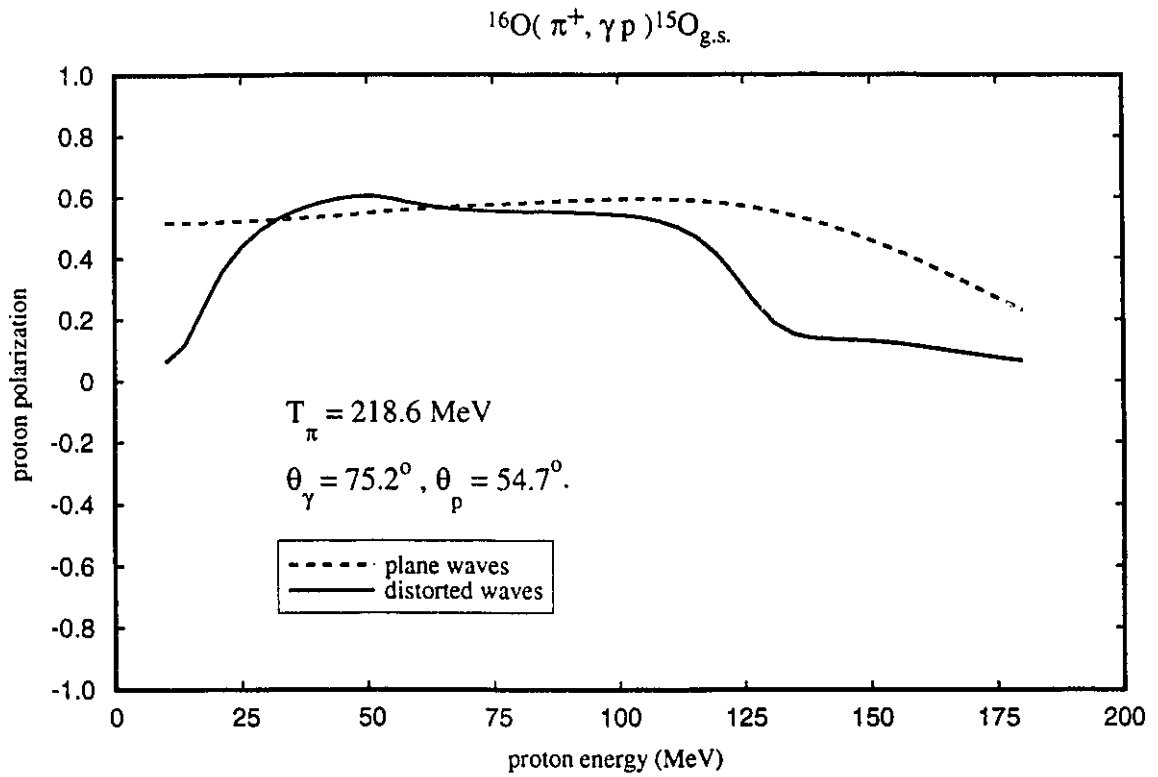


Figure 5-16. Cross section as a function of proton energy. The kinematic conditions are $T_{\pi} = 218.6$ MeV with $\theta_{\gamma} = 75.2^{\circ}$ and $\theta_{p} = 54.7^{\circ}$.

Dashed curve - pion and proton plane waves,
 solid curve - proton distorted by the global E and A dependent potential, while the pion is distorted by the potential of Oset.



* cross section $\equiv d\sigma/d\Omega_{\pi} d\Omega_p dE_p$ ($\mu\text{b/sr sr MeV}$)

Figure 5-17. Proton polarization as a function of proton energy. The kinematic conditions are $T_{\pi} = 218.6 \text{ MeV}$., with $\theta_{\gamma} = 75.2^{\circ}$ and $\theta_p = 54.7^{\circ}$.

Dashed curve - pion and proton plane waves.
 solid curve - proton distorted by the global E and A dependent potential, while the pion is distorted by the potential of Oset.

Chapter 6 - Conclusion

We have considered a relativistic model of nuclear pion photoproduction using the photon, pion, nucleon and delta as the elementary particles in the problem. Beginning with the model lagrangian of pion photoproduction on a free nucleon, developed by Olsson and Osypowski [Ol75] and later by Blomqvist and Laget [BL76], we have extended this to the case of production on a nucleon bound in a nucleus and treat the nuclear dynamics according to the model recently proposed by Walecka and his coworkers [SW86]. The pion and nucleon wave functions are solutions of relativistic equations; the pion being described by the Klein-Gordon equation, while the nucleons are described using the Dirac equation. These equations contain potentials through which the particles interact with the nucleus. Thus our model remains fully relativistic, and we do not employ a factorization approximation, as is done in the calculations by Blomqvist and Laget [BL77], in which the cross section has the form of equation (1-2).

In carrying out the detailed calculations of the various contributions to the amplitude, the following approximations have been made. The propagators are taken to be the momentum space propagators multiplied by a coordinate space δ -function, removing the integration at one vertex, i.e. we have imposed a locality condition on the nonlocal propagators. It should be pointed out that the Born terms with the photon coupling to electric charge are not gauge invariant in the distorted wave calculation, although they are gauge invariant when the pion and proton are described by plane waves. The terms in which the photon couples to the anomalous magnetic moment of the nucleon, and the delta diagrams are each separately gauge invariant for both the plane and distorted wave calculations.

We have examined the sensitivity of the model to variations in the distorting potentials of the pion and the proton. We have considered two types of proton potentials. The first has been parametrized with energy dependence only, and determined specifically for the ^{12}C nucleus. The second has been parametrized with dependence on projectile energy and target mass; the parameters are determined from elastic scattering data for a wide range of proton energies and a number of target nuclei from carbon to lead. The calculated observables are not very sensitive to the differences in the proton

potentials.

Similarly we have considered four different pion potentials, one containing a pure s-wave part of the pion-nucleon scattering amplitude, and three potentials of the Kisslinger form containing s- and p-wave contributions. The s-wave only potential does not reproduce the pion elastic scattering data, and can give significantly different results from the potentials which include the p-wave. The three Kisslinger type potentials give similar results for the pion elastic scattering and also produce similar results in the pion photoproduction calculations. The inclusion of distortions in the pion and proton wave functions reduces the magnitude of the cross section by roughly a factor of two from the cross section calculated with pion and proton plane wave functions, the degree of reduction depending on the particular kinematic situation considered.

Various prescriptions for the bound state potentials have also been considered. Negative pion photoproduction is not very sensitive to the changes in the bound state wave function resulting from the use of different potentials. At low momentum transfers the bound state wave function is well determined by the requirement that the eigenenergy of the wave function reproduces the experimentally measured separation energy. The observables calculated using different bound state wave functions then show only slight differences since the bound state wave functions are very similar. The differences in the bound state wave functions become apparent at higher momentum transfer as in the $1p_{3/2}$ level of ^{12}C shown in figure 4-6. In the region of momentum transfer between 2 fm^{-1} and 3 fm^{-1} the momentum space wave functions have minima which are clearly different. We would naïvely expect that the calculated observables show differences reflecting the differences in the wave functions, and this is indeed the case when the pion and proton are described by plane waves. When the distortions are included in the pion and proton wave functions the calculated observables differ only slightly because the calculation is no longer a simple Fourier transform of the bound state wave function. The end result is that changes in the bound state wave function have little effect on the calculated observables in the cases we have studied.

The increasing contribution of the delta diagrams is clear as the energy of the incident photon is gradually increased towards the delta region, as would be expected. The calculated cross section is largest in the region where the momentum transfer to the

residual nucleus is small. The magnitude of the cross section falls fairly quickly with momentum transfer, but there is a wide kinematic range over which the cross section is greater than $0.1 \mu\text{b/sr srMeV}$ and the momentum transfer is greater than 1 fm^{-1} . These cross sections should be comfortably measurable at the new electron beam facilities.

The most important ingredient in this model for negative pion photoproduction seems to be the reaction mechanism, i.e. the six diagrams of figure 2-2, through which the initial state photon and neutron interact and produce the pion and proton detected in the final state. In principle the treatment of intermediate states requires that the full finite-range integration be performed, and that the propagating particle be allowed to interact with the medium. These requirements are however very difficult to implement. As a first step we have performed a local approximation in which the propagator is taken to be the momentum space propagator multiplying a coordinate space δ -function. This approximation is not as severe as it might first appear, since the seagull diagram of figure 2-2a) is evaluated exactly, and fortunately it is the largest single contributor in many of the calculations which we have considered. The other important terms are the s-channel delta diagram and the pion pole, and the full nonlocal calculation must be done for these diagrams. A group from Ohio University [Li92] have recently reported a nonrelativistic momentum space calculation of pion photoproduction on a nucleus. They find that the nonlocal effects of their calculation are small in most cases considered, and we would not expect to find any significant change from this result.

As we have seen, the set of diagrams comprised of the seagull, the pion pole and the proton pole are gauge invariant only when the pion and proton wave functions are taken to be plane waves. Inclusion of distorting potentials leads to loss of the invariance for this set of diagrams. The other diagrams which we have included (anomalous magnetic moment coupling and $\Delta(1232)$ poles) are each separately gauge invariant whether the pion and proton wave functions are plane or distorted waves. We are not aware of a method of restoring the gauge invariance without sacrificing the potentials which do such a good job of describing elastic scattering data.

We have considered pion photoproduction on ^{12}C for kinematics very close to those of the free reaction, $\gamma + n \rightarrow \pi^- + p$. The angles of the proton and pion as well as the kinetic energy of the proton were held at the values given by the elementary process, and the corresponding pion energy was then calculated. This results in a situation where the

momentum transfer to the residual nucleus is very small (less than 0.1 fm^{-1}). The calculated analyzing power due to linearly polarized photons is almost the same regardless of whether the reaction takes place on a free neutron or a $1p_{3/2}$ neutron bound in the ^{12}C nucleus, in the situation where the momentum transfer to the residual nucleus is very small. We found that the calculated results are in agreement with analyzing power data measured for the free reaction. Measurements of analyzing power for pion photoproduction on a nucleus would probably not be of great interest in this region as the results do not change much from the free case.

There are two important points brought out by this study. The first is that the diagrams proceeding through the formation of an intermediate $\Delta(1232)$ are not the dominant contributors to charged pion photoproduction in the region of the delta resonance. The Born terms are generally the major contributors to the reaction cross section; the delta contributions are somewhat less, even in the resonance region. The degree of contribution depends on the kinematics of the reaction, but we have found no instance, in which the cross section is of measurable magnitude, in which the cross section calculated from the delta diagrams is larger than that calculated from the Born terms alone. Secondly this reaction is not sensitive to the details of the nuclear structure input. At first this lack of sensitivity may seem unfortunate as we appear to limit the usefulness of the reaction for nuclear structure studies, but this in fact may be a blessing in disguise. Pion photoproduction on a nucleus is only sensitive to the reaction mechanism, and a nonlocal calculation with the inclusion of interaction between the propagating particles should be an excellent laboratory for studying the effects of the nuclear medium on the propagating particles. The Ohio group have in fact noted the point that the calculated results are very sensitive to changes in the mass of the isobar. This indicates that a delta-nucleus potential could have a sizeable effect on the results.

Comparisons with the few existing measurements have been carried out. The data from Tomsk, both 1979 [GS79] and 1990 [AG90], are not exclusive, i.e. the resolution of the experiment was such that the final state of the nucleus was unknown and in the analysis of the data a ground state was assumed for the residual nucleus. Even so we did obtain reasonable agreement with some of the data. The knockout of the $1s_{1/2}$ state of ^{12}C [GS79] was quite well described by our model, but we could not reproduce the

asymmetry between the two peaks apparent in the cross section for knockout of the $1p_{3/2}$ neutron. In addition we obtained excellent agreement with the data for a photon energy of $E_\gamma = 340 \pm 23$ MeV [AG90], while we agreed in some regions with the data for constant outgoing pion energy, and we were below the data by more than a factor of two in other regions. The MIT experiment [Ph89, Ph92], although claiming to be the first exclusive coincidence measurement of pion photoproduction on a nucleus, could not resolve the ground state of the final nucleus from the excited state at 6.2 MeV, so their results are not exclusive either. We obtained a reasonable description of the MIT data for the backward pion angle, and for the forward pion angle the calculation was a factor of two to three above the data.

A measurement of the related reaction $(\pi^+, \gamma p)$ has been made at TRIUMF (experiment 550). We have calculated observables for the kinematics at which the TRIUMF data were taken. In one case the delta diagrams are the major contributors to the calculated cross section, indicating that this reaction may be more sensitive to the interaction of the propagating delta with the nuclear medium. We have had the opportunity to compare one preliminary set of data with the results of our model, and the shape of the data agrees with the predicted shape. The normalization of the data has not yet been finalized so we cannot make any other statements regarding agreement in the comparison. We look forward to the completion of the data analysis for this experiment.

The present model may be extended to include a proper treatment of nonlocality as well as interactions of the propagating particle. The pion pole diagram can possibly be evaluated using a numerical technique developed by Cooper and Maxwell [Co89]. The nucleon poles generally contribute to a smaller degree than the pion pole but should be evaluated properly as a step toward the evaluation of the finite-range integrals involved in the delta diagrams. The model can also be extended to higher energies by including diagrams involving other nucleon excited states i.e. high mass nucleons and deltas, as well as the interactions of heavier mesons.

The current model can also be extended to the (γ, π^-) reaction. In this case the final state proton remains bound in the residual nucleus. If the resulting proton bound state can be described as a good shell model state, the calculation for (γ, π^-) will be numerically simpler than our calculation for $(\gamma, \pi^- p)$ since the sum over the proton partial waves required in the latter is removed.

Note that (γ, p) and (γ, π) are both high momentum transfer reactions, and both have difficulties with agreement between experiment and data in some kinematic regions. The diagrams contributing to our pion photoproduction model also contribute to these other reactions, but in the reaction we have considered we have the freedom to examine the low momentum transfer region allowing us to verify our understanding of the basic mechanism. We seek a description of photon induced reactions within a consistent framework, namely that involving a Dirac equation description of the nucleons involved in the reaction. This Dirac formalism has provided a better description of (γ, p) data than nonrelativistic models, but agreement breaks down at high momentum transfers where correlation effects, meson exchange diagrams and delta excitations may become important.

High duty factor electron beam facilities will allow good quality data for the reaction $(\gamma, \pi^- p)$ to be obtained in the near future. The data which currently exist are insufficient because of the large error bars and the scatter present in the data. We need high statistics, high precision data, where the final state of the nucleus is known in order to test the validity of our model over a range of momentum transfers, and to understand the reaction mechanism when interactions are included for the propagating particles.

References

- [AG90] P.S. Anan'in and I.V. Glavanakov, *Sov. J. Nucl. Phys.* **52** (1990) 205.
- [Ah75] J. Ahrens et al., *Nuclear Physics* **A251** (1975) 479.
- [Ah85] J. Ahrens, *Nuclear Physics* **A446** (1985) 229.
- [Aj82] F. Ajzenberg-Selove, *Nucl. Phys.* **A375** (1982) 1.
- [Aj85] F. Ajzenberg-Selove, *Nucl. Phys.* **A433** (1985) 1.
- [An76] P.S. Anan'in, I.V. Glavanakov and V.N. Stibunov, *JETP Lett.* **23** (1976) 269.
- [Ar72] P.E. Argan, G. Audit, N. De Botton, J.M. Laget, J. Martin, C. Schuhl and G. Thamas, *Phys. Rev. Lett.* **29** (1972) 1191.
- [Ar74] H. Arenhövel, *Nucl. Phys.* **A247** (1975) 473.
- [Ar77] P.E. Argan, G. Audit, A. Bloch, J.L. Faure, J.M. Laget, J. Martin, G. Thamas and C. Schuhl, *Nucl. Phys.* **A296** (1977) 373.
- [Ar81] J. Arends et al., *Physics Letters* **98B** (1981) 423.
- [Ar87] R.A. Arndt, John S. Hyslop III and L. David Roper, *Phys. Rev.* **D35** (1987) 128.
- [Ar90] R.A. Arndt, Zhujun Li, L.D. Roper and R.L. Workman, *Phys. Rev. Lett.* **65** (1990) 157.
- [AS72] Milton Abramowitz and Irene A. Stegun, *Handbook of Mathematical Functions*, Dover (1972).
- [BD64] J.D. Bjorken and S.D. Drell, *Relativistic Quantum Mechanics*, McGraw-Hill Book Company (1964).
- [BD65] J.D. Bjorken and S.D. Drell, *Relativistic Quantum Fields*, McGraw-Hill Book Company (1965).
- [Be68] F.A. Berends, A. Donnachie and D.H. Weaver, *Nucl. Phys.* **B4** (1968) 1.
- [Be89] M. Benmerrouche, R.M. Davidson and Nimai C. Mukhopadhyay, *Phys. Rev.* **C39** (1989) 2339.
- [BL77] I. Blomqvist and J.M. Laget, *Nuclear Physics* **A280** (1977) 405.
- [Bo80] N.N. Bogoliubov and D.V. Shirkov, *Introduction to the Theory of Quantized Fields*, John Wiley and Sons (1980).
- [BW75] G.E. Brown and W. Weise, *Physics Reports* **C22** (1975) 281.

- [Ca66] R.S. Caswell and L.C. Maximon, National Bureau of Standards Technical Note 409 (Nov. 15 1966).
- [Ch57] G.F. Chew, M.L. Goldberger, F.E. Low and Y. Nambu, Phys. Rev. **106** (1957) 134.
- [Ch83] C. Choller et al., Physics Letters **127B** (1983) 331.
- [Co82] E.D. Cooper and H.S. Sherif, Phys. Rev. **C25** (1982) 3024.
- [Co87] E.D. Cooper, K.H. Hicks and B.K. Jennings, Nucl. Phys. **A470** (1987) 523.
- [Co89] E.D. Cooper and O.V. Maxwell, Nucl. Phys. **A493** (1989) 468.
- [Co92] E.D. Cooper, S. Hama, B.C. Clark and R.L. Mercer, Global Dirac Phenomenology for Proton-Nucleus Elastic Scattering, preprint.
- [De66] V. Devanathan, Nuclear Physics **87** (1966) 477-480.
- [Do91] E. Donoghue et al., Phys. Rev. **C43** (1991) 213.
- [EK80] J.M. Eisenberg and D.S. Koltun, Theory of Meson Interactions with Nuclei, John Wiley and Sons (1980).
- [Er66] M. Ericson and T.E.O. Ericson, Annals of Physics **36** (1966) 323.
- [EW88] T. Ericson and W. Weise, Pions and Nuclei, Clarendon Press (1988).
- [Fa57] U. Fano, Rev. Mod. Phys. **29** (1957) 74.
- [Fa91] Farzin Farzanpay, University of Oregon, private communication.
- [Fa93] Farzin Farzanpay, University of Oregon, private communication.
- [Fe72] R.P. Feynman, Photon-Hadron Interactions, W.A. Benjamin (1972).
- [FM84] S. Frullani and J. Mougey, Advances in Nuclear Physics, vol. 14 (1984) 1.
- [Ga88] C. Garcia-Recio, E. Oset and L.L. Salcedo, Phys. Rev. **C37** (1988) 194.
- [Gan88] V.B. Ganenko et al., JETP Lett. **47** (1988) 519.
- [Gl80] I.V. Glavanakov, Sov. J. Nucl. Phys. **31** (1980) 181.
- [Gl82] I.V. Glavanakov, Sov. J. Nucl. Phys. **35** (1982) 509.
- [Gl89] I.V. Glavanakov, Sov. J. Nucl. Phys. **49** (1989) 58.
- [Go71] N.V. Goncharov, A.I. Derebchinskii, A.A. Zybalov, O.G. Konovalov, S.G. Tonapetyan and V.M. Khvorostyan, JETP **33** (1971) 843.
- [Go80] H. Goldstein, Classical Mechanics 2nd ed., Addison-Wesley Publishing Company (1980).
- [Go92] Research Summaries of the 1992 Gordon Conference on Photonic Reactions, Tilton, New Hampshire, Printed courtesy of The Saskatchewan

Accelerator Laboratory, Aug. 10-14 (1992).

- [GS79a] I.V. Glavanakov and V.N. Stibunov, *Sov. J. Nucl. Phys.* **30** (1979) 465.
- [GS79b] I.V. Glavanakov and V.N. Stibunov, *Sov. J. Nucl. Phys.* **29** (1979) 746.
- [GW64] M.L. Goldberger and K.M. Watson, Collision Theory, John Wiley and Sons Inc. (1964).
- [Ha90] S. Hama, B.C. Clark, E.D. Cooper, H.S. Sherif and R.L. Mercer, *Phys. Rev.* **C41** (1990) 2737.
- [Ha91] S. Hama, Ohio State University, private communication (1991).
- [Ha92] S. Hama, Ohio State University, private communication (1992).
- [Hac92] Evan Hackett, University of Alberta, private communication (1992).
- [Hay92] Evans Hayward, private communication.
- [Ho63] P.E. Hodgson, The Optical Model of Elastic Scattering, Oxford at the Clarendon Press (1963).
- [Ho92] S. Hoibraten, private communication (1992).
- [HS86] C.J. Horowitz and B.D. Serot, *Nucl. Phys.* **A368** (1986) 503.
- [Hu90] P.K.A. de Witt Huberts, *Journal of Physics* **G16** (1990) 507-544.
- [Ja70] D.F. Jackson, Nuclear Reactions, Methuen and Co. Ltd (1970).
- [Ja71] D.F. Jackson in Advances in Nuclear Physics, Volume 4 (M. Baranger and E. Vogt editors), Plenum Press (1971).
- [Ja75] J.D. Jackson, Classical Electrodynamics, 2nd ed., John Wiley and Sons (1975).
- [Ja90] J. Jaki et al., *Phys. Lett.* **B238** (1990) 36.
- [Jo86] J.I. Johansson, M.Sc. Thesis, University of Alberta, unpublished (1986).
- [Jo88] J.I. Johansson, E.D. Cooper and H.S. Sherif, *Nucl. Phys.* **A476** (1988) 663.
- [Ka88] A.N. Kamal and M. Araki, *Phys. Rev.* **C38** (1988) 1335.
- [Ki55] L.S. Kisslinger, *Phys. Rev.* **98** (1955) 761.
- [Ki85] P. Kitching, W.J. McDonald, Th.A.J. Maris and C.A.Z. Vasconcellos, *Advances in Nuclear Physics*, Vol. 15 (1985) 43.
- [Kl91] R.A.M. Klomp, V.G.J. Stoks and J.J. de Swart, *Phys. Rev.* **C44** (1991) 1258.
- [KMT59] A.K. Kerman, H. McManus and R.M. Thaler, *Annals of Physics*, **8** (1959) 551.

- [Ko85] A.M. Kobos, E.D. Cooper, J.I. Johansson and H.S. Sherif, Nucl. Phys. **A445** (1985) 605.
- [Ko89] S. Kowalski in the Proceedings of the 1989 IEEE Particle Accelerator Conference: accelerator science and technology, Chicago, Il., Mar. 20-23 (1989) 1.
- [La72] J.M. Laget, Nuclear Physics **A194** (1972) 81.
- [La81] J.M. Laget, Physics Reports **69** (1981) 1-84.
- [Le81] A. Leprêtre, H. Beil, R. Bergère, P. Carlos, J. Fagot, A. DeMiniac and A. Veyssière, Nuclear Physics **A367** (1981) 237.
- [Li92] Xiao-Dong Li, L.E. Wright and C. Bennhold, preprint submitted to Phys. Rev. C (1992).
- [Lo88] G. Lotz and H.S. Sherif, Phys. Lett. **B210** (1988) 45.
- [Lo89] G. Lotz, Ph.D. Thesis, University of Alberta, unpublished (1989).
- [Lo92] G.M. Lotz and H.S. Sherif, Nucl. Phys. **A537** (1992) 285-302.
- [Ma58] F. Mandl, Proc. Phys. Soc. (London) **71** (1958) 177.
- [Ma89] R. Machleidt, Advances in Nuclear Physics, Volume 19 (1989).
- [Mc83] J.A. McNeil, L. Ray and S.J. Wallace, Phys. Rev. **C27** (1983) 2123.
J.A. McNeil, J.R. Shepard and S.J. Wallace, Phys. Rev. Lett. **50** (1983) 1439.
- [Mc88] J.P. McDermott, E. Rost, J.R. Shepard and C.Y. Cheung, Phys. Rev. Lett. **61**, 814 (1988).
- [Me77] D. Menze, W. Pfeil and R. Wilcke, ZAED Compilation of Pion Photoproduction Data, Physikalisches Institute der Universität Bonn, Germany (1977).
- [MS84] F. Mandl and G. Shaw, Quantum Field Theory, John Wiley and Sons (1984).
- [Ni69] K. Nishijima, Fields and Particles, W.A. Benjamin Inc. (1969).
- [Ni92] J. Nieves, E. Oset and C. Garcia-Recio, preprint A Theoretical Approach to Pionic Atoms and the Problem of the Anomalies (1992).
- [No24] B.V. Noumerov, Monthly Notices of the Royal Astronomical Society **84** (1924) 180 and 592.
- [Ol75] M.G. Olsson and E.T. Osypowski, Nucl. Phys. **B87** (1975) 399.
- [Pa92] Particle Data Group, Review of Particle Properties, Phys. Rev. **D45** (1992) 1.

- [Ph89] L.D. Pham, Ph.D. Thesis, Massachusetts Institute of Technology, unpublished (1989).
- [Ph92] L.D. Pham et al., Phys. Rev. **C46** (1992) 621.
- [Ra89] J. Raynal, H.S. Sherif, A.M. Kobos, E.D. Cooper and I. Johansson, Phys. Lett. **B218** (1989) 403.
- [Ri90] B.G. Ritchie et al., Phys. Rev. **C41** (1990) 1668.
- [RS41] W. Rarita and J. Schwinger, Phys. Rev. **60** (1941) 61.
- [Se90] K.K. Seth et al., Phys. Rev. **C41** (1990) 2800.
- [Sh84] J.R. Shepard, E. Rost and J. Piekarewicz, Phys. Rev. **C30** (1984) 1604.
- [SMC79] K. Stricker, H. McManus and J.A. Carr, Phys. Rev. **C19** (1979) 929.
- [SMC80] K. Stricker, J.A. Carr and H. McManus, Phys. Rev. **C22** (1980) 2043.
- [So84] R.J. Sobie et al., Phys. Rev. **C30** (1984) 1612.
- [ST81] M.K. Singham and F. Tabakin, Annals of Physics **135** (1981) 71.
- [SV68] Hirotaka Sugawara and Frank Von Hippel, Phys. Rev. **172** (1968) 1764.
- [SW86] B.D. Serot and J.D. Walecka, Advances in Nuclear Physics, Volume 16, Plenum Press (1986).
- [Ta84] L. Taitor and L.E. Wright, Phys. Rev. **C30** (1984) 989.
- [TC87] A.E. Thorlacius and E.D. Cooper, Journal of Computational Physics, **72** (1987) 70.
- [Th76] M. Theis, Phys. Lett. **63B** (1976) 43.
- [Um56] H. Umezawa, Quantum Field Theory, North-Holland Publishing Company, (1956).
- [Wa69] R.L. Walker, Phys. Rev. **182** (1969) 1729.
- [Wa85] S.J. Wallace in the Proceedings of the LAMPF Workshop on Dirac Approaches to Nuclear Physics, Proceedings No. LA-10438-C, (1985) 87.
- [Za88] R.N. Zare, Angular Momentum, John Wiley and Sons (1988).

Appendix A - Isospin Considerations

A.1 Field Operators

In writing a lagrangian which involves the interaction of different types of particles, we need to find a representation of the field operators involving creation and annihilation operators of the various particles. For our case we need to be sure that the creation and destruction of electric charge occurs in a way that holds the total charge before the interaction equal to the total charge after the interaction. This type of conserved quantity arises from an invariance of the lagrangian density of the system under phase changes of the particles. In this appendix we combine the work of Bjorken and Drell [BD65] with that of Serot and Walecka [SW86] to obtain an unambiguous description of field operators which are consistent with charge conservation.

The lagrangian density for a system of interacting pions and nucleons is

$$\mathcal{L} = \bar{\Psi} (i \not{\partial} - m) \Psi + \frac{1}{2} (\partial_{\mu} \vec{\phi} \cdot \partial^{\mu} \vec{\phi} - m_{\pi}^2 \vec{\phi} \cdot \vec{\phi}) + \mathcal{L}_{\pi NN} \quad (\text{A-1})$$

where the interaction lagrangian commonly takes one of two forms

$$\text{pseudoscalar :} \quad -i g_{\pi} \bar{\Psi} \gamma_5 \vec{\tau} \cdot \vec{\phi} \Psi \quad (\text{A-2a})$$

$$\text{pseudovector :} \quad -\frac{f_{\pi}}{m_{\pi}} \bar{\Psi} \gamma_5 \vec{\tau} \cdot \not{\partial} \vec{\phi} \Psi \quad (\text{A-2b})$$

The nucleon field is an isospinor, containing both the proton and neutron fields $\Psi = \begin{bmatrix} \Psi_p \\ \Psi_n \end{bmatrix}$ while the pion (isovector) is described by a triplet of real pseudoscalar fields $\vec{\phi} = (\phi_1, \phi_2, \phi_3)$. The charged states of the pion will be expressed in terms of the three pseudoscalar fields and will be the states that are actually used in the rest of this work.

First we consider one of the simplest transformations available to us, to clarify the effect of the invariance of the lagrangian. Perform a global infinitesimal phase transformation on the nucleon spinor, while leaving the pion unchanged, by

$$\begin{aligned} \Psi(x) &\rightarrow \Psi'(x) = e^{i\alpha} \Psi(x) \equiv \Psi(x) + i\alpha \Psi(x) \\ \phi_i(x) &\rightarrow \phi_i(x) = \phi_i(x) \end{aligned} \quad (\text{A-3})$$

where α is an infinitesimal constant. We are changing the phase of the proton and neutron fields by the same amount. The lagrangian density (A-1) is readily shown to be invariant under this transformation by simple substitution, since the derivative operators have no

effect on the rotation parameter α . The variation in the lagrangian is then

$$\begin{aligned}\delta \mathcal{L} &= \frac{\partial \mathcal{L}}{\partial \psi} \delta \psi + \frac{\partial \mathcal{L}}{\partial (\partial_\mu \psi)} \delta (\partial_\mu \psi) \\ &= \partial_\mu \left[\frac{\partial \mathcal{L}}{\partial (\partial_\mu \psi)} \delta \psi \right] = 0\end{aligned}\tag{A-4}$$

where we have used the Euler-Lagrange equations

$$\partial_\mu \frac{\partial \mathcal{L}}{\partial (\partial_\mu \psi)} - \frac{\partial \mathcal{L}}{\partial \psi} = 0\tag{A-5}$$

to rewrite the variation of the lagrangian density as a four dimensional divergence. We now have the divergence of a quantity being zero, i.e. $\partial^\mu j_\mu = 0$, so the invariance of our lagrangian under a phase transformation leads to a conserved current, a result known as Noether's theorem [MS84]. We define the conserved current, B^μ , for this transformation by

$$\alpha B^\mu = - \left[\frac{\partial \mathcal{L}}{\partial (\partial_\mu \psi)} \delta \psi \right]\tag{A-6}$$

We calculate this conserved current explicitly from the infinitesimal variation in the field and the derivative of the lagrangian with respect to the gradient of the field

$$\delta \psi = i \alpha \psi(x) \quad \frac{\partial \mathcal{L}}{\partial (\partial_\mu \psi)} = i \bar{\psi}(x) \gamma^\mu\tag{A-7}$$

The conserved current associated with a global phase transformation of the baryon fields is then

$$B^\mu = \bar{\psi} \gamma^\mu \psi\tag{A-8}$$

By integrating the zeroth component of this conserved current over all space we get a "charge" that is a constant of the motion, in this case the baryon number

$$\begin{aligned}B &= \int B^0(x) d^3x \\ &= \int \left[\psi_p^\dagger(x) \psi_p(x) + \psi_n^\dagger(x) \psi_n(x) \right] d^3x\end{aligned}\tag{A-9}$$

which is just the number of protons and neutrons minus the number of antiprotons and antineutrons. We see that the fact that our lagrangian is invariant under a change of phase of the baryon (proton and neutron) fields forces us to have a constant baryon number.

Now consider a transformation which changes the phase of only the charged

particles and has no effect on the neutral particles in the system. We make an infinitesimal rotation in isospin space of the form

$$\begin{aligned}\psi(x) &\rightarrow \psi'(x) = e^{i\theta(1+\tau_3)/2} \psi(x) \equiv \psi(x) + \frac{i\theta}{2} (1 + \tau_3) \psi(x) \\ \pi_i(x) &\rightarrow \pi'_i(x) = e^{i\theta T_3} \pi_i(x) \equiv \pi_i(x) + i\theta T_3 \pi_i(x)\end{aligned}\quad (\text{A-10})$$

where θ is a real infinitesimal constant and τ_3 is the third Pauli matrix for isospin 1/2. T_3 is the 3x3 matrix which gives the third component of isospin for an isospin one, and has the components $T_3 = \text{diag}(1, 0, -1)$ with the off-diagonal elements all equal to zero. The charged pion field has components

$$\vec{\pi}(x) = \begin{bmatrix} \pi_+(x) \\ \pi_0(x) \\ \pi_-(x) \end{bmatrix} \quad (\text{A-11})$$

The charged field components are written in terms of the components of the real field as

$$\begin{aligned}\pi_{\pm}(x) &= \frac{1}{\sqrt{2}} [\varphi_1(x) \mp \varphi_2(x)] \\ \pi_0(x) &= \varphi_3(x)\end{aligned}\quad (\text{A-12})$$

so the real field undergoes the transformation equivalent to that of the charged field

$$\varphi_i(x) \rightarrow \varphi'_i(x) \equiv \varphi_i(x) - [\vec{\theta} \times \vec{\varphi}]_i \quad (\text{A-13})$$

where we have $\vec{\theta} = (0, 0, \theta)$.

The lagrangian density (A-1) is invariant under this transformation which leads us to a conserved current j^μ which we write as

$$\theta j^\mu(x) = - \left[\frac{\partial \mathcal{L}}{\partial(\partial_\mu \psi)} \delta\psi \right] - \left[\frac{\partial \mathcal{L}}{\partial(\partial_\mu \varphi_i)} \delta\varphi_i \right] \quad (\text{A-14})$$

To calculate $j^\mu(x)$ we collect the necessary pieces, the variations of the fields and the derivatives of the lagrangian with respect to the gradient of the fields, as we did before

$$\begin{aligned}\delta\psi(x) &= \frac{i\theta}{2} (1 + \tau_3) \psi(x) & \delta\varphi_i(x) &= - [\vec{\theta} \times \vec{\varphi}(x)]_i \\ \frac{\partial \mathcal{L}}{\partial(\partial_\mu \psi)} &= i \bar{\psi}(x) \gamma^\mu & \left[\frac{\partial \mathcal{L}}{\partial(\partial_\mu \varphi_i)} \right]_{PS} &= \partial^\mu \varphi_i(x)\end{aligned}\quad (\text{A-15})$$

where we have used the pseudoscalar interaction term in the lagrangian. Combining these pieces gives the conserved electromagnetic current, with the pseudoscalar interaction, as

$$j^\mu(x) = \bar{\psi}(x) \gamma^\mu \frac{1}{2} (1 + \tau_3) \psi(x) + \partial^\mu \vec{\varphi}(x) \cdot [\vec{\theta} \times \vec{\varphi}(x)] \quad (\text{A-16})$$

Integrating the zeroth component of the electromagnetic current gives us the total charge (actually the number of charges) of the system as a conserved quantity, which we can write as a sum of nucleon and pion charges.

$$Q = \int d^3x \left\{ \frac{1}{2} \psi^\dagger (1 + \tau_3) \psi + \phi_1 \dot{\phi}_2 - \phi_2 \dot{\phi}_1 \right\} = Q_N + Q_\pi \quad (\text{A-17})$$

where the dot over the real field denotes the derivative with respect to time.

The nucleon charge is just the net charge of protons and antiprotons

$$Q_N = \int d^3x \psi_p^\dagger \psi_p \quad (\text{A-18})$$

To calculate the nucleon charge we expand the Dirac field in terms of creation and annihilation operators as

$$\psi(x) = \frac{1}{(2\pi)^{3/2}} \sum_s \int d^3k \left(\frac{m}{E} \right)^{1/2} \left\{ b_s(\vec{k}) u_s(k) e^{-ik \cdot x} + d_s^\dagger(\vec{k}) v_s(k) e^{ik \cdot x} \right\} \quad (\text{A-19})$$

Using (A-19) and its hermitian conjugate in the expression for the nucleon charge (A-18) recalling the anti-commutation relations for the creation and annihilation operators for a fermion

$$\begin{aligned} \{ b_s(\vec{k}), b_{s'}^\dagger(\vec{k}') \} &= \delta_{s,s'} \delta^3(\vec{k} - \vec{k}') \\ \{ d_s(\vec{k}), d_{s'}^\dagger(\vec{k}') \} &= \delta_{s,s'} \delta^3(\vec{k} - \vec{k}') \end{aligned} \quad (\text{A-20})$$

gives after a bit of algebra

$$Q_N = \sum_s \int d^3k \left\{ b_s^\dagger(\vec{k}) b_s(\vec{k}) - d_s^\dagger(\vec{k}) d_s(\vec{k}) \right\} + \sum_s \int d^3k \delta^3(0) \quad (\text{A-21})$$

To get rid of the infinite term use a normal ordered operator for the charge : Q_N in which creation operators are placed to the left of annihilation operators and fermion operators change sign when their order is changed

$$: b_s(\vec{k}) b_s^\dagger(\vec{k}) : = - b_s^\dagger(\vec{k}) b_s(\vec{k}) \quad (\text{A-22})$$

The nucleon charge is then

$$Q_N = \sum_s \int d^3k \left\{ b_s^\dagger(\vec{k}) b_s(\vec{k}) - d_s^\dagger(\vec{k}) d_s(\vec{k}) \right\} \quad (\text{A-23})$$

which is in units of the quantum of electric charge. The actual charge of the system is then obtained by multiplying by a unit of charge with a sign which we must choose by deciding on the charge of the particle which our creation operators will create. We fix the charges of all the nucleons and pions that are created by setting

$$\boxed{q = e > 0} \quad (\text{A-24})$$

so that $b_s^\dagger(\vec{k})$ creates a proton of spin s , momentum \vec{k} and charge e (a proton), while $d_s^\dagger(\vec{k})$ creates an antiproton with spin s , momentum \vec{k} and charge $-e$. There is no ambiguity left in the charges of the pion fields.

The normal ordered pion charge operator is

$$Q_\pi = \int d^3x : (\phi_1 \dot{\phi}_2 - \phi_2 \dot{\phi}_1) : \quad (\text{A-25})$$

The i^{th} component of the scalar field is written in terms of creation and annihilation operators as

$$\phi_i(x) = \frac{1}{(2\pi)^{3/2}} \int \frac{d^3k}{\sqrt{2\omega_k}} \{ a_i(\vec{k}) e^{-ik \cdot x} + a_i^\dagger(\vec{k}) e^{ik \cdot x} \} \quad (\text{A-26})$$

Use this in the pion charge operator and recall that for bosons there is no sign change when normal ordering and on performing the required algebra the charge due to mesons is

$$Q_\pi = -i \int d^3k \{ a_1^\dagger(\vec{k}) a_2(\vec{k}) - a_2^\dagger(\vec{k}) a_1(\vec{k}) \} \quad (\text{A-27})$$

This is difficult to interpret in terms of the creation of charged states so we make the following definitions

$$\begin{aligned} a(\vec{k}) &= \frac{1}{\sqrt{2}} [a_1(\vec{k}) + i a_2(\vec{k})] \\ b(\vec{k}) &= \frac{1}{\sqrt{2}} [a_1(\vec{k}) - i a_2(\vec{k})] \end{aligned} \quad (\text{A-28})$$

so the pion charge operator is then

$$Q_\pi = \int d^3k \{ b^\dagger(\vec{k}) b(\vec{k}) - a^\dagger(\vec{k}) a(\vec{k}) \} \quad (\text{A-29})$$

and we have that $b^\dagger(\vec{k})$ creates a pion with momentum \vec{k} and charge e , while $a^\dagger(\vec{k})$ creates a pion with momentum \vec{k} and charge $-e$. We write the field for the positively charged pion to be consistent with the action of the nucleon spinor on a positive charge so

$$\pi^+(x) = \frac{1}{(2\pi)^{3/2}} \int \frac{d^3k}{\sqrt{2\omega_k}} \{ a^\dagger(\vec{k}) e^{ik \cdot x} + b(\vec{k}) e^{-ik \cdot x} \} \quad (\text{A-30})$$

i.e. $\pi^+(x)$ destroys a positively charged particle in the initial state. The negative and neutral pion fields are written similarly as

$$\begin{aligned} \pi^-(x) &= \frac{1}{(2\pi)^{3/2}} \int \frac{d^3k}{\sqrt{2\omega_k}} \{ a(\vec{k}) e^{-ik \cdot x} + b^\dagger(\vec{k}) e^{ik \cdot x} \} \\ \pi^0(x) &= \frac{1}{(2\pi)^{3/2}} \int \frac{d^3k}{\sqrt{2\omega_k}} \{ a_3(\vec{k}) e^{-ik \cdot x} + a_3^\dagger(\vec{k}) e^{ik \cdot x} \} \end{aligned} \quad (\text{A-31})$$

Now, just for fun, consider the effects of an isospin rotation that affects all the fields so we have the transformations

$$\begin{aligned}\psi(x) &\rightarrow \psi'(x) = e^{i\vec{\tau}\cdot\vec{\Theta}/2} \psi(x) \equiv \psi(x) + \frac{i}{2} \vec{\tau} \cdot \vec{\Theta} \psi(x) \\ \varphi_i(x) &\rightarrow \varphi'_i(x) = e^{i\vec{T}\cdot\vec{\Theta}} \varphi_i(x) \equiv \varphi_i(x) + i \vec{T} \cdot \vec{\Theta} \varphi_i(x)\end{aligned}\quad (\text{A-32})$$

where $\vec{\Theta} = (\Theta_1, \Theta_2, \Theta_3)$ are real infinitesimal constants and the τ_i are the Pauli matrices for isospin. Use the adjoint representation of the spin one SU(2) generators so the matrix elements of the T_i are $(T_i)_{jk} = -i \epsilon_{ijk}$ and the rotated pion field can be written as

$$\varphi'_i(x) \equiv \varphi_i(x) - [\vec{\Theta} \times \vec{\varphi}(x)]_i \quad (\text{A-33})$$

The lagrangian is invariant under the transformation of the fields so we define the conserved isovector current \vec{T}^μ as we have defined our other currents before by

$$\vec{\Theta} \cdot \vec{T}^\mu = - \left[\frac{\partial \mathcal{L}}{\partial(\partial_\mu \psi)} \delta \psi \right] - \left[\frac{\partial \mathcal{L}}{\partial(\partial_\mu \varphi_i)} \delta \varphi_i \right] \quad (\text{A-34})$$

to calculate \vec{T}^μ we collect the necessary pieces in the usual fashion to get the conserved isovector current as (with the pseudoscalar interaction)

$$\vec{T}^\mu = \frac{1}{2} \bar{\psi} \gamma^\mu \vec{\tau} \psi + \vec{\varphi} \times \partial^\mu \vec{\varphi} \quad (\text{A-35})$$

Using the baryon current B^μ and the third component of the isovector current \vec{T}^μ we can write the conserved electromagnetic current as

$$j^\mu = \frac{1}{2} B^\mu + T_3^\mu = \frac{1}{2} \psi^\dagger \gamma^\mu (1 + \tau_3) \psi + [\vec{\varphi} \times \partial^\mu \vec{\varphi}]_3 \quad (\text{A-36})$$

which is just what we had for the electromagnetic current before.

A.2 The $T = 1/2$ to $T = 3/2$ Isospin Transition Operator

The isospin matrix elements of a system in which we have pions and nucleons interacting to form deltas are of the form [SV68]

$$\langle \frac{3}{2}, \mu | \vec{T} \cdot \vec{\varphi} | \frac{1}{2}, \nu \rangle \quad (\text{A-37})$$

where the nucleon isospinor has two components to describe the proton and the neutron which we can write as

$$|p\rangle = |\frac{1}{2}, \frac{1}{2}\rangle = \begin{bmatrix} 1 \\ 0 \end{bmatrix} \quad |n\rangle = |\frac{1}{2}, -\frac{1}{2}\rangle = \begin{bmatrix} 0 \\ 1 \end{bmatrix} \quad (\text{A-38})$$

and the four charge states of the delta can be described by a four component spinor in

isospin space as

$$|\Delta^{++}\rangle = \left| \frac{3}{2}, \frac{3}{2} \right\rangle = \begin{bmatrix} 1 \\ 0 \\ 0 \\ 0 \end{bmatrix} \quad \dots \quad |\Delta^{-}\rangle = \left| \frac{3}{2}, -\frac{3}{2} \right\rangle = \begin{bmatrix} 0 \\ 0 \\ 0 \\ 1 \end{bmatrix} \quad (\text{A-39})$$

The charge states of the pion are written in terms of the three components of an uncharged scalar field

$$\vec{\varphi} = (\varphi_1, \varphi_2, \varphi_3) \quad (\text{A-40})$$

as

$$\begin{aligned} \varphi_1^{-1} &= \frac{1}{\sqrt{2}} (\varphi_1 - i \varphi_2) \\ \varphi_1^1 &= -\frac{1}{\sqrt{2}} (\varphi_1 + i \varphi_2) \\ \varphi_1^0 &= \varphi_3 \end{aligned} \quad (\text{A-41})$$

We want to calculate the matrix elements of the T_i . These matrices must be 4x2 objects in order to connect the delta and nucleon spinors as we have written them above.

Expand the dot product of the pion field and the isospin transition matrices in terms of the charge states of the pion field as

$$\begin{aligned} \vec{T} \cdot \vec{\varphi} &= \sum_{\gamma} (-)^{\gamma} T_1^{\gamma} \varphi_1^{-\gamma} \\ &= T^{-} \pi^{-} + T^{+} \pi^{+} + T^0 \pi^0 \end{aligned} \quad (\text{A-42})$$

where we have written the transition matrices as the components of a spherical tensor of rank one

$$\begin{aligned} T_1^1 &= -\frac{1}{\sqrt{2}} (T_1 + i T_2) \\ T_1^{-1} &= \frac{1}{\sqrt{2}} (T_1 - i T_2) \\ T_1^0 &= T_3 \end{aligned} \quad (\text{A-43})$$

and the matrix which raises the isospin projection of the nucleon by one unit is $T^{+} = -T_1^1$ while the operator which lowers the isospin projection by one unit is $T^{-} = T_1^{-1}$ and finally we have the operator $T^0 = T_1^0$ which does not change the projection of isospin of the nucleon. The charge states of the pion are related to the components of the spherical tensor by

$$\begin{aligned} \pi^{+} &= \varphi_1^{-1} \\ \pi^0 &= \varphi_1^0 \\ \pi^{-} &= -\varphi_1^1 \end{aligned} \quad (\text{A-44})$$

The matrix elements of the spherical components of \vec{T} are written in terms of its reduced matrix element using the Wigner-Eckart theorem

$$\begin{aligned}
T_{\mu\nu}^{\gamma} &= \langle \frac{3}{2}, \mu | T_1^{\gamma} | \frac{1}{2}, \nu \rangle \\
&= (-)^{3/2-\mu} \begin{pmatrix} 3/2 & 1 & 1/2 \\ -\mu & \gamma & \nu \end{pmatrix} \langle \frac{3}{2} || T^1 || \frac{1}{2} \rangle
\end{aligned} \tag{A-45}$$

What happens for $\gamma = 1$? The action of T_1^1 on the nucleon is to raise the isospin by one unit and the projection by one unit so we have

$$T_1^1 | \frac{1}{2}, \nu \rangle = | \frac{3}{2}, \nu + 1 \rangle \tag{A-46}$$

and for $\nu = 1/2$ we get the state of greatest weight $| \frac{3}{2}, \frac{3}{2} \rangle$. From Equation (A-45) we then have the reduced matrix element as

$$\langle \frac{3}{2} || T^1 || \frac{1}{2} \rangle = 2 \tag{A-47}$$

With the reduced matrix element in hand we can calculate the elements of the \vec{T} matrices using the Wigner-Eckart theorem. First we evaluate the components of the spherical matrices

$$\begin{aligned}
T_{\mu\nu}^1 &= 2 (-)^{3/2-\mu} \begin{pmatrix} 3/2 & 1 & 1/2 \\ -\mu & 1 & \nu \end{pmatrix} \\
&= \delta_{\mu, 3/2} \delta_{\nu, 1/2} + \frac{1}{\sqrt{3}} \delta_{\mu, 1/2} \delta_{\nu, -1/2} \\
&= \begin{bmatrix} 1 & 0 \\ 0 & 1/\sqrt{3} \\ 0 & 0 \\ 0 & 0 \end{bmatrix}
\end{aligned} \tag{A-48}$$

similarly we have the other two matrices as

$$T_{\mu\nu}^{-1} = \begin{bmatrix} 0 & 0 \\ 0 & 0 \\ 1/\sqrt{3} & 0 \\ 0 & 1 \end{bmatrix} \quad T_{\mu\nu}^0 = \sqrt{\frac{2}{3}} \begin{bmatrix} 0 & 0 \\ 1 & 0 \\ 0 & 1 \\ 0 & 0 \end{bmatrix} \tag{A-49}$$

We calculate the vector components from these spherical components by inverting equations (A-43) to get the isospin transition matrices to be

$$T_1 = \frac{1}{\sqrt{2}} \begin{bmatrix} -1 & 0 \\ 0 & -1/\sqrt{3} \\ 1/\sqrt{3} & 0 \\ 0 & 1 \end{bmatrix} \quad T_2 = \frac{i}{\sqrt{2}} \begin{bmatrix} 1 & 0 \\ 0 & 1/\sqrt{3} \\ 1/\sqrt{3} & 0 \\ 0 & 1 \end{bmatrix} \quad T_3 = \sqrt{\frac{2}{3}} \begin{bmatrix} 0 & 0 \\ 1 & 0 \\ 0 & 1 \\ 0 & 0 \end{bmatrix} \tag{A-50}$$

We can check this method by calculating the matrix elements of the spin 1/2 to spin 1/2 isospin matrices

$$T_{\mu\nu}^{\gamma} = \langle \frac{1}{2}, \mu | T_1^{\gamma} | \frac{1}{2}, \nu \rangle \tag{A-51}$$

using the reduced matrix element

$$\langle \frac{1}{2} || T^1 || \frac{1}{2} \rangle = \sqrt{6} \tag{A-52}$$

This yields the Pauli isospin matrices as it should.

Appendix B - Approximating Propagators

In the present calculations the final state interactions are taken into account. This necessitates that the integrals over space be done numerically. We also have the added complexity of three particles in the final state which means a large increase in the time required to do partial wave sums. There is nothing we can do about the number of particles in the final state but perhaps we can make some (reasonable?) approximations to reduce the number of integrations we need to do. In the following we are interested in what happens when doing space integrations and thus shall not include spin in the discussion.

Consider the reaction $1 + 2 \rightarrow 3 + 4$ in which two scalar particles interact through the exchange of a different scalar particle as shown in figure B-1.

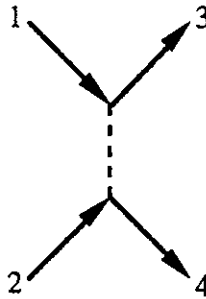


Figure B-1. Two scalar particles interact through the exchange of a different scalar particle.

The s-matrix for this diagram is proportional to an eight dimensional coordinate space integral

$$S_{fi} = A \int d^4x d^4y \varphi_4^*(x) \varphi_2(x) \underline{\phi(x)} \phi^\dagger(y) \varphi_3^*(y) \varphi_1(y) \quad (\text{B-1})$$

where A contains all the constants that we don't want to deal with now. Compare (B-1) to the s-matrix for the pion pole contribution (2-48), which involves nucleon spinors and a contraction over pion fields.

The contraction of the scalar field is related to the Feynman propagator, which can be written as a four dimensional integral over the momentum of the intermediate

particle [BD65]

$$\begin{aligned} \overline{\phi(x)} \phi^\dagger(y) &= i \Delta_F(x-y) \\ &= \frac{i}{(2\pi)^4} \int d^4k \frac{e^{-ik \cdot (x-y)}}{k^2 - m^2 + i\epsilon} \end{aligned} \quad (\text{B-2})$$

Particle 1 is going to be an exact plane wave (the photon) so its wave function is

$$\phi_1(y) = e^{-ik_1 \cdot y} \quad (\text{B-3})$$

Assume for the moment that particle 3 is a plane wave as well

$$\phi_3(y) = e^{-ik_3 \cdot y} \quad (\text{B-4})$$

which allows us to do the integration over y

$$\int d^4y e^{iy \cdot (k - k_1 + k_3)} = (2\pi)^4 \delta^4(k - k_1 + k_3) \quad (\text{B-5})$$

and yields the condition for conservation of 4-momentum at the vertex where $k = k_1 - k_3$ is the momentum of the exchanged particle.

Using the δ -function we can now do the integration over momentum to give

$$S_{\bar{n}} = \frac{iA}{(k_1 - k_3)^2 - m^2} \int d^4x \phi_4^*(x) \phi_2(x) e^{-ix \cdot (k_1 - k_3)} \quad (\text{B-6})$$

Note that if we take plane waves for particles 2 and 4 and do the integration over x to get a δ -function between the initial and final momenta

$$\int d^4x e^{ix \cdot k_4} e^{-ix \cdot k_2} e^{-ix \cdot (k_1 - k_3)} = (2\pi)^4 \delta^4(k_4 - k_2 - k_1 + k_3) \quad (\text{B-7})$$

This is the statement of energy and momentum conservation between the initial and final states, which is in 4-momentum language $k_1 + k_2 = k_3 + k_4$.

If we now consider a propagator of the form

$$\Delta_F(x-y) = \frac{1}{(k_1 - k_3)^2 - m^2} \delta^4(x-y) \quad (\text{B-8})$$

in the s-matrix (B-1) we get exactly the same result as we did using the propagator of (B-2)

$$S_{\bar{n}} = \frac{iA(2\pi)^4}{(k_1 - k_3)^2 - m^2} \delta^4(k_4 - k_2 - k_1 + k_3) \quad (\text{B-9})$$

If the propagator has gradients acting on it we have

$$\partial_x^\mu \partial_y^\nu \Delta_F(x-y) = \frac{1}{(2\pi)^4} \int d^4k k^\mu k^\nu \frac{e^{-ik \cdot (x-y)}}{k^2 - m^2 + i\epsilon} \quad (\text{B-10})$$

and following through the same steps as above we get

$$\partial_x^\mu \partial_y^\nu \Delta_F(x-y) = \frac{(k_1-k_3)^\mu (k_1-k_3)^\nu}{(k_1-k_3)^2 - m^2} \delta^4(x-y) \quad (\text{B-11})$$

and this is actually a form we will use.

Now consider the reaction $1 + 2 \rightarrow 3 + 4$ in which two scalar particles collide and turn into a fermion which then decays into two scalar particles as shown in figure B-2 (a supersymmetric type of thing)

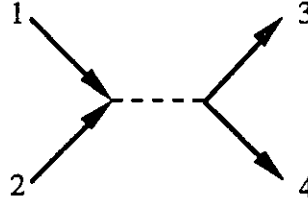


Figure B-2.

The s-matrix for this diagram is

$$S_{fi} = A \int d^4x d^4y \phi_4^*(x) \phi_3^*(x) \underline{\psi(x)} \bar{\psi}(y) \phi_2(y) \phi_1(y) \quad (\text{B-12})$$

where the contraction is now over fermion fields and is [BD65]

$$\begin{aligned} \underline{\psi(x)} \bar{\psi}(y) &= i S_F(x-y) \\ &= \frac{i}{(2\pi)^4} \int d^4p \frac{\not{p} + m}{p^2 - m^2 + i\epsilon} e^{-ip \cdot (x-y)} \end{aligned} \quad (\text{B-13})$$

We are going to be able to do one of the integrals only if both of particles 1 and 2 or both of 3 and 4 are plane waves. If we compare with the s-matrix for the neutron pole (3-53) we see that particles 1 and 2 are the photon and the bound state neutron. A bound state isn't very close to a plane wave so assume that particles 3 and 4 are plane waves and we can do the integration over x as

$$\int d^4x e^{-ix \cdot (k-k_3-k_4)} = (2\pi)^4 \delta^4(k - k_3 - k_4) \quad (\text{B-14})$$

so the momentum of the propagating particle is the sum of the outgoing momenta, as we expect. Using this δ -function we can do the integration over momentum to give

$$S_{fi} = iA \frac{k_3 + k_4 + m}{(k_3+k_4)^2 - m^2} \int d^4y \phi_2(y) \phi_1(y) e^{iy \cdot (k_3+k_4)} \quad (\text{B-15})$$

and if we take plane waves for particles 1 and 2 we get the δ -function which gives 4-momentum conservation, as it must.

If we take the propagator to be

$$S_F(x-y) = \frac{k_3 + k_4 + m}{(k_3+k_4)^2 - m^2} \delta^4(x-y) \quad (\text{B-16})$$

we get exactly the same result for the s-matrix therefore this is what we are going to do.

The form which we take for the propagators does not change the plane wave results at all. To evaluate these diagrams in which we will describe the nucleons and the pion by distorted waves we assume, for the s-channel diagrams, that both of the outgoing particles have momentum distributions that are strongly peaked near the plane wave value. For the u- and t-channel diagrams we assume that the particle connected to the photon vertex has most of its momentum components near the plane wave value.

The contractions that we will use are then:

$$\partial_x^\mu \underline{\pi^+(x)} \partial_y^\nu \underline{\pi^-(y)} = i \frac{(k_1-k_3)^\mu (k_1-k_3)^\nu}{(k_1-k_3)^2 - m_\pi^2} \delta^4(x-y) \quad (\text{B-17})$$

with $k_1 \rightarrow k_\gamma$ and $k_3 \rightarrow k_\pi$

$$\underline{\psi_p(x)} \bar{\psi}_p(y) = i \frac{k_1 - k_3 + m_p}{(k_1-k_3)^2 - m_p^2} \delta^4(x-y) \quad (\text{B-18})$$

with $k_1 \rightarrow k_\gamma$ and $k_3 \rightarrow k_p$

$$\underline{\psi_n(x)} \bar{\psi}_n(y) = i \frac{k_3 + k_4 + m_n}{(k_3+k_4)^2 - m_n^2} \delta^4(x-y) \quad (\text{B-19})$$

with $k_3 \rightarrow k_\pi$ and $k_4 \rightarrow k_p$

$$\underline{\Delta_0^\mu(x)} \bar{\Delta}_0^\nu(y) = i \frac{\not{p}_\Delta + m_\Delta}{p_\Delta^2 - m_\Delta^2 + i m_\Delta \Gamma_\Delta} \left[g^{\mu\nu} - \frac{1}{3} \gamma^\mu \gamma^\nu - \frac{1}{3 m_\Delta} (\gamma^\mu p_\Delta^\nu - \gamma^\nu p_\Delta^\mu) - \frac{2}{3 m_\Delta^2} p_\Delta^\mu p_\Delta^\nu \right] \delta^4(x-y)$$

with $p_\Delta = k_3 + k_4 = k_\pi + k_p$

(B-20)

$$\underline{\Delta_+^\mu(x)} \bar{\Delta}_+^\nu(y) = i \frac{\not{p}_\Delta + m_\Delta}{p_\Delta^2 - m_\Delta^2 + i m_\Delta \Gamma_\Delta} \left[g^{\mu\nu} - \frac{1}{3} \gamma^\mu \gamma^\nu - \frac{1}{3 m_\Delta} (\gamma^\mu p_\Delta^\nu - \gamma^\nu p_\Delta^\mu) - \frac{2}{3 m_\Delta^2} p_\Delta^\mu p_\Delta^\nu \right] \delta^4(x-y)$$

with $p_\Delta = k_1 - k_3 = k_\gamma - k_p$

(B-21)

For the Δ propagators we use the one frequently found in the literature [Be89] but we have modified the denominator to include the width of the Δ , Γ_Δ . The delta propagator is discussed in more detail in section 3.2.4.

Appendix C - Angular Integrals

The angular integrals that we evaluate are not difficult in that the generalized spherical harmonics can be expanded in terms of spherical harmonics and spin functions to give an integral over four spherical harmonics, which can be evaluated by coupling three of the spherical harmonics together into a single spherical harmonic and some Clebsch-Gordan coefficients. The integral is then expressed in terms of sums over Clebsch-Gordan coefficients (or equivalently Wigner 3-j symbols). The only problem with doing this is that, for our reaction, there are partial wave sums over three particles and the time to do these sums is prohibitive. We need forms for the integrals which are as fast as possible to evaluate, so we use spherical tensor techniques to express the angular integrals in terms of 6-j and 9-j symbols which we can then manipulate to get something reasonably fast. The book on angular momentum theory by Zare [Za88] is very helpful in this area.

We want to calculate angular integrals of the form

$$A \begin{bmatrix} \kappa & \kappa_B & L_\pi & L_\gamma & \xi \\ M & M_B & M_\pi & M_\gamma & \xi \end{bmatrix} = \int \mathcal{Y}_{L_1/2J}^{M_1} \dagger \Gamma \mathcal{Y}_{L_B/2J_B}^{M_B} Y_{L_\pi}^{M_\pi}(\Omega) Y_{L_\gamma}^0(\Omega) d\Omega \quad (C-1)$$

where Γ is a complex 2x2 matrix which can be written in terms of the 2x2 unit matrix, $\mathbf{1}$, and the usual Pauli spin matrices as

$$\begin{aligned} \Gamma &= C\mathbf{1} + \vec{D} \cdot \vec{\sigma} \\ &= C\mathbf{1} + \sum_{\gamma} (-)^{\gamma} D_1^{-\gamma} \sigma_1^{\gamma} \end{aligned} \quad (C-2)$$

and we have written the scalar product as a sum of spherical tensors of rank one. The components of an ordinary Cartesian vector $\vec{A} = (A_1, A_2, A_3)$ can be used to form a spherical tensor of the first rank by writing

$$\begin{aligned} A_1^1 &= -\frac{1}{\sqrt{2}} (A_1 + i A_2) \\ A_1^{-1} &= \frac{1}{\sqrt{2}} (A_1 - i A_2) \\ A_1^0 &= A_3 \end{aligned} \quad (C-3)$$

This spherical tensor transforms under rotations just the way the spherical harmonics do, and if you calculate the spherical tensor of rank one associated with the position vector you will get a spherical tensor proportional to the spherical harmonic of rank one $r_1^\mu = 2 \left[\frac{\pi}{3} \right]^{1/2} Y_1^\mu$.

The integral (C-1) can then be written in terms of angular integrals which transform under rotations as a scalar and a spherical tensor of rank one

$$A \begin{bmatrix} \kappa & \kappa_B & L_\pi & L_\gamma & \xi \\ M & M_B & M_\pi & L_\gamma & \xi \end{bmatrix} = C S \begin{bmatrix} \kappa & \kappa_B & L_\pi & L_\gamma \\ M & M_B & M_\pi & L_\gamma \end{bmatrix} + \sum_\gamma (-)^\gamma D_1^{-\gamma} T_1^\gamma \begin{bmatrix} \kappa & \kappa_B & L_\pi & L_\gamma \\ M & M_B & M_\pi & L_\gamma \end{bmatrix} \quad (C-4)$$

where the scalar and tensor angular integrals are

$$S \begin{bmatrix} \kappa & \kappa_B & L_\pi & L_\gamma \\ M & M_B & M_\pi & L_\gamma \end{bmatrix} = \int \mathcal{Y}_{L_1/2J_1}^{M_1 \dagger} \mathcal{Y}_{L_B/2J_B}^{M_B} Y_{L_\pi}^{M_\pi}(\Omega) Y_{L_\gamma}^0(\Omega) d\Omega \quad (C-5)$$

$$T_1^\gamma \begin{bmatrix} \kappa & \kappa_B & L_\pi & L_\gamma \\ M & M_B & M_\pi & L_\gamma \end{bmatrix} = \int \mathcal{Y}_{L_1/2J_1}^{M_1 \dagger} \sigma_1^\gamma \mathcal{Y}_{L_B/2J_B}^{M_B} Y_{L_\pi}^{M_\pi}(\Omega) Y_{L_\gamma}^0(\Omega) d\Omega$$

The spherical harmonics associated with the photon and pion in both integrals can be coupled to a single spherical harmonic by using

$$Y_{L_1}^{M_1}(\Omega) Y_{L_2}^{M_2}(\Omega) = (-)^{M_A} \frac{\widehat{L}_1 \widehat{L}_2}{\sqrt{4\pi}} \sum_A \widehat{A} \begin{pmatrix} L_1 & L_2 & A \\ 0 & 0 & 0 \end{pmatrix} \begin{pmatrix} L_1 & L_2 & A \\ M_1 & M_2 & -M_A \end{pmatrix} Y_A^{M_A}(\Omega) \quad (C-6)$$

where the quantities in brackets are the Wigner 3-j symbols which are nonzero only if the three angular momentum projections obey the condition $M_A = M_1 + M_2$ (the sum of the three projections must be zero in the 3-j symbol). We have also defined $\widehat{L} = (2L+1)^{1/2}$. The Wigner 3-j coefficient is related to the perhaps more familiar Clebsch-Gordan coefficient by

$$\begin{pmatrix} L_1 & L_2 & A \\ M_1 & M_2 & -M_A \end{pmatrix} = (-)^{L_1 - L_2 + M_A} \widehat{A}^{-1} (L_1, L_2; M_1, M_2 | A, M_A) \quad (C-7)$$

Our scalar and tensor integrals can then be written as

$$\begin{aligned}
S \begin{bmatrix} \kappa & \kappa_B & L_\pi & L_\gamma \\ M & M_B & M_\pi & M_\gamma \end{bmatrix} &= (-)^{M_\pi} \frac{\hat{L}_\pi \hat{L}_\gamma}{\sqrt{4\pi}} \sum_A \hat{A} \begin{pmatrix} L_\pi & L_\gamma & A \\ 0 & 0 & 0 \end{pmatrix} \begin{pmatrix} L_\pi & L_\gamma & A \\ M_\pi & 0 & -M_A \end{pmatrix} I_S \\
I_S &= \int \mathcal{Y}_{L1/2J}^M \dagger \mathcal{Y}_{L_B 1/2J_B}^{M_B} Y_A^{M_A}(\Omega) d\Omega \\
T_1^\gamma \begin{bmatrix} \kappa & \kappa_B & L_\pi & L_\gamma \\ M & M_B & M_\pi & M_\gamma \end{bmatrix} &= (-)^{M_\pi} \frac{\hat{L}_\pi \hat{L}_\gamma}{\sqrt{4\pi}} \sum_A \hat{A} \begin{pmatrix} L_\pi & L_\gamma & A \\ 0 & 0 & 0 \end{pmatrix} \begin{pmatrix} L_\pi & L_\gamma & A \\ M_\pi & 0 & -M_A \end{pmatrix} I_T \\
I_T &= \int \mathcal{Y}_{L1/2J}^M \dagger \sigma_1^\gamma \mathcal{Y}_{L_B 1/2J_B}^{M_B} Y_A^{M_A}(\Omega) d\Omega
\end{aligned} \tag{C-8}$$

and we can concentrate on the integrals I_S and I_T .

First we work on I_S because it's the simple looking one. I_S is the matrix element of a spherical harmonic of rank A between spherical basis wave functions formed by coupling spherical harmonics to spin wave functions, and we can write it as

$$I_S = \langle L, 1/2, J, M | Y_A^{M_A} | L_B, 1/2, J_B, M_B \rangle \tag{C-9}$$

We can separate the dependence on angular momentum projections from the dependence on the reduced matrix element by using the Wigner-Eckart theorem

$$I_S = (-)^{J-M} \begin{pmatrix} J & A & J_B \\ -M & M_A & M_B \end{pmatrix} \langle L, 1/2, J || Y^A || L_B, 1/2, J_B \rangle \tag{C-10}$$

The reduced matrix element contains an integration over spherical harmonics and a matrix element between spin states acting on the unit operator, which is one. We then get

$$I_S = (-)^{J+J_B+A+L+1/2-M} \hat{J} \hat{J}_B \begin{pmatrix} J & A & J_B \\ -M & M_A & M_B \end{pmatrix} \left\{ \begin{matrix} L & J & 1/2 \\ J_B & L_B & A \end{matrix} \right\} \langle L || Y^A || L_B \rangle \tag{C-11}$$

The last thing that we need for this is the reduced matrix element of the spherical harmonic of rank A

$$\langle L || Y^A || L_B \rangle = \frac{1}{\sqrt{4\pi}} (-)^L \hat{A} \hat{L} \hat{L}_B \begin{pmatrix} L & L_B & A \\ 0 & 0 & 0 \end{pmatrix} \tag{C-12}$$

using (C-12) in (C-11), along with the fact that an odd permutation of the columns of a 3-j symbol results in a phase factor involving the sum of the angular momenta, allows us to write

$$I_S = (-)^{1/2-M} \frac{1}{\sqrt{4\pi}} \hat{A} \hat{L} \hat{L}_B \hat{J} \hat{J}_B \begin{pmatrix} L & L_B & A \\ 0 & 0 & 0 \end{pmatrix} \begin{pmatrix} J & J_B & A \\ -M & M_B & M_A \end{pmatrix} \left\{ \begin{matrix} L & J & 1/2 \\ J_B & L_B & A \end{matrix} \right\} \tag{C-13}$$

This expression can be simplified further by noticing that the product of a 3-j symbol with all projections equal to zero and a related 6-j symbol with one of the entries equal to $1/2$ can be simplified to a single 3-j symbol [Ma58] as

$$\begin{pmatrix} L & L_B & A \\ 0 & 0 & 0 \end{pmatrix} \begin{pmatrix} L & J & 1/2 \\ J_B & L_B & A \end{pmatrix} = (-)^{2J} (\widehat{L} \widehat{L}_B)^{-1} \frac{1}{2} [1 + (-)^{L+L_B+A}] \begin{pmatrix} J & J_B & A \\ 1/2 & -1/2 & 0 \end{pmatrix} \quad (C-14)$$

so that I_S becomes

$$I_S = (-)^{2J+1/2-M} \frac{1}{\sqrt{4\pi}} \widehat{A} \widehat{J} \widehat{J}_B \frac{1}{2} [1 + (-)^{L+L_B+A}] \begin{pmatrix} J & J_B & A \\ 1/2 & -1/2 & 0 \end{pmatrix} \begin{pmatrix} J & J_B & A \\ -M & M_B & M_A \end{pmatrix} \quad (C-15)$$

and the scalar angular integral is

$$\begin{aligned} S \begin{pmatrix} K & K_B & L_\pi & L_\gamma \\ M & M_B & M_\pi & M_\gamma \end{pmatrix} &= (-)^{2J+1/2-M+M_\pi} \frac{\widehat{L}_\pi \widehat{L}_\gamma \widehat{J} \widehat{J}_B}{4\pi} \\ &\times \sum_A (2A+1) \frac{1}{2} [1 + (-)^{L+L_B+A}] \\ &\times \begin{pmatrix} J & J_B & A \\ 1/2 & -1/2 & 0 \end{pmatrix} \begin{pmatrix} J & J_B & A \\ -M & M_B & M_A \end{pmatrix} \begin{pmatrix} L_\pi & L_\gamma & A \\ 0 & 0 & 0 \end{pmatrix} \begin{pmatrix} L_\pi & L_\gamma & A \\ M_\pi & 0 & -M_A \end{pmatrix} \end{aligned} \quad (C-16)$$

The tensor angular integral I_T can be evaluated in the same way as the scalar integral but first we have to couple σ_1^γ and $Y_A^{M_A}$ into a spherical tensor operator using the standard angular momentum coupling

$$\sigma_1^\gamma Y_A^{M_A}(\Omega) = (-)^{A-1} \sum_{C M_C} (-)^{M_C} \widehat{C} \begin{pmatrix} A & 1 & C \\ M_A & \gamma & -M_C \end{pmatrix} T_C^{M_C} \quad (C-17)$$

so we have I_T written in terms of a spherical tensor operator and spherical basis states as we had for I_S

$$I_T = (-)^{A-1} \sum_{C M_C} (-)^{M_C} \widehat{C} \begin{pmatrix} A & 1 & C \\ M_A & \gamma & -M_C \end{pmatrix} \langle L, 1/2, J, M | T_C^{M_C} | L_B, 1/2, J_B, M_B \rangle \quad (C-18)$$

The dependence of the matrix element on the projections of angular momentum can be separated from the matrix element by again using the Wigner-Eckart theorem

$$\begin{aligned} \langle L, 1/2, J, M | T_C^{M_C} | L_B, 1/2, J_B, M_B \rangle \\ = (-)^{J-M} \begin{pmatrix} J & C & J_B \\ -M & M_C & M_B \end{pmatrix} \langle L, 1/2, J || T^C || L_B, 1/2, J_B \rangle \end{aligned} \quad (C-19)$$

The reduced matrix element can be written in terms of the reduced matrix elements of the spherical tensors of which it is comprised, and a Wigner 9-j symbol

$$\begin{aligned} \langle L, 1/2, J || T^C || L_B, 1/2, J_B \rangle \\ = \widehat{C} \widehat{J} \widehat{J}_B \langle L || Y^A || L_B \rangle \langle 1/2 || \sigma^1 || 1/2 \rangle \begin{Bmatrix} L & L_B & A \\ 1/2 & 1/2 & 1 \\ J & J_B & C \end{Bmatrix} \end{aligned} \quad (C-20)$$

where the reduced matrix element of the spherical harmonic has crossed our path before in (C-12) and the reduced matrix element of the Pauli spinor is

$$\langle 1/2 \parallel \sigma^1 \parallel 1/2 \rangle = \sqrt{6} \quad (\text{C-21})$$

Putting these together and using the symmetry relations of the Wigner 3-j symbols to write

$$\begin{pmatrix} J & C & J_B \\ -M & M_C & M_B \end{pmatrix} = \begin{pmatrix} J & J_B & C \\ M & -M_B & -M_C \end{pmatrix} \quad (\text{C-22})$$

along with the facts that $L + L_B + A$ must be even and $M_B = M + M_C$ allow us to write I_T as

$$I_T = \sqrt{\frac{3}{2\pi}} (-)^{J+L_B+M_B} \hat{A} \hat{L} \hat{J} \hat{L}_B \hat{J}_B \begin{pmatrix} L & L_B & A \\ 0 & 0 & 0 \end{pmatrix} \times \sum_{C M_C} (2C+1) \begin{pmatrix} A & 1 & C \\ M_A & \gamma & M_C \end{pmatrix} \begin{pmatrix} J & J_B & C \\ M & -M_B & M_C \end{pmatrix} \begin{pmatrix} L & L_B & A \\ 1/2 & 1/2 & 1 \\ J & J_B & C \end{pmatrix} \quad (\text{C-23})$$

where the sum over M_C covers all possible values of the projection of C so we are free to make the replacement $M_C \rightarrow -M_C$ without changing the result. This sum can be verified by expanding the original expression for integral I_T into its component spin wave functions, Pauli matrices and spherical harmonics. Computing this integral explicitly in this form results in a sum of 3-j coefficients, six of which can be combined into the 9-j symbol above.

We had managed to rewrite a 3-j and the 6-j from I_S as a single 3-j symbol by using (C-14), now the 9-j symbol in I_T can be written as a sum over three 6-j symbols. By doing some appropriate massaging we can reduce the number of angular momentum sums that have to be done and so increase the speed with which T_1^Y is calculated.

The 9-j can be rearranged and is expanded in terms of 6-j's as

$$\begin{pmatrix} A & L & L_B \\ 1 & 1/2 & 1/2 \\ C & J & J_B \end{pmatrix} = \sum_K (-)^{2K} (2K+1) \begin{pmatrix} A & 1 & C \\ J & J_B & K \end{pmatrix} \begin{pmatrix} L & 1/2 & J \\ 1 & K & 1/2 \end{pmatrix} \begin{pmatrix} L_B & 1/2 & J_B \\ K & A & L \end{pmatrix} \quad (\text{C-24})$$

A sum over one angular momentum of two 3-j's and a 6-j can be rewritten as a product of a phase and two 3-j's [Za88]

$$\sum_{J_6} (-)^{J_6} (2J_6+1) \begin{pmatrix} J_2 & J_4 & J_6 \\ M_2 & M_4 & -M_6 \end{pmatrix} \begin{pmatrix} J_5 & J_1 & J_6 \\ M_5 & M_1 & M_6 \end{pmatrix} \begin{pmatrix} J_1 & J_2 & J_3 \\ J_4 & J_5 & J_6 \end{pmatrix} = (-)^{J_1+J_2-J_3+J_4+J_5-M_1-M_4} \begin{pmatrix} J_1 & J_2 & J_3 \\ M_1 & M_2 & -M_3 \end{pmatrix} \begin{pmatrix} J_4 & J_5 & J_3 \\ M_4 & M_5 & M_3 \end{pmatrix} \quad (\text{C-25})$$

and with the symmetry properties of the 3-j and 6-j symbols

$$\begin{pmatrix} A & 1 & C \\ M_A & \gamma & M_C \end{pmatrix} = (-)^{A+1+C} \begin{pmatrix} A & 1 & C \\ -M_A & -\gamma & -M_C \end{pmatrix} \quad (C-26)$$

$$\begin{pmatrix} A & 1 & C \\ J & J_B & K \end{pmatrix} = \begin{pmatrix} J_B & A & K \\ 1 & J & C \end{pmatrix}$$

we can write the sum over C as

$$\begin{aligned} \sum_C (2C+1) \begin{pmatrix} A & 1 & C \\ M_A & \gamma & M_C \end{pmatrix} \begin{pmatrix} J & J_B & C \\ M & -M_B & M_C \end{pmatrix} \begin{pmatrix} A & 1 & C \\ J & J_B & K \end{pmatrix} \\ = (-)^{J+2J_B+A+M_B+\gamma} \begin{pmatrix} J_B & A & K \\ M_B & M_A & M_K \end{pmatrix} \begin{pmatrix} 1 & J & K \\ -\gamma & M & M_K \end{pmatrix} \end{aligned} \quad (C-27)$$

Putting these results together with (C-14) gives the tensor angular integral as

$$\begin{aligned} T_1^\gamma \begin{bmatrix} \hat{n} \\ M & M_B & M_\pi & L_\gamma \end{bmatrix} &= \frac{1}{2\pi} \sqrt{\frac{3}{2}} (-)^{2J+L+\gamma+M_\pi} \hat{J}_B \hat{J}_\pi \hat{L}_\gamma \\ &\times \sum_A (2A+1) \frac{1}{2} [1 + (-)^{L+L_B+A}] \begin{pmatrix} L_\pi & L_\gamma & A \\ 0 & 0 & 0 \end{pmatrix} \begin{pmatrix} L_\pi & L_\gamma & A \\ M_\pi & 0 & -M_A \end{pmatrix} \\ &\times \sum_K (2K+1) \begin{pmatrix} J_B & A & K \\ -1/2 & 0 & 1/2 \end{pmatrix} \begin{pmatrix} J_B & A & K \\ M_B & M_A & M_K \end{pmatrix} \begin{pmatrix} 1 & J & K \\ -\gamma & M & M_K \end{pmatrix} \begin{Bmatrix} L & 1/2 & J \\ 1 & K & 1/2 \end{Bmatrix} \end{aligned} \quad (C-28)$$

Note that there are lots of constraints on the angular momenta which are summed over so the actual number of terms that need to be evaluated is quite small. The projections of A and K are determined by the input projections:

- i) $M_A = M_\pi$
- ii) $M_K = -(M_B + M_\pi)$
 $= \gamma - M$

In addition A and K are constrained so:

- i) $L + L_B + A = \text{even}$
- ii) $L_\pi + L_\gamma + A = \text{even}$
- iii) $|L_\pi - L_\gamma| \leq A \leq L_\pi + L_\gamma$
- iv) $|J_B - A| \leq K \leq J_B + A$
- v) $|J - 1| \leq K \leq J + 1$
- vi) $|L - 1/2| \leq K \leq L + 1/2$

The expression (C-28) for the tensor integral is two to three times faster to calculate than the equivalent expression involving the 9-j symbol explicitly, with the subroutines for 3-, 6- and 9-j coefficients that we have [Ca66], and a similar saving in time is gained by using (C-16) for the scalar integral instead of the expression involving the 6-j symbol.

Appendix D - Observables

D.1 Cross Section

We have obtained expressions for the plane wave and distorted wave s-matrices for the charged pion photoproduction reaction on a nucleus $A(\gamma, \pi^- p)A-1$ in chapter 3. These s-matrices must be related to the quantities that are actually measured experimentally. This we now proceed to do.

Begin with the compact form for the s-matrix for the $(\gamma, \pi^- p)$ reaction as written in eqn. (3-112)

$$S_{fi} = \frac{\sqrt{2}}{\pi} e \frac{f_\pi}{m_\pi} \left(\frac{E_p + m}{E_p E_\pi E_\gamma} \right)^{1/2} \delta(E_p + E_\pi - E_\gamma - E_B) \sum_{J_B M_B} (J_f, J_B; M_f, M_B | J_i, M_i) \mathcal{J}_{J_i J_f(J_B)} Z_{\xi M_B}^{s_f} \quad (D-1)$$

Now square S_{fi} to form a transition probability

$$|S_{fi}|^2 = \frac{2}{\pi^2} e^2 \frac{f_\pi^2}{m_\pi^2} \left(\frac{E_p + m}{E_p E_\pi E_\gamma} \right) [\delta(E_p + E_\pi - E_\gamma - E_B)]^2 \sum_{J_B M_B J_B' M_B'} (J_f, J_B; M_f, M_B | J_i, M_i) (J_f, J_B'; M_f, M_B' | J_i, M_i) \mathcal{J}_{J_i J_f(J_B)} \mathcal{J}_{J_i J_f(J_B')} Z_{\xi M_B}^{s_f} [Z_{\xi M_B'}^{s_f}]^* \quad (D-2)$$

Following Bjorken and Drell [BD64] we consider transitions in a time interval T. We can then identify the square of the delta function as

$$[\delta(E_p + E_\pi - E_\gamma - E_B)]^2 = \frac{T}{2\pi} \delta(E_p + E_\pi - E_\gamma - E_B) \quad (D-3)$$

Divide the transition probability by T to get the transition rate (transition probability per unit time) to a definite final state where the outgoing particles have momenta \vec{p}_π and \vec{p}_p , and multiply by the number of final states $d^3 p_\pi d^3 p_p$ to get the transition rate to a group of final states with momenta in the range \vec{p}_π to $\vec{p}_\pi + d\vec{p}_\pi$ and \vec{p}_p to $\vec{p}_p + d\vec{p}_p$ due to the interaction of a photon with one target nucleus. The differential cross section is the transition rate into this group of final states for one scattering center and unit incident flux

$$d\sigma = \frac{|S_{fi}|^2}{T} \frac{1}{J_{inc}} d^3 p_\pi d^3 p_p \quad (D-4)$$

The incident flux for delta-function normalization is

$$J_{\text{inc}} = \frac{v_{\text{rel}}}{(2\pi)^3} \quad (\text{D-5})$$

The velocity of the photon is $v_\gamma = c = 1$ while the velocity of the target nucleus is $v_A = p_A/E_A$. The relative velocity of the incident particles $v_{\text{rel}} = |\vec{v}_\gamma - \vec{v}_A|$, is for collinear beams the number of particles passing through a unit area per unit time. In the lab frame $\vec{v}_A = \vec{0}$ so $v_{\text{rel}} = 1$ while in the center of momentum frame

$$v_{\text{rel}} = 1 + \frac{|\vec{p}_A|}{E_A} \quad (\text{D-6})$$

The incident flux in the lab frame is then simply

$$J_{\text{inc}} = \frac{1}{(2\pi)^3} \quad (\text{D-7})$$

Sum over the phase space (i.e. integrate over the momenta of the outgoing particles)

$$\begin{aligned} & \int \frac{|S_{\text{fi}}|^2}{T} \frac{1}{J_{\text{inc}}} d^3 p_\pi d^3 p_p \\ &= 8 e^2 \frac{f_\pi^2}{m_\pi^2} \sum_{J_B M_B J_B' M_B'} (J_f, J_B; M_f, M_B | J_i, M_i) (J_f, J_B'; M_f, M_B' | J_i, M_i) \\ & \quad \times \mathcal{J}_{J_i J_f(J_B)} \mathcal{J}_{J_i J_f(J_B')} \\ & \quad \times \int Z_{\xi M_B}^{s_f} [Z_{\xi M_B'}^{s_f}]^* \left(\frac{E_p + m}{E_p E_\pi E_\gamma} \right) \delta(E_p + E_\pi - E_\gamma - E_B) d^3 p_\pi d^3 p_p \end{aligned} \quad (\text{D-8})$$

Use the relativistic energy momentum relation $E^2 = p^2 + m^2$ to rewrite the momentum integrals as integrals over energy since we have $p^2 dp = p E dE$ and then do one of the energy integrals using the delta function to get

$$\begin{aligned} & \int Z_{\xi M_B}^{s_f} [Z_{\xi M_B'}^{s_f}]^* \left(\frac{E_p + m}{E_p E_\pi E_\gamma} \right) \delta(E_p + E_\pi - E_\gamma - E_B) d^3 p_\pi d^3 p_p \\ &= Z_{\xi M_B}^{s_f} [Z_{\xi M_B'}^{s_f}]^* \left(\frac{E_p + m}{E_\gamma} \right) p_\pi p_p d\Omega_\pi d\Omega_p dE_p \end{aligned} \quad (\text{D-9})$$

The target is unpolarized and the polarization of the proton isn't measured so average the initial spin projections and sum over the final spin projections so the cross section is

$$d\sigma = \frac{1}{2} \frac{1}{(2J_i + 1)} \sum_{M_i M_f} \int \frac{|S_{\text{fi}}|^2}{T} \frac{1}{J_{\text{inc}}} d^3 p_\pi d^3 p_p \quad (\text{D-10})$$

where the factor of 1/2 comes from averaging over the two possible photon polarization states.

The sums over the initial and final nuclear projections act on the two Clebsch-Gordan coefficients in equation (D-8) and recalling the completeness relation for the Clebsch-Gordan coefficients allows us to write

$$\sum_{M_i M_f} (J_f, J_B; M_f, M_B | J_i, M_i) (J_f, J_B; M_f, M_B | J_i, M_i) = \frac{(2J_i + 1)}{(2J_B + 1)} \delta_{J_B J_B'} \delta_{M_B M_B'} \quad (\text{D-11})$$

and when we put these results together the cross section is

$$\frac{d\sigma}{d\Omega_\pi d\Omega_p dE_p} = 4 e^2 \frac{f_\pi^2}{m_\pi^2} \left(\frac{E_p + m}{E_\gamma} \right) p_\pi p_p \sum_{J_B M_B} \frac{J_{J_i J_f}^2(J_B)}{2J_B + 1} |Z_{\xi M_B}^{sr}|^2 \quad (\text{D-12})$$

Introduce the dimensionless forms of the coupling constants $\alpha = e^2/4\pi$ and $\beta = f_\pi^2/4\pi$ and include all the factors of \hbar and c so the cross section for the $(\gamma, \pi^- p)$ reaction is

$$\frac{d\sigma}{d\Omega_\pi d\Omega_p dE_p} = 4 (4\pi)^2 \frac{1}{\hbar c} \frac{\alpha \beta}{m_\pi^2 c^4} \left(\frac{E_p + mc^2}{E_\gamma} \right) p_{\pi c} p_{p c} \sum_{J_B M_B} \frac{J_{J_i J_f}^2(J_B)}{2J_B + 1} |Z_{\xi M_B}^{sr}|^2 \quad (\text{D-13})$$

The scattering wave functions that we have used are all normalized to delta functions so the spherical Bessel functions from these states are dimensionless. The radial functions from the bound state have dimensions of $l^{-3/2}$, so the function $|Z_{\xi M_B}^{sr}|^2$ has dimensions of length cubed. That length is in fermis and if the energies and masses are in MeV while the momenta are in MeV/c and with $\hbar c$ in MeV-fm the cross section will have units of $\text{fm}^2/(\text{sr}^2 \text{MeV})$.

D.2 Polarization

In order to calculate the polarization of the outgoing proton we need to describe the spin state of the proton. The easiest way to do this is through the density matrix [Fa57]. We define the density matrix so that the cross section is

$$\begin{aligned} d\sigma &= \text{Tr } \rho \\ &= \sum_n \rho_{nn} \end{aligned} \quad (\text{D-14})$$

where the index n refers to the set of angular momentum projections $\{ \xi, \mu, M_B \}$. The density matrix then has six indices and comparing with equation (D-13) allows us to write the density matrix in terms of the z -matrix as

$$\rho_{\xi\xi' M_B M_B'}^{s_f s_f'} = A Z_{\xi M_B}^{s_f} [Z_{\xi' M_B'}^{s_f'}]^* \quad (\text{D-15})$$

A is a constant involving phase space and spin factors. We define the density matrix of the final state proton by taking traces over the initial photon and bound state projections to get

$$\rho_{\text{proton}}^{s_f s_f'} = \sum_{\xi M_B} \rho_{\xi\xi' M_B M_B'}^{s_f s_f'} \quad (\text{D-16})$$

The expectation value of the spin operator (polarization) is then given by

$$\vec{P} = \langle \vec{\sigma} \rangle = \frac{\text{Tr} (\rho_{\text{proton}} \vec{\sigma})}{\text{Tr} \rho_{\text{proton}}} \quad (\text{D-17})$$

In order to check that we have a consistent formalism we consider a system of spin 1/2 particles whose polarization we are free to manipulate. We calculate the expectation value of the z-component of the spin by

$$\begin{aligned} \langle \sigma_z \rangle &= \frac{\text{Tr} (\rho \sigma_z)}{\text{Tr} \rho} \\ &= \frac{\text{Tr} \left(\begin{bmatrix} \rho_{11} & \rho_{12} \\ \rho_{21} & \rho_{22} \end{bmatrix} \begin{bmatrix} 1 & 0 \\ 0 & -1 \end{bmatrix} \right)}{\rho_{11} + \rho_{22}} \\ &= \frac{\rho_{11} - \rho_{22}}{\rho_{11} + \rho_{22}} \end{aligned} \quad (\text{D-18})$$

and we see that we must have

$$\begin{aligned} \rho_{11} &\rightarrow \rho_{1/2 \ 1/2} \\ \rho_{22} &\rightarrow \rho_{-1/2 \ -1/2} \end{aligned} \quad (\text{D-19})$$

so that the polarization will be -1 when the system is prepared with 100% of the protons having the z-component of their spin in the negative z direction (spin down).

The polarization in the y-direction for the reaction ($\gamma, \pi^- p$) is then

$$\begin{aligned} \langle \sigma_y \rangle &= \frac{\text{Tr} (\rho \sigma_y)}{\text{Tr} \rho} \\ &= -2 \frac{\text{Im} \sum_{\xi M_B} Z_{\xi M_B}^{1/2} [Z_{\xi M_B}^{-1/2}]^*}{\text{Tr} \rho} \end{aligned} \quad (\text{D-20})$$

where we have reintroduced the z-matrix of equation (D-15).

D.3 Asymmetry (or Analysing Power)

The asymmetry for photons polarized either parallel or perpendicular to the scattering plane is written as

$$A = \frac{d\sigma_{\perp} - d\sigma_{\parallel}}{d\sigma_{\perp} + d\sigma_{\parallel}} \quad (\text{D-21})$$

where $d\sigma_{\perp(\parallel)}$ is the differential cross section with the incident photon polarization perpendicular (parallel) to the scattering plane.

In terms of the formalism of chapter 3 (see equation (3-102) and above) $d\sigma_{\parallel}$ has $\xi = 0$ so the photon polarization vector is along the x-axis, in the scattering (x - z) plane, $\vec{e}_{\xi=0} = (1, 0, 0)$ and $d\sigma_{\perp}$ has $\xi = \pi/2$ so the polarization vector is perpendicular to the scattering plane $\vec{e}_{\xi=\pi/2} = (0, 1, 0)$.

Note that we have adopted the definition of A given by Menze, Pfeil and Wilke [Me77], but the negative of this definition is also used [Ga88].

Appendix E - Time Ordering With Derivative Coupling

Consider the interaction of two fermions through the exchange of a scalar field with derivative coupling. The s-matrix in second order is proportional to the integral

$$S \propto \int d^4x d^4y \langle f | T \{ [\bar{\psi} \gamma_\mu \psi \partial^\mu \phi]_x [\bar{\psi} \gamma_\nu \psi \partial^\nu \phi]_y \} | i \rangle \quad (\text{E-1})$$

We have an ambiguity here when we expand the time ordered product in terms of normal products and contractions. We have the freedom to first integrate by parts to move the derivative operators off the scalar fields. Then we can do the time ordering to get the propagator for the scalar field and finally shift the derivative operators back to the propagator. Alternatively we can do the time ordering of the fields with the derivatives where they are. The first is known as Wick time ordering and the second is Dyson time ordering [Bo80].

The s-matrix can be expanded in a series in powers of either the interaction lagrangian or the hamiltonian [Ni69] as

$$\begin{aligned} S &= 1 + \sum_{n=1}^{\infty} \frac{i^n}{n!} \int d^4x_1 \cdots d^4x_n T_W [\mathcal{L}_{\text{int}}(x_1) \cdots \mathcal{L}_{\text{int}}(x_n)] \\ &= 1 + \sum_{n=1}^{\infty} \frac{(-i)^n}{n!} \int d^4x_1 \cdots d^4x_n T_D [\mathcal{H}_{\text{int}}(x_1) \cdots \mathcal{H}_{\text{int}}(x_n)] \end{aligned} \quad (\text{E-2})$$

where T_W and T_D refer to the Wick and Dyson time ordering products respectively. When the interaction lagrangian does not contain the time derivative of any fields the interaction hamiltonian is simply the negative of the interaction lagrangian

$$\mathcal{H}_{\text{int}} = - \mathcal{L}_{\text{int}} \quad (\text{E-3})$$

and the two time orderings are equivalent. The difference in orderings enters when the lagrangian contains time derivatives. Consider the vacuum expectation value of the fields with derivatives

$$\langle 0 | T [\partial_x^\mu \phi(x) \partial_y^\nu \phi(y)] | 0 \rangle \quad (\text{E-4})$$

The Wick time ordering is defined to have the derivatives acting on the Feynman propagator for the fields

$$\begin{aligned} \langle 0 | T_W [\partial_x^\mu \phi(x) \partial_y^\nu \phi(y)] | 0 \rangle &\equiv \partial_x^\mu \partial_y^\nu \langle 0 | T [\phi(x) \phi(y)] | 0 \rangle \\ &= i \partial_x^\mu \partial_y^\nu \Delta_F(x-y) \end{aligned} \quad (\text{E-5})$$

while the Dyson time ordering keeps the derivatives on the fields as

$$\begin{aligned}
 \langle 0 | T_D [\partial_x^\mu \varphi(x) \partial_y^\nu \varphi(y)] | 0 \rangle &= \theta(x_0 - y_0) \langle 0 | \partial_x^\mu \varphi(x) \partial_y^\nu \varphi(y) | 0 \rangle \\
 &\quad + \theta(y_0 - x_0) \langle 0 | \partial_y^\nu \varphi(y) \partial_x^\mu \varphi(x) | 0 \rangle \\
 &= \langle 0 | T_W [\partial_x^\mu \varphi(x) \partial_y^\nu \varphi(y)] | 0 \rangle = \dots \delta_{\mu 0} \delta_{\nu 0} \delta^4(x - y)
 \end{aligned}
 \tag{E-6}$$

In our calculations we use the expansion of the s-matrix in terms of the interaction lagrangian (E-2) with the Wick time ordering (E-5).

Appendix F - Free Process $\gamma + n \rightarrow \pi^- + p$

In this appendix we discuss a lagrangian model of pion photoproduction on a free neutron. The lagrangian has been examined previously by Olsson and Osypowski [O175] and Blomqvist and Laget [BL77]. The nonrelativistic amplitude for pion photoproduction, which has been derived by Blomqvist and Laget from the relativistic amplitude, is presented.

F.1 Elementary Pion Photoproduction $\gamma + N \rightarrow \pi + N$

The details of the lagrangian model are discussed in chapter 3, where we derive the s-matrix for the photoproduction of a negatively charged pion from a nucleus. The details of that calculation are applicable to this (simpler) calculation, and so we refer the reader desiring more details to chapter 3. Here we give some results without filling in the details.

We start with the lagrangian for a system of pions and nucleons with a pseudovector interaction term, and using the minimal substitution to introduce interactions with photons results in the non-delta interaction terms:

$$\begin{aligned}
 \mathcal{L}_{\pi NN} &= -\frac{f_\pi}{m_\pi} \bar{\psi} \gamma_5 [\tau_- \not{\partial} \pi^- + \tau_+ \not{\partial} \pi^+ + \tau_3 \not{\partial} \pi^0] \psi \\
 \mathcal{L}_{\gamma NN} &= -e \bar{\psi} \not{A} \frac{1+\tau_3}{2} \psi - \frac{\kappa_p \mu_N}{2} \bar{\psi} \sigma^{\mu\nu} F_{\mu\nu} \frac{1+\tau_3}{2} \psi - \frac{\kappa_n \mu_N}{2} \bar{\psi} \sigma^{\mu\nu} F_{\mu\nu} \frac{1-\tau_3}{2} \psi \\
 \mathcal{L}_{\gamma\pi\pi} &= \frac{ie}{2} A^\mu [\pi^+ \partial_\mu \pi^- + \partial_\mu \pi^- \pi^+ - \pi^- \partial_\mu \pi^+ - \partial_\mu \pi^+ \pi^-] \\
 \mathcal{L}_{\gamma\pi\pi} &= \frac{e^2}{2} A_\mu A^\mu \{ \pi^+ \pi^- + \pi^- \pi^+ \} \\
 \mathcal{L}_{\gamma\pi NN} &= -ie \frac{f_\pi}{m_\pi} \bar{\psi} \gamma_5 \not{A} [\tau_+ \pi^+ - \tau_- \pi^-] \psi
 \end{aligned} \tag{F-1}$$

where the unit of charge is positive ($e > 0$). The magnitudes of the anomalous magnetic moments for the proton and neutron are $\kappa_p = 1.79$ and $\kappa_n = -1.91$. The interaction terms involving the propagation of a Δ isobar are [Ka88, O175]

$$\begin{aligned}
 \mathcal{L}_{\pi N\Delta} &= \frac{f_{\pi N\Delta}}{m_\pi} \{ \bar{\psi}_\Delta^\mu \vec{T} \cdot \partial_\mu \vec{\phi} \psi + \bar{\psi} (\vec{T} \cdot \partial_\mu \vec{\phi})^\dagger \psi_\Delta^\mu \} \\
 \mathcal{L}_{\gamma N\Delta} &= ie \frac{f_{\gamma N\Delta}}{m_\pi} \{ \bar{\psi}_\Delta^\mu T_3 \gamma^\nu \gamma_5 F_{\mu\nu} \psi + \bar{\psi} T_3^\dagger \gamma^\mu \gamma_5 F_{\mu\nu} \psi_\Delta^\nu \}
 \end{aligned} \tag{F-2}$$

where the 4x2 isospin matrices \vec{T} which connect the isospin T=1/2 nucleon with the isospin T=3/2 isobar are

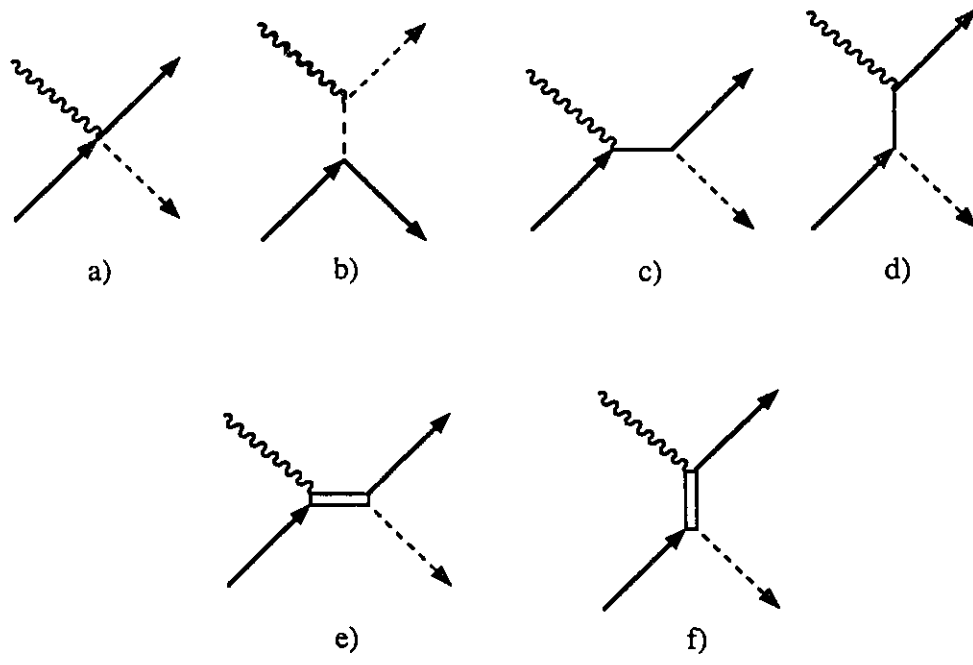


Figure F-1. Diagrams contributing to the elementary pion photoproduction process $\gamma + n \rightarrow \pi^- + p$. a) to d) are the Born terms, e) and f) are the s- and u-channel Δ diagrams.

$$T_1 = \frac{1}{\sqrt{2}} \begin{bmatrix} -1 & 0 \\ 0 & -1/\sqrt{3} \\ 1/\sqrt{3} & 0 \\ 0 & 1 \end{bmatrix} \quad T_2 = \frac{i}{\sqrt{2}} \begin{bmatrix} 1 & 0 \\ 0 & 1/\sqrt{3} \\ 1/\sqrt{3} & 0 \\ 0 & 1 \end{bmatrix} \quad T_3 = \sqrt{\frac{2}{3}} \begin{bmatrix} 0 & 0 \\ 1 & 0 \\ 0 & 1 \\ 0 & 0 \end{bmatrix} \quad (\text{F-3})$$

The initial neutron and final proton are described by 4-component Dirac spinors [BD64]. The neutron has spin projection ν while the proton has spin projection μ . The total s-matrix for the reaction $\gamma + n \rightarrow \pi^- + p$ can then be written as

$$S_{fi} = \sqrt{2} e \frac{f_\pi}{m_\pi} (2\pi)^{-2} \delta^4(k_n + k_\gamma - k_p - k_\pi) \frac{1}{4} \left(\frac{(E_p + m_p)(E_n + m_n)}{E_p E_n E_\pi E_\gamma} \right)^{1/2} \quad (\text{F-4})$$

$$\times \langle \frac{1}{2}, \mu | \left[\mathbb{1}, \frac{\vec{\sigma} \cdot \vec{k}_p}{E_p + m_p} \right] \Gamma_{\text{total}} \left[\begin{array}{c} \mathbb{1} \\ \frac{\vec{\sigma} \cdot \vec{k}_n}{E_n + m_n} \end{array} \right] | \frac{1}{2}, \nu \rangle$$

where the total 4x4 operator acting on the nucleon spinors is the sum of the operators from all of the diagrams we consider $\Gamma_{\text{total}} = \sum_i \Gamma_i$. The sum extends over the diagrams included in our model, which are shown in figure F-1. We write these vertex operators in terms of the four momenta of the particles and the Dirac gamma matrices as 4x4 dimensionless matrices:

$$\begin{aligned}
\Gamma_{\text{seagull}} &= \gamma_0 \gamma_5 \not{\epsilon}_p \\
\Gamma_{\text{pion}} &= -2 \frac{\epsilon_p \cdot k}{k^2 - m_\pi^2} \gamma_0 \gamma_5 \not{k} & k = k_\gamma - k_\pi \\
\Gamma_{\text{proton}}^e &= \gamma_0 \not{\epsilon}_p \frac{k + m}{k^2 - m_p^2} \gamma_5 \not{k}_\pi & k = k_p - k_\gamma \\
\Gamma_{\text{proton}}^\mu &= \frac{\kappa_p}{4m_p} \gamma_0 [k_\gamma, \not{\epsilon}_p] \frac{k + m}{k^2 - m_p^2} \gamma_5 \not{k}_\pi & k = k_p - k_\gamma \\
\Gamma_{\text{neutron}}^\mu &= \frac{\kappa_n}{4m_p} \gamma_0 \gamma_5 \not{k}_\pi \frac{k + m}{k^2 - m_n^2} [k_\gamma, \not{\epsilon}_p] & k = k_\pi + k_p \\
\Gamma_{\Delta-s} &= -\frac{f_{\gamma N \Delta} f_{\pi N \Delta}}{3 f_\pi m_\pi} \gamma_0 \frac{\not{p}_\Delta + m_\Delta}{p_\Delta^2 - m_\Delta^2 + i m_\Delta \Gamma_\Delta} k_\mu^\pi & p_\Delta = k_p + k_\pi \\
&\quad \times [g^{\mu\nu} - \frac{1}{3} \gamma^\mu \gamma^\nu - \frac{1}{3 m_\Delta} (\gamma^\mu p_\Delta^\nu - \gamma^\nu p_\Delta^\mu) - \frac{2}{3 m_\Delta^2} p_\Delta^\mu p_\Delta^\nu] \\
&\quad \times [k_\gamma \epsilon_{\nu p} - k_\nu^\gamma \not{\epsilon}_p] \gamma_5 \\
\Gamma_{\Delta-u} &= \frac{f_{\gamma N \Delta} f_{\pi N \Delta}}{3 f_\pi m_\pi} \gamma_0 \gamma_5 [k_\gamma \epsilon_{\mu p} - k_\mu^\gamma \not{\epsilon}_p] \frac{\not{p}_\Delta + m_\Delta}{p_\Delta^2 - m_\Delta^2 + i m_\Delta \Gamma_\Delta} & p_\Delta = k_p - k_\gamma \\
&\quad \times [g^{\mu\nu} - \frac{1}{3} \gamma^\mu \gamma^\nu - \frac{1}{3 m_\Delta} (\gamma^\mu p_\Delta^\nu - \gamma^\nu p_\Delta^\mu) - \frac{2}{3 m_\Delta^2} p_\Delta^\mu p_\Delta^\nu] k_\nu^\pi
\end{aligned} \tag{F-5}$$

The s-matrix for the reaction $\gamma + p \rightarrow \pi^+ + n$ is obtained in the same way with similar results.

We can write the s-matrix of equation (F-4) in a more concise form as:

$$S_{fi} = \sqrt{2} e \frac{f_\pi}{m_\pi} (2\pi)^{-2} \delta^4(k_n + k_\gamma - k_p - k_\pi) \frac{1}{4} \left(\frac{(E_p + m_p)(E_n + m_n)}{E_p E_n E_\pi E_\gamma} \right)^{1/2} Z_{\xi \nu}^\mu \tag{F-6}$$

where $Z_{\xi \nu}^\mu$ is a function of the polarization of the initial photon, the spin projection of the final proton μ and the projection of the initial neutron ν , and is exactly the matrix element of the vertex operators between the initial and final state Dirac spinors.

The cross section in the center of momentum frame is then obtained in the usual way [BD64] as

$$\begin{aligned}
\frac{d\sigma}{d\Omega_\pi} &= \frac{\alpha \beta (hc)^2}{m_\pi^2 c^4} \frac{1}{8} \left[\frac{(E_p + m_p)(E_n + m_n)}{E_p E_n E_\gamma} \right] p_{\pi c} \\
&\quad \times \frac{1}{\left(1 + \frac{|\vec{k}_n|}{E_n}\right) \left(1 + \frac{E_\pi}{E_p}\right)} \sum_{\mu \nu \xi} |Z_{\xi \nu}^\mu|^2
\end{aligned} \tag{F-7}$$

where α is the fine structure constant $\alpha = 1/137$ and $\beta = 0.079$. The factor $\left(1 + \frac{|\vec{k}_n|}{E_n}\right)$ is the relative velocity of the photon and the neutron in the center of momentum frame, and the phase space integration in the calculation of the cross section yields a factor of $\left(1 + \frac{E_\pi}{E_p}\right)$. We show angular distributions for the differential cross section and analyzing power for photon energies of $E_\gamma = 250, 300, 350$ and 400 MeV in figures F-2 to F-5. The analyzing power is due to a linearly polarized photon, with the polarization either in the scattering plane or perpendicular to the scattering plane. The data are from the compilation of pion photoproduction data of Menze, Pfeil and Wilcke [Me77]. At $E_\gamma = 250$ MeV the calculations and data agree quite well, but the calculation of differential cross section is slightly above the data at the largest angles. When we increase the photon energy to $E_\gamma = 300$ MeV (figure F-3) the shape of the cross section is reproduced although the calculation is slightly below the data for angles up to 100 degrees. The calculation does not reproduce the bump in the analyzing power data for angles larger than 90° , but the calculation is in agreement with the smaller angle data. For a photon energy of $E_\gamma = 350$ MeV, as shown in figure F-4, the calculated cross section is above the data for angles larger than 60° . The calculated analyzing power is smaller than the data for angles larger than 60° , but larger than the two data points at smaller angles. The last angular distribution we consider is figure F-5, where the photon energy is $E_\gamma = 400$ MeV. The calculated differential cross section is once again larger than the data for angles greater than 60° . The calculated analyzing power is below all but one data point at 60° .

The total cross section is obtained by integrating the differential cross sections over all angles, and is shown as a function of the total energy in the center of momentum frame in figure F-6. The data are from [Me77]. The solid line shows the cross section calculated with all the diagrams of figure F-1 included. The peak is shifted to higher energies relative to the data by 15 to 20 MeV, and the calculation remains above the data for center of momentum energies past the peak. We have given the delta a mass of 1232 MeV and a constant width of 120 MeV [Pa92]. The data can be reproduced by changing the mass of the delta and giving the width of the delta an energy dependence, as has been done by Walker [Wa69]. The parametrization is fairly arbitrary as the behaviour of the tail of the resonance is not well understood [Fe72], and so we will proceed with a constant width for

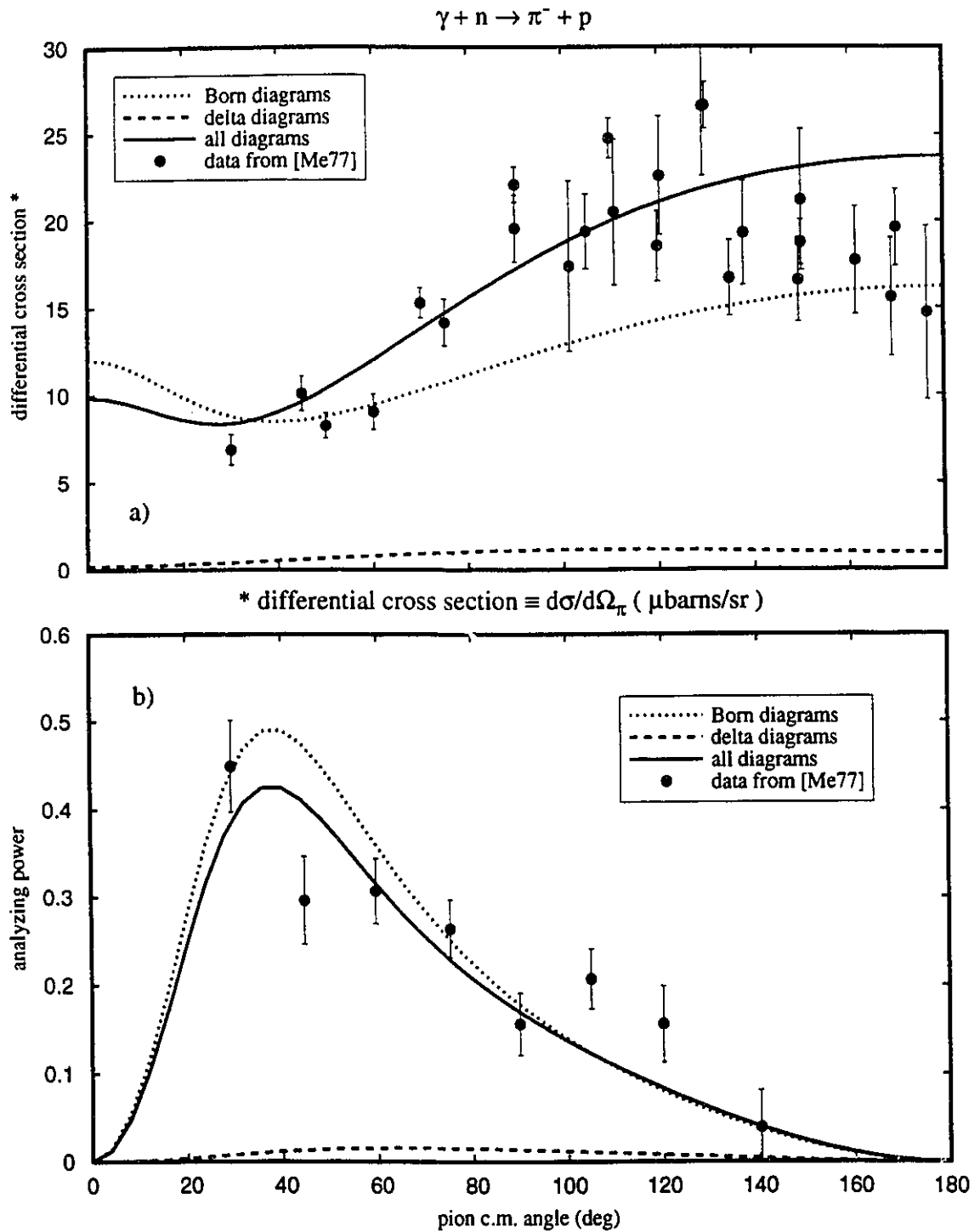


Figure F-2. Observables as a function of pion c.m. angle for negative pion photoproduction on a free neutron. The photon lab energy is $E_\gamma = 250$ MeV. The mass of the Δ is 1232 MeV, and its width is 120 MeV. a) differential cross section, b) analyzing power due to linearly polarized photons.

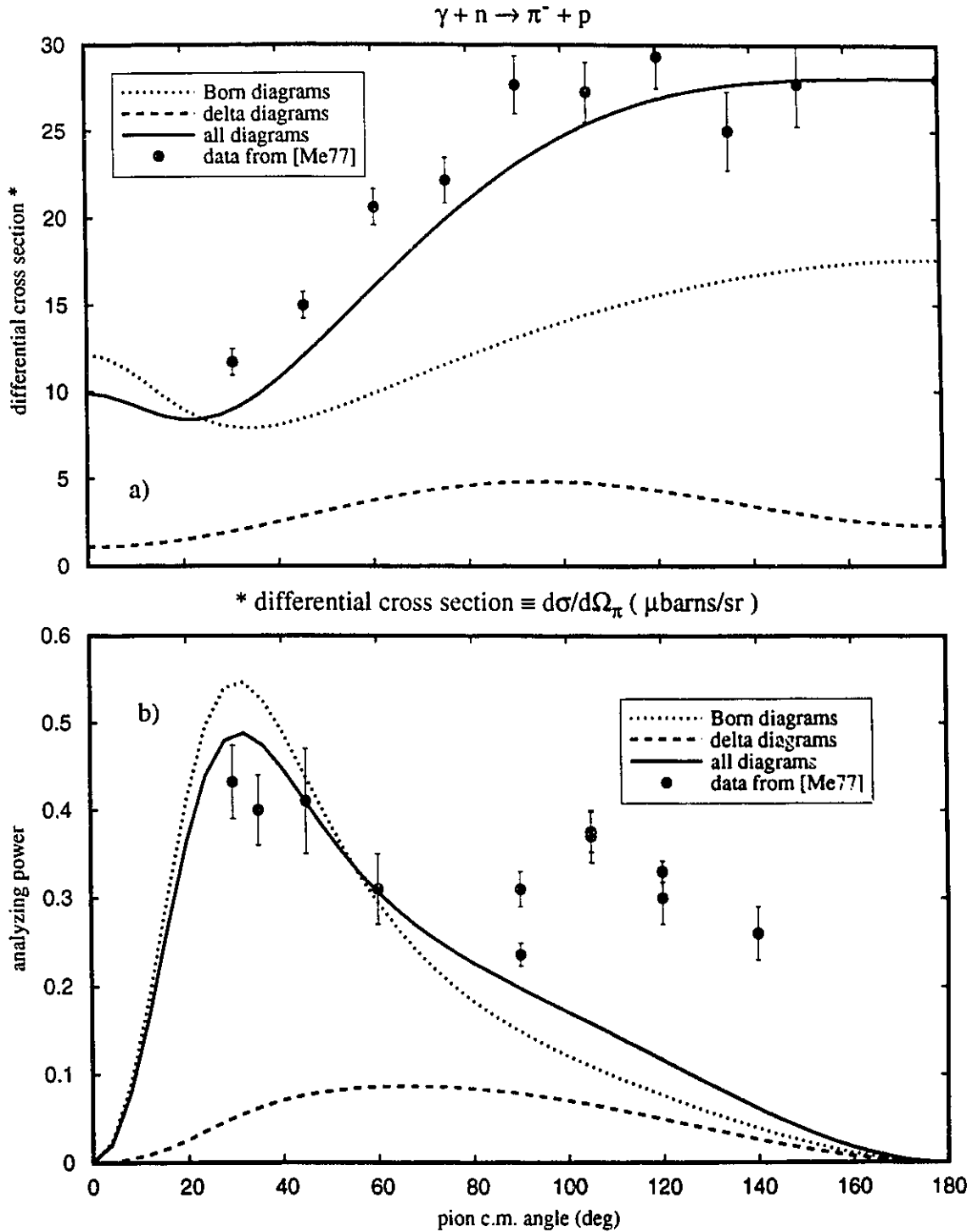


Figure F-3. Observables as a function of pion c.m. angle for negative pion photoproduction on a free neutron. The photon lab energy is $E_\gamma = 300$ MeV. The mass of the Δ is 1232 MeV, and its width is 120 MeV. a) differential cross section, b) analyzing power due to linearly polarized photons.

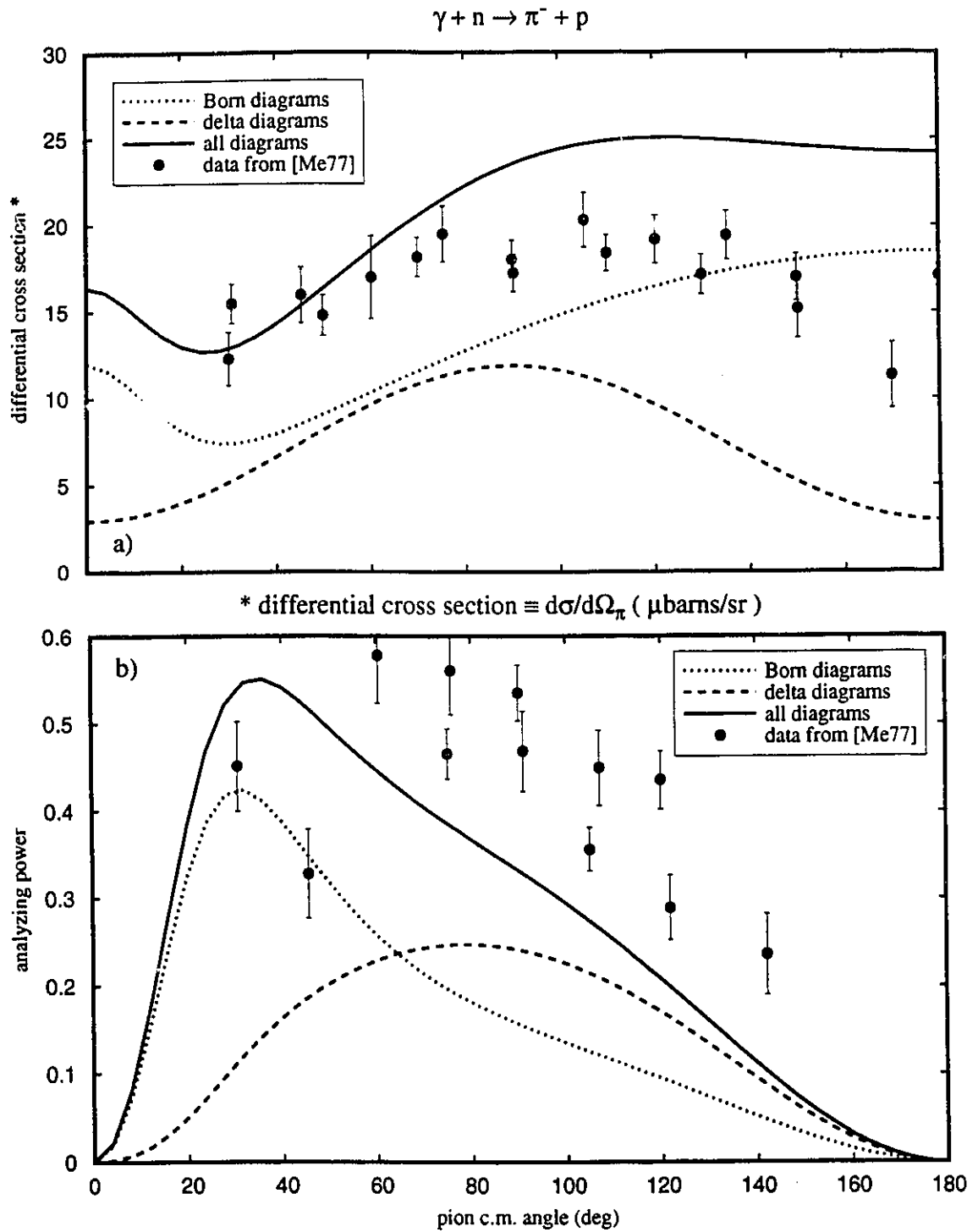


Figure F-4. Observables as a function of pion c.m. angle for negative pion photoproduction on a free neutron. The photon lab energy is $E_\gamma = 350$ MeV. The mass of the Δ is 1232 MeV, and its width is 120 MeV. a) differential cross section, b) analyzing power due to linearly polarized photons.

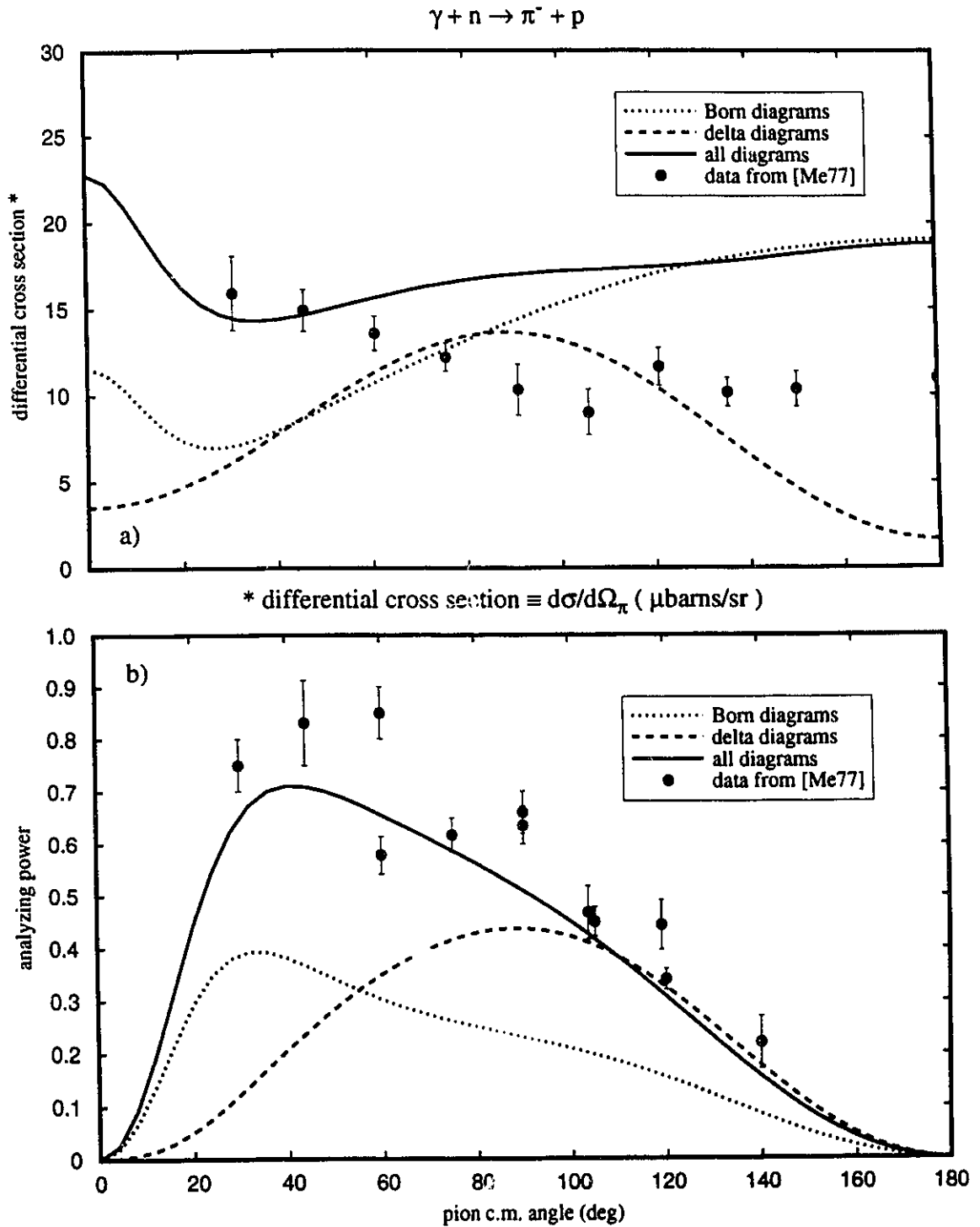


Figure F-5. Observables as a function of pion c.m. angle for negative pion photoproduction on a free neutron. The photon lab energy is $E_{\gamma} = 400$ MeV. The mass of the Δ is 1232 MeV, and its width is 120 MeV. a) differential cross section, b) analyzing power due to linearly polarized photons.

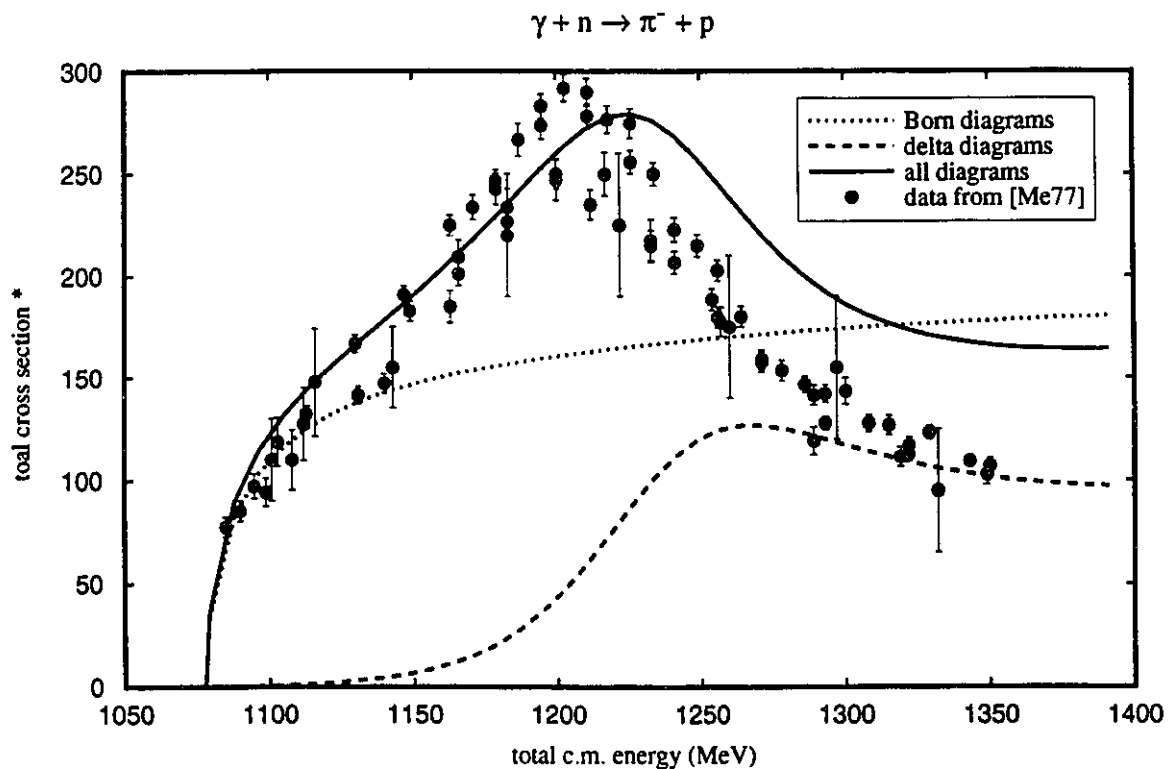


Figure F-6. Total cross section as a function of total center of mass energy. The mass of the Δ is 1232 MeV, and its width is 120 MeV. Dotted curve - Born diagrams only, dashed curve - delta diagrams, solid curve - all diagrams included.

the delta. The agreement of our simple model with the experimental data is not excellent, but improvement will require the introduction of parameters whose behaviour in the nuclear medium is not clear so we will restrict ourselves to the model of the delta we have examined.

F.2 The Pion Photoproduction Operator of Blomqvist and Laget

Starting from the lagrangian model of Olsson and Osypowski [Ol75], Blomqvist and Laget [BL77] developed a nonrelativistic operator for elementary pion photoproduction which they intended for use in nuclear physics applications.

Blomqvist and Laget [BL77] use the t-matrix for the pion photoproduction reaction, which is related to the s-matrix that we have written in equation F-4 through

$$S_{fi} = \delta_{fi} - i (2\pi)^4 \delta^4(k_p + k_\pi - k_n - k_\gamma) T_{fi} \quad (F-8)$$

The form of the t-matrix in the relativistic calculation can be found by comparing equations (F-4) and (F-8). The pion photoproduction operator of Blomqvist and Laget is obtained by taking a nonrelativistic limit. They include the Born terms a)-d) of figure F-1 as well as the s-channel delta diagram figure F-1e). The amplitudes for the various diagrams are written in momentum space and the nonrelativistic limit taken in the following way:

- i) in the vertex operators, baryon wave functions and the numerator of the propagators, terms of order p/m are saved where p is any momentum and m is the mass of the nucleon
- ii) treat the denominator of the propagator in a relativistic way to avoid possible cancellations between terms of order p/m of higher so the full matrix element is valid to order $(p/m)^2$
- iii) use the relativistic expression for the phase space factor
- iv) use relativistic kinematics.

The t-matrix for the Born terms can then be written as:

$$\begin{aligned}
T_{fi}^{\text{Born}} = \sqrt{2} e \frac{f_\pi}{m_\pi} < \frac{1}{2}, \mu | \left\{ \begin{aligned}
& i \vec{\sigma} \cdot \vec{\epsilon} - 2i \frac{\vec{\epsilon} \cdot \vec{k}_\pi \vec{\sigma} \cdot (\vec{k}_\gamma - \vec{k}_\pi)}{(k_\gamma - k_\pi)^2 - m_\pi^2} \\
& - i \frac{\vec{\epsilon} \cdot \vec{k}_p \vec{\sigma} \cdot \vec{k}_\pi}{E_u (p_u^0 - E_u)} + i \frac{E_\pi m_p \vec{\sigma} \cdot \vec{\epsilon}}{E_u (p_u^0 + E_u)} \\
& + \mu_p \frac{\vec{\sigma} \cdot (\vec{k}_\gamma \times \vec{\epsilon}) \vec{\sigma} \cdot \vec{k}_\pi}{2E_u (p_u^0 - E_u)} \\
& + \mu_n \frac{\vec{\sigma} \cdot \vec{k}_\pi \vec{\sigma} \cdot (\vec{k}_\gamma \times \vec{\epsilon})}{2E_s (p_s^0 - E_s)} \end{aligned} \right\} | \frac{1}{2}, \nu >
\end{aligned} \tag{F-9}$$

where the intermediate 4-momentum in the s-channel is $p_s = k_\pi + k_p$ while in the u-channel we have the momentum of the propagating particle as $p_u = k_p - k_\gamma$. Note that the propagating particles are off shell so that $p_u^0 \neq E_u = (\vec{p}_u^2 + m^2)^{1/2}$, and the same is true for the s-channel. The t-matrix for the s-channel delta diagram can be written as

$$\begin{aligned}
T_{fi}^\Delta = -\frac{\sqrt{2}}{3} f_{\gamma N \Delta} f_{\pi N \Delta} \frac{1}{p_\Delta^2 - m_\Delta^2 + i m_\Delta \Gamma} \\
< \frac{1}{2}, \mu | [\vec{S}^\dagger \cdot (\frac{E_\pi}{m_p} \vec{p}_\Delta - \vec{k}_\pi)] \\
[\vec{\epsilon} \cdot \vec{S} \times (\vec{k}_\gamma - \frac{m_\Delta - m_p}{m_p} \vec{k}_\pi)] | \frac{1}{2}, \nu >
\end{aligned} \tag{F-10}$$

The S_i are 4x2 matrices which connect spin 1/2 and spin 3/2 [SV68, Ar74] just as the isospin matrices of appendix A connect isospin 1/2 with isospin 3/2.

This operator has been used in a momentum space calculation of the (γ, π) reaction [Ta84], as well as DWIA calculations for the reaction $(\gamma, \pi^- p)$ [GS79a, GS79b, Ph89, Ph92].